

Analysis of the Mechanical Performance of a Biodegradable Magnesium Stent in a Remodelling Artery

Enda L. Boland B.E.



A thesis submitted to the National University of Ireland as fulfilment of
the requirements for the Degree of Doctor of Philosophy.

September 2018

Discipline of Biomedical Engineering,
College of Engineering and Informatics,
National University of Ireland Galway.

Supervisor: **Prof. Peter E. McHugh**

Contents

Abstract	vi
Acknowledgements	viii
List of Publications	ix
1 Introduction and Background.....	1
1.1 The Heart and Coronary Arteries	1
1.1.1 Coronary Artery Disease and Atherosclerosis	2
1.1.2 Treatments for Coronary Artery Disease	3
1.2 Coronary Stents	5
1.2.1 Plain Old Balloon Angioplasty	6
1.2.2 Bare Metal Stents	6
1.2.3 Drug Eluting Stents	8
1.2.4 Biodegradable Stents.....	8
1.3 Neointimal Remodelling - What happens after stenting?	10
1.4 Computational Modelling of Stents	11
1.5 Objectives of Thesis	12
1.6 Thesis Structure	13
References	15
2 Literature Review	21
2.1 Chapter Overview.....	21
2.2 Introduction	21
2.3 Magnesium	23
2.4 Corrosion of Magnesium.....	25
2.4.1 Micro-Galvanic Corrosion	25
2.4.2 Pitting Corrosion	26

2.4.3	Intergranular Corrosion.....	26
2.4.4	Stress Corrosion Cracking	27
2.4.5	Corrosion Fatigue.....	27
2.4.6	Uniform Corrosion	27
2.4.7	Corrosion of Biodegradable Magnesium Stents	27
2.5	Computational Models for Material Degradation	28
2.5.1	Uniform Corrosion Model.....	29
2.5.2	Stress Corrosion Model.....	31
2.5.3	Pitting Corrosion Model.....	32
2.5.4	Physically-based Corrosion Model	35
2.6	Computational Models for Remodelling of the Artery	37
	References	40
3	Computational Modelling of the Mechanical Performance of a Magnesium Stent Undergoing Uniform and Pitting Corrosion in a Remodelling Artery	47
3.1	Chapter Overview.....	47
3.2	Introduction	47
3.3	Methods	51
3.3.1	Stent and Stent Corrosion	51
3.3.2	Artery and Neointima.....	55
3.3.3	Boundary and Loading Conditions	59
3.3.4	Small Stented Artery Model.....	61
3.4	Results	62
3.4.1	Parameter Study – Properties of Magnesium Corrosion Product	62
3.4.2	Parameter Study – Properties of Activated Neointima	63
3.4.3	Pattern of Neointimal Formation	64

3.4.4	Stent Recoil vs Mass Loss due to Degradation.....	65
3.5	Discussion	67
3.5.1	Parameter Study – Properties of Magnesium Corrosion Product	67
3.5.2	Parameter Study – Properties of Activated Neointima	67
3.5.3	Pattern of Neointimal Formation	68
3.5.4	Stent Recoil vs Mass Loss due to Degradation.....	68
3.5.5	Limitations	71
3.6	Conclusion.....	72
References.....		73
4	Mechanical and Corrosion Testing of Magnesium WE43 Specimens for Pitting Corrosion Model Calibration	79
4.1	Chapter Overview.....	79
4.2	Introduction	79
4.3	Methods	82
4.3.1	Sample Preparation	82
4.3.2	Mechanical Testing.....	82
4.3.3	Immersion Testing	83
4.3.4	Corrosion Model Overview	90
4.3.5	Corrosion Model Calibration	90
4.4	Results	92
4.4.1	Mechanical Testing.....	92
4.4.2	Immersion Testing	94
4.4.3	Corrosion Model Calibration	99
4.5	Discussion	102
4.5.1	Mechanical Testing.....	102

4.5.2	Immersion Testing	102
4.5.3	Corrosion Model Calibration	103
4.5.4	Limitations	105
4.6	Conclusions	106
References		107
5	Computational Modelling of Magnesium Stent Mechanical Performance in a Remodelling Artery: Effects of Multiple Remodelling Stimuli.....	111
5.1	Chapter Overview.....	111
5.2	Introduction	111
5.3	Methods	115
5.3.1	Stent Deployment and Recoil (SDR) Model.....	117
5.3.2	Blood Flow (BF) Model.....	121
5.3.3	Neointimal Remodelling (NR) Model	123
5.4	Results	135
5.4.1	Stent Deployment and Recoil (SDR) Model.....	135
5.4.2	Blood Flow (BF) Model.....	137
5.4.3	Neointimal Remodelling (NR) Model	139
5.5	Discussion	147
5.5.1	Stent Deployment and Recoil (SDR) Model.....	147
5.5.2	Blood Flow (BF) Model.....	147
5.5.3	Neointimal Remodelling (NR) Model	148
5.5.4	Limitations	153
5.6	Conclusions	154
References		156
6	Conclusions and Recommendations	162

6.1	Chapter Overview.....	162
6.2	Thesis Summary.....	162
6.3	Main Findings of Thesis.....	163
6.4	Implications for Regulatory Approval Modelling.....	166
6.5	Recommendations for Future Research.....	166
6.6	Final Conclusions.....	168
	References.....	170

Abstract

Coronary stents made from degradable biomaterials such as magnesium alloy are an emerging technology in the treatment of coronary artery disease. Biodegradable stents provide mechanical support to the artery during the initial scaffolding period after which the artery will have remodelled. The subsequent resorption of the stent biomaterial by the body has potential to reduce the risk associated with long-term placement of these devices, such as in-stent restenosis, late stent thrombosis, and fatigue fracture. Computational modelling such as finite-element analysis has proven to be an extremely useful tool in the continued design and development of these medical devices. What is lacking in computational modelling literature is the representation of the active response of the arterial tissue in the weeks and months following stent implantation, i.e., neointimal remodelling. The phenomenon of neointimal remodelling is particularly interesting and significant in the case of biodegradable stents, when both stent degradation and neointimal remodelling can occur simultaneously, presenting the possibility of a mechanical interaction and transfer of load between the degrading stent and the remodelling artery.

A computational modelling framework is developed that combines magnesium alloy degradation and neointimal remodelling, which is capable of simulating both uniform (best case) and localised pitting (realistic) stent corrosion in a remodelling artery. The framework is used to evaluate the effects of the neointima on the mechanics of the stent, when the stent is undergoing uniform or pitting corrosion, and to assess the effects of the neointimal formation rate relative to the overall stent degradation rate (for both uniform and pitting conditions).

Experimental mechanical and corrosion testing is conducted to characterise the mechanical and corrosion behaviour of magnesium WE43 alloy, a candidate base material for biodegradable magnesium stents. Previously developed uniform and pitting corrosion models are calibrated based on in vitro mechanical and corrosion testing of magnesium WE43 alloy specimens. The calibrated pitting corrosion model can capture the mechanical and corrosion behaviour of magnesium WE43, including the

experimentally observed non-linear reduction in failure strength with mass loss, whereas the uniform corrosion model is incapable of capturing this trend.

An enhanced computational modelling framework is developed, building on the previous investigations, that combines magnesium alloy degradation and neointimal remodelling in order to simulate corrosion of a magnesium stent in a remodelling artery. The enhanced computational modelling framework, accounts for two major physiological stimuli responsible for neointimal remodelling and is combined with the magnesium stent pitting corrosion model, which has been calibrated for Mg WE43 alloy. The enhanced modelling framework is used to simulate different neointimal growth patterns and to explore the effects the neointimal remodelling has on the mechanical performance (scaffolding support) of a bioabsorbable magnesium stent.

In conclusion, the work performed in this thesis utilising computational modelling and experimental corrosion testing has led to an enhanced understanding of the mechanical performance of biodegradable magnesium stents in a remodelling artery.

Acknowledgements

Firstly, I would like to express my sincere gratitude to my supervisor, Prof. Peter McHugh for his knowledge, support and guidance.

I also wish to acknowledge the Irish Research Council for Science, Engineering and Technology and the College of Engineering and Informatics, NUI Galway who funded this PhD research and the SFI/HEA Irish Centre for High-End Computing (ICHEC) for the provision of computational facilities and support.

Thanks also to the NUI Galway technical staff particularly Mr. William Kelly, Mr. David Connolly, Mr. Pat Kelly, and Dr. Eadaoin Timmins for technical assistance and to Ms. Jane Bowman for all the help throughout the years.

I would like to thank all my friends and colleagues at NUI Galway especially the main men Donnacha, Conor, Brian, Shane, Paddy and Tarek.

I would like to thank Lisa for being a such welcome distraction from my work over the last few years.

Finally, to my parents Colm and Yvonne, and my sisters, Aisling and Sinead, thank you for always being there and for your support, encouragement, financial assistance and never-ending questions.

List of Publications

The work presented in this thesis has appeared in the following publications:

Chapter 2: Boland, E.L., Shine, R., Kelly, N., Sweeney, C.A., McHugh, P.E., 2016b. A Review of Material Degradation Modelling for the Analysis and Design of Bioabsorbable Stents. *Ann. Biomed. Eng.* 44, 341–356. <https://doi.org/10.1007/s10439-015-1413-5>

Chapter 3: Boland, E.L., Grogan, J.A., Conway, C., McHugh, P.E., 2016a. Computer Simulation of the Mechanical Behaviour of Implanted Biodegradable Stents in a Remodelling Artery. *JOM* 68, 1198–1203. <https://doi.org/10.1007/s11837-015-1761-5>

Boland, E.L., Grogan, J.A., McHugh, P.E., 2017. Computational Modeling of the Mechanical Performance of a Magnesium Stent Undergoing Uniform and Pitting Corrosion in a Remodeling Artery. *J. Med. Device.* 11, 021013. <https://doi.org/10.1115/1.4035895>

Chapter 4: Boland, E.L., Shirazi, R.N., Grogan, J.A., McHugh, P.E., 2018. Mechanical and Corrosion Testing of Magnesium WE43 Specimens for Pitting Corrosion Model Calibration. *Adv. Eng. Mater.* 1–11. <https://doi.org/10.1002/adem.201800656>

The following articles, arising from work in this thesis, are in submission:

Chapter 5: Boland, E.L., Grogan, J.A., McHugh, P.E., 2018. Computation Modelling of Magnesium Stent Mechanical Performance in a Remodelling Artery: Effects of Multiple Remodelling Stimuli

1 Introduction and Background

1.1 The Heart and Coronary Arteries

The heart is a muscular organ that pumps blood throughout the body, supplying oxygen and nutrients to the cells, tissues and other organs via the blood vessels of the circulatory system. The heart muscle itself, or myocardium, also requires a constant supply of blood to maintain normal function. The coronary arteries are narrow tubular vessels which originate at the base of the aorta (Figure 1.1) and distribute oxygen-rich blood throughout the myocardium.

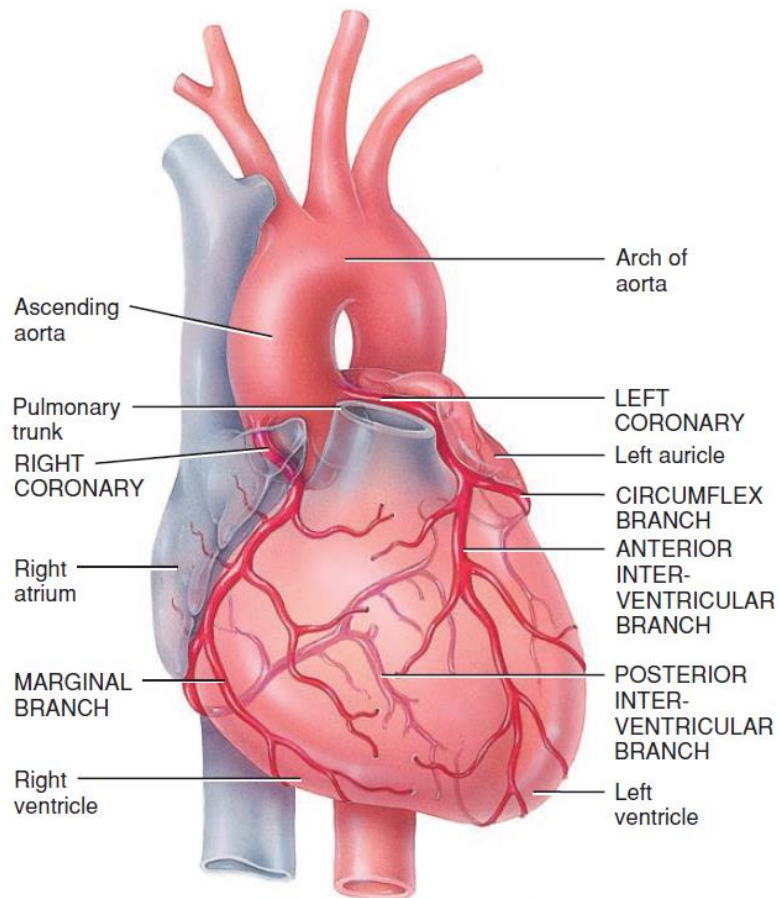


Figure 1.1. Anatomy of heart and coronary arteries (Tortora and Derrickson, 2014).

The walls of a typical coronary artery are shown in Figure 1.2, consisting of three distinct layers the intima, media and adventitia. The intima forms inner lining of the blood vessel and is lined with a layer of endothelial cells, or endothelium, which are in direct contact with the blood as it flows through the vessel. The central media layer consists of mainly smooth muscle cells and elastic fibres. It is responsible for constricting and dilating the vessel in response to stimuli to control blood flow and pressure. The adventitia is the most external layer of the artery. The adventitia consists of mainly collagen fibres and its primary function is to provide structural support and anchor the vessel to the myocardium.

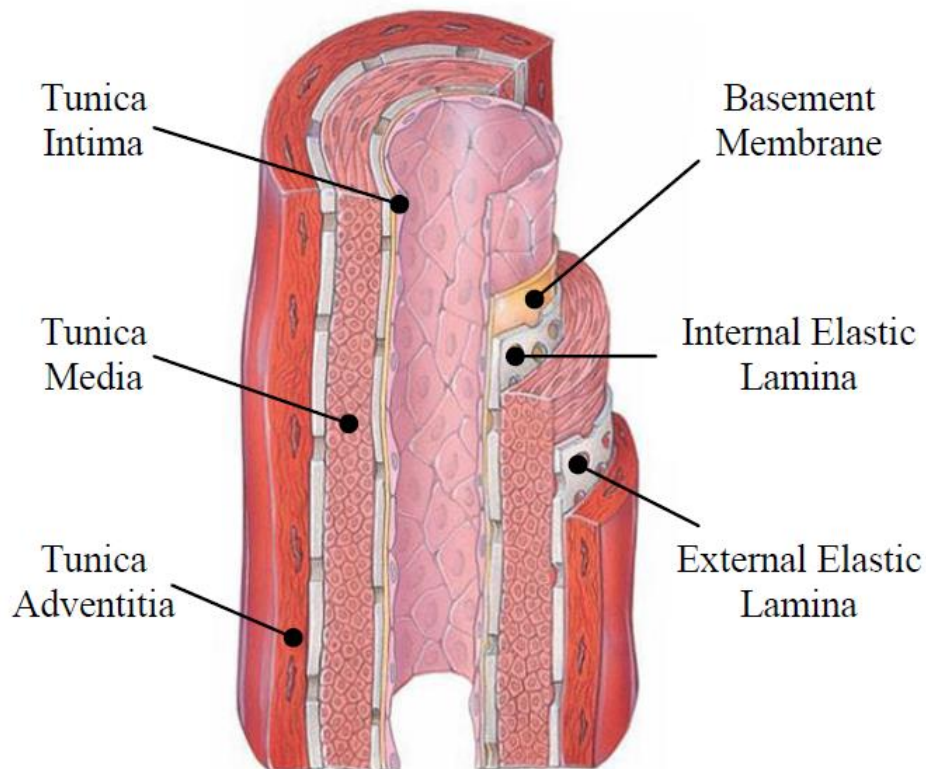


Figure 1.2. Cross section of a typical coronary artery illustrating intima, media and adventitia layers (Tortora and Derrickson, 2014).

1.1.1 Coronary Artery Disease and Atherosclerosis

Coronary artery disease (CAD) results from reduced blood flow in the coronary arteries that supply the myocardium. CAD, also known as coronary heart disease or ischemic heart disease, is the leading cause of death in Europe, accounting for 19 % in males and

20 % in females of all European deaths in 2016 (Townsend et al., 2016). CAD is defined as the narrowing or occlusion of the blood vessels of the heart typically caused by the accumulation of fatty deposits known as atherosclerotic plaque, within the intimal layer of the coronary arteries. This accumulation of plaque is called atherosclerosis and can also affect vessels other than the coronary arteries. Atherosclerotic plaques interfere with blood flow by blocking part of the lumen of the blood vessel.

Atherosclerosis of the coronary arteries can lead to a reduction in blood supply to the myocardium can cause chest pain (angina) in some individuals while others with the same condition may have no obvious signs or symptoms (Tortora and Derrickson, 2014).

Furthermore, atherosclerotic plaques form a roughened surface that can initiate the clotting mechanism, which can result in thrombus formation, completely blocking the coronary artery resulting in myocardial infarction (heart attack) (Rizzo, 2015).

Vulnerable atherosclerotic plaques are susceptible to rupture, which can result in thrombus formation at the plaque site or can cause the release of deposits, or emboli, into the blood stream which may cause myocardial infarction when they travel downstream and block a narrower section of the coronary artery (Sakakura et al., 2013).

1.1.2 Treatments for Coronary Artery Disease

The primary treatments for CAD are coronary artery bypass graft (CABG) and percutaneous coronary intervention (PCI). CABG, often simply referred to as bypass surgery, is a highly invasive traumatic surgical procedure for CAD treatment. The CABG procedure involves creating of an alternative route for the blood to flow from the aorta to the myocardial tissue and bypassing the blockage site of the coronary artery. The saphenous vein is first removed from the upper thigh. The saphenous vein graft is sutured to the base of the aorta at one end and to coronary artery downstream of the plaque location at the other end as illustrated in Figure 1.3.

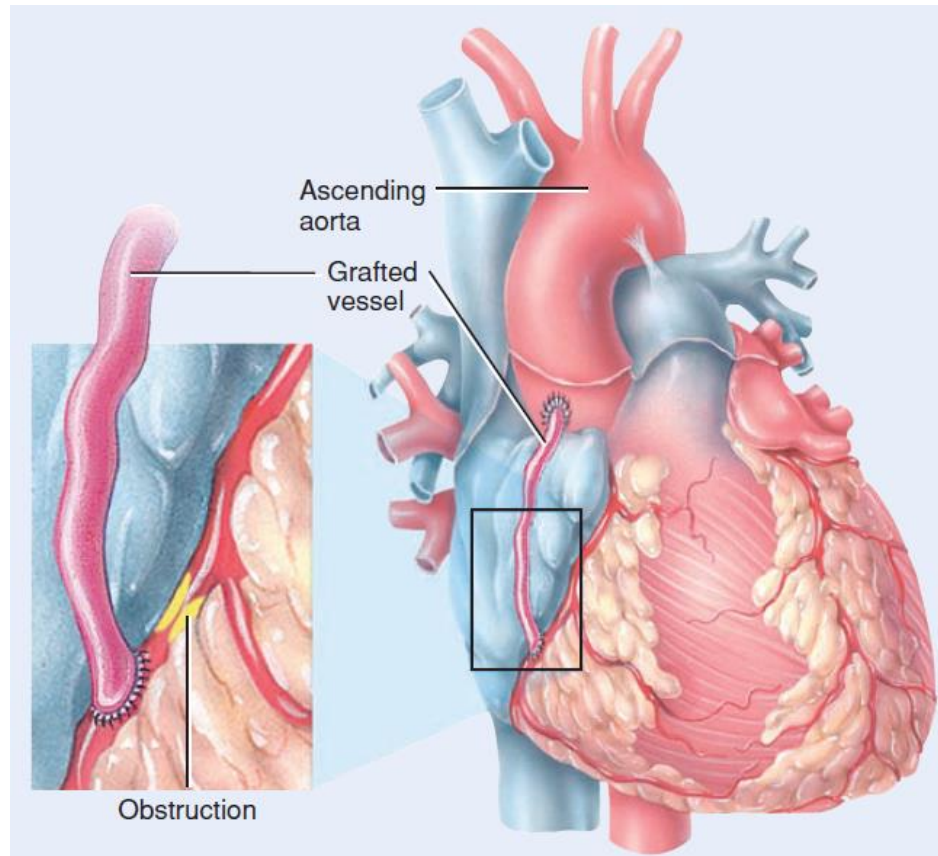


Figure 1.3. Illustration of the CABG procedure (Tortora and Derrickson, 2014).

Percutaneous coronary intervention (PCI), formerly known as balloon angioplasty with stent implantation, is a minimally invasive procedure for the treatment of CAD and has largely replaced CABG due to its success and relative safety. An illustration of the PCI procedure is provided in Figure 1.4 and involves creation of an incision in the femoral artery of the leg and insertion of a balloon-tipped catheter and crimped coronary stent. The balloon-tipped catheter and crimped stent are tracked through the vasculature via a guidewire and radiopaque markers until the stent is located at the site of the occlusion. Inflation of the balloon compresses the atherosclerotic plaque and deploys the stent, reopening the narrowed coronary artery and restoring blood flow to the myocardium. The balloon is deflated and along with the catheter is removed, while the stent remains in place to provide scaffolding support to artery and maintain the increased arterial lumen.

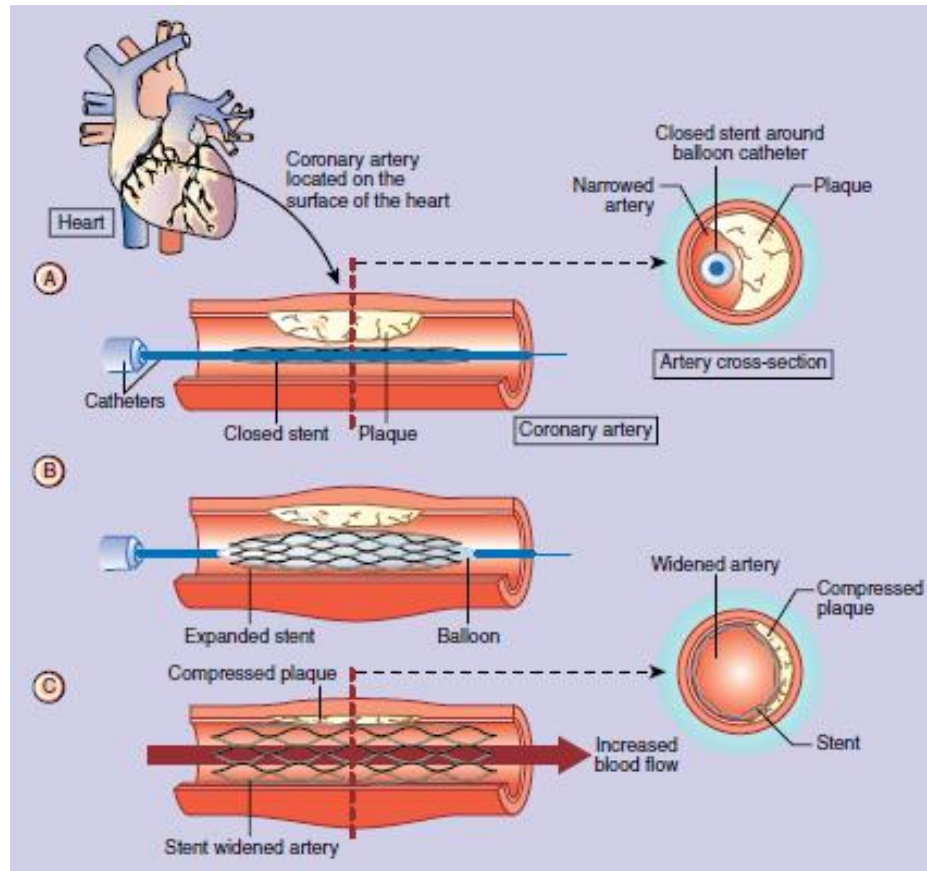


Figure 1.4. Image illustrating the PCI procedure (adapted from Peate and Nair, (2016)) showing (A) balloon-tipped catheter with crimped stent at the site of an atherosclerotic plaque occluding the coronary artery, (B) balloon inflation resulting in plaque compression and stent deployment, (C) deployed stent providing arterial scaffolding support to maintain the increased arterial lumen.

1.2 Coronary Stents

Coronary stents are small, tubular, expandable, mesh-like devices. Crimped coronary stents, before balloon expansion, must have a small outer diameter so the stent and balloon catheter delivery system can be navigated from the femoral artery to the narrow occlusion in the coronary vasculature. At the site of occlusion, the stent is expanded by the balloon to approximately three times the original crimped diameter. This change in diameter is facilitated by the opening of hinge-like geometries throughout the stent profile. Plastic deformation in the hinge region allows the stent to maintain its expanded shape after deflation of the balloon and prevent elastic recoil of the previously occluded artery.

Early permanent coronary stents were made from medical grade stainless steel (SS) 316L. Newer generations of permanent coronary stents are made from chromium containing alloys such as cobalt chromium (CC) L605 alloy (Abbott XIENCE, Biotronik PRO-Kinetic Energy), which has facilitated stent designs with thinner strut dimensions due to the superior mechanical properties of the chromium-based alloy. Some recently developed permanent stents (Medtronic RESOLUTE ONYX, Boston Scientific REBEL) have incorporated platinum into its base material, which has allowed development of thinner struts while simultaneously improving radiopacity of the device. Medtronic RESOLUTE ONYX is made from of a cobalt-based alloy shell surrounding a platinum-iridium alloy core, while the Boston Scientific REBEL stent is made from a platinum-chromium alloy.

There are numerous balloon expandable permanent coronary stents on the market today. The designs can be generally grouped into laser cut stents, where the stent geometry is cut from thin walled tubing, or less common wire stents, where a thin wire is manipulated into sinusoidal patterns that are welded at certain junctions along the length (Medtronic INTEGRITY, Medtronic RESOLUTE ONYX).

1.2.1 Plain Old Balloon Angioplasty

The first percutaneous procedure to treat CAD was performed by Grüntzig in 1977 (Grüntzig et al., 1979). A balloon angioplasty procedure without the deployment of a stent was performed, a treatment now often referred to as plain old balloon angioplasty (POBA). POBA undoubtable revolutionised the treatment of CAD at the time, however the success of this technique was compromised by high instances of re-blockage of the coronary arteries after treatment. This re-blockage was primarily caused by elastic recoil of the artery shortly after the procedure or by post-angioplasty restenosis (Iqbal et al., 2013; Simard et al., 2014).

1.2.2 Bare Metal Stents

Implantation of coronary bare metal stents (BMS) during PCI was introduced to address the problems of POBA, by providing radial support to the expanded artery and preventing elastic recoil and reducing instances of or by post-angioplasty restenosis. The

introduction of BMS significantly reduced the occurrence of vessel recoil and collapse, leading to a 30 % reduction in the overall incidence of restenosis when compared to balloon angioplasty alone (Fischman et al., 1994; Serruys et al., 1994).

A drawback to use of a BMS however is a high risk of developing in-stent restenosis (ISR) as illustrated in Figure 1.5. Injury to the vessel wall upon stent deployment results in proliferation and migration of vascular smooth muscle cells at the treatment site, leading to the formation of new tissue, called neointima, around the struts of the stent. Excessive neointima formation significantly reduces the lumen diameter of the artery, leading to re-occlusion of the vessel, which is known as ISR. Typically the treatment of ISR requires repeat surgery to re-open the vessel and restore blood flow, known as target lesion revascularisation (TLR).

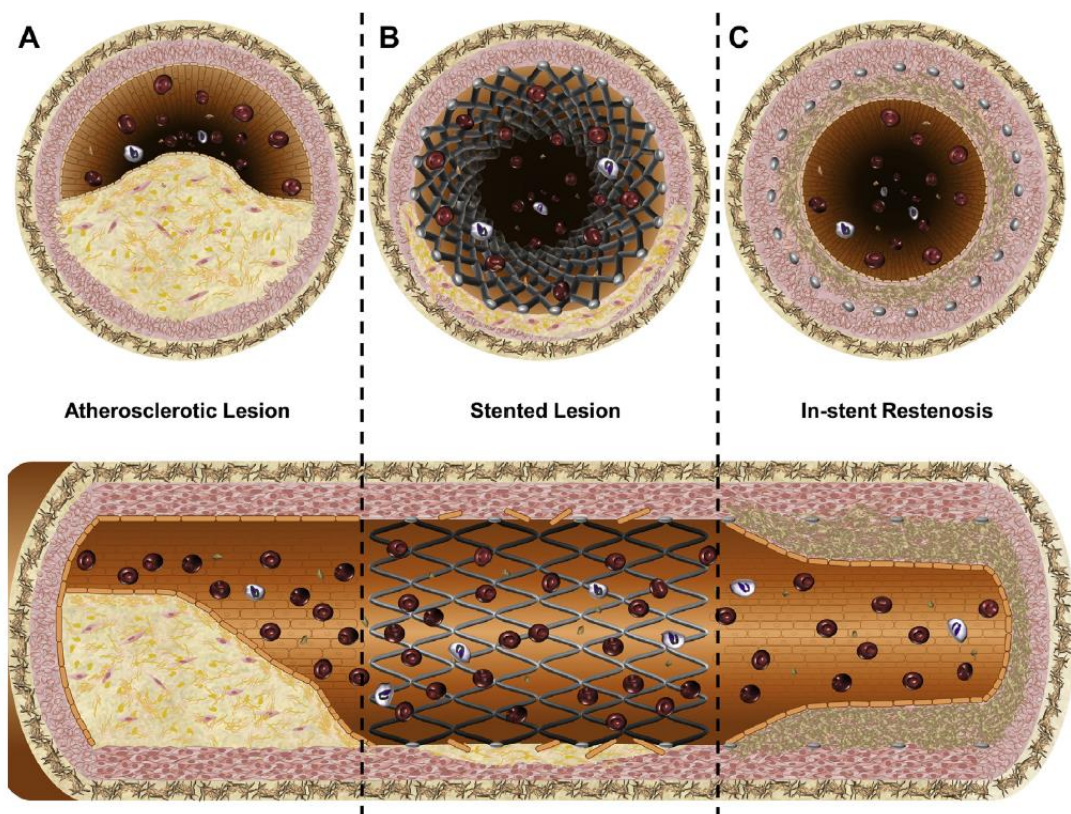


Figure 1.5. Cross sectional and longitudinal views of artery depicting progression of in-stent restenosis (ISR). (A) Atherosclerotic plaque causing obstruction to blood flow in the artery lumen. (B) After PCI and stent implantation, the atherosclerotic plaque is compressed, and the artery lumen is expanded restoring blood flow. (C) ISR after excessive neointima formation in response to PCI and stent implantation resulting in recurrence of an obstruction to blood flow in the artery. Adapted from Simard et al., (2014).

1.2.3 Drug Eluting Stents

A new generation of stents coated in a layer of anti-proliferative drugs was subsequently developed. These drugs inhibit the healing response of the body in the stented region and are contained in thin polymer coatings on the outer surface of the stent. The introduction of drug eluting stents (DES) resulted in a significant reduction in the incidence of ISR, in turn leading to reductions in the incidence of (TLR) of between 58% and 70% in DES relative to BMS (Stettler et al., 2007). This success has led to the widespread adoption of DES, which are now used in approximately 75% of all revascularizations (surgeries including PCI and coronary artery bypass grafting) in the US (Maluenda et al., 2009).

Despite the success of the current generation of DES leading to improved safety, concern persists over their long-term safety and the risk of late and very late stent thrombosis (ST) (Iqbal et al., 2013). ST is the sudden occlusion of a stent coronary artery due to the formation of a thrombosis. ST has extremely high associated incidences of death (approx. 20% - 40%) and myocardial infarction (approx. 50% to 70%) (Holmes et al., 2010). Early ST is defined as ST occurring within 1 month of stent implantation, late ST refers to the thrombotic event occurring between 1 month and 1 year after stent implantation, while very late ST refers to ST occurring beyond 1 year after stent implantation.

1.2.4 Biodegradable Stents

Significant research has been conducted in the area of coronary stents/scaffolds made from resorbable metallic and polymeric biomaterials, resulting in a number of these devices achieving approval for use in the European market (Sotomi et al., 2017). These next generation bioabsorbable stents have the potential to completely revolutionise the treatment of coronary artery disease.

It can be claimed the need for a stent is temporary as it is only required for the initial scaffolding period after which the artery will have remodelled (Hermawan et al., 2010), therefore stents made from degradable biomaterials such as PLLA (Gogas et al., 2012; Patel and Banning, 2013) and magnesium alloy (Erbel et al., 2007; Haude et al., 2016, 2013) are emerging.

The primary advantage of resorbable devices over permanent stents is their temporary presence which, from a theoretical point of view, means only a healed coronary artery will be left behind following degradation of the stent. Therefore, long term clinical problems associated with permanent stents such as ISR (Mitra and Agrawal, 2006), late ST (Holmes et al., 2010; Ong et al., 2005), stent fatigue fracture and the need for prolonged treatment with dual antiplatelet therapy (Garg and Serruys, 2010; Gomez-Lara et al., 2011) could be eliminated, while simultaneously restoring vasomotion of the artery. Furthermore, bioabsorbable stents permit the use of repeat treatments to the same site (Ormiston and Serruys, 2009) and have potential for use in areas of complex anatomy, where a conventional stent would permanently obstruct side branches (Ormiston and Serruys, 2009), or for paediatric patients (Zartner et al., 2005) where a conventional stent may become mechanically unstable in growing vessels.

Bioabsorbable stents have so far been designed from either metal or polymer materials. Metals generally have superior mechanical stiffness and strength compared to polymers, an attractive characteristic for use in load bearing applications such as coronary stents.

A review of the literature shows that metals such as magnesium alloys (Haude et al., 2017, 2013; Waksman et al., 2017; Zartner et al., 2005) and iron alloys (Peuster et al., 2001; Waksman et al., 2008) and polymers such as Poly(L-lactic acid) PLLA (Gogas et al., 2012; Tamai et al., 2000), Poly(lactic-co-glycolic acid) PLGA (Murphy et al., 1991) and Polycaprolactone (Tormala et al., 1998) have been the materials most commonly investigated for use in bioabsorbable stents.

Recently three stents/scaffolds made from a bioresorbable polymer, Poly(L-lactic acid) PLLA, have achieved market approval in Europe (CE marking), including the Abbott Absorb bioresorbable vascular scaffold (subsequently withdrawn), the Elixir Medical DESolve scaffold and the Arterial Remodelling Technologies Pure bioresorbable scaffold (Boland et al., 2016b; McMahon et al., 2018).

The Biotronik Magmaris resorbable scaffold made from a magnesium alloy (Figure 1.6) has also been approved in Europe (Biotronik, 2016) highlighting the considerable potential of these types of medical devices.

The focus of this work is on biodegradable magnesium stents/scaffold such as the Magmaris resorbable scaffold.



Figure 1.6. Image of Biotronik Magmaris resorbable magnesium scaffold crimped onto its balloon catheter delivery system (Biotronik, 2018).

1.3 Neointimal Remodelling - What happens after stenting?

The response of the artery to the stent is of critical importance to the long-term success of the PCI procedure. The ideal response of the artery to stenting is when the stent struts become covered in a new layer of tissue, called the neointima (Figure 1.7), with a perfectly functioning endothelium, through the action of cells such, as smooth muscles cells (SMCs) and endothelial cells, in the surrounding tissues.

Ideally, the SMCs proliferate enough to cover the stent struts in neointima, and after that the endothelium recovers its function and suppresses SMC growth (Zun et al., 2017). However, the healing is not always perfect. Sometimes, especially if the stent is covered in anti-proliferative drugs, the growth stops too early, leaving some struts uncovered, greatly increasing the risk of late ST formation (Finn et al., 2007; Holmes et al., 2010; Joner et al., 2006). In other cases, the growth is too intensive, and it causes a repeat narrowing of the lumen, or ISR (Figure 1.5).

Neointimal formation is modulated by several local factors, including the vessel wall trauma caused during stent deployment, the plaque burden, and the composition of the underlying plaque, as well as local endothelial shear stress (ESS) patterns (Bourantas et al., 2014).

The phenomenon of neointimal remodelling is particularly interesting and significant in the case of biodegradable stents, when both stent degradation and neointimal remodelling can occur simultaneously (Hermawan et al., 2010) presenting the possibility of a mechanical interaction and transfer of load between the degrading stent and the remodelling artery.

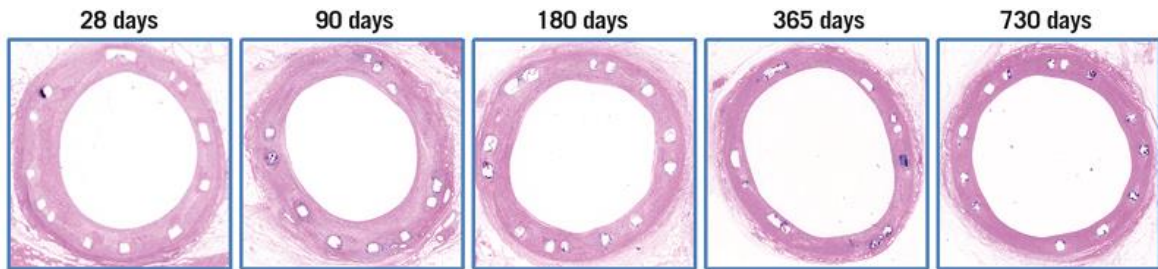


Figure 1.7. Representative H&E cross-sections of a Magmaris stent in a porcine artery at different timepoints up to two years post implantation. Neointimal remodelling causes the Magmaris stent struts to be encapsulated by the new neointimal tissue. Reprinted from EuroIntervention 13/4, Waksman et al., Second-generation magnesium scaffold Magmaris: device design and preclinical evaluation in a porcine coronary artery model, 440-449, Copyright (2017), with permission from Europa Digital & Publishing. (Waksman et al., 2017).

1.4 Computational Modelling of Stents

Computational modelling such as finite element (FE) analysis has proven to be an extremely useful tool in the continued design and development of medical devices such as coronary stents. Computational modelling of the mechanics of permanent balloon expandable coronary stents has received significant attention in the literature, and simulations relating to the entire stent lifecycle have been reported, including stent tracking to the diseased site, balloon expansion, recoil, *in-vivo* loading, drug-elution and fatigue fracture, for example as reported in Conway et al., (2014, 2012), Gervaso et al., (2008), Gijssen et al., (2008) Grogan et al., (2012), Sweeney et al., (2012), Zunino et al., (2009), and as reviewed in Martin and Boyle, (2011), McHugh et al., (2016), Morlacchi and Migliavacca, (2013). In contrast, due to their more recent emergence, the literature on computational modelling of the mechanics of both metallic and polymeric biodegradable stents is much more limited; example reports include Bobel et al., (2015), Debusschere et al., (2015), Grogan et al., (2013, 2011), Soares et al., (2008), Wu et al., (2013, 2011, 2010).

Further, for biodegradable stents, what is lacking in computational modelling literature is the representation of the active response of the arterial tissue in the weeks and months following stent implantation, i.e. neointimal remodelling.

1.5 Objectives of Thesis

The overall objectives of this thesis are (i) to develop a computational modelling framework in finite element analysis, capable of accurately simulating what happens in the artery after implantation of a magnesium stent, i.e. corrosion of the magnesium stent and neointimal remodelling of the artery and (ii) using the modelling framework, to investigate the effects of the presence of the neointima on the mechanical performance of the biodegrading magnesium stent.

The achievement of these objectives, i.e. the development of the modelling framework and the generation of an understanding of the combined degradation-remodelling mechanical effects, should be of significant use for the continued design, development and performance enhancement of these next generation medical devices.

The specific objectives of this thesis are as follows:

- To develop a remodelling framework capable of simulating corrosion of the magnesium stent and neointimal remodelling of the artery by combining/adapting two separate modelling approaches published in the literature; a continuum model for simulating the response of the artery to stenting (Lally and Prendergast, 2006) and uniform and pitting corrosion models for magnesium alloy (Grogan et al., 2011).
- Using the modelling framework, to investigate the effects of the presence of the neointima on the mechanical performance (scaffolding support) of the biodegrading stent
- To experimentally characterise the mechanical and corrosion behaviour of Mg WE43 and to determine the effect corrosion has on the mechanical integrity of the material.

- Using these results, to calibrate the previously developed uniform and pitting corrosion models (Grogan et al., 2011) for the Mg WE43 alloy. The corrosion models have been originally calibrated for Mg AZ31 alloy. The calibration for Mg WE43 alloy will allow the more appropriate usage of these computational models for application to the analysis of magnesium alloy stents.
- To build on the initial achievements of the thesis work, to develop an enhanced computational modelling framework that accounts for two major physiological stimuli responsible for neointimal remodelling, and to combine this with a pitting corrosion model calibrated for Mg WE43 alloy.
- Using the enhanced computational modelling framework, to simulate different neointimal growth patterns, to examine the transient change in lumen diameter due to neointimal remodelling and stent corrosion and to explore the effects the neointimal remodelling has on the mechanical performance (scaffolding support) of the bioabsorbable magnesium stent.

1.6 Thesis Structure

Chapter 1 contains an introduction and background to CAD, including details on the heart, coronary arteries, atherosclerosis, treatments for CAD, details on different types of coronary stents (BMS, DES and biodegradable stents), problems associated with stenting (ISR and ST), and details on how the artery responds to the stenting procedure. Also included in this chapter are the objectives of the thesis.

Chapter 2 outlines different types of corrosion that magnesium and magnesium alloys are susceptible to, and the current computational modelling techniques used to model magnesium material degradation of bioabsorbable stents. The content of this chapter has appeared in a review paper published in the *Annals of Biomedical Engineering*, which was co-written by this author (joint first author) (Boland et al., 2016b). Also included in Chapter 2 is brief review on continuum models used to model the response of the artery to stent implantation.

In **Chapter 3**, a computational modelling framework is developed that combines magnesium alloy degradation and neointimal remodelling, which is capable of

simulating both uniform (best case) and localised pitting (realistic) stent corrosion in a remodelling artery. The framework is used to evaluate the effects of the neointima on the mechanics of the stent, when the stent is undergoing uniform or pitting corrosion, and to assess the effects of the neointimal formation rate relative to the overall stent degradation rate (for both uniform and pitting conditions). The content of this chapter has been published in two journal articles, one in *JOM* (Boland et al., 2016a) and one in *Journal of Medical Devices* (Boland et al., 2017).

In **Chapter 4**, experimental mechanical and corrosion testing is conducted to characterise the mechanical and corrosion behaviour of magnesium WE43 alloy, a candidate base material for biodegradable magnesium alloy stents. Previously developed uniform and pitting corrosion models are subsequently recalibrated for the Mg WE43 alloy, based on the results of the mechanical and corrosion experiments. This content has appeared in an article published in *Advanced Engineering Materials* (Boland et al., 2018).

Chapter 5 builds on the previous investigations reported in Chapter 3 to develop a computational modelling framework that combines magnesium alloy degradation and neointimal remodelling in order to simulate corrosion of a magnesium stent in a remodelling artery. An enhanced computational modelling framework, using the continuum approach, that accounts for two major physiological stimuli responsible for neointimal remodelling is developed. This model is combined with the magnesium stent pitting corrosion model, which has been calibrated for Mg WE43 alloy as outlined in Chapter 4. The enhanced modelling framework is used to simulate different neointimal growth patterns and to explore the effects the neointimal remodelling has on the mechanical performance (scaffolding support) of a bioabsorbable magnesium stent. A journal paper based on the content of this chapter is in submission.

The primary conclusions of the thesis work are summarised and recommendations for future work are discussed in **Chapter 6**.

References

- Biotronik, 2018. Magmaris Resorbable Magnesium Scaffold (RMS) [WWW Document]. URL <https://www.biotronik.com/en-gb/products/coronary/magmaris> (accessed 8.23.18).
- Biotronik, 2016. BIOTRONIK Announces CE Mark for Magmaris, the First Clinically-Proven Bioresorbable Magnesium Scaffold [WWW Document]. URL [https://www.biotronik.com/files/F284043E451B1C61C1257FD2004B5842/\\$FILE/160615_BIOTRONIK_PR_Magmaris_CE_Approval_EN.pdf](https://www.biotronik.com/files/F284043E451B1C61C1257FD2004B5842/$FILE/160615_BIOTRONIK_PR_Magmaris_CE_Approval_EN.pdf) (accessed 8.2.16).
- Bobel, A.C., Petisco, S., Sarasua, J.R., Wang, W., McHugh, P.E., 2015. Computational Bench Testing to Evaluate the Short-Term Mechanical Performance of a Polymeric Stent. *Cardiovasc. Eng. Technol.* 6, 519–532. <https://doi.org/10.1007/s13239-015-0235-9>
- Boland, E.L., Grogan, J.A., Conway, C., McHugh, P.E., 2016a. Computer Simulation of the Mechanical Behaviour of Implanted Biodegradable Stents in a Remodelling Artery. *JOM* 68, 1198–1203. <https://doi.org/10.1007/s11837-015-1761-5>
- Boland, E.L., Grogan, J.A., McHugh, P.E., 2017. Computational Modeling of the Mechanical Performance of a Magnesium Stent Undergoing Uniform and Pitting Corrosion in a Remodeling Artery. *J. Med. Device.* 11, 021013. <https://doi.org/10.1115/1.4035895>
- Boland, E.L., Shine, R., Kelly, N., Sweeney, C.A., McHugh, P.E., 2016b. A Review of Material Degradation Modelling for the Analysis and Design of Bioabsorbable Stents. *Ann. Biomed. Eng.* 44, 341–356. <https://doi.org/10.1007/s10439-015-1413-5>
- Boland, E.L., Shirazi, R.N., Grogan, J.A., McHugh, P.E., 2018. Mechanical and Corrosion Testing of Magnesium WE43 Specimens for Pitting Corrosion Model Calibration. *Adv. Eng. Mater.* 1–11. <https://doi.org/10.1002/adem.201800656>
- Bourantas, C. V., Papafaklis, M.I., Kotsia, A., Farooq, V., Muramatsu, T., Gomez-Lara, J., Zhang, Y.J., Iqbal, J., Kalatzis, F.G., Naka, K.K., Fotiadis, D.I., Dorange, C., Wang, J., Rapoza, R., Garcia-Garcia, H.M., Onuma, Y., Michalis, L.K., Serruys, P.W., 2014. Effect of the endothelial shear stress patterns on neointimal proliferation following drug-eluting bioresorbable vascular scaffold implantation: An optical coherence tomography study. *JACC Cardiovasc. Interv.* 7, 315–324. <https://doi.org/10.1016/j.jcin.2013.05.034>
- Conway, C., McGarry, J.P., McHugh, P.E., 2014. Modelling of Atherosclerotic Plaque for Use in a Computational Test-Bed for Stent Angioplasty. *Ann. Biomed. Eng.* 42, 2425–2439. <https://doi.org/10.1007/s10439-014-1107-4>
- Conway, C., Sharif, F., McGarry, J.P., McHugh, P.E., 2012. A Computational Test-Bed to Assess Coronary Stent Implantation Mechanics Using a Population-Specific Approach. *Cardiovasc. Eng. Technol.* 3, 374–387. <https://doi.org/10.1007/s13239->

012-0104-8

- Debusschere, N., Segers, P., Dubruel, P., Verhegghe, B., De Beule, M., 2015. A finite element strategy to investigate the free expansion behaviour of a biodegradable polymeric stent. *J. Biomech.* 48, 2012–8. <https://doi.org/10.1016/j.jbiomech.2015.03.024>
- Erbel, R., Di Mario, C., Bartunek, J., Bonnier, J., de Bruyne, B., Eberli, F.R., Erne, P., Haude, M., Heublein, B., Horrigan, M., Ilesley, C., Böse, D., Koolen, J., Lüscher, T.F., Weissman, N., Waksman, R., 2007. Temporary scaffolding of coronary arteries with bioabsorbable magnesium stents: a prospective, non-randomised multicentre trial. *Lancet* 369, 1869–1875. [https://doi.org/10.1016/S0140-6736\(07\)60853-8](https://doi.org/10.1016/S0140-6736(07)60853-8)
- Finn, A. V., Joner, M., Nakazawa, G., Kolodgie, F., Newell, J., John, M.C., Gold, H.K., Virmani, R., 2007. Pathological correlates of late drug-eluting stent thrombosis: Strut coverage as a marker of endothelialization. *Circulation* 115, 2435–2441. <https://doi.org/10.1161/CIRCULATIONAHA.107.693739>
- Fischman, D.L., Leon, M.B., Baim, D.S., Schatz, R.A., Savage, M.P., Penn, I., Detre, K., Veltri, L., Ricci, D., Nobuyoshi, M., Cleman, M., Heuser, R., Almond, D., Teirstein, P.S., Fish, R.D., Colombo, A., Brinker, J., Moses, J., Shaknovich, A., Hirshfeld, J., Bailey, S., Ellis, S., Rake, R., Goldberg, S., 1994. A Randomized Comparison of Coronary-Stent Placement and Balloon Angioplasty in the Treatment of Coronary Artery Disease. *N. Engl. J. Med.* 331, 496–501. <https://doi.org/10.1056/NEJM199408253310802>
- Garg, S., Serruys, P.W., 2010. Coronary stents: Current status. *J. Am. Coll. Cardiol.* 56, S1–S42. <https://doi.org/10.1016/j.jacc.2010.06.007>
- Gervaso, F., Capelli, C., Petrini, L., Lattanzio, S., Di Virgilio, L., Migliavacca, F., 2008. On the effects of different strategies in modelling balloon-expandable stenting by means of finite element method. *J. Biomech.* 41, 1206–12. <https://doi.org/10.1016/j.jbiomech.2008.01.027>
- Gijzen, F.J.H., Migliavacca, F., Schievano, S., Socci, L., Petrini, L., Thury, A., Wentzel, J.J., van der Steen, A.F.W., Serruys, P.W.S., Dubini, G., 2008. Simulation of stent deployment in a realistic human coronary artery. *Biomed. Eng. Online* 7, 23. <https://doi.org/10.1186/1475-925X-7-23>
- Gogas, B., Farooq, V., Onuma, Y., Serruys, P., 2012. The ABSORB bioresorbable vascular scaffold: an evolution or revolution in interventional cardiology. *Hell. J. Cardiol.*
- Gomez-Lara, J., Brugaletta, S., Farooq, V., Onuma, Y., Diletti, R., Windecker, S., Thuesen, L., McClean, D., Koolen, J., Whitbourn, R., Dudek, D., Smits, P.C., Chevalier, B., Regar, E., Veldhof, S., Rapoza, R., Ormiston, J.A., Garcia-Garcia, H.M., Serruys, P.W., 2011. Head-to-head comparison of the neointimal response between metallic and bioresorbable everolimus-eluting scaffolds using optical

- coherence tomography. *JACC Cardiovasc. Interv.* 4, 1271–1280. <https://doi.org/10.1016/j.jcin.2011.08.016>
- Grogan, J.A., Leen, S.B., McHugh, P.E., 2013. Optimizing the design of a bioabsorbable metal stent using computer simulation methods. *Biomaterials* 34, 8049–8060. <https://doi.org/10.1016/j.biomaterials.2013.07.010>
- Grogan, J.A., Leen, S.B., McHugh, P.E., 2012. Comparing coronary stent material performance on a common geometric platform through simulated bench testing. *J. Mech. Behav. Biomed. Mater.* 12, 129–138. <https://doi.org/10.1016/j.jmbbm.2012.02.013>
- Grogan, J.A., O'Brien, B.J., Leen, S.B., McHugh, P.E., 2011. A corrosion model for bioabsorbable metallic stents. *Acta Biomater.* 7, 3523–3533. <https://doi.org/10.1016/j.actbio.2011.05.032>
- Grüntzig, A.R., Senning, Å., Siegenthaler, W.E., 1979. Nonoperative Dilatation of Coronary-Artery Stenosis. *N. Engl. J. Med.* 301, 61–68. <https://doi.org/10.1056/NEJM197907123010201>
- Haude, M., Erbel, R., Erne, P., Verheye, S., Degen, H., Bose, D., Vermeersch, P., Wijnbergen, I., Weissman, N., Prati, F., Waksman, R., Koolen, J., 2013. Safety and performance of the drug-eluting metal scaffold (DREAMS) in patients with de-novo coronary lesions: 12 month results of the prospective, multicentre, first-in-man BIOSOLVE-1 trial. *Lancet* 9, 836–844.
- Haude, M., Ince, H., Abizaid, A., Toelg, R., Lemos, P.A., Von Birgelen, C., Christiansen, E.H., Wijns, W., Neumann, F.J., Kaiser, C., Eeckhout, E., Lim, S.T., Escaned, J., Garcia-Garcia, H.M., Waksman, R., 2016. Safety and performance of the second-generation drug-eluting absorbable metal scaffold in patients with de-novo coronary artery lesions (BIOSOLVE-II): 6 month results of a prospective, multicentre, non-randomised, first-in-man trial. *Lancet* 387, 31–39. [https://doi.org/10.1016/S0140-6736\(15\)00447-X](https://doi.org/10.1016/S0140-6736(15)00447-X)
- Haude, M., Ince, H., Kische, S., Abizaid, A., Tölg, R., Lemos, P.A., Van Mieghem, N.M., Verheye, S., Von Birgelen, C., Christiansen, E.H., Wijns, W., Garcia-Garcia, H.M., Waksman, R., 2017. Sustained safety and clinical performance of a drug-eluting absorbable metal scaffold up to 24 months: Pooled outcomes of BIOSOLVE-II and BIOSOLVE-III. *EuroIntervention* 13, 432–439. <https://doi.org/10.4244/EIJ-D-17-00254>
- Hermawan, H., Dubé, D., Mantovani, D., 2010. Developments in metallic biodegradable stents. *Acta Biomater.* 6, 1693–1697. <https://doi.org/10.1016/j.actbio.2009.10.006>
- Holmes, D.R., Kereiakes, D.J., Garg, S., Serruys, P.W., Dehmer, G.J., Ellis, S.G., Williams, D.O., Kimura, T., Moliterno, D.J., 2010. Stent Thrombosis. *J. Am. Coll. Cardiol.* 56, 1357–1365. <https://doi.org/10.1016/j.jacc.2010.07.016>
- Iqbal, J., Gunn, J., Serruys, P.W., 2013. Coronary stents: Historical development, current status and future directions. *Br. Med. Bull.* 106, 193–211.

<https://doi.org/10.1093/bmb/ldt009>

- Joner, M., Finn, A. V., Farb, A., Mont, E.K., Kolodgie, F.D., Ladich, E., Kutys, R., Skorija, K., Gold, H.K., Virmani, R., 2006. Pathology of Drug-Eluting Stents in Humans. Delayed Healing and Late Thrombotic Risk. *J. Am. Coll. Cardiol.* 48, 193–202. <https://doi.org/10.1016/j.jacc.2006.03.042>
- Lally, C., Prendergast, P.J., 2006. Simulation of In-stent Restenosis for the Design of Cardiovascular Stents, in: Holzapfel, G., Ogden, R. (Eds.), *Mechanics of Biological Tissue SE* - 18. Springer Berlin Heidelberg, pp. 255–267. https://doi.org/10.1007/3-540-31184-X_18
- Maluenda, G., Lemesle, G., Waksman, R., 2009. A Critical Appraisal of the Safety and Efficacy of Drug-Eluting Stents. *Clin. Pharmacol. Ther.* 85, 474–480. <https://doi.org/10.1038/clpt.2009.8>
- Martin, D.M., Boyle, F.J., 2011. Computational structural modelling of coronary stent deployment: a review. *Comput. Methods Biomech. Biomed. Engin.* 14, 331–348. <https://doi.org/10.1080/10255841003766845>
- McHugh, P., Barakat, A., McGinty, S., 2016. Medical Stents: State of the Art and Future Directions. *Ann. Biomed. Eng.* 44, 274–275. <https://doi.org/10.1007/s10439-015-1526-x>
- McMahon, S., Bertollo, N., Cearbhaill, E.D.O., Salber, J., Pierucci, L., Duffy, P., Dürig, T., Bi, V., Wang, W., 2018. Bio-resorbable polymer stents: a review of material progress and prospects. *Prog. Polym. Sci.* 83, 79–96. <https://doi.org/10.1016/j.progpolymsci.2018.05.002>
- Mitra, A.K., Agrawal, D.K., 2006. In stent restenosis: bane of the stent era. *J. Clin. Pathol.* 59, 232–9. <https://doi.org/10.1136/jcp.2005.025742>
- Morlacchi, S., Migliavacca, F., 2013. Modeling stented coronary arteries: Where we are, where to go. *Ann. Biomed. Eng.* 41, 1428–1444. <https://doi.org/10.1007/s10439-012-0681-6>
- Murphy, J.G., Schwartz, R.S., Huber, K.C., Holmes Jr., D.R., 1991. Polymeric stents: modern alchemy or the future? *J Invasive Cardiol* 3, 144–148.
- Ong, A.T.L., McFadden, E.P., Regar, E., de Jaegere, P.P.T., van Domburg, R.T., Serruys, P.W., 2005. Late angiographic stent thrombosis (LAST) events with drug-eluting stents. *J. Am. Coll. Cardiol.* 45, 2088–92. <https://doi.org/10.1016/j.jacc.2005.02.086>
- Ormiston, J. a., Serruys, P.W.S., 2009. Bioabsorbable coronary stents. *Circ. Cardiovasc. Interv.* 2, 255–260. <https://doi.org/10.1161/CIRCINTERVENTIONS.109.859173>
- Patel, N., Banning, A.P., 2013. Bioabsorbable scaffolds for the treatment of obstructive coronary artery disease: the next revolution in coronary intervention? *Heart* 99, 1236–43. <https://doi.org/10.1136/heartjnl-2012-303346>

- Peate, I., Nair, M., 2016. *Fundamentals of Anatomy and Physiology - For Nursing and Healthcare Students*, 2nd Editio. ed. John Wiley & Sons.
- Peuster, M., Wohlsein, P., Brüggmann, M., Ehlerding, M., Seidler, K., Fink, C., Brauer, H., Fischer, A., Hausdorf, G., 2001. A novel approach to temporary stenting: Degradable cardiovascular stents produced from corrodible metal - Results 6-18 months after implantation into New Zealand white rabbits. *Heart* 86, 563–569.
- Rizzo, D.C., 2015. *Fundamentals of Anatomy & Physiology*, 3rd ed. Cengage Learning.
- Sakakura, K., Nakano, M., Otsuka, F., Ladich, E., Kolodgie, F.D., Virmani, R., 2013. Pathophysiology of atherosclerosis plaque progression. *Hear. Lung Circ.* 22, 399–411. <https://doi.org/10.1016/j.hlc.2013.03.001>
- Serruys, P.W., de Jaegere, P., Kiemeneij, F., Macaya, C., Rutsch, W., Heyndrickx, G., Emanuelsson, H., Marco, J., Legrand, V., Materne, P., Belardi, J., Sigwart, U., Colombo, A., Goy, J.J., van den Heuvel, P., Delcan, J., Morel, M., 1994. A Comparison of Balloon-Expandable-Stent Implantation with Balloon Angioplasty in Patients with Coronary Artery Disease. *N. Engl. J. Med.* 331, 489–495. <https://doi.org/10.1056/NEJM199408253310801>
- Simard, T., Hibbert, B., Ramirez, F.D., Froeschl, M., Chen, Y.X., O'Brien, E.R., 2014. The Evolution of Coronary Stents: A Brief Review. *Can. J. Cardiol.* 30, 35–45. <https://doi.org/10.1016/j.cjca.2013.09.012>
- Soares, J.S., Moore, J.E.J., Rajagopal, K.R., 2008. Constitutive Framework for Biodegradable Polymers with Applications to Biodegradable Stents. *ASAIO J.* 54, 295–301. <https://doi.org/10.1097/MAT.0b013e31816ba55a>
- Sotomi, Y., Onuma, Y., Collet, C., Tenekecioglu, E., Virmani, R., Kleiman, N.S., Serruys, P.W., 2017. Bioresorbable scaffold: The emerging reality and future directions. *Circ. Res.* 120, 1341–1352. <https://doi.org/10.1161/CIRCRESAHA.117.310275>
- Stettler, C., Wandel, S., Allemann, S., Kastrati, A., Morice, M.C., Schomig, A., Pfisterer, M.E., Stone, G.W., Leon, M.B., de Lezo, J.S., Goy, J.J., Park, S.J., Sabate, M., Suttrop, M.J., Kelbaek, H., Spaulding, C., Menichelli, M., Vermeersch, P., Dirksen, M.T., Cervinka, P., Petronio, A.S., Nordmann, A.J., Diem, P., Meier, B., Zwahlen, M., Reichenbach, S., Trelle, S., Windecker, S., Juni, P., 2007. Outcomes associated with drug-eluting and bare-metal stents: a collaborative network meta-analysis. *Lancet* 370, 937–948. [https://doi.org/10.1016/s0140-6736\(07\)61444-5](https://doi.org/10.1016/s0140-6736(07)61444-5)
- Sweeney, C.A., McHugh, P.E., McGarry, J.P., Leen, S.B., 2012. Micromechanical methodology for fatigue in cardiovascular stents. *Int. J. Fatigue* 44, 202–216. <https://doi.org/10.1016/j.ijfatigue.2012.04.022>
- Tamai, H., Igaki, K., Kyo, E., Kosuga, K., Kawashima, A., Matsui, S., Komori, H., Tsuji, T., Motohara, S., Uehata, H., 2000. Initial and 6-month results of biodegradable poly-L-lactic acid coronary stents in humans. *Circulation* 102, 399–

404.

- Tormala, P., Pohjonen, T., Rokkanen, P., 1998. Bioabsorbable polymers: materials technology and surgical applications. *Proc Inst Mech Eng H* 212, 101–111.
- Tortora, G., Derrickson, B., 2014. *Principles of Anatomy & Physiology*, 13th ed, Igarss 2014. Wiley. <https://doi.org/10.1007/s13398-014-0173-7.2>
- Townsend, N., Wilson, L., Bhatnagar, P., Wickramasinghe, K., Rayner, M., Nichols, M., 2016. Cardiovascular disease in Europe: Epidemiological update 2016. *Eur. Heart J.* 37, 3232–3245. <https://doi.org/10.1093/eurheartj/ehw334>
- Waksman, R., Pakala, R., Baffour, R., Seabron, R., Hellinga, D., Tio, F.O., 2008. Short-term effects of biocorrosible iron stents in porcine coronary arteries. *J. Interv. Cardiol.* 21, 15–20.
- Waksman, R., Zumstein, P., Pritsch, M., Wittchow, E., Haude, M., Lapointe-Corriveau, C., Leclerc, G., Joner, M., 2017. Second-generation Magnesium Scaffold Magmaris, Device Design, and Preclinical Evaluation in a Porcine Coronary Artery Model. *EuroIntervention* 38. <https://doi.org/10.4244/EIJ-D-16-00915>
- Wu, W., Chen, S., Gastaldi, D., Petrini, L., Mantovani, D., Yang, K., Tan, L., Migliavacca, F., 2013. Experimental data confirm numerical modeling of the degradation process of magnesium alloys stents. *Acta Biomater.* 9, 8730–8739. <https://doi.org/10.1016/j.actbio.2012.10.035>
- Wu, W., Gastaldi, D., Yang, K., Tan, L., Petrini, L., Migliavacca, F., 2011. Finite element analyses for design evaluation of biodegradable magnesium alloy stents in arterial vessels. *Mater. Sci. Eng. B Solid-State Mater. Adv. Technol.* 176, 1733–1740. <https://doi.org/10.1016/j.mseb.2011.03.013>
- Wu, W., Petrini, L., Gastaldi, D., Villa, T., Vedani, M., Lesma, E., Previtali, B., Migliavacca, F., 2010. Finite element shape optimization for biodegradable magnesium alloy stents. *Ann. Biomed. Eng.* 38, 2829–2840. <https://doi.org/10.1007/s10439-010-0057-8>
- Zartner, P., Cesnjevar, R., Singer, H., Weyand, M., 2005. First successful implantation of a biodegradable metal stent into the left pulmonary artery of a preterm baby. *Catheter. Cardiovasc. Interv.* 66, 590–4. <https://doi.org/10.1002/ccd.20520>
- Zun, P.S., Anikina, T., Svitenkov, A., Hoekstra, A.G., 2017. A comparison of fully-coupled 3D in-stent restenosis simulations to In-vivo Data. *Front. Physiol.* 8, 1–12. <https://doi.org/10.3389/fphys.2017.00284>
- Zunino, P., D'Angelo, C., Petrini, L., Vergara, C., Capelli, C., Migliavacca, F., 2009. Numerical simulation of drug eluting coronary stents: Mechanics, fluid dynamics and drug release. *Comput. Methods Appl. Mech. Eng.* 198, 3633–3644. <https://doi.org/10.1016/j.cma.2008.07.019>

2 Literature Review

2.1 Chapter Overview

This chapter presents a short review on the use of magnesium as a medical implant material, the different types of corrosion magnesium and magnesium alloys are susceptible to and the current techniques used in computational modelling of material degradation for bioabsorbable magnesium stents.

The content of this chapter has appeared in a review paper published in the *Annals of Biomedical Engineering*, which was co-written by this author (joint first author) (Boland et al., 2016b). Also included in Chapter 2 is brief review on continuum and discrete models used to model the response of the artery to stent implantation.

2.2 Introduction

Coronary stents have revolutionised the treatment of coronary artery disease. While coronary artery stenting is now relatively mature, significant scientific and technological challenges still remain, particularly in tackling the complications associated with long-term placement of the device.

One of the most fertile technological growth areas is biodegradable stents. It is possible to generate stents that will break down in the body once the initial necessary scaffolding period (6-12 months) (Hermawan et al., 2010) is past and which can promote arterial remodelling (Durand et al., 2014). Bioabsorbable stents have so far been designed from either metal or polymer materials. Such technologies permit the use of repeat treatments (surgical or percutaneous) to the same site (Ormiston and Serruys, 2009) and have potential for use in areas of complex anatomy, where a conventional stent would permanently obstruct side branches (Ormiston and Serruys, 2009), or for paediatric patients (Zartner et al., 2005) where a conventional stent may become mechanically unstable in growing vessels. Bioabsorbable stents present possibilities for the controlled local delivery of antiproliferative drugs, which could reduce the need for long-term use of antiplatelet therapy. Ultimately, bioabsorbable stents possess great potential in

addressing the long-term clinical problems associated with permanent stents, such as in-stent restenosis (Mitra and Agrawal, 2006), late stent thrombosis (Ong et al., 2005) and stent fatigue fracture (Sweeney et al., 2012) while effectively allowing the restoration of vasomotion potential.

From the perspective of designing new generation bioabsorbable stents, the phenomenon of biodegradation, through either surface corrosion in the case of metals (Grogan et al., 2011) or bulk degradation in the case of polymers (Shirazi et al., 2014), adds significant complications, in comparison to permanent stents. For example, capturing the effects of the *in-vivo* environment, including dynamic loading, blood-flow and neointimal remodelling, etc. on the rates of degradation or corrosion with computational techniques is a challenging task.

This has implications for the development and use of computational modelling for bioabsorbable stents, as part of the analysis and design process (Grogan et al., 2013; Wu et al., 2010).

A review of the literature shows that metals such as magnesium alloys (Haude et al., 2013, 2016b; Waksman et al., 2009; Zartner et al., 2005) and iron alloys (Peuster et al., 2001; Waksman et al., 2008) and polymers such as Poly(L-lactic acid) PLLA (Gogas et al., 2012; Tamai et al., 2000), Poly(lactic-co-glycolic acid) PLGA (Murphy et al., 1991), and Polycaprolactone (Tormala et al., 1998) have been the materials most commonly investigated for use in bioabsorbable stents.

Metals generally have superior mechanical stiffness and strength compared to polymers, an attractive characteristic for use in load bearing applications such as coronary stents. Magnesium and iron based alloys are considered favourable materials for bioabsorbable metallic stents as they both are naturally present in the human body, have good biocompatibility and have degradation products which do not cause toxicity (Hermawan et al., 2010; Zheng et al., 2014).

Problems associated with iron-based bioabsorbable stents include incompatibility with certain imaging devices (MRI) and slow *in-vivo* degradation rates reported in preliminary animal studies (Peuster et al., 2006; Zheng et al., 2014). To the best of the

authors' knowledge iron-based bioabsorbable stents have not proceeded beyond animal trail stage.

Magnesium-based bioabsorbable stents have progressed significantly faster with the Biotronik Magmaris resorbable scaffold, made from a magnesium alloy (Figure 1.6), achieving approval in Europe (Biotronik, 2016), highlighting the considerable potential of these types of medical devices.

Due to this advancement, and that iron stents would behave mechanically like permanent stents in the short to medium term, computational modelling (using finite elements (FE)) of bioabsorbable metallic stent degradation has been almost exclusively focused on magnesium alloy stents.

2.3 Magnesium

Magnesium (Mg) is the fourth most abundant element found within the human body and is easily absorbed and excreted by the human body (Staiger et al., 2006; Walker et al., 2014). High-purity magnesium is limited for use in many applications due to its low strength (Bowen et al., 2012; Campos et al., 2013). Magnesium alloys can provide improved mechanical strength (Gu et al., 2009), which is particularly important for use in load bearing applications, but typically alloying decreases corrosion resistance compared to high-purity magnesium (Song and Song, 2007).

Mg and its alloys are used as implants with a temporary function, such as plates and stents, which provide a temporary mechanical support and corrode completely after the tissue healing.

The use of magnesium and magnesium alloys in cardiovascular implants is not a new concept. The first clinical application was reported in 1878 by the physician Edward C. Huse, who successfully used magnesium wire ligatures to stop bleeding vessels (Huse, 1878; Witte, 2010).

The application of magnesium as a bioabsorbable metallic stent is a more recent development, which was begun around 1998 by Heublin and co-workers (Heublein et al., 2003; Witte, 2010). More recently, Biotronik have conducted three clinical trials

examining bioabsorbable stents using a magnesium alloy backbone as outlined in the recent review paper by Rapetto and Leoncini, (2017) and in Table 2.1.

The Biotronik AMS-1 (Absorbable Metallic Stent) was investigated during the Progress-AMS clinical trial (Erbel et al., 2007). To address the radial strength issues highlighted during the Progress-AMS trial, improvements were made to the stent geometric design and Mg WE43 base material. A paclitaxel-eluting drug and PLGA bioresorbable polymer were also added by Biotronik to the AMS and this device was subsequently termed the Drug-Eluting Absorbable Metal Scaffold or DREAMS. DREAMS was investigated during the BIOSOLVE-I clinical trial (Haude et al., 2013). Following the results of the BIOSOLVE-I clinical trial, further scaffold design refinements were conducted and the PLGA paclitaxel-eluting coating was replaced with a PLLA sirolimus-eluting coating, leading to the manufacture of the Biotronik second-generation DREAMS (DREAMS 2G). The DREAMS 2G was investigated during the BIOSOLVE-II clinical trial (Haude et al., 2016a). Following the success of the BIOSOLVE-II clinical trial, Biotronik DREAMS 2G, now known as the Biotronik Magmaris scaffold, achieved approval in Europe in June 2016 (Biotronik, 2016).

Table 2.1. Summary of recent research conducted on bioresorbable magnesium stents leading to the approval of the Biotronik Magmaris device in June 2016. Adapted from Rapetto and Leoncini, (2017).

BRS type	Study	Reference	Mg alloy	BRS design	Strut thickness, width/ cross-section shape	Crossing profile (mm)	Mg resorption time (month)	Drug type/elution	Polymer coating
Slottet-tube prototype	Animal model	Heublein <i>et al.</i> 2003	AE21	–	150–200 μm /uneven thickness, unpolished surface	–	1	No	No
Lekton Magic	Animal model	Di Mario <i>et al.</i> 2004	WE43	4 crown/4 links	165 μm x 80 μm / rectangular, polished surface	1.2	1	No	No
AMS1	PROGRESS- AMS	Erbel <i>et al.</i> 2007	WE43	4 crown/4 links	165 μm x 80 μm / rectangular, polished surface	1.6	1	No	No
AMS2	None	–	WE43 refined	4 crown/4 links	120 μm x 130 μm /squared, polished surface	1.5	2	No	No
AMS 3, DREAMS 1G	BIOSOLVE-I	Haude <i>et al.</i> 2013	WE43 refined	6 crown/3 links	120 μm x 130 μm /squared, polished surface	1.5	3	Paclitaxel 0.07 $\mu\text{g}/\text{mm}^2$	1 μm PLGA
DREAMS 2G, BIOSOLVE-II Magmaris	BIOSOLVE-II	Haude <i>et al.</i> 2015	WE43 refined	6 crown/2 links 2 markers	150 μm x 140 μm ?/ squared, polished surface	1.75	12	Sirolimus 1.4 $\mu\text{g}/\text{mm}^2$	7 μm PLLA

^{*}, 2.5 mm diameter stent: 120 μm strut thickness; 3.0–3.5 mm diameter stent: 150 μm strut thickness. Mg, magnesium; BRS, bioresorbable scaffolds.

2.4 Corrosion of Magnesium

Detailed reviews of magnesium degradation through corrosion can be found in Song and Atrens, (1999), Witte et al., (2008) and Zheng et al., (2014), a brief summary is presented here.

Magnesium and magnesium alloys are known to degrade in aqueous environments by an electrochemical reaction with water to produce magnesium hydroxide and hydrogen gas. The overall reaction equation is:



As shown by Equation 2.1, one molecule of hydrogen gas is produced for every atom of magnesium dissolved.

A thin oxide layer naturally forms on the surface of magnesium in air. When the magnesium is placed in an aqueous solution the oxide layer acts as a semipermeable barrier, resisting corrosion. Localised corrosion, in regions where the protective coating has broken down or is obstructed by the presence of impurities or at grain boundaries, can lead to the formation of local anodes and cathodes on the magnesium surface so that the above electrochemical reaction can occur.

Magnesium alloys when implanted *in-vivo* corrode by various mechanisms including, but not limited to: (a) micro-galvanic corrosion, (b) localised (pitting) corrosion, (c) intergranular corrosion, (d) stress corrosion cracking and (e) corrosion fatigue.

2.4.1 Micro-Galvanic Corrosion

Magnesium is one of the most anodic metals having a standard electrode potential of 2.38 V. Magnesium alloys are highly susceptible to micro-galvanic corrosion. Micro-galvanic corrosion is an electrochemical process where an anode (+), a cathode (-) and an electrolyte form a galvanic cell. This occurs at a local or micro level along the corrosion surface. The magnesium material tends to act as the anode, while alloying elements, impurities, or grain boundaries form the cathode as they usually contain a greater volume of more cathodic metals, such as aluminium and iron (Figure 2.1a). When the magnesium material comes in contact with a corrosive media (electrolyte), a

galvanic cell is formed, resulting in heavy localised corrosion in the anodic material adjacent to the cathode (Song and Atrens, 1999), as shown in Figure 2.1b.

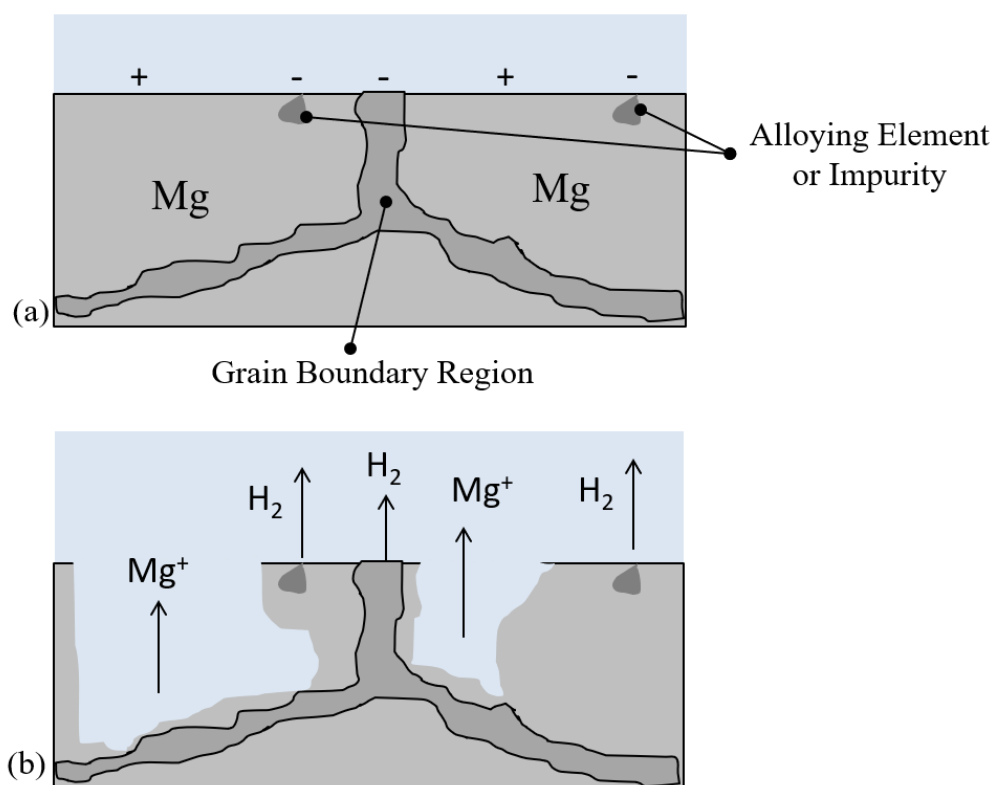


Figure 2.1. Schematic of the micro-galvanic corrosion process. (a) Grain boundaries, alloying elements or impurities at as local negative cathodes of the galvanic cell on the corrosion surface, while the adjacent magnesium forms the positive anodes of the galvanic cell. This results in emission of hydrogen gas at the cathode and corrosion of the adjacent anodic regions. Adapted from Grogan, (2013).

2.4.2 Pitting Corrosion

Pitting corrosion is a localised form of corrosion where holes, or pits, are produced in the material. Formation of pits in magnesium appears to be irregular and tends to spread laterally and cover the whole surface. There does not seem to be much tendency for deep pitting (Song and Atrens, 2007). The corrosion of magnesium alloys in neutral or alkaline salt solutions typically takes the form of pitting (Song and Atrens, 1999).

2.4.3 Intergranular Corrosion

Magnesium and magnesium alloys are virtually immune to intergranular corrosion. Corrosion does not penetrate inwards along the grain boundaries, because the grain-

boundary phases are invariably cathodic to the grain interior. Corrosion tends to be concentrated in the area adjoining the grain boundary, until eventually the grain may be undercut and falls out (Song and Atrens, 1999).

2.4.4 Stress Corrosion Cracking

Stress Corrosion Cracking (SCC) can occur in magnesium alloys subject to mechanical stress in a corrosive environment. SCC can cause the development of sub-critical crack growth under mechanical loading conditions considered to be safe. When the critical crack size is reached a combination of the crack plus the applied load causes sudden fracture formation and failure of the device (Winzer et al., 2005).

2.4.5 Corrosion Fatigue

Corrosion fatigue can occur when magnesium is subject to cyclic stress in a corrosive environment. Similar to SCC, it can lead to premature crack formation, and device failure at relatively low stress levels (Gastaldi et al., 2011).

2.4.6 Uniform Corrosion

Uniform corrosion is when corrosion occurs homogeneously over the entire exposed surface of the metal (e.g. rust formation on exposed surface of mild steel). However uniform corrosion is relatively unrealistic assumption for corrosion of uncoated magnesium and magnesium alloys as these materials in neutral or alkaline salt solutions are typically subject to localised pitting corrosion (Song and Atrens, 1999). Uniform corrosion represents the optimal corrosion behaviour due to its predictability and for the maintenance of structural integrity of the metal during the corrosion process, so it is often useful to compare realistic pitting corrosion behaviour with the optimal uniform corrosion case.

2.4.7 Corrosion of Biodegradable Magnesium Stents

The corrosion mechanism considered most relevant for the biodegradable magnesium stent application are micro-galvanic corrosion and pitting corrosion.

Biotronik have not disclosed the exact magnesium alloy used for the Magmaris bioresorbable scaffold. However an earlier magnesium alloy stent from Biotronik, the

AMS stent, was constructed from a magnesium alloy containing the same alloying elements as Mg WE43 alloy (yttrium, zirconium and rare earth metals) (Waksman et al., 2006). A recent review paper by Rapetto and Leoncini, (2017) has stated that the Magmaris scaffold is made from a refined Mg WE43 alloy, while separately Sotomi et al., (2017b) have reported that the Magmaris scaffold is made from a magnesium alloy with a composition of 93 % Mg and 7 % rare earth elements.

As mentioned previously, magnesium alloys such as Mg WE43 are susceptible to micro-galvanic corrosion when exposed to a corrosive media. This is the likely corrosion mechanism for the biodegradable magnesium stent. However, as highlighted by the observations in Chapter 4 (Mechanical and Corrosion Testing of Mg WE43 Specimens), the underlying micro-galvanic corrosion process leads to the development of macro-sized corrosion pits. Therefore, for the biodegradable magnesium stent application, micro-galvanic corrosion, leading to pitting corrosion, is considered the most important corrosion mechanism.

2.5 Computational Models for Material Degradation

A brief overview and key equations of degradation models applied to bioabsorbable magnesium stents is provided in Table 2.2. A detailed description of each is provided in subsequent sections.

Table 2.2. Summary of material degradation models that have been used to investigate the performance of bioabsorbable magnesium stents (Boland et al., 2016b).

Authors	Model Type	Brief Description	Key Equations	Code
Gastaldi <i>et al.</i> (2011)	Phenomological-uniform corrosion	Element deletion model using CDM methodology by introducing damage parameter for uniform corrosion D_U and effective Cauchy stress tensor $\tilde{\sigma}_ij$.	$\sigma_{ij} = \tilde{\sigma}_{ij}(1 - D)$ $\frac{dD_U}{dt} = \frac{\dot{\delta}_U}{L_e} K_U$	Abaqus/Explicit (VUSDFLD)
Gastaldi <i>et al.</i> (2011)	Phenomological-stress corrosion	Element deletion model using CDM methodology by introducing damage parameter for stress corrosion D_{SC} and effective Cauchy stress tensor $\tilde{\sigma}_ij$. Stress corrosion activated if equivalent stress is greater than threshold stress.	$\sigma_{ij} = \tilde{\sigma}_{ij}(1 - D)$ $\frac{dD_{SC}}{dt} = \frac{L_e}{\delta_{SC}} \left(\frac{S\sigma_{eq}^*}{1 - D_{SC}} \right)^R$ When $\sigma_{eq}^* \geq \sigma_{th} \geq 0$	Abaqus/Explicit (VUSDFLD)
Grogan <i>et al.</i> (2011)	Phenomological-uniform corrosion	Element deletion model using CDM methodology by introducing damage parameter for uniform corrosion D_U and effective Cauchy stress tensor $\tilde{\sigma}_ij$.	$\sigma_{ij} = \tilde{\sigma}_{ij}(1 - D)$ $\frac{dD_U}{dt} = \frac{\dot{\delta}_U}{L_e} K_U$	Abaqus/Explicit (VUMAT)
Grogan <i>et al.</i> (2011)	Phenomological-pitting corrosion	Element deletion model using CDM methodology by introducing damage parameter for uniform corrosion D_U and effective Cauchy stress tensor $\tilde{\sigma}_ij$.	$\sigma_{ij} = \tilde{\sigma}_{ij}(1 - D)$ $\frac{dD_p}{dt} = \frac{\dot{\delta}_U}{L_e} \lambda_e K_U$	Abaqus/Explicit (VUMAT)
Grogan <i>et al.</i> (2014)	Phenomological-uniform corrosion	ALE model utilising adaptive meshing which allows boundaries of the FE mesh to be moved independently. Corrosion rate directly inputted as velocity of moving stent surface.	-	Abaqus/Standard (UFIELD, UEXTERNALDB, UMESHMOTION)
Grogan <i>et al.</i> (2014)	Physical-uniform corrosion	Physical model based on the diffusion of metallic ions from the surface of the stent. Velocity of the moving stent surface depends on metallic ion concentration gradient.	$\mathbf{v} = \frac{D_{ion}(\nabla C \cdot \mathbf{n})}{C_{sol} - C_{sat}}$	Abaqus/Standard (UFIELD, UEXTERNALDB, UMESHMOTION)

2.5.1 Uniform Corrosion Model

Uniform corrosion modelling, where corrosion is considered to occur at a uniform rate over the exposed surface of the bioabsorbable stent, is perhaps the simplest form of bioabsorbable stent degradation modelling.

Gastaldi et al., (2011) and Grogan et al., (2011) used a continuum damage mechanics (CDM) approach to simulate uniform corrosion in bioabsorbable stent FE models by employing sequential finite element removal from the exterior surface of the bioabsorbable stent. Grogan et al., (2013) developed this further to model uniform corrosion using an arbitrary Lagrangian-Eulerian (ALE) adaptive meshing technique.

The CDM methodology introduces a local dimensionless damage parameter D which accounts for the loss of mechanical integrity of the stent material due to corrosion. In the FE context, for a partially corroded finite element, the elemental Cauchy stress σ_{ij} (the stress at the integration point, assuming a single integration point per 3D element) is related to the effective Cauchy stress (the stress in the remaining uncorroded material within the element) $\tilde{\sigma}_{ij}$ through the following:

$$\sigma_{ij} = \tilde{\sigma}_{ij}(1 - D) \quad (2.2)$$

Initially, when $D = 0$ the material in the element is undamaged but as corrosion progresses, D increases. When $D \approx 1$ the material is completely corroded and is no longer able to support stress ($\sigma_{ij} = 0$) and the element is removed from the model. This model is applied to surface elements exposed to the corrosive environment, and in turn to the elements in the new surface that is generated by element removal. In the particular case of uniform corrosion, the evolution of the (uniform) damage parameter D_U for surface elements is given by:

$$\frac{dD_U}{dt} = \frac{\delta_U}{L_e} k_U \quad (2.3)$$

where k_U is the material corrosion kinetic parameter, δ_U and L_e are the respective material and FE model characteristic lengths that are introduced to reduce finite element

mesh sensitivity. The approach was implemented in Abaqus/Explicit (DS SIMULIA, USA) by both groups through user subroutines VUSDFLD (Gastaldi et al., 2011) and VUMAT (Grogan et al., 2011). The models were initially calibrated using results from *in-vitro* immersion tests of magnesium alloy samples. Gastaldi et al., (2011) tested mass loss of cylindrical samples of five commercially available alloys. Grogan et al., (2011) recorded the mass loss rate of thin rectangular films of magnesium alloy AZ31 in load free and uniform tension states. Both calibrated uniform corrosion models accurately replicated the mass loss rates observed experimentally.

An arbitrary Lagrangian-Eulerian (ALE) implementation of the uniform corrosion model was presented by Grogan et al., (2013) as part of a geometrical optimisation strategy applied to bioabsorbable stents to highlight how the scaffolding ability of these devices can be prolonged by enhancing stent design. This approach utilises adaptive meshing which allows the boundaries of the FE mesh to be moved independently of the underlying material between analysis increments. This simulates the effects of material removal, as any material outside of the FE mesh in an increment does not contribute to mechanical behaviour, and the nodes on the external surface move at a velocity equal to the corrosion rate (in the form $[LT^{-1}]$) of the material. Grogan et al., (2013) used Abaqus/Standard (DS SIMULIA, USA) with the UMESHMOTION user subroutine. This approach is attractive as it is more efficient and less mesh sensitive than the element removal approaches, however less flexible in accounting for complex geometrical changes as would occur in localised corrosion representations (Grogan et al., 2011).

Uniform corrosion has been demonstrated to represent the best case scenario for bioabsorbable stent degradation, in terms of arterial scaffolding duration, in comparison to more inhomogeneous and localised corrosion mechanisms (Grogan et al., 2013, 2011). The above formulations, while simple to implement and powerful in simulating how an bioabsorbable stent would optimally perform, as presented, (Gastaldi et al., 2011; Grogan et al., 2013, 2011) do not account for the reality of localised surface corrosion or the possibility of stress modulated corrosion because they are controlled by

a prescribed uniform material corrosion rate. Enhanced formulations that address such issues are summarised below.

2.5.2 Stress Corrosion Model

Gastaldi et al., (2011) presented a Stress Corrosion (SC) model (implemented in Abaqus/Explicit) adapted from the work of da Costa-Mattos et al., (2008), who used CDM to create a model to describe the damage induced by SC in austenitic stainless steel. The evolution equation for the damage parameter in this (stress corrosion) case D_{SC} is:

$$\frac{dD_{SC}}{dt} = \frac{L_e}{\delta_{SC}} \left(\frac{S\sigma_{eq}^*}{1 - D_{SC}} \right)^R \quad (2.4)$$

when $\sigma_{eq}^* \geq \sigma_{th} \geq 0$ and $\frac{dD_{SC}}{dt} = 0$ when $\sigma_{eq}^* < \sigma_{th}$

where δ_{SC} and L_e are the respective material and FE model characteristic lengths, R and S are constants related to kinetics of the SC process and σ_{eq}^* is the equivalent stress for the SC mechanism (maximum principal stress in this case). If the value of equivalent stress σ_{eq}^* is below a threshold stress σ_{th} the SC process does not occur. A threshold stress of 50 % of the yield stress of magnesium alloy ZM21 was selected (Gastaldi et al., 2011).

Gastaldi et al., (2011) coupled the SC model with the uniform corrosion model described previously and applied both corrosion mechanisms to a bioabsorbable stent geometry. The initial results of the simulations were considered to be phenomenologically consistent with experimental observations. This coupled formulation was further studied by Wu et al., (2013, 2011) who completed *in-vitro* corrosion tests on two bioabsorbable stent designs (a patented stent design (CON) and an optimised stent design (OPT)) and compared results against simulated predictions for one ring models of the same designs, as shown in Figure 2.2, validating the overall applicability and practical usefulness of the model in stent design and performance assessment.

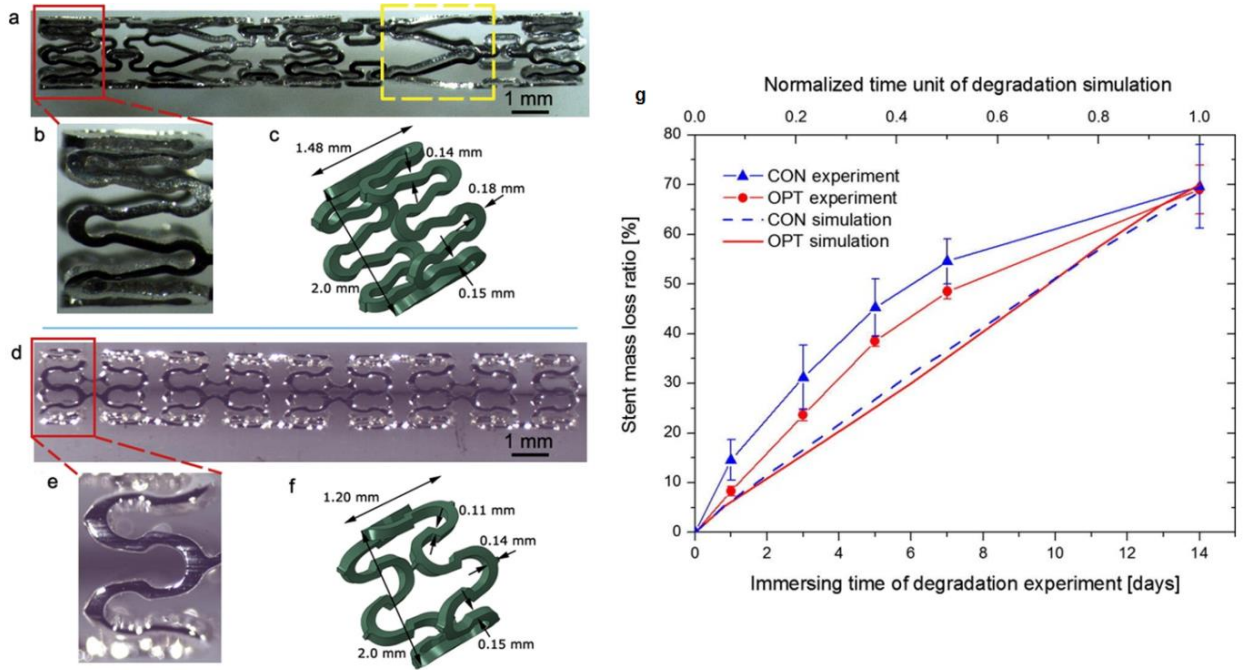


Figure 2.2 (a) The original configuration of a CON sample (a and b) and an OPT sample (d and e). The dimensions of the CON and OPT models in the simulation (c and f) are shown. Note that the CON model only considered the short ring of the CON design. (g) Mass loss ratio of the CON and OPT samples for the experiment and the corresponding models for the simulations (Wu et al., 2013).

However, magnesium alloys are subject to localised pitting corrosion *in-vivo* (Alvarez-Lopez and Pereda, 2010; Witte et al., 2006). Thus, the omission of the pitting corrosion mechanism in the coupled uniform and SC approach may be considered a limitation.

2.5.3 Pitting Corrosion Model

Grogan et al., (2011) presented a model for pitting corrosion by expanding on the aforementioned CDM uniform corrosion element removal model through the inclusion of a pitting parameter λ_e to capture the effects of localised or pitting corrosion. The phenomenological uniform and pitting corrosion models of Grogan et al., (2011), which were initially developed for use with the Abaqus/Explicit software have been subsequently adapted for use with the Abaqus/Standard software (Debusschere et al., 2016).

The evolution equation for the damage parameter in this (pitting corrosion) case D_p is:

$$\frac{dD_p}{dt} = \frac{\delta_U}{L_e} \lambda_e k_U \quad (2.5)$$

Each element on the corrosion surface is randomly assigned a pitting parameter λ_e through the use of Weibull distribution-based random number generator (Grogan et al., 2011). An element assigned a larger value of λ_e degrades faster than its neighbours and nucleates a surface pit when removed ($D_p \approx 1$). Subsequently, the elements adjacent to the pit are assigned pitting parameters λ_e given by:

$$\lambda_e = \beta \lambda_n \quad (2.6)$$

where λ_n is the pitting parameter of the pit nucleating element and β is a dimensionless parameter that controls the acceleration/deceleration of pit growth. In Grogan et al., (2011) the model parameters k_U , β and the Weibull probability distribution function were calibrated and the model quantitatively validated by comparison with results from three separate *in-vitro* immersion experiments which measured the corrosion rate of magnesium alloy AZ31 foils in (i) load free, (ii) corrosion followed by tensile loading, and (iii) corrosion during tensile loading cases (Grogan et al., 2011). The pitting corrosion model was then applied to a stent geometry based on the Biotronik AMS stent (Waksman, 2007; Waksman et al., 2006) and generated a stent degradation and collapse pattern that is qualitatively very similar to clinical trial observations for bioabsorbable stent, for example Waksman, (2007) as highlighted in Figure 2.3.

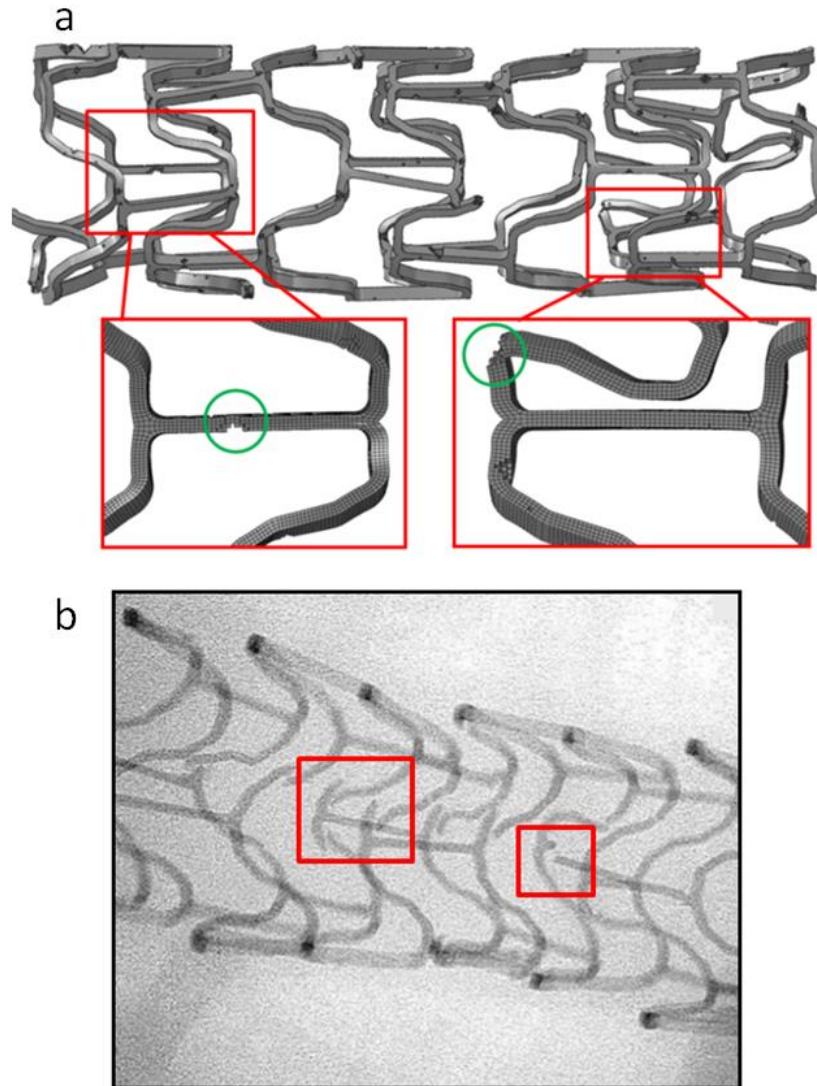


Figure 2.3 (a) Computational simulation of a magnesium stent subject to pitting corrosion model (Grogan et al., 2011). (b) In-vivo image of Biotronik AMS stent four weeks after implantation (Waksman, 2007).

Highlighted regions show qualitatively similar break regions due to corrosion.

A limitation of the pitting corrosion formulation as presented (Grogan et al., 2011) is the randomness of the location of pit nucleation. While pitting is certainly realistic (Song and Atrens, 1999), pit locations are more than likely influenced by sites of surface defects from the manufacturing process, surface defects from angioplasty procedure, or areas of stress concentration as motivated by the aforementioned work of Wu et al., (2013) who experimentally reported an increase in magnesium stent fractures in hinge regions.

2.5.4 Physically-based Corrosion Model

The formulations presented above can be fundamentally classified as phenomenological, in that they capture the overall phenomena of degradation (and are quantitatively calibrated to generate realistically meaningful predictions) but do not explicitly represent the multi-physics processes generating the degradation. In an attempt to address this in the context of bioabsorbable stent analysis, Grogan et al., (2014) presented a physically-based model that incorporates corrosion product (assumed to be magnesium ion) diffusion from the stent surface into the corrosive medium, using this as the controlling variable for the corrosion process, coupled with corroding stent surface retreat. The model used an ALE approach similar to that described above for uniform corrosion, without the limitation that corrosion had to be strictly spatially uniform and was implemented in Abaqus/Standard with UMESHMOTION. The model was used to simulate the behaviour of a hypothetical pure magnesium bioabsorbable stent, on the basis that pure magnesium, although inferior in terms of mechanical properties (Friedrich and Mordike, 2006), has a greater tendency to corrode through diffusion controlled ion transfer rather than micro-galvanic corrosion, making the model more physically appropriate.

Using the ALE approach, the corrosion surface moves at a velocity \mathbf{v} , determined through:

$$\mathbf{v} = \frac{D_{ion} (\nabla c \cdot \mathbf{n})}{c_{sol} - c_{sat}} \quad (2.7)$$

Where c_{sol} is the concentration of magnesium in the stent, c_{sat} is the saturation concentration of magnesium in the corrosive environment, D_{ion} is the diffusivity of magnesium ions in the corrosive environment, $(\nabla c \cdot \mathbf{n})$ is normal component of the magnesium ion concentration gradient vector ∇c , with \mathbf{n} as the local normal vector to the corrosion surface. Figure 2.4a shows a contour plot of predicted magnesium ion concentration in the corrosive environment over time. As the device corrodes its dimensions are reduced. The initially sharp edges of the device are rounded as corrosion

progresses, as shown in Figure 2.4b (Grogan et al., 2014). This model gives interesting insight into bioabsorbable stent degradation including the prediction of a simple power-law dependence of bioabsorbable stent mass (and hence scaffolding ability) on time, controlled by D_{ion} and c_{sat} .

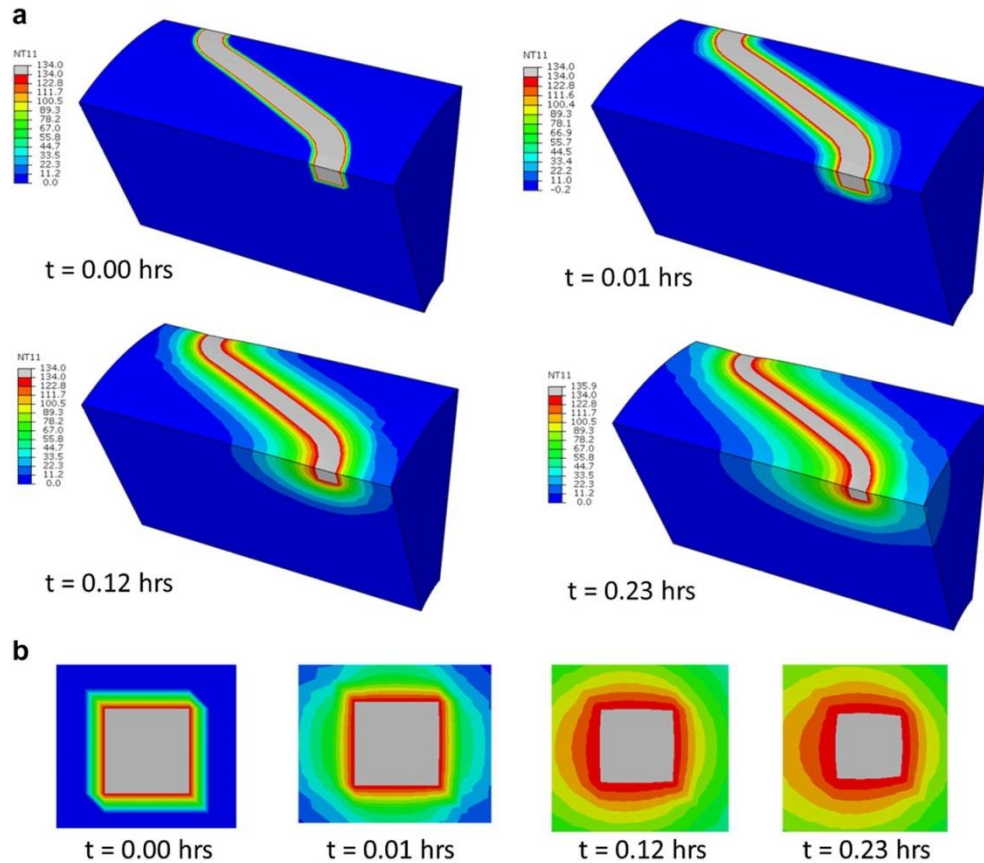


Figure 2.4 Contour plots from the physical corrosion model of predicted magnesium ion concentration in kg m^{-3} in the corrosive environment over time. In (a) the upper half of the model has been removed for illustrative purposes. Grey regions correspond to non-corroded metal. (b) Illustration of the changing dimensions of a cross-section of the hinge as it corrodes (Grogan et al., 2014).

The model is efficient and usable in its own right, but from a practical perspective it could be best used to calibrate the corrosion parameters (even as functions of time) in the simpler uniform corrosion formulation (Gastaldi et al., 2011; Grogan et al., 2011) described above to simulate bioabsorbable stent performance in different corrosive environments, at least for diffusion-controlled corrosion, given the practical usefulness of the uniform corrosion model (especially with stress dependence) (Wu et al., 2013).

Limitations of the model as presented (Grogan et al., 2014) include a focus on diffusion-control and a simple material system (pure magnesium) where micro-galvanic corrosion is less dominant. Multi-physics simulations for more complex magnesium alloys and the geometrical complexity of pitting would present challenges.

The corrosion models considered most appropriate for the computational approach utilised in this thesis are the phenomenological coupled stress and uniform corrosion model of Gastaldi et al., (2011) and the phenomenological pitting corrosion model of Grogan et al., (2011). Both of these corrosion modelling approaches have shown to accurately predict the corrosion behaviour of biodegradable magnesium stents as demonstrated by Wu et al., (2013) for the coupled stress and uniform corrosion model and in Figure 2.3 for the pitting corrosion model (Grogan et al., 2011).

For the computational simulations outlined in the following chapters, the magnesium stents are modelled at a device level scale, where micro-galvanic corrosion leading to pitting corrosion, is considered the principal corrosion mechanism. The pitting corrosion model (Grogan et al., 2011) is chosen over the coupled stress and uniform corrosion model (Gastaldi et al., 2011) going forward, as it is considered a more accurate representation of the principal corrosion mechanism.

The uniform corrosion model (Gastaldi et al., 2011; Grogan et al., 2011) is also used in the following chapters of this thesis, as a comparison of the ideal corrosion behaviour, with respect to maintaining mechanical integrity of the stent, with the more realistic pitting corrosion behaviour.

2.6 Computational Models for Remodelling of the Artery

In relation to the simulation of tissue remodelling, mechanobiological models for predicting the response of multicellular biological systems, for in-stent restenosis and neointimal development applications, have been reported. They can be grouped into two categories: (i) discrete cell based models (Boyle et al., 2011, 2010; Caiazzo et al., 2011; Nolan and Lally, 2018; Tahir et al., 2013; Zahedmanesh and Lally, 2012), such as cellular automata (CA) or agent-based models (ABM) and (ii) continuum models (Boland et al., 2017, 2016a; Lally and Prendergast, 2006), which usually can be

formulated in terms of partial differential equations in space and time (Hwang et al., 2009).

Discrete models such as CA and ABM use a bottom up approach where each individual cell is modelled explicitly. The behaviour of individual cells at a local level is governed by a set of rules, and the global behaviour of the system emerges through the local interaction of cells.

Finite element models used to quantify mechanical stresses in the artery after stenting have been coupled with discrete models to predict the collective response of the cells in the artery wall to tissue damage and the resulting in-stent restenosis or neointimal development. Such models have been initially developed in 2D (Boyle et al., 2011; Nolan and Lally, 2017; Zahedmanesh and Lally, 2012) but have been expanded for use on 3D geometries (Boyle et al., 2013).

Hoekstra and co-workers have also developed a multiscale model of in-stent restenosis. Here an ABM to predict smooth muscle cell proliferation and re-endothelization is fully coupled with CFD blood flow simulations. This multiscale model was initially developed for 2D (Caiazzo et al., 2011; Tahir et al., 2013) and has also recently been expanded to the predict neointimal development on 3D stent geometry (Zun et al., 2017). An advantage of using agent-based or CA approaches to model cell populations is their ability to better capture the discrete nature of events occurring at the cellular level (Nolan and Lally, 2017).

Continuum models have been utilised extensively in orthopaedic applications to model cell differentiation and predict tissue regeneration and bone remodelling (Burke and Kelly, 2012; Gómez-Benito et al., 2005; Lacroix et al., 2002; Scannell and Prendergast, 2009). Literature is much more limited on the use of continuum models to simulate the response of the artery to stenting when compared with cell-based models. However, Lally and Prendergast, (2006) successfully used a continuum damage model to simulate in-stent restenosis of the coronary arteries after stent deployment. The Lally and Prendergast, (2006) continuum damage model is initiated by elevated stresses in the coronary artery after stent implantation.

Continuum approaches, using partial differential equations, are more suited to modelling of the bulk material behaviour (Nolan and Lally, 2017), and they have the advantage of ease of implementation in the finite element context for practical stent performance simulations when compared to discrete models. For these reasons, the continuum approach is utilised by the models described in Chapter 3 and Chapter 5 of this thesis.

In Chapter 3, the Lally and Prendergast, (2006) continuum model is comprehensively explained as it is adapted and implemented in finite element software (Abaqus) to simulate neointimal remodelling of the coronary artery after magnesium stent implantation.

References

- Alvarez-Lopez, M., Pereda, M., 2010. Corrosion behaviour of AZ31 magnesium alloy with different grain sizes in simulated biological fluids. *Acta Biomater.*
- Biotronik, 2016. BIOTRONIK Announces CE Mark for Magmaris, the First Clinically-Proven Bioresorbable Magnesium Scaffold [WWW Document]. URL [https://www.biotronik.com/files/F284043E451B1C61C1257FD2004B5842/\\$FILE/160615_BIOTRONIK_PR_Magmaris_CE_Approval_EN.pdf](https://www.biotronik.com/files/F284043E451B1C61C1257FD2004B5842/$FILE/160615_BIOTRONIK_PR_Magmaris_CE_Approval_EN.pdf) (accessed 8.2.16).
- Boland, E.L., Grogan, J.A., Conway, C., McHugh, P.E., 2016a. Computer Simulation of the Mechanical Behaviour of Implanted Biodegradable Stents in a Remodelling Artery. *JOM* 68, 1198–1203. <https://doi.org/10.1007/s11837-015-1761-5>
- Boland, E.L., Grogan, J.A., McHugh, P.E., 2017. Computational Modeling of the Mechanical Performance of a Magnesium Stent Undergoing Uniform and Pitting Corrosion in a Remodeling Artery. *J. Med. Device.* 11, 021013. <https://doi.org/10.1115/1.4035895>
- Boland, E.L., Shine, R., Kelly, N., Sweeney, C.A., McHugh, P.E., 2016b. A Review of Material Degradation Modelling for the Analysis and Design of Bioabsorbable Stents. *Ann. Biomed. Eng.* 44, 341–356. <https://doi.org/10.1007/s10439-015-1413-5>
- Bowen, P.K., Drelich, J., Goldman, J., Buxbaum, R.E., Rajachar, R.M., 2012. New approaches in evaluating metallic candidates for bioabsorbable stents. *Emerg. Mater. Res.* 1, 237–255. <https://doi.org/10.1680/emr.12.00017>
- Boyle, C.J., Lennon, A.B., Early, M., Kelly, D.J., Lally, C., Prendergast, P.J., 2010. Computational simulation methodologies for mechanobiological modelling: a cell-centred approach to neointima development in stents. *Phil. Trans. R. Soc. A* 368, 2919–2935. <https://doi.org/10.1098/rsta.2010.0071>
- Boyle, C.J., Lennon, A.B., Prendergast, P.J., 2013. Application of a mechanobiological simulation technique to stents used clinically. *J. Biomech.* 46, 918–924. <https://doi.org/10.1016/j.jbiomech.2012.12.014>
- Boyle, C.J., Lennon, A.B., Prendergast, P.J., 2011. In Silico Prediction of the Mechanobiological Response of Arterial Tissue: Application to Angioplasty and Stenting. *J. Biomech. Eng.* 133, 081001. <https://doi.org/10.1115/1.4004492>
- Burke, D.P., Kelly, D.J., 2012. Substrate stiffness and oxygen as regulators of stem cell differentiation during skeletal tissue regeneration: A mechanobiological model. *PLoS One* 7. <https://doi.org/10.1371/journal.pone.0040737>
- Caiazzo, A., Evans, D., Falcone, J.L., Hegewald, J., Lorenz, E., Stahl, B., Wang, D., Bernsdorf, J., Chopard, B., Gunn, J., Hose, R., Krafczyk, M., Lawford, P., Smallwood, R., Walker, D., Hoekstra, A., 2011. A Complex Automata approach for in-stent restenosis: Two-dimensional multiscale modelling and simulations. *J.*

Comput. Sci. 2, 9–17. <https://doi.org/10.1016/j.jocs.2010.09.002>

- Campos, C.M., Muramatsu, T., Iqbal, J., Zhang, Y.J., Onuma, Y., Garcia-Garcia, H.M., Haude, M., Lemos, P.A., Warnack, B., Serruys, P.W., 2013. Bioresorbable drug-eluting magnesium-alloy scaffold for treatment of coronary artery disease. *Int. J. Mol. Sci.* 14, 24492–24500. <https://doi.org/10.3390/ijms141224492>
- da Costa-Mattos, H.S., Bastos, I.N., Gomes, J. a C.P., 2008. A simple model for slow strain rate and constant load corrosion tests of austenitic stainless steel in acid aqueous solution containing sodium chloride. *Corros. Sci.* 50, 2858–2866. <https://doi.org/10.1016/j.corsci.2008.07.020>
- Debusschere, N., Segers, P., Dubruel, P., Verheghe, B., De Beule, M., 2016. A Computational Framework to Model Degradation of Biocorrosible Metal Stents Using an Implicit Finite Element Solver. *Ann. Biomed. Eng.* 44, 382–390. <https://doi.org/10.1007/s10439-015-1530-1>
- Durand, E., Sharkawi, T., Leclerc, G., Raveleau, M., van der Leest, M., Vert, M., Lafont, A., 2014. Head-to-head comparison of a drug-free early programmed dismantling polylactic acid bioresorbable scaffold and a metallic stent in the porcine coronary artery: six-month angiography and optical coherence tomographic follow-up study. *Circ. Cardiovasc. Interv.* 7, 70–79. <https://doi.org/10.1161/CIRCINTERVENTIONS.113.000738>
- Erbel, R., Di Mario, C., Bartunek, J., Bonnier, J., de Bruyne, B., Eberli, F.R., Erne, P., Haude, M., Heublein, B., Horrigan, M., Ilesley, C., Böse, D., Koolen, J., Lüscher, T.F., Weissman, N., Waksman, R., 2007. Temporary scaffolding of coronary arteries with bioabsorbable magnesium stents: a prospective, non-randomised multicentre trial. *Lancet* 369, 1869–1875. [https://doi.org/10.1016/S0140-6736\(07\)60853-8](https://doi.org/10.1016/S0140-6736(07)60853-8)
- Friedrich, H.E., Mordike, B.L., 2006. *Magnesium technology*. Springer.
- Gastaldi, D., Sassi, V., Petrini, L., Vedani, M., Trasatti, S., Migliavacca, F., 2011. Continuum damage model for bioresorbable magnesium alloy devices - Application to coronary stents. *J. Mech. Behav. Biomed. Mater.* 4, 352–365. <https://doi.org/10.1016/j.jmbbm.2010.11.003>
- Gogas, B., Farooq, V., Onuma, Y., Serruys, P., 2012. The ABSORB bioresorbable vascular scaffold: an evolution or revolution in interventional cardiology. *Hell. J. Cardiol.*
- Gómez-Benito, M.J., García-Aznar, J.M., Kuiper, J.H., Doblaré, M., 2005. Influence of fracture gap size on the pattern of long bone healing: A computational study. *J. Theor. Biol.* 235, 105–119. <https://doi.org/10.1016/j.jtbi.2004.12.023>
- Grogan, J.A., 2013. *The Mechanical Performance of Permanent and Bioabsorbable Metal Stents*. National University of Ireland Galway.
- Grogan, J.A., Leen, S.B., McHugh, P.E., 2014. A physical corrosion model for

- bioabsorbable metal stents. *Acta Biomater.* 10, 2313–2322. <https://doi.org/10.1016/j.actbio.2013.12.059>
- Grogan, J.A., Leen, S.B., McHugh, P.E., 2013. Optimizing the design of a bioabsorbable metal stent using computer simulation methods. *Biomaterials* 34, 8049–8060. <https://doi.org/10.1016/j.biomaterials.2013.07.010>
- Grogan, J.A., O'Brien, B.J., Leen, S.B., McHugh, P.E., 2011. A corrosion model for bioabsorbable metallic stents. *Acta Biomater.* 7, 3523–3533. <https://doi.org/10.1016/j.actbio.2011.05.032>
- Gu, X., Zheng, Y., Cheng, Y., Zhong, S., Xi, T., 2009. In vitro corrosion and biocompatibility of binary magnesium alloys. *Biomaterials* 30, 484–498. <https://doi.org/10.1016/j.biomaterials.2008.10.021>
- Haude, M., Erbel, R., Erne, P., Verheye, S., Degen, H., Böse, D., Vermeersch, P., Wijnbergen, I., Weissman, N., Prati, F., Waksman, R., Koolen, J., 2013. Safety and performance of the drug-eluting absorbable metal scaffold (DREAMS) in patients with de-novo coronary lesions: 12 month results of the prospective, multicentre, first-in-man BIOSOLVE-I trial. *Lancet* 381, 836–844. [https://doi.org/10.1016/S0140-6736\(12\)61765-6](https://doi.org/10.1016/S0140-6736(12)61765-6)
- Haude, M., Ince, H., Abizaid, A., Toelg, R., Lemos, P.A., Von Birgelen, C., Christiansen, E.H., Wijns, W., Neumann, F.J., Kaiser, C., Eeckhout, E., Lim, S.T., Escaned, J., Garcia-Garcia, H.M., Waksman, R., 2016a. Safety and performance of the second-generation drug-eluting absorbable metal scaffold in patients with de-novo coronary artery lesions (BIOSOLVE-II): 6 month results of a prospective, multicentre, non-randomised, first-in-man trial. *Lancet* 387, 31–39. [https://doi.org/10.1016/S0140-6736\(15\)00447-X](https://doi.org/10.1016/S0140-6736(15)00447-X)
- Haude, M., Ince, H., Abizaid, A., Toelg, R., Lemos, P.A., Von Birgelen, C., Christiansen, E.H., Wijns, W., Neumann, F.J., Kaiser, C., Eeckhout, E., Lim, S.T., Escaned, J., Onuma, Y., Garcia-Garcia, H.M., Waksman, R., 2016b. Sustained safety and performance of the second-generation drug-eluting absorbable metal scaffold in patients with de novo coronary lesions: 12-month clinical results and angiographic findings of the BIOSOLVE-II first-in-man trial. *Eur. Heart J.* 37, 2701–2709. <https://doi.org/10.1093/eurheartj/ehw196>
- Hermawan, H., Dubé, D., Mantovani, D., 2010. Developments in metallic biodegradable stents. *Acta Biomater.* 6, 1693–1697. <https://doi.org/10.1016/j.actbio.2009.10.006>
- Heublein, B., Rohde, R., Kaese, V., Niemeyer, M., Hartung, W., Haverich, A., 2003. Biocorrosion of magnesium alloys: a new principle in cardiovascular implant technology? *Heart* 89, 651–6. <https://doi.org/10.1136/HEART.89.6.651>
- Huse, E.C., 1878. A new ligature. *Chicago Med J Exam* 172.
- Hwang, M., Garbey, M., Berceci, S.A., Tran-Son-Tay, R., 2009. Rule-based simulation of multi-cellular biological systems-a review of modeling techniques. *Cell. Mol.*

- Bioeng. 2, 285–294. <https://doi.org/10.1007/s12195-009-0078-2>
- Lacroix, D., Prendergast, P.J., Li, G., Marsh, D., 2002. Biomechanical model to simulate tissue differentiation and bone regeneration: application to fracture healing. *Med. Biol. Eng. Comput.* 40, 14–21. <https://doi.org/10.1007/BF02347690>
- Lally, C., Prendergast, P.J., 2006. Simulation of In-stent Restenosis for the Design of Cardiovascular Stents, in: Holzapfel, G., Ogden, R. (Eds.), *Mechanics of Biological Tissue SE* - 18. Springer Berlin Heidelberg, pp. 255–267. https://doi.org/10.1007/3-540-31184-X_18
- Mitra, A.K., Agrawal, D.K., 2006. In stent restenosis: bane of the stent era. *J. Clin. Pathol.* 59, 232–9. <https://doi.org/10.1136/jcp.2005.025742>
- Murphy, J.G., Schwartz, R.S., Huber, K.C., Holmes Jr., D.R., 1991. Polymeric stents: modern alchemy or the future? *J Invasive Cardiol* 3, 144–148.
- Nolan, D.R., Lally, C., 2018. An investigation of damage mechanisms in mechanobiological models of in-stent restenosis. *J. Comput. Sci.* 24, 132–142. <https://doi.org/10.1016/j.jocs.2017.04.009>
- Nolan, D.R., Lally, C., 2017. Coupled finite element-agent-based models for the simulation of vascular growth and remodeling. *Numer. Methods Adv. Simul. Biomech. Biol. Process.* 283–300. <https://doi.org/10.1016/B978-0-12-811718-7.00016-2>
- Ong, A.T.L., McFadden, E.P., Regar, E., de Jaegere, P.P.T., van Domburg, R.T., Serruys, P.W., 2005. Late angiographic stent thrombosis (LAST) events with drug-eluting stents. *J. Am. Coll. Cardiol.* 45, 2088–92. <https://doi.org/10.1016/j.jacc.2005.02.086>
- Ormiston, J. a., Serruys, P.W.S., 2009. Bioabsorbable coronary stents. *Circ. Cardiovasc. Interv.* 2, 255–260. <https://doi.org/10.1161/CIRCINTERVENTIONS.109.859173>
- Peuster, M., Hesse, C., Schloo, T., Fink, C., Beerbaum, P., von Schnakenburg, C., 2006. Long-term biocompatibility of a corrodible peripheral iron stent in the porcine descending aorta. *Biomaterials* 27, 4955–62.
- Peuster, M., Wohlsein, P., Brüggmann, M., Ehlerding, M., Seidler, K., Fink, C., Brauer, H., Fischer, A., Hausdorf, G., 2001. A novel approach to temporary stenting: Degradable cardiovascular stents produced from corrodible metal - Results 6-18 months after implantation into New Zealand white rabbits. *Heart* 86, 563–569.
- Rapetto, C., Leoncini, M., 2017. Magmaris: A new generation metallic sirolimus-eluting fully bioresorbable scaffold: Present status and future perspectives. *J. Thorac. Dis.* 9, S903–S913. <https://doi.org/10.21037/jtd.2017.06.34>
- Scannell, P.T., Prendergast, P.J., 2009. Cortical and interfacial bone changes around a non-cemented hip implant: Simulations using a combined strain/damage remodelling algorithm. *Med. Eng. Phys.* 31, 477–488.

<https://doi.org/10.1016/j.medengphy.2008.11.007>

- Shirazi, R.N., Aldabbagh, F., Erxleben, A., Rochev, Y., McHugh, P., 2014. Nanomechanical properties of poly(lactic-co-glycolic) acid film during degradation. *Acta Biomater.* 10, 4695–4703. <https://doi.org/10.1016/j.actbio.2014.08.004>
- Song, G., Atrens, A., 2007. Recent insights into the mechanism of magnesium corrosion and research suggestions. *Adv. Eng. Mater.* 9, 177–183. <https://doi.org/10.1002/adem.200600221>
- Song, G., Song, S., 2007. A possible biodegradable magnesium implant material. *Adv. Eng. Mater.* 9, 298–302. <https://doi.org/10.1002/adem.200600252>
- Song, G.L., Atrens, A., 1999. Corrosion mechanisms of magnesium alloys. *Adv. Eng. Mater.* 1, 11–33. [https://doi.org/10.1002/\(SICI\)1527-2648\(199909\)1:1<11::AID-ADEM11>3.0.CO;2-N](https://doi.org/10.1002/(SICI)1527-2648(199909)1:1<11::AID-ADEM11>3.0.CO;2-N)
- Sotomi, Y., Onuma, Y., Ormiston, J., Serruys, P.W., 2017. Bioresorbable Scaffold Technologies. *Circ. J.* 509–520. <https://doi.org/10.1253/circj.CJ-10-1135>
- Staiger, M.P., Pietak, A.M., Huadmai, J., Dias, G., 2006. Magnesium and its alloys as orthopedic biomaterials: A review. *Biomaterials* 27, 1728–1734. <https://doi.org/10.1016/j.biomaterials.2005.10.003>
- Sweeney, C.A., McHugh, P.E., McGarry, J.P., Leen, S.B., 2012. Micromechanical methodology for fatigue in cardiovascular stents. *Int. J. Fatigue* 44, 202–216. <https://doi.org/10.1016/j.ijfatigue.2012.04.022>
- Tahir, H., Bona-Casas, C., Hoekstra, A.G., 2013. Modelling the Effect of a Functional Endothelium on the Development of In-Stent Restenosis. *PLoS One* 8. <https://doi.org/10.1371/journal.pone.0066138>
- Tamai, H., Igaki, K., Kyo, E., Kosuga, K., Kawashima, A., Matsui, S., Komori, H., Tsuji, T., Motohara, S., Uehata, H., 2000. Initial and 6-month results of biodegradable poly-l-lactic acid coronary stents in humans. *Circulation* 102, 399–404.
- Tormala, P., Pohjonen, T., Rokkanen, P., 1998. Bioabsorbable polymers: materials technology and surgical applications. *Proc Inst Mech Eng H* 212, 101–111.
- Waksman, R., 2007. Absorbable Metal Stent, Clinical Update and DREAMS: Concept and preclinical Data, Innovations of Cardiovascular Interventions. *Innovations of Cardiovascular Interventions*, Tel-Aviv.
- Waksman, R., Erbel, R., Di Mario, C., Bartunek, J., de Bruyne, B., Eberli, F.R., Erne, P., Haude, M., Horigan, M., Ilsley, C., Bose, D., Bonnier, H., Koolen, J., Luscher, T.F., Weissman, N.J., 2009. Early- and Long-Term Intravascular Ultrasound and Angiographic Findings After Bioabsorbable Magnesium Stent Implantation in Human Coronary Arteries. *JACC Cardiovasc. Interv.* 2, 312–320.

<https://doi.org/10.1016/j.jcin.2008.09.015>

- Waksman, R., Pakala, R., Baffour, R., Seabron, R., Hellinga, D., Tio, F.O., 2008. Short-term effects of biocorrosible iron stents in porcine coronary arteries. *J. Interv. Cardiol.* 21, 15–20.
- Waksman, R., Pakala, R., Kuchulakanti, P.K., Baffour, R., Hellinga, D., Seabron, R., Tio, F.O., Wittchow, E., Hartwig, S., Harder, C., Rohde, R., Heublein, B., Andreae, A., Waldmann, K.H., Haverich, A., 2006. Safety and efficacy of bioabsorbable magnesium alloy stents in porcine coronary arteries. *Catheter. Cardiovasc. Interv.* 68, 607–617. <https://doi.org/10.1002/ccd.20727>
- Walker, J., Shadanbaz, S., Woodfield, T.B.F., Staiger, M.P., Dias, G.J., 2014. Magnesium biomaterials for orthopedic application: A review from a biological perspective. *J. Biomed. Mater. Res. - Part B Appl. Biomater.* 102, 1316–1331. <https://doi.org/10.1002/jbm.b.33113>
- Winzer, N., Atrens, A., Song, G., Ghali, E., Dietzel, W., Kainer, K.U., Hort, N., Blawert, C., 2005. A critical review of the Stress Corrosion Cracking (SCC) of magnesium alloys. *Adv. Eng. Mater.* 7, 659–693. <https://doi.org/10.1002/adem.200500071>
- Witte, F., 2010. The history of biodegradable magnesium implants: A review. *Acta Biomater.* 6, 1680–1692. <https://doi.org/10.1016/j.actbio.2010.02.028>
- Witte, F., Fischer, J., Nellesen, J., Crostack, H., 2006. In vitro and in vivo corrosion measurements of magnesium alloys. *Biomaterials*.
- Witte, F., Hort, N., Vogt, C., Cohen, S., Kainer, K.U., Willumeit, R., Feyerabend, F., 2008. Degradable biomaterials based on magnesium corrosion. *Curr. Opin. Solid State Mater. Sci.* 12, 63–72. <https://doi.org/10.1016/j.cossms.2009.04.001>
- Wu, W., Chen, S., Gastaldi, D., Petrini, L., Mantovani, D., Yang, K., Tan, L., Migliavacca, F., 2013. Experimental data confirm numerical modeling of the degradation process of magnesium alloys stents. *Acta Biomater.* 9, 8730–8739. <https://doi.org/10.1016/j.actbio.2012.10.035>
- Wu, W., Gastaldi, D., Yang, K., Tan, L., Petrini, L., Migliavacca, F., 2011. Finite element analyses for design evaluation of biodegradable magnesium alloy stents in arterial vessels. *Mater. Sci. Eng. B Solid-State Mater. Adv. Technol.* 176, 1733–1740. <https://doi.org/10.1016/j.mseb.2011.03.013>
- Wu, W., Petrini, L., Gastaldi, D., Villa, T., Vedani, M., Lesma, E., Previtali, B., Migliavacca, F., 2010. Finite element shape optimization for biodegradable magnesium alloy stents. *Ann. Biomed. Eng.* 38, 2829–2840. <https://doi.org/10.1007/s10439-010-0057-8>
- Zahedmanesh, H., Lally, C., 2012. A multiscale mechanobiological modelling framework using agent-based models and finite element analysis: Application to vascular tissue engineering. *Biomech. Model. Mechanobiol.* 11, 363–377. <https://doi.org/10.1007/s10237-011-0316-0>

- Zartner, P., Cesnjevar, R., Singer, H., Weyand, M., 2005. First successful implantation of a biodegradable metal stent into the left pulmonary artery of a preterm baby. *Catheter. Cardiovasc. Interv.* 66, 590–4. <https://doi.org/10.1002/ccd.20520>
- Zheng, Y.F., Gu, X.N., Witte, F., 2014. Biodegradable metals. *Mater. Sci. Eng. R Reports* 77, 1–34. <https://doi.org/10.1016/j.mser.2014.01.001>
- Zun, P.S., Anikina, T., Svitenkov, A., Hoekstra, A.G., 2017. A comparison of fully-coupled 3D in-stent restenosis simulations to In-vivo Data. *Front. Physiol.* 8, 1–12. <https://doi.org/10.3389/fphys.2017.00284>

3 Computational Modelling of the Mechanical Performance of a Magnesium Stent Undergoing Uniform and Pitting Corrosion in a Remodelling Artery

3.1 Chapter Overview

In this chapter, a computational modelling framework is developed that combines magnesium alloy degradation and neointimal remodelling, which is capable of simulating both uniform (best case) and localised pitting (realistic) stent corrosion in a remodelling artery. The framework is used to evaluate the effects of the neointima on the mechanics of the stent, when the stent is undergoing uniform or pitting corrosion, and to assess the effects of the neointimal formation rate relative to the overall stent degradation rate (for both uniform and pitting conditions).

The content of this chapter has been published in two journal articles, one in *JOM* (Boland et al., 2016a) and one in *Journal of Medical Devices* (Boland et al., 2017).

3.2 Introduction

Coronary stents have revolutionised the treatment of coronary artery disease by providing mechanical support to the artery following the angioplasty procedure and overcoming problems such as acute recoil and late negative remodelling (Waksman et al., 2013). While coronary artery stenting is now relatively mature, significant scientific and technological challenges still remain. It can be claimed that the need for a stent is temporary as it is only required for the initial scaffolding period after which the artery will have remodelled (Hermawan et al., 2010), therefore stents made from degradable biomaterials such as PLLA (Gogas et al., 2012; Patel and Banning, 2013) and magnesium alloy (Erbel et al., 2007; Haude et al., 2013, 2016) are emerging.

Biodegradable stents have potential advantages over the current generation of permanent stents, including possible reduced risk of in-stent restenosis (Mitra and Agrawal, 2006)

and late stent thrombosis (Ong et al., 2005), use in the growing vessels of paediatric patients (Zartner et al., 2005) and the restoration of vasomotion potential.

As discussed previously, computational modelling such as finite element analysis has proven to be an extremely useful tool in the continued design and development of these medical devices. Computational modelling of the mechanics of permanent balloon expandable coronary stents has received significant attention in the literature, and simulations relating to the entire stent lifecycle have been reported, including stent tracking to the diseased site, balloon expansion, recoil, *in-vivo* loading, drug-elution and fatigue fracture, for example as reported in Conway et al., (2014, 2012), (Gervaso et al., 2008), Gijssen et al., (2008), Grogan et al., (2012), Sweeney et al., (2012), Zunino et al., (2009) and as reviewed in Martin and Boyle, (2011) McHugh et al., (2016) and Morlacchi and Migliavacca, (2013). In contrast, due to their more recent emergence, the literature on computational modelling of the mechanics of both metallic and polymeric biodegradable stents is much more limited; example reports include Bobel et al., (2015), Grogan et al., (2013, 2011), Soares et al., (2008), Wu et al., (2013, 2011, 2010), with a review on biodegradation modelling presented in Boland et al., (2016b). Further, for biodegradable stents, what is lacking in computational modelling literature is the representation of the active response of the arterial tissue in the weeks and months following stent implantation, i.e. neointimal remodelling.

The phenomenon of neointimal remodelling is particularly interesting and significant in the case of biodegradable stents, when both stent degradation and neointimal remodelling can occur simultaneously (Hermawan et al., 2010), presenting the possibility of a mechanical interaction and transfer of load between the degrading stent and the remodelling artery.

The focus of the present work is on magnesium biodegradable stents. The Biotronik Magmaris resorbable magnesium scaffold has recently been approved in Europe (Biotronik, 2016) highlighting the considerable potential of these types of medical devices.

As reviewed by Boland et al., (2016b) and in Chapter 2, the literature on the computational modelling of magnesium alloy degradation for the stent application is relatively limited. Reports include the phenomenological uniform and stress corrosion models of Gastaldi et al., (2011), the phenomenological uniform and pitting corrosion models of Grogan et al., (2011), which were developed for use with the Abaqus/Explicit software (subsequently adapted for use with the Abaqus/Standard software (Debusschere et al., 2016)), and the physically-based uniform corrosion model of Grogan et al., (2014).

Uniform corrosion is the simplest form of degradation modelling where the exposed surface of the material is degraded at a uniform rate (Gastaldi et al., 2011; Grogan et al., 2011). Uniform corrosion is a highly idealised and relatively unrealistic assumption for corroding magnesium. However, the method is moderately easy to implement and it does represent a best case condition (relative to non-uniform corrosion) for the maintenance of device structural integrity during degradation (Grogan et al., 2011).

Gastaldi et al., (2011) developed a phenomenological stress corrosion model using the continuum damage mechanics (CDM) approach. The associated damage evolution law for the stress corrosion model is dependent on an equivalent stress (maximum principal stress in this case) in the material being greater than a threshold stress. Elements subject to high stresses will corrode faster than elements subject to low stresses while elements subject to stress below the threshold stress will not corrode at all. Wu et al., (2013, 2011) conducted *in-vitro* corrosion tests of magnesium alloy stents and compared results with computational stent corrosion predictions using the stress corrosion model coupled with a similarly developed uniform corrosion model validating the overall usefulness of the model in stent design and performance assessment. However magnesium alloys are subject to localised pitting corrosion *in-vivo* (Alvarez-Lopez and Pereda, 2010; Witte et al., 2006) so the absence of this corrosion mechanism in the coupled uniform and stress corrosion model is a limitation. In contrast, localised pitting corrosion is accounted for in the phenomenological pitting corrosion model of Grogan et al., (2011) through the selective element removal from the finite element mesh, driven by a Weibull probability distribution.

A physically-based uniform corrosion model accounting for the multi-physics processes involved in magnesium stent degradation (including magnesium ion transport) has been reported by Grogan et al., (2014).

However, this model has only been applied to pure magnesium to date, and the model is more complex to implement and use, relative to the aforementioned phenomenological models, for practical stent performance simulations.

In relation to the simulation of tissue remodelling, mechanobiological models for predicting the response of multicellular biological systems, for in-stent restenosis and neointimal development applications, have been reported. They can be grouped into two categories: (i) discrete cell based models such as cellular automata (CA) (Boyle et al., 2011, 2010; Caiazzo et al., 2011; Tahir et al., 2013) and agent-based models (ABM) (Zahedmanesh and Lally, 2012) which simulate each individual cell's behaviour and the interactions between cells, enabling the observation of the emergent system behaviour, and (ii) continuum models, which usually can be formulated in terms of partial differential equations in space and time (Hwang et al., 2009).

Discrete models such as CA and ABM use a bottom up approach where each individual cell is modelled explicitly. The behaviour of individual cells at a local level is governed by a set of rules, and the global behaviour of the system emerges through the local interaction of cells. Cell based models developed to predict the response of arteries to stenting have typically used specially developed software such as COAST (Caiazzo et al., 2011; Tahir et al., 2013), BREVE (Zahedmanesh and Lally, 2012), and MechanoBiology ToolKit (Boyle et al., 2011) which are coupled with finite element models of the artery and stent. Previous studies of this type have used 2D models for the artery and stent (Boyle et al., 2011; Caiazzo et al., 2011; Tahir et al., 2013; Zahedmanesh and Lally, 2012), while more recently Boyle et al. advanced the use of these models as a pre-clinical tool to predict long-term outcomes of stent designs by applying the method to 3D geometries for permanent stents (Boyle et al., 2013).

Mechanobiological models using the continuum approach have been utilised extensively in orthopaedic applications to model cell differentiation and predict tissue regeneration

and bone remodelling (Burke and Kelly, 2012; Gómez-Benito et al., 2005; Lacroix et al., 2002). Literature is much more limited on the use of continuum models to simulate the response of the artery to stenting when compared with cell-based models. However, Lally and Prendergast, (2006) successfully used a continuum model to simulate in-stent restenosis, and such models, being continuum based, have the advantage of ease of implementation in the finite element context for practical stent performance simulations.

Against this backdrop, the first objective of the present chapter is to develop a combined magnesium alloy stent degradation and neointimal remodelling computational modelling framework, that is capable of simulating both uniform (best case) and localised pitting (realistic) stent corrosion.

The second objective is to investigate the effects of the presence of the neointima on the mechanical performance (scaffolding support) of the biodegrading stent; specifically, to evaluate the effects of the presence of the neointima when the stent is undergoing uniform or pitting corrosion, and to assess the effects of the neointimal formation rate relative to the overall stent degradation rate (for both uniform and pitting conditions). The achievement of these objectives, i.e. the development of the modelling framework and the understanding of the combined degradation-remodelling mechanical effects, should be of significant use for the continued design and development of these next generation medical devices.

3.3 Methods

The constitutive models presented are based on the assumption of finite deformation kinematics. This is implemented in Abaqus/Explicit software (DS-SIMULIA, RI, USA) by exploiting the NLGEOM (non-linear geometry) feature throughout all steps in the simulation.

3.3.1 Stent and Stent Corrosion

The stent is modelled using the properties of magnesium (Mg) AZ31 alloy as a model magnesium alloy material system (Grogan et al., 2012, 2011) where elasticity is considered linear and isotropic and described through Young's modulus and Poisson's

ratio, while plasticity is described using J_2 flow theory and isotropic hardening. The stent geometry is a representation of the Biotronik Magmaris stent (formerly known as the second-generation DREAMS (DREAMS 2G) as discussed in Chapter 2) (Figure 3.1) with a thickness of $150\ \mu\text{m}$ (Kitabata et al., 2014).

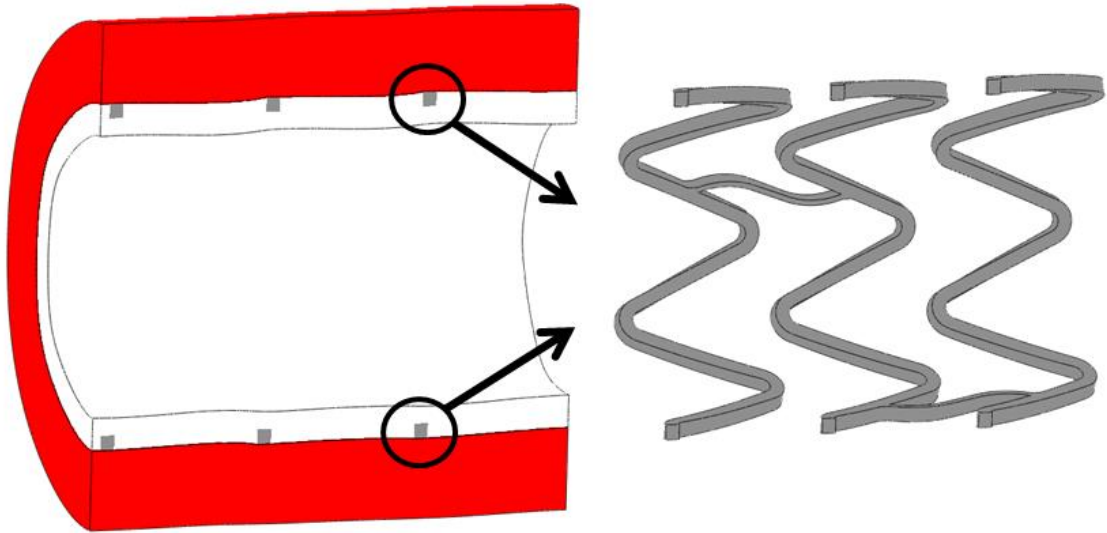


Figure 3.1. Finite element model for stent corrosion in a remodelling artery with artery (red), Biotronik Magmaris stent geometry (grey) and ghost/neointima (white).

The magnesium degradation models used in this study are adapted from the phenomenological uniform and pitting corrosion models of Grogan et al., (2011). Uniform corrosion provides desirable magnesium corrosion mechanics and is idealistic in terms of the stent providing long term scaffolding support to the artery during corrosion. The pitting corrosion model provides a more realistic and accurate model for how the magnesium stent corrodes *in-vivo*. Furthermore, the phenomenological approach offers robust practicality and ease of implementation in finite element software for practical stent performance simulations, relative to, for example, the physically-based approach of Grogan et al., (2014). The uniform and pitting corrosion models have been developed for use in both Abaqus/Explicit (Grogan et al., 2011) and Abaqus/Standard (DS-SIMULIA, RI, USA) (Debusschere et al., 2016) software. The Abaqus/Explicit solver is chosen for this work due to its superior contact enforcement method, so the Grogan et al., (2011) implementation of the uniform and pitting corrosion models were used as the basis for the present work.

Both the uniform and pitting corrosion models have been comprehensively explained previously in the literature (Boland et al., 2016b; Grogan et al., 2011), and in Chapter 2, so a brief summary is provided here with reference to the present application. Magnesium corrosion is a predominantly surface based phenomenon (Song and Atrens, 1999). Elements on the exterior surface of the stent which would be exposed to the corrosive environment are selected as part of the corrosion surface. The elastic and plastic properties of the elements on the corrosion surface are linearly reduced with increasing damage D . The damage parameter D is proportional to the material corrosion rate k_U . When an element is completely damaged ($D \approx 1$) the corrosion surface is then updated to include neighbouring elements via an element connectivity map. For uniform corrosion this results in a gradual external to internal corrosion process.

The pitting corrosion model differs from the uniform version by the inclusion of a dimensionless pitting parameter λ_e . The damage evolution law for pitting corrosion is described according to the below equation

$$\frac{dD}{dt} = \frac{\delta_U}{L_e} \lambda_e k_U \quad (3.1)$$

where δ_U and L_e are the respective material and FE model characteristic lengths and k_U is the material corrosion rate parameter. Each element on the corrosion surface is initially assigned a random pitting parameter λ_e through the use of Weibull distribution-based random number generator. Elements on the corrosion surface which are assigned a larger random number are more susceptible to pitting corrosion. Once an element on the corrosion surface has been completely degraded, the rate of the neighbouring element degradation is controlled by a further parameter (a pit growth rate parameter) β according to:

$$\lambda_e = \beta \lambda_n \quad (3.2)$$

where λ_n is the pitting parameter of the fully degraded element and β is a dimensionless parameter that controls the acceleration/deceleration of pit growth. Therefore for the pitting corrosion model, three parameters (material corrosion rate, k_U [h^{-1}], Weibull function parameter, γ , and growth rate parameter, β) must be determined. These parameters were calibrated and model performance validated against data generated in independent corrosion and corrosion with loading experiments performed on Mg AZ31 (Grogan et al., 2011). The material corrosion rate k_U for the uniform and pitting corrosion simulations are chosen to ensure that the both models have similar mass loss profiles and that the stent is completely degraded at the end of the simulation (Figure 3.2). In this way the recoil of the stent throughout the entire duration of stent corrosion is captured in the simulation.

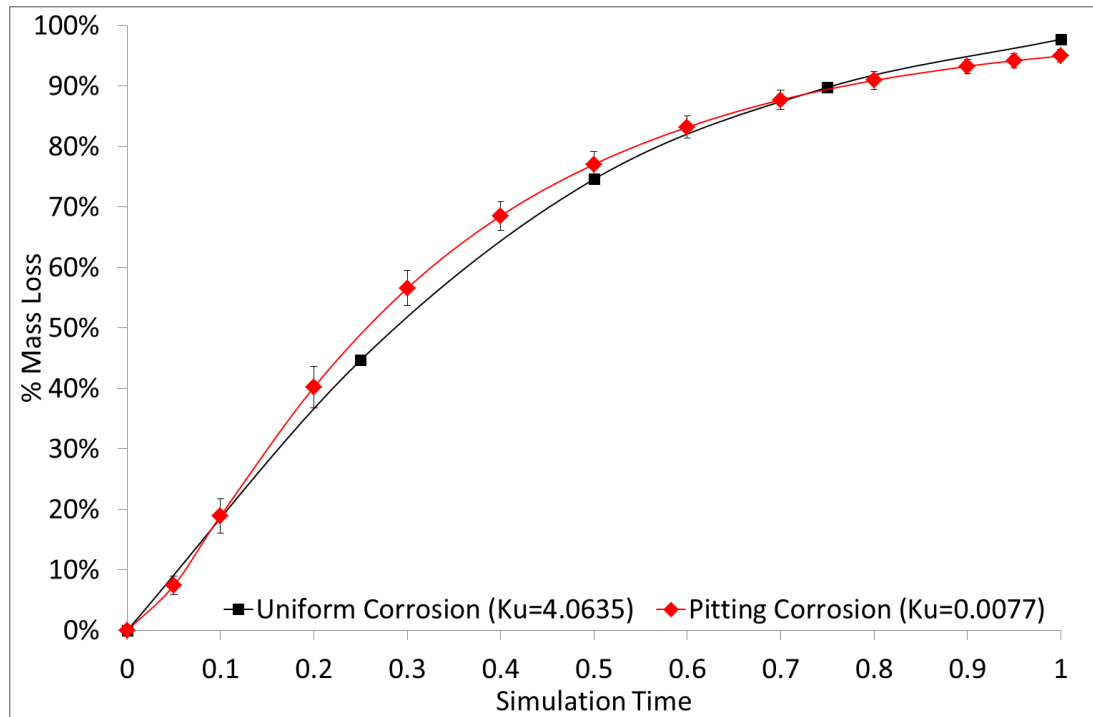


Figure 3.2. Plot of percentage stent mass loss versus simulation time for uniform and pitting corrosion models. Error bars for pitting corrosion represent a single standard deviation from the mean ($n=5$).

In Grogan and co-workers' implementations of the uniform and pitting corrosion models (Grogan et al., 2013, 2011), element deletion is used to remove completely damaged

elements ($D \approx 1$) from the simulation. However, in the present work the corrosion models are adapted to exclude element deletion; instead completely damaged elements are modelled as magnesium corrosion product which is assumed to be a soft elastic incompressible material. The retention of the corrosion product is considered more physiologically realistic than complete corrosion product elimination/element removal. There are also practical computational advantages for modelling corrosion product instead of element deletion as use of element deletion with a stent embedded in an artery would result in holes or gaps in the mesh.

3.3.2 Artery and Neointima

A three-layer artery of inner diameter 3.0 mm, with artery layer thicknesses taken from the work of Holzapfel et al., (2005), is modelled using an isotropic reduced sixth-order hyperelastic material model, with model parameters taken from Gervaso et al., (2008), based on experimental tissue testing by Holzapfel et al., (2005).

To represent the growth of neointima, given its practical implementation advantages in finite element software, the continuum approach is used, based on the work of Lally and Prendergast, (2006). The arterial lumen is filled with mesh of deactivated finite elements, namely the “ghost mesh” (Figure 3.1), with negligible initial mechanical properties. The elements in the ghost mesh become activated according to the neointimal remodelling algorithm which is described in detail below. The activation of elements in the ghost mesh is representative of the remodelling of the artery through the growth of new neointimal tissue and entails a change in the material properties assigned to those elements. The newly activated elements change from a very soft material to a stiffer material.

A detailed search of the literature to determine appropriate mechanical properties to assign to the neointima proved inconclusive, possibly due to the difficulties in obtaining this material for testing. However, it is assumed here that the neointima is an incompressible elastic material with similar properties to the intima. Incompressible ($\nu = 0.49$) linear elastic material properties are assigned to both the deactivated ghost mesh and activated neointima; the use of linear elastic properties for the neointima is

motivated by their use previously in a similar application (Lally and Prendergast, 2006), and also it is practically convenient to change the Young's modulus of a material in Abaqus software via field variables and user subroutine. In any event, initial simulations showed that the maximum principal strain levels experienced in the ghost mesh elements (either deactivated or activated) are quite low (<5 %) meaning that it is not unreasonable to consider neointimal elasticity to be linear for the loading ranges of interest here.

An effective Young's modulus is deduced from the isotropic hyperelastic model representation of the arterial intimal tissue (Gervaso et al., 2008; Holzapfel et al., 2005), using low strain (≈ 5 %) simulated tensile testing, generating a value of 0.05 MPa this is selected as the Young's modulus of neointimal tissue.

Elastic properties of the deactivated ghost mesh are also initially taken from Lally and Prendergast, (2006) (Young's modulus = 0.05 MPa). Minimising this property is essential to ensure that the deactivated elements have negligible effect on the simulation results, however too low a value can cause numerical issues such as mesh distortion and simulation failure. It is found that a Young's modulus value of 0.01 MPa for the deactivated ghost mesh provided optimum balance between minimising the effect the deactivated ghost mesh has on results without causing distortion of the mesh. Thus, this value is used throughout the analysis.

The mechanobiological model (remodelling algorithm) used to predict neointimal development via the activation of elements in the ghost mesh uses the CDM approach (Lally and Prendergast, 2006). Here the process is implemented in Abaqus/Explicit software through a thermal analogy utilising VUSDFLD and VUAMP subroutines. The model considered here is driven by stress in the artery due to the presence of the stent. It is acknowledged that the model in its current form does not account for other factors known to effect neointimal formation such as endothelial shear stress (Bourantas et al., 2014; Koskinas et al., 2012; Malek, 1999; Wentzel et al., 2001), which is a limitation.

Maximum principal stress in the artery due to stent deployment, which corresponds with the maximum tensile load in the artery, is used to generate a damage parameter d , through Miner's Law and an experimentally characterised S-N curve for porcine

coronary arterial tissue (Lally and Prendergast, 2006), which acts like a source term that results in the recruitment of cells into the artery and the subsequent diffusion of these cells into the ghost mesh.

If the concentration of cells at the nodes is denoted by n , the rate of change in the cell concentration, $\frac{dn}{dt}$, is computed by

$$\frac{dn}{dt} = k\nabla^2 n + cd \quad (3.3)$$

where k is the diffusion coefficient of cells in arterial tissue, ∇^2 is the Laplace operator, d is the damager parameter and c is a constant ($c = 1$) which relates the damage parameter to cell proliferation rate. The first part of Equation 3.3 is simply Fick's Law of diffusion which can be related to Fourier's Law of thermal conduction using a thermal analogy (Hose et al., 2004) and implemented in Abaqus using a coupled temperature-displacement simulation. The damage parameter d is incorporated using individual thermal heat flux loads for every element in the artery, with the damage parameter d of each element controlling the magnitude of each individual thermal heat flux load via the VUSDFLD and VUAMP subroutines.

This model is based on the fundamental assumption that neointimal growth is influenced by the damage caused to the artery during stent deployment (Bourantas et al., 2014) and that the tissue gradually propagates radially inwards, eventually resulting in the encapsulation of the stent strut by the neointima (Waksman et al., 2013). In an effort to capture this effect a condition is placed on the ghost mesh where cells cannot diffuse into deactivated ghost elements until directly adjacent elements have become activated. This condition is achieved by increasing the diffusivity of deactivated ghost elements from an initial value of zero up to 0.016 mm²/day for activated neointima (Lally and Prendergast, 2006) when directly adjacent elements have been activated (Table 3.1).

Table 3.1. An overview of cell diffusion properties used for the materials in the model. These properties can be used to influence or apply certain conditions to the neointimal remodelling algorithm.

	Diffusivity <i>mm²/day</i>	No. of cells to increase concentration of cells by one unit dimensionless	Concentration threshold <i>no. of cells</i>
Adventitia	0.016	1000	N/A
Media	0.016	1000	N/A
Intima	0.016	1000	N/A
Magnesium stent	0	4500 / 22000	N/A
Deactivated ghost	0	4500 / 22000	45/220
Activated neointima	0.016	4500 / 22000	45/220

The number of cells required to increase the concentration of cells by one unit is equivalent to specific heat capacity through the thermal analogy. Initially a value of 1.0 is used for this property however for larger scale models with small element sizes this results in an impractically small minimum stable time increment ($\approx 10^{-9}$) for the coupled thermal-displacement Abaqus/Explicit solver (with mass scaling) as per Equation 2 in Koric et al., (2009). Increasing the value of this parameter by a factor of 1000 allows the simulation to run with a larger more practical minimum stable time increment ($\approx 10^{-6}$).

Further analysis of this parameter demonstrates that changing the value selected for the stent and ghost mesh effects the rate at which the remodelling simulation progresses. A low value results in faster neointimal growth while a higher value results in slower neointimal growth. The chosen values used for each of the materials in the model are shown in, with 4500 corresponding to completed neointimal remodelling after 33 % stent mass loss and 22000 corresponding to completed neointimal remodelling after 67 % stent mass loss.

Elements in the ghost mesh become activated (assigned tissue mechanical properties) when the local cell concentration reaches a threshold level. Low threshold levels (Table 3.1) are selected to ensure that neointimal remodelling begins at the commencement of the stent degradation simulations.

The thickness of the ghost mesh is selected as 0.32 mm based on maximal neointimal thickness values reported for the Biotronik 1st generation DREAMS stent 6 months after implantation (Waksman et al., 2013). This thickness is important as it controls the maximum amount of neointimal remodelling that may occur during the simulation.

3.3.3 Boundary and Loading Conditions

Due to complexities in creating the ghost mesh of deactivated elements the deployment of the stent is not explicitly simulated. To create the condition where the stent is providing scaffolding support to the artery a different method is used, which has been previously reported (Bedoya et al., 2006; Lally et al., 2005; Lally and Prendergast, 2006; Timmins et al., 2007). The initial geometry of the stent is approximated as that of a deployed stent. Firstly, a 5 % axial in situ prestretch is applied to artery in accordance with Holzapfel et al., (2005) and as applied by Zahedmanesh and Lally, (2009). Next, a pressure load is applied to the internal surface of the artery to expand it radially. Subsequently, the artery is moved over the stent and the pressure load on the artery removed, allowing the artery to relax onto the stent. While this approach for creating the condition of a stent providing scaffolding support to the artery neglects the plastic deformation in the stent due to deployment, this technique does not affect the corrosion modelling approach of (Grogan et al., 2011) which in the present form is not explicitly strain or stress modulated. This method is considered acceptable for this study as it is focused on stent degradation mechanics and neointimal remodelling of the artery following stent implantation.

To reduce the computational requirements of the simulations only half of the artery, three-ring stent and neointima are modelled (Figure 3.1) with appropriate symmetry boundary conditions subsequently applied to the corresponding surfaces. Eight node linear reduced integration brick elements with distortion control are used for the representation of the three-layer artery (characteristic element length (L_e) = 0.073 mm), magnesium stent (L_e = 0.0173 mm) and ghost mesh (L_e = 0.0173 mm).

The mesh density is focused on the area of interest which in this case is the stent and the ghost mesh which have 125,000 and 1,400,000 elements, respectively, while the artery mesh has 68,000 elements. These mesh sizes are chosen based on the results of a mesh

sensitivity analysis while also maintaining practical convenience in simulation size and computational run time.

To analyse the combined effects of stent degradation (uniform and pitting) and neointimal remodelling a number of models are considered, including: (i) stent degradation with no neointimal remodelling, (ii) stent degradation with complete neointimal remodelling at the start of the degradation simulation (instantaneous remodelling), and (iii) stent degradation with gradual neointimal remodelling.

Stent degradation with no neointimal remodelling and stent degradation with instantaneous neointimal remodelling are two extreme cases (i.e. no remodelling and very fast remodelling when compared with the stent degradation rate). Stent degradation with gradual remodelling is considered the most physiologically relevant case as both processes, viz. stent corrosion and gradual growth of neointimal tissue, happen simultaneously. As stated in Hermawan et al., (2010), the arterial remodelling process can be expected to be completed between 6-12 months after stent implantation while a total period of 12-24 months for complete stent degradation is considered reasonable. Therefore, the gradual remodelling simulation is formulated to have a faster remodelling rate than stent degradation rate. The specific artery remodelling to stent mass loss ratios investigated for the gradual remodelling simulation are 0.33:1 and 0.67:1 which means that complete arterial remodelling has been achieved after approximately 33 % or 67 % mass loss of the stent, respectively.

The Abaqus/Explicit solver is chosen for this research due to its superior contact enforcement method. To minimise dynamic effects, to avoid ambiguous displacement fluctuations by energy dissipation (Conway et al., 2014) and to maintain an average ratio of kinetic to internal energy of 5 % for the analysis, the Rayleigh damping coefficient ($\alpha = 8000$) is applied to a layer of shell elements on both the external surface of the artery and internal surface of ghost mesh.

All analyses are performed on a single hyperthreaded SGI ICE X high-performance computer having 2 x 12 core processors and 64GB of RAM. Analyses of stent degradation with no remodelling and stent degradation with instantaneous remodelling

require approximately 2500 CPU hours while stent degradation with gradual remodelling require approximately 3500 CPU hours.

3.3.4 Small Stented Artery Model

To determine the effects that the material properties of the stent corrosion product have on the arterial scaffolding support provided by the biodegradable magnesium stent, a parameter study is conducted using a small stent, artery and ghost mesh geometry, as shown in Figure 3.3. This model is also used to assess the effects of neointimal property variation.

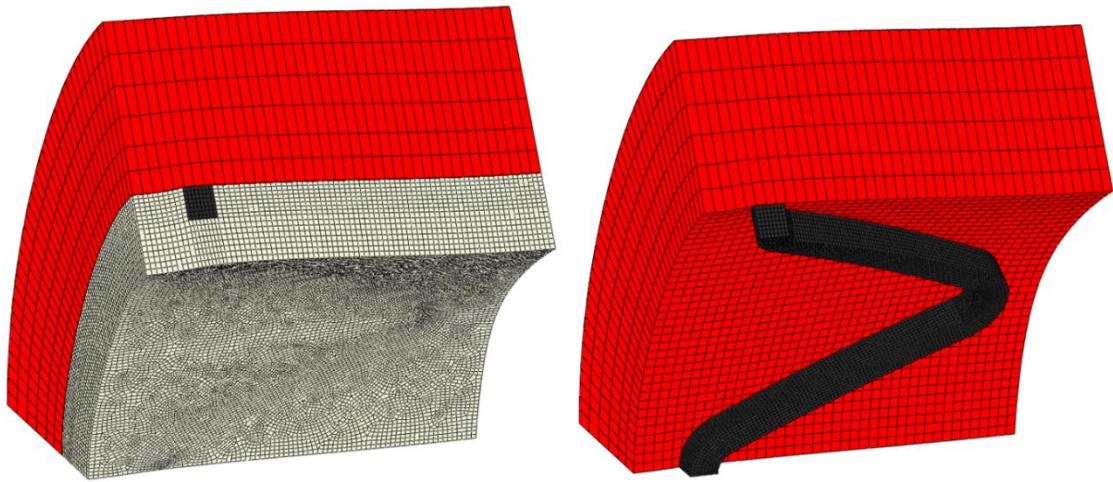


Figure 3.3. Finite element model showing the small model set-up for the initial parameter studies investigating the effects of the material properties of magnesium corrosion product and material properties of the activated neointima on the recoil of the degrading stent. The artery is coloured red, the stent struts are coloured black and ghost mesh / neointima is shown in white (left image).

To minimise the computational requirements of the simulations only one stent hinge consisting of two stent struts along with the corresponding artery and neointima are modelled. Appropriate symmetry boundary conditions are subsequently applied to the corresponding flat surfaces.

For consistency between the large model (Figure 3.1) and the small model (Figure 3.3) the characteristic length (L_e) of the elements in the artery, stent and ghost mesh are the same for both models. For the small model, the mesh density is focused on the area of

interest which in this case is the stent and the ghost mesh which have 13,300 and 154,600 elements, respectively, while the artery mesh has 8,850 elements.

Analyses of the small model are performed on the same single hyperthreaded SGI ICE X high-performance computer (2 x 12 core processors and 64GB of RAM) as the large model and require approximately 240 CPU hours per simulation.

3.4 Results

3.4.1 Parameter Study – Properties of Magnesium Corrosion Product

Using the small model set up shown in Figure 3.3, the values of Young's modulus of magnesium corrosion product are varied without neointimal remodelling activation and uniform corrosion of the stent. In relation to assessing overall stent scaffolding ability during degradation, the average percentage loss of radial scaffolding support (% stent recoil) is calculated from the displacements of the central nodes in the stent struts and plotted against stent mass loss.

As illustrated in Figure 3.4, the properties of magnesium corrosion product have minimal effect on recoil rates of the degrading stent. There is virtually no difference between overall stent recoil rate when the Young's modulus assigned to the stent corrosion product is increased by a factor of twenty (from 0.05 MPa to 10 MPa). For comparison the Young's modulus of uncorroded Mg AZ31 is 44 GPa. The plot of Figure 3.4 indicates that once the material properties assigned to the magnesium corrosion product is sufficiently small compared with the uncorroded value ($10 \text{ MPa} / 44 \text{ GPa} = 0.023 \%$), the inclusion of corrosion product does not effect to overall recoil of the stent as it degrades.

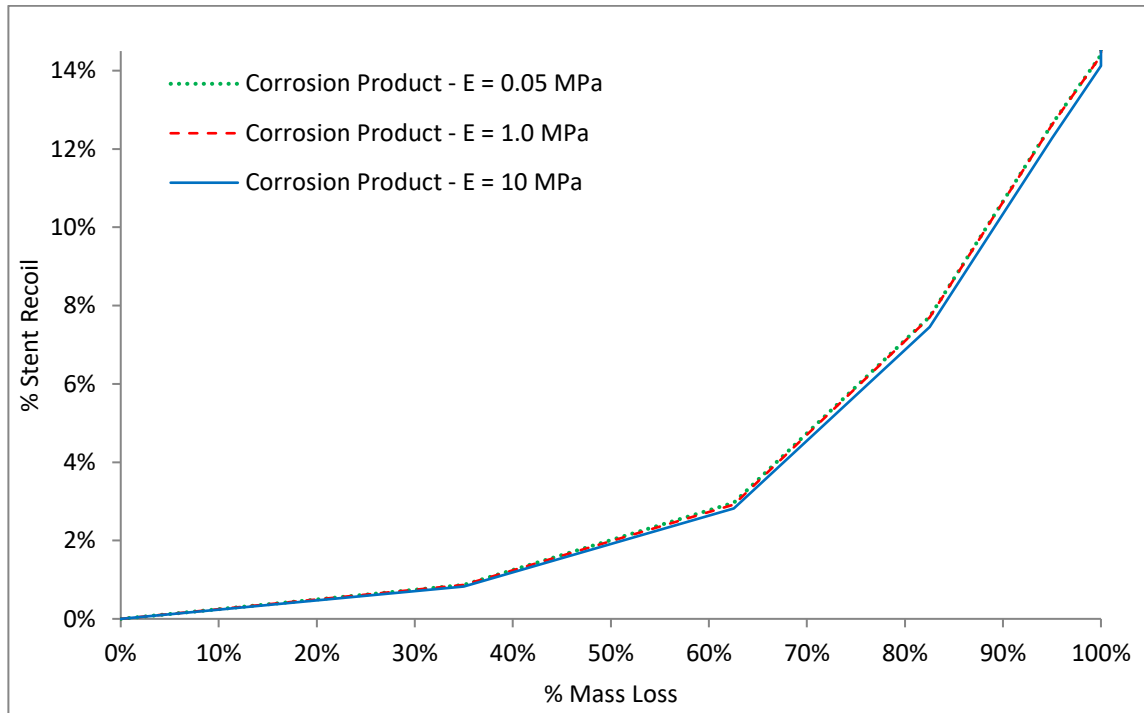


Figure 3.4. Analysing the effect that Mg corrosion product properties has on stent recoil rates (uniform corrosion, no remodelling).

3.4.2 Parameter Study – Properties of Activated Neointima

In a further analysis, using the smaller model set up shown in Figure 3.3, the properties of the neointimal tissue are varied for the same stent degradation rate with instantaneous remodelling to quantify the effect that they have on stent recoil rates. An initial neointimal Young's modulus value of 1 MPa is reduced first to 0.5 MPa and then to 0.1 MPa, with the results shown in Figure 3.5. For comparison a simulation of no neointimal remodelling ($E = 0.01$ MPa) is also included in Figure 3.5.

The lower values of 0.5 MPa and 0.1 MPa are chosen to explore the critical dependence of the results on the neointimal tissue properties given that diseased arterial tissue properties are highly variable (Holzapfel et al., 2005). Figure 3.5 demonstrates that the elastic properties of the new neointimal tissue are the dominant parameter which controls stent recoil rate in the model. Stent recoil at the end of the degradation simulation changes from 1.4 % to 2.9 % to 7.9 % depending on the selected Young's modulus value of the neointimal tissue (1 MPa, 0.5 MPa or 0.1 MPa, respectively), with

the no remodelling simulation as expected corresponding to the highest percentage of stent after stent degradation (14.2 %).

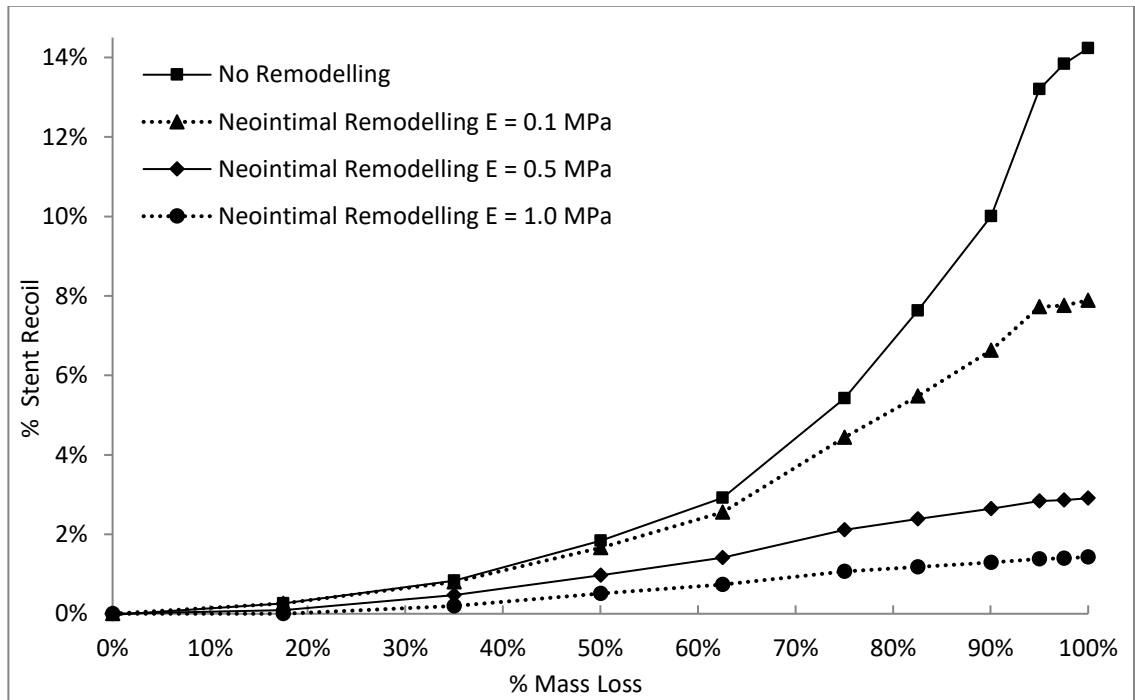


Figure 3.5. Analysing the effect that neointimal tissue properties have on stent recoil rates (uniform corrosion, instantaneous remodelling).

3.4.3 Pattern of Neointimal Formation

Figure 3.6 shows the progression of neointima formation into the ghost mesh and around the stent struts for gradual remodelling with the larger model geometry for the case of stent pitting corrosion (Figure 3.1). The neointima formation initiates at the arterial lumen and gradually propagates radially inwards until the entire ghost mesh has become activated. It is interesting to note that neointima formation rate is accentuated local to the stent struts, consistent with these being the locations of highest stress on deployment. This neointimal growth pattern is typical of what is seen for these simulations irrespective of whether uniform or pitting corrosion is simulated.

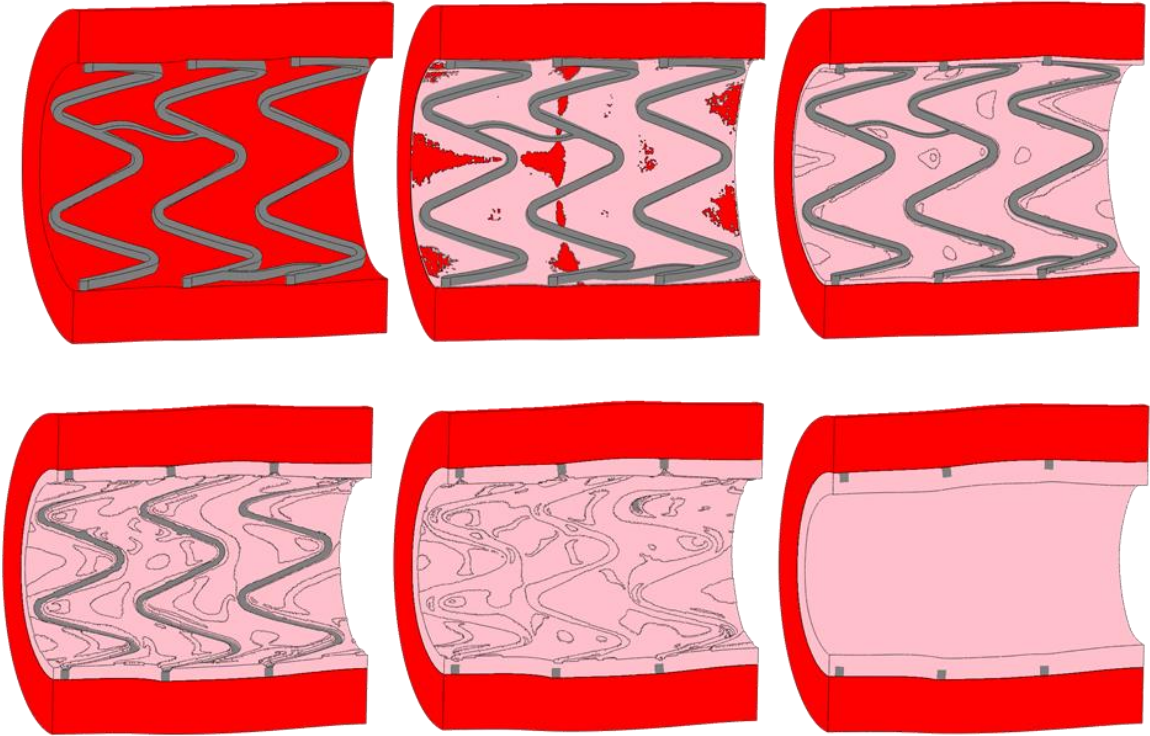


Figure 3.6. Model images demonstrating gradual neointimal development (pink) during the artery remodelling simulation with pitting corrosion (pitting gradual remodelling 67 %). The neointimal development is non-uniform and accentuated in the areas around the stent struts where arterial stresses due to stent deployment are highest.

3.4.4 Stent Recoil vs Mass Loss due to Degradation

In relation to assessing overall stent scaffolding ability during degradation, the average percentage loss of radial scaffolding support (% stent recoil) is calculated from the displacements of the central nodes in the stent struts and plotted against stent mass loss, as shown in Figure 3.7. As shown in Figure 3.7, there is a significant difference in the radial recoil of the stent between the no neointimal remodelling case and the cases with neointimal remodelling (instantaneous and gradual). With no neointimal remodelling the stent recoil at the end of the simulation for both uniform and pitting corrosion is 12.5 % while with neointimal remodelling (instantaneous and gradual) the recoil is significantly reduced to 8.6 %.

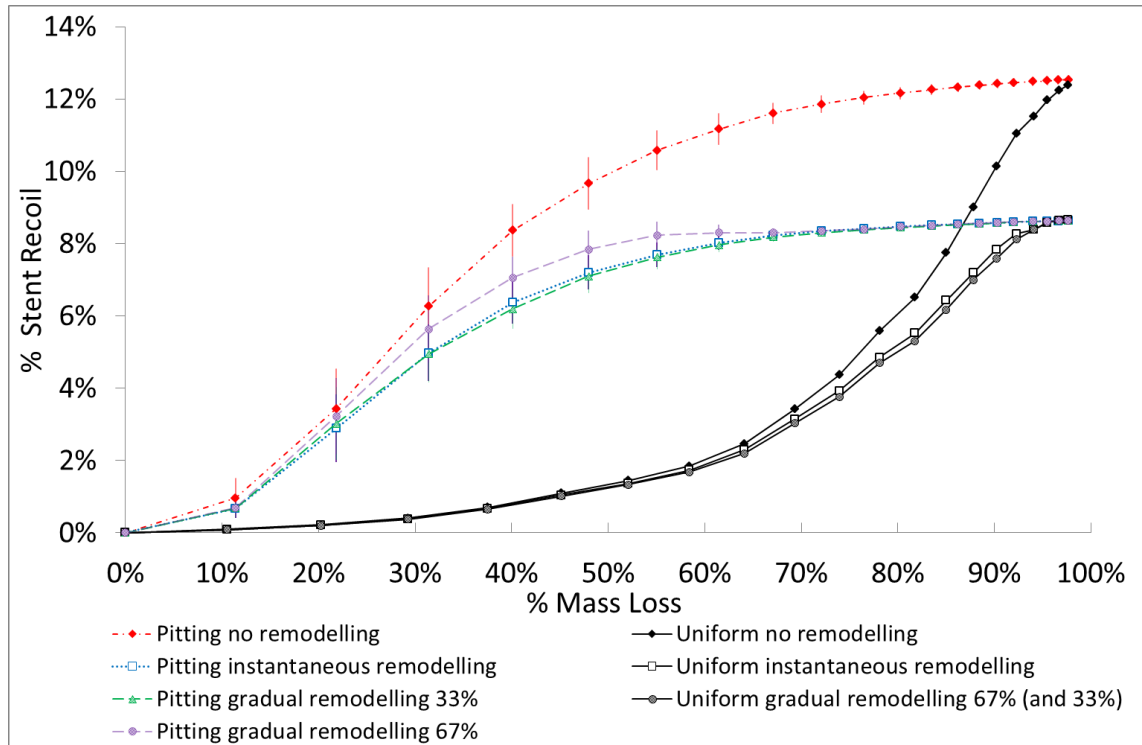


Figure 3.7. Plot of percentage stent recoil versus percentage stent mass loss uniform and pitting corrosion with no remodelling, instantaneous remodelling and gradual remodelling (33 % and 67 %), as explained the in text. Error bars represent a single standard deviation from the mean (n=5).

As mentioned in the methods section for this model, gradual remodelling with uniform and pitting corrosion is formulated so that the neointimal remodelling rate is faster than the stent corrosion rate. The specific artery remodelling to stent mass loss ratios investigated for the gradual remodelling simulation are 0.33:1 and 0.67:1 which means that complete arterial remodelling has been achieved after approximately 33 % or 67 % mass loss of the stent. These gradual remodelling curves are also plotted on Figure 3.7 and are labelled gradual remodelling 33 % and gradual remodelling 67 %, respectively.

For the uniform corrosion case, the plots for the 33 % and 67 % gradual remodelling simulations are indistinguishable so for clarity only the 67 % curve is included in Figure 3.7. As shown in the figure, the percentage stent recoil of the uniform gradual remodelling 67 % simulation is analogous to the uniform instantaneous remodelling simulation throughout the entire mass loss profile of the stent.

For the pitting corrosion case, the plots for the 33 % and 67 % gradual remodelling simulations are significantly different and both are included in Figure 3.7. As shown in the figure, the percentage recoil of the gradual remodelling 33 % simulation is virtually identical to that of the instantaneous remodelling simulation throughout the entire mass loss profile of the stent. However, the percentage stent recoil of the gradual remodelling 67 % falls in between the two extreme remodelling cases (no remodelling and instantaneous remodelling) for the first portion of the simulation before gradually transitioning and joining the instantaneous remodelling curve when the neointima has completely remodelled (at ~67 % stent mass loss).

As shown in Figure 3.7, the type of corrosion, uniform or pitting, dictates how quickly the degrading stent loses its ability to provide arterial scaffolding support. Pitting corrosion causes the stent to recoil at a much faster rate than uniform corrosion for all types of remodelling. This is illustrated in Figure 3.7 by the high stent recoil rate in the initial part of the simulation and the gradual reduction in stent recoil rate in the latter portion of the simulation. Essentially the opposite happens for the stent subject to uniform corrosion, which has low recoil during the initial part of the simulation with the recoil rate gradually increasing as the stent degrades.

3.5 Discussion

3.5.1 Parameter Study – Properties of Magnesium Corrosion Product

As shown in Figure 3.4, inclusion of magnesium corrosion product as an alternative to element deletion has little influence on the mechanical performance of the magnesium alloy stent, once the mechanical properties of the corrosion product (Young's modulus) are a sufficiently small percentage ($< 0.023\%$) of those of the original magnesium alloy.

3.5.2 Parameter Study – Properties of Activated Neointima

Figure 3.5 demonstrates that the elastic properties of the new neointimal tissue are the dominant parameter which controls stent recoil rate in the model. A stiffer neointimal material would result in lower stent recoil values (Figure 3.5) therefore the appropriate representation of mechanical properties for the new neointimal tissue critically important in ensuring accuracy of the simulation. The literature is limited in experimental testing

of neointimal tissue, perhaps due to the difficulties in obtaining this biological material, so further experimentation to accurately characterise its mechanical properties is most definitely required.

3.5.3 Pattern of Neointimal Formation

As shown in Figure 3.6 the neointimal development for gradual remodelling is initially concentrated in regions around the stent struts where arterial stresses are highest. From analysis of the reported simulations, it is clear that the stent corrosion method (i.e. uniform or pitting) has only minor effects on the neointimal development, indicating that the arterial stress immediately after stent deployment is the most important stress parameter in this model. Conversely, the cellular diffusion properties (Table 3.1) assigned to the neointimal material have significant effects on determining when neointimal remodelling begins and the rate at which it proceeds.

3.5.4 Stent Recoil vs Mass Loss due to Degradation

As shown in Figure 3.7, there is a significant reduction in stent recoil when remodelling occurs (instantaneous or gradual) which suggests that the neointimal tissue provides scaffolding support to the artery as the stent degrades. The stiffness of activated neointimal material ($E = 0.05$ MPa) is the parameter which most significantly contributes to the reduction in stent recoil in Figure 3.7. A stiffer neointimal material would result in lower stent recoil values (Figure 3.5) therefore, the appropriate representation of mechanical properties for the new neointimal tissue is vital to ensure accuracy of the simulation. The literature is limited in experimental testing of neointimal tissue, perhaps due to the difficulties in obtaining this biological material, so further experimentation to accurately characterise its mechanical properties is most definitely required.

The results from the gradual remodelling simulations for both uniform and pitting corrosion when compared with the extreme cases (no remodelling and instantaneous remodelling) provide a number of insights into the mechanics of biodegradable magnesium stents.

As previously mentioned in Section 3.4.4, the uniform gradual remodelling 33 % and 67 % stent recoil versus mass loss curves are indistinguishable and are also remarkably similar to the stent recoil versus mass loss curve for the uniform instantaneous remodelling case (Figure 3.7). The similarities of these results indicate that for the uniform corrosion case, due low levels of stent recoil during the majority of the simulation, the rate of neointimal remodelling is not particularly important.

Pitting corrosion significantly affects the mechanical integrity of the stent even under low levels of degradation (mass loss) which results in higher levels of stent recoil when compared to the uniform case. Despite this, the plot of percentage recoil versus percentage mass loss for the pitting gradual remodelling 33 % simulation is still remarkably similar to the pitting instantaneous remodelling simulation. This indicates that the neointimal material adjacent to the stent struts and the arterial lumen, which is activated first according the remodelling algorithm (Figure 3.6), provides the majority of scaffolding support to the stent.

The percentage stent recoil of the pitting gradual remodelling 67 % falls in between the two extreme remodelling cases (pitting no remodelling and pitting instantaneous remodelling) for the first portion of the simulation. This result is expected as all three simulations have the same stent degradation rate with the only difference between them being the varying degrees of activated neointimal material. As the volume of activated neointimal material increases the pitting gradual remodelling simulation gradually transitions and eventually joins the pitting instantaneous remodelling curve when the neointima has completely remodelled (at 67 % stent mass loss).

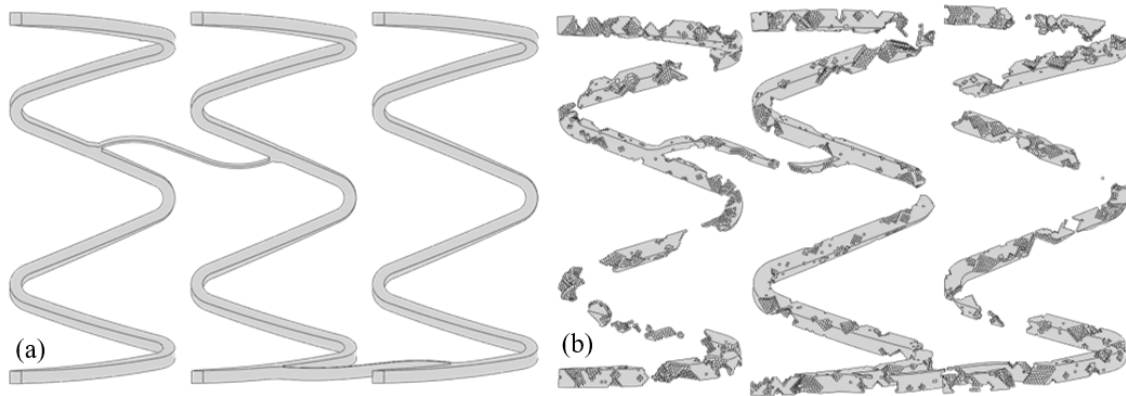


Figure 3.8. Model images showing uncorroded stent material after 45 % mass loss (degradation) for both uniform (a) and pitting (b) corrosion.

The rate at which the stent recoils in Figure 3.7 depends on the type of corrosion, either uniform or pitting. This result can be understood by consideration of the images in Figure 3.8, which show the remaining uncorroded stent material after 45 % mass loss, for the uniform corrosion case and for the pitting corrosion case. The particular pitting stent geometry illustrated in Figure 3.8b results from the stochastic nature of the selection of the corrosion pit nuclei. Uniform corrosion is an idealistic but non-physiological corrosion process which results in sequential degradation of layers of material (layers of finite elements) progressing inward from the original stent strut surface. This produces an internal core of non-degraded magnesium (Figure 3.8a) that is aligned with the original stent geometry, that continues to provide scaffolding support to the artery over a significant range of the degradation history, and that, in particular, results in low stent recoil in the initial stages of the simulation. Pitting corrosion is a more physiological and significantly more severe corrosion process; it is an inhomogeneous process with pits originating at a number of randomly assigned locations on the initial corrosion surface and proceeding to grow through the stent strut (Figure 3.8b), resulting in early strut fragmentation. Pitting corrosion significantly affects the mechanical integrity of the stent even after low amounts of degradation, which is evidenced by the large amounts of stent recoil after small loss in mass relative to the uniform corrosion cases.

The corrosion simulations clearly demonstrate the critical importance of the fundamental corrosion behaviour of the material in determining the overall stent performance and the

severe negative effects of pitting corrosion. The results presented here would indicate that the reduction in the pitting tendency of these materials, by the generation of enhanced magnesium alloys, manufacturing methods and surface treatments, has the potential to significantly enhance the development of biodegradable magnesium alloy stents.

Further model development, parameter studies and experimental validation are clearly required here; nevertheless, this results could contribute to the explanation as to why biodegradable metals stents degrade and lose scaffolding capability more slowly *in-vivo*, where tissue remodelling is occurring, in comparison to *in-vitro* (Grogan et al., 2011).

3.5.5 Limitations

The model developed in this work has a number of limitations. The mechanobiological model used for neointimal development is driven by maximum principal stresses in the artery and does not include other factors known to effect neointimal formation such as endothelial shear stress (Bourantas et al., 2014; Koskinas et al., 2012; Malek, 1999; Wentzel et al., 2001). This will be address in Chapter 5.

The selection of 0.32 mm as the thickness of the ghost mesh based on maximal neointimal thickness values reported for the Biotronik 1st generation DREAMS stent 6 months after implantation (Waksman et al., 2013) is potentially a crucial parameter in the model and may be considered a limitation. However, the present results suggest that the elements closest to the stent struts and arterial lumen provide the majority of scaffolding support, which indicates that a variation in the maximum neointimal thickness would have only a minor effect on the stent scaffolding performance.

The stent is modelled using Mg AZ31 alloy as the uniform and pitting corrosion parameters used were calibrated and validated by *in-vitro* corrosion experiments on samples of this material (Grogan et al., 2011), where the material is selected as a model magnesium alloy system. However magnesium-aluminium based alloys are not recommended as biomaterials due to the neuro-toxicity of the aluminium element (Zheng et al., 2014) meaning the use of this material to model biodegradable magnesium stents is a limitation. The generation and use of corrosion parameters for alternative

biocompatible magnesium alloys such as Mg WE43 is necessary, and will be addressed in Chapter 4.

In the current uniform and pitting corrosion model the stent corrosion rate is a constant and is not affected by the remodelling of the artery around the stent struts. *In-vitro* corrosion experiments on pure magnesium samples have shown that covered samples have slower degradation rate than uncovered samples (Bowen et al., 2012), indicating that the use of a constant stent corrosion rate may be a limitation.

Finally, the pitting corrosion model used in this work is effective in simulating the overall corrosion mechanism and the development of stochastic corrosion pits along the corrosion surface of the stent. However, a limitation of the pitting corrosion model in the current form is that it does not account for the underlying micro-galvanic corrosion process, which leads to the development of macro-scale corrosion pits. A more physically-based corrosion model which accounts for the micro-galvanic corrosion process and corrosion at a granular level would be an interesting development and potentially improve the accuracy of the corrosion model.

3.6 Conclusion

In this chapter, a mechanobiological model for neointimal development has been successfully implemented in Abaqus/Explicit software and combined with two distinct magnesium corrosion models (uniform and pitting). The developed model allows for quantitative prediction of the short and long-term mechanical performance of biodegradable metal stents as a function of the material properties and fundamental material corrosion behaviour, and as such should be of value to stent developers.

This work has shown that the active response of the artery following stent implantation should not be ignored when modelling biodegradable stents as it can have a significant effect on recoil of the stent and scaffolding support provided to the artery. Furthermore, the results presented here would indicate that the reduction in the pitting tendency of these materials, by the production of alternative magnesium alloys, manufacturing methods and surface treatments, has the potential to significantly enhance the development of biodegradable magnesium alloy stents.

References

- Alvarez-Lopez, M., Pereda, M., 2010. Corrosion behaviour of AZ31 magnesium alloy with different grain sizes in simulated biological fluids. *Acta Biomater.*
- Bedoya, J., Meyer, C.A., Timmins, L.H., Moreno, M.R., Moore, J.E., 2006. Effects of stent design parameters on normal artery wall mechanics. *J. Biomech. Eng.* 128, 757–65. <https://doi.org/10.1115/1.2246236>
- Biotronik, 2016. BIOTRONIK Announces CE Mark for Magmaris, the First Clinically-Proven Bioresorbable Magnesium Scaffold [WWW Document]. URL [https://www.biotronik.com/files/F284043E451B1C61C1257FD2004B5842/\\$FILE/160615_BIOTRONIK_PR_Magmaris_CE_Approval_EN.pdf](https://www.biotronik.com/files/F284043E451B1C61C1257FD2004B5842/$FILE/160615_BIOTRONIK_PR_Magmaris_CE_Approval_EN.pdf) (accessed 8.2.16).
- Bobel, A.C., Petisco, S., Sarasua, J.R., Wang, W., McHugh, P.E., 2015. Computational Bench Testing to Evaluate the Short-Term Mechanical Performance of a Polymeric Stent. *Cardiovasc. Eng. Technol.* 6, 519–532. <https://doi.org/10.1007/s13239-015-0235-9>
- Boland, E.L., Grogan, J.A., Conway, C., McHugh, P.E., 2016a. Computer Simulation of the Mechanical Behaviour of Implanted Biodegradable Stents in a Remodelling Artery. *JOM* 68, 1198–1203. <https://doi.org/10.1007/s11837-015-1761-5>
- Boland, E.L., Grogan, J.A., McHugh, P.E., 2017. Computational Modeling of the Mechanical Performance of a Magnesium Stent Undergoing Uniform and Pitting Corrosion in a Remodeling Artery. *J. Med. Device.* 11, 021013. <https://doi.org/10.1115/1.4035895>
- Boland, E.L., Shine, R., Kelly, N., Sweeney, C.A., McHugh, P.E., 2016b. A Review of Material Degradation Modelling for the Analysis and Design of Bioabsorbable Stents. *Ann. Biomed. Eng.* 44, 341–356. <https://doi.org/10.1007/s10439-015-1413-5>
- Bourantas, C. V., Papafaklis, M.I., Kotsia, A., Farooq, V., Muramatsu, T., Gomez-Lara, J., Zhang, Y.J., Iqbal, J., Kalatzis, F.G., Naka, K.K., Fotiadis, D.I., Dorange, C., Wang, J., Rapoza, R., Garcia-Garcia, H.M., Onuma, Y., Michalis, L.K., Serruys, P.W., 2014. Effect of the endothelial shear stress patterns on neointimal proliferation following drug-eluting bioresorbable vascular scaffold implantation: An optical coherence tomography study. *JACC Cardiovasc. Interv.* 7, 315–324. <https://doi.org/10.1016/j.jcin.2013.05.034>
- Bowen, P.K., Gelbaugh, J.A., Mercier, P.J., Goldman, J., Drelich, J., 2012. Tensile testing as a novel method for quantitatively evaluating bioabsorbable material degradation. *J. Biomed. Mater. Res. - Part B Appl. Biomater.* 100B, 2101–2113. <https://doi.org/10.1002/jbm.b.32775>
- Boyle, C.J., Lennon, A.B., Early, M., Kelly, D.J., Lally, C., Prendergast, P.J., 2010. Computational simulation methodologies for mechanobiological modelling: a cell-

- centred approach to neointima development in stents. *Phil. Trans. R. Soc. A* 368, 2919–2935. <https://doi.org/10.1098/rsta.2010.0071>
- Boyle, C.J., Lennon, A.B., Prendergast, P.J., 2013. Application of a mechanobiological simulation technique to stents used clinically. *J. Biomech.* 46, 918–924. <https://doi.org/10.1016/j.jbiomech.2012.12.014>
- Boyle, C.J., Lennon, A.B., Prendergast, P.J., 2011. In Silico Prediction of the Mechanobiological Response of Arterial Tissue: Application to Angioplasty and Stenting. *J. Biomech. Eng.* 133, 081001. <https://doi.org/10.1115/1.4004492>
- Burke, D.P., Kelly, D.J., 2012. Substrate stiffness and oxygen as regulators of stem cell differentiation during skeletal tissue regeneration: A mechanobiological model. *PLoS One* 7. <https://doi.org/10.1371/journal.pone.0040737>
- Caiazzo, A., Evans, D., Falcone, J.L., Hegewald, J., Lorenz, E., Stahl, B., Wang, D., Bernsdorf, J., Chopard, B., Gunn, J., Hose, R., Krafczyk, M., Lawford, P., Smallwood, R., Walker, D., Hoekstra, A., 2011. A Complex Automata approach for in-stent restenosis: Two-dimensional multiscale modelling and simulations. *J. Comput. Sci.* 2, 9–17. <https://doi.org/10.1016/j.jocs.2010.09.002>
- Conway, C., McGarry, J.P., McHugh, P.E., 2014. Modelling of Atherosclerotic Plaque for Use in a Computational Test-Bed for Stent Angioplasty. *Ann. Biomed. Eng.* 42, 2425–2439. <https://doi.org/10.1007/s10439-014-1107-4>
- Conway, C., Sharif, F., McGarry, J.P., McHugh, P.E., 2012. A Computational Test-Bed to Assess Coronary Stent Implantation Mechanics Using a Population-Specific Approach. *Cardiovasc. Eng. Technol.* 3, 374–387. <https://doi.org/10.1007/s13239-012-0104-8>
- Debusschere, N., Segers, P., Dubruel, P., Verheghe, B., De Beule, M., 2016. A Computational Framework to Model Degradation of Biocorrosible Metal Stents Using an Implicit Finite Element Solver. *Ann. Biomed. Eng.* 44, 382–390. <https://doi.org/10.1007/s10439-015-1530-1>
- Erbel, R., Di Mario, C., Bartunek, J., Bonnier, J., de Bruyne, B., Eberli, F.R., Erne, P., Haude, M., Heublein, B., Horrigan, M., Ilesley, C., Böse, D., Koolen, J., Lüscher, T.F., Weissman, N., Waksman, R., 2007. Temporary scaffolding of coronary arteries with bioabsorbable magnesium stents: a prospective, non-randomised multicentre trial. *Lancet* 369, 1869–1875. [https://doi.org/10.1016/S0140-6736\(07\)60853-8](https://doi.org/10.1016/S0140-6736(07)60853-8)
- Gastaldi, D., Sassi, V., Petrini, L., Vedani, M., Trasatti, S., Migliavacca, F., 2011. Continuum damage model for bioresorbable magnesium alloy devices - Application to coronary stents. *J. Mech. Behav. Biomed. Mater.* 4, 352–365. <https://doi.org/10.1016/j.jmbbm.2010.11.003>
- Gervaso, F., Capelli, C., Petrini, L., Lattanzio, S., Di Virgilio, L., Migliavacca, F., 2008. On the effects of different strategies in modelling balloon-expandable stenting by

- means of finite element method. *J. Biomech.* 41, 1206–12. <https://doi.org/10.1016/j.jbiomech.2008.01.027>
- Gijzen, F.J.H., Migliavacca, F., Schievano, S., Socci, L., Petrini, L., Thury, A., Wentzel, J.J., van der Steen, A.F.W., Serruys, P.W.S., Dubini, G., 2008. Simulation of stent deployment in a realistic human coronary artery. *Biomed. Eng. Online* 7, 23. <https://doi.org/10.1186/1475-925X-7-23>
- Gogas, B., Farooq, V., Onuma, Y., Serruys, P., 2012. The ABSORB bioresorbable vascular scaffold: an evolution or revolution in interventional cardiology. *Hell. J Cardiol.*
- Gómez-Benito, M.J., García-Aznar, J.M., Kuiper, J.H., Doblaré, M., 2005. Influence of fracture gap size on the pattern of long bone healing: A computational study. *J. Theor. Biol.* 235, 105–119. <https://doi.org/10.1016/j.jtbi.2004.12.023>
- Grogan, J.A., Leen, S.B., McHugh, P.E., 2014. A physical corrosion model for bioabsorbable metal stents. *Acta Biomater.* 10, 2313–2322. <https://doi.org/10.1016/j.actbio.2013.12.059>
- Grogan, J.A., Leen, S.B., McHugh, P.E., 2013. Optimizing the design of a bioabsorbable metal stent using computer simulation methods. *Biomaterials* 34, 8049–8060. <https://doi.org/10.1016/j.biomaterials.2013.07.010>
- Grogan, J.A., Leen, S.B., McHugh, P.E., 2012. Comparing coronary stent material performance on a common geometric platform through simulated bench testing. *J. Mech. Behav. Biomed. Mater.* 12, 129–138. <https://doi.org/10.1016/j.jmbbm.2012.02.013>
- Grogan, J.A., O'Brien, B.J., Leen, S.B., McHugh, P.E., 2011. A corrosion model for bioabsorbable metallic stents. *Acta Biomater.* 7, 3523–3533. <https://doi.org/10.1016/j.actbio.2011.05.032>
- Haude, M., Erbel, R., Erne, P., Verheye, S., Degen, H., Bose, D., Vermeersch, P., Wijnbergen, I., Weissman, N., Prati, F., Waksman, R., Koolen, J., 2013. Safety and performance of the drug-eluting metal scaffold (DREAMS) in patients with de-novo coronary lesions: 12 month results of the prospective, multicentre, first-in-man BIOSOLVE-1 trial. *Lancet* 9, 836–844.
- Haude, M., Ince, H., Abizaid, A., Toelg, R., Lemos, P.A., Von Birgelen, C., Christiansen, E.H., Wijns, W., Neumann, F.J., Kaiser, C., Eeckhout, E., Lim, S.T., Escaned, J., Garcia-Garcia, H.M., Waksman, R., 2016. Safety and performance of the second-generation drug-eluting absorbable metal scaffold in patients with de-novo coronary artery lesions (BIOSOLVE-II): 6 month results of a prospective, multicentre, non-randomised, first-in-man trial. *Lancet* 387, 31–39. [https://doi.org/10.1016/S0140-6736\(15\)00447-X](https://doi.org/10.1016/S0140-6736(15)00447-X)
- Hermawan, H., Dubé, D., Mantovani, D., 2010. Developments in metallic biodegradable stents. *Acta Biomater.* 6, 1693–1697. <https://doi.org/10.1016/j.actbio.2009.10.006>

- Holzapfel, G.A., Sommer, G., Gasser, C.T., Regitnig, P., 2005. Determination of layer-specific mechanical properties of human coronary arteries with nonatherosclerotic intimal thickening and related constitutive modeling. *Am. J. Physiol. Heart Circ. Physiol.* 289, H2048-58. <https://doi.org/10.1152/ajpheart.00934.2004>
- Hose, D.R., Narracott, A.J., Griffiths, B., Mahmood, S., Gunn, J., Sweeney, D., Lawford, P. V., 2004. A thermal analogy for modelling drug elution from cardiovascular stents. *Comput. Methods Biomech. Biomed. Engin.* 7, 257–64. <https://doi.org/10.1080/10255840412331303140>
- Hwang, M., Garbey, M., Berceci, S.A., Tran-Son-Tay, R., 2009. Rule-based simulation of multi-cellular biological systems-a review of modeling techniques. *Cell. Mol. Bioeng.* 2, 285–294. <https://doi.org/10.1007/s12195-009-0078-2>
- Kitabata, H., Waksman, R., Warnack, B., 2014. Bioresorbable metal scaffold for cardiovascular application: Current knowledge and future perspectives. *Cardiovasc. Revascularization Med.* 15, 109–116. <https://doi.org/10.1016/j.carrev.2014.01.011>
- Koric, S., Hibbeler, L.C., Thomas, B.G., 2009. Explicit Coupled Thermo-Mechanical Finite-Element Model of Continuous Casting of Steel in Funnel Molds.
- Koskinas, K.C., Chatzizisis, Y.S., Antoniadis, A.P., Giannoglou, G.D., 2012. Role of endothelial shear stress in stent restenosis and thrombosis: Pathophysiologic mechanisms and implications for clinical translation. *J. Am. Coll. Cardiol.* 59, 1337–1349. <https://doi.org/10.1016/j.jacc.2011.10.903>
- Lacroix, D., Prendergast, P.J., Li, G., Marsh, D., 2002. Biomechanical model to simulate tissue differentiation and bone regeneration: application to fracture healing. *Med. Biol. Eng. Comput.* 40, 14–21. <https://doi.org/10.1007/BF02347690>
- Lally, C., Dolan, F., Prendergast, P.J., 2005. Cardiovascular stent design and vessel stresses: A finite element analysis. *J. Biomech.* 38, 1574–1581. <https://doi.org/10.1016/j.jbiomech.2004.07.022>
- Lally, C., Prendergast, P.J., 2006. Simulation of In-stent Restenosis for the Design of Cardiovascular Stents, in: Holzapfel, G., Ogden, R. (Eds.), *Mechanics of Biological Tissue SE - 18*. Springer Berlin Heidelberg, pp. 255–267. https://doi.org/10.1007/3-540-31184-X_18
- Malek, A.M., 1999. Hemodynamic Shear Stress and Its Role in Atherosclerosis. *JAMA* 282, 2035. <https://doi.org/10.1001/jama.282.21.2035>
- Martin, D.M., Boyle, F.J., 2011. Computational structural modelling of coronary stent deployment: a review. *Comput. Methods Biomech. Biomed. Engin.* 14, 331–348. <https://doi.org/10.1080/10255841003766845>
- McHugh, P., Barakat, A., McGinty, S., 2016. Medical Stents: State of the Art and Future Directions. *Ann. Biomed. Eng.* 44, 274–275. <https://doi.org/10.1007/s10439-015-1526-x>

- Mitra, A.K., Agrawal, D.K., 2006. In stent restenosis: bane of the stent era. *J. Clin. Pathol.* 59, 232–9. <https://doi.org/10.1136/jcp.2005.025742>
- Morlacchi, S., Migliavacca, F., 2013. Modeling stented coronary arteries: Where we are, where to go. *Ann. Biomed. Eng.* 41, 1428–1444. <https://doi.org/10.1007/s10439-012-0681-6>
- Ong, A.T.L., McFadden, E.P., Regar, E., de Jaegere, P.P.T., van Domburg, R.T., Serruys, P.W., 2005. Late angiographic stent thrombosis (LAST) events with drug-eluting stents. *J. Am. Coll. Cardiol.* 45, 2088–92. <https://doi.org/10.1016/j.jacc.2005.02.086>
- Patel, N., Banning, A.P., 2013. Bioabsorbable scaffolds for the treatment of obstructive coronary artery disease: the next revolution in coronary intervention? *Heart* 99, 1236–43. <https://doi.org/10.1136/heartjnl-2012-303346>
- Soares, J.S., Moore, J.E.J., Rajagopal, K.R., 2008. Constitutive Framework for Biodegradable Polymers with Applications to Biodegradable Stents. *ASAIO J.* 54, 295–301. <https://doi.org/10.1097/MAT.0b013e31816ba55a>
- Song, G.L., Atrens, A., 1999. Corrosion mechanisms of magnesium alloys. *Adv. Eng. Mater.* 1, 11–33. [https://doi.org/10.1002/\(SICI\)1527-2648\(199909\)1:1<11::AID-ADEM11>3.0.CO;2-N](https://doi.org/10.1002/(SICI)1527-2648(199909)1:1<11::AID-ADEM11>3.0.CO;2-N)
- Sweeney, C.A., McHugh, P.E., McGarry, J.P., Leen, S.B., 2012. Micromechanical methodology for fatigue in cardiovascular stents. *Int. J. Fatigue* 44, 202–216. <https://doi.org/10.1016/j.ijfatigue.2012.04.022>
- Tahir, H., Bona-Casas, C., Hoekstra, A.G., 2013. Modelling the Effect of a Functional Endothelium on the Development of In-Stent Restenosis. *PLoS One* 8. <https://doi.org/10.1371/journal.pone.0066138>
- Timmins, L.H., Moreno, M.R., Meyer, C.A., Criscione, J.C., Rachev, A., Moore, J.E., 2007. Stented artery biomechanics and device design optimization. *Med. Biol. Eng. Comput.* 45, 505–513. <https://doi.org/10.1007/s11517-007-0180-3>
- Waksman, R., Prati, F., Bruining, N., Haude, M., Böse, D., Kitabata, H., Erne, P., Verheye, S., Degen, H., Vermeersch, P., Di Vito, L., Koolen, J., Erbel, R., 2013. Serial observation of drug-eluting absorbable metal scaffold: Multi-imaging modality assessment. *Circ. Cardiovasc. Interv.* 6, 644–653. <https://doi.org/10.1161/CIRCINTERVENTIONS.113.000693>
- Wentzel, J.J., Krams, R., Schuurbijs, J.C., Oomen, J. a, Kloet, J., van Der Giessen, W.J., Serruys, P.W., Slager, C.J., 2001. Relationship between neointimal thickness and shear stress after Wallstent implantation in human coronary arteries. *Circulation* 103, 1740–1745. <https://doi.org/10.1161/01.CIR.103.13.1740>
- Witte, F., Fischer, J., Nellesen, J., Crostack, H., 2006. In vitro and in vivo corrosion measurements of magnesium alloys. *Biomaterials*.

- Wu, W., Chen, S., Gastaldi, D., Petrini, L., Mantovani, D., Yang, K., Tan, L., Migliavacca, F., 2013. Experimental data confirm numerical modeling of the degradation process of magnesium alloys stents. *Acta Biomater.* 9, 8730–8739. <https://doi.org/10.1016/j.actbio.2012.10.035>
- Wu, W., Gastaldi, D., Yang, K., Tan, L., Petrini, L., Migliavacca, F., 2011. Finite element analyses for design evaluation of biodegradable magnesium alloy stents in arterial vessels. *Mater. Sci. Eng. B Solid-State Mater. Adv. Technol.* 176, 1733–1740. <https://doi.org/10.1016/j.mseb.2011.03.013>
- Wu, W., Petrini, L., Gastaldi, D., Villa, T., Vedani, M., Lesma, E., Previtali, B., Migliavacca, F., 2010. Finite element shape optimization for biodegradable magnesium alloy stents. *Ann. Biomed. Eng.* 38, 2829–2840. <https://doi.org/10.1007/s10439-010-0057-8>
- Zahedmanesh, H., Lally, C., 2012. A multiscale mechanobiological modelling framework using agent-based models and finite element analysis: Application to vascular tissue engineering. *Biomech. Model. Mechanobiol.* 11, 363–377. <https://doi.org/10.1007/s10237-011-0316-0>
- Zahedmanesh, H., Lally, C., 2009. Determination of the influence of stent strut thickness using the finite element method: Implications for vascular injury and in-stent restenosis. *Med. Biol. Eng. Comput.* 47, 385–393. <https://doi.org/10.1007/s11517-009-0432-5>
- Zartner, P., Cesnjevar, R., Singer, H., Weyand, M., 2005. First successful implantation of a biodegradable metal stent into the left pulmonary artery of a preterm baby. *Catheter. Cardiovasc. Interv.* 66, 590–4. <https://doi.org/10.1002/ccd.20520>
- Zheng, Y.F., Gu, X.N., Witte, F., 2014. Biodegradable metals. *Mater. Sci. Eng. R Reports* 77, 1–34. <https://doi.org/10.1016/j.mser.2014.01.001>
- Zunino, P., D’Angelo, C., Petrini, L., Vergara, C., Capelli, C., Migliavacca, F., 2009. Numerical simulation of drug eluting coronary stents: Mechanics, fluid dynamics and drug release. *Comput. Methods Appl. Mech. Eng.* 198, 3633–3644. <https://doi.org/10.1016/j.cma.2008.07.019>

4 Mechanical and Corrosion Testing of Magnesium WE43 Specimens for Pitting Corrosion Model Calibration

4.1 Chapter Overview

Computational modelling can play an important role in the analysis, design and development of complex medical devices such as biodegradable coronary stents. In this study, experimental mechanical and corrosion testing is conducted to characterise the mechanical and corrosion behaviour of magnesium WE43 alloy, a candidate base material for biodegradable magnesium alloy stents. Previously developed uniform and pitting corrosion models are calibrated based on *in-vitro* mechanical and corrosion testing of magnesium WE43 alloy specimens. The calibrated pitting corrosion model can capture the mechanical and corrosion behaviour of magnesium WE43, including the experimentally observed non-linear reduction in failure strength with mass loss, whereas the uniform corrosion model is incapable of capturing this trend. The calibrated corrosion models will be used in future research on magnesium alloy stents.

The content of this chapter has appeared in a journal article in *Advanced Engineering Materials* (Boland et al., 2018).

4.2 Introduction

As previously indicated, medical implants made from biomaterials are attracting significant interest due to the potential to avoid long-term complications associated with permanent devices. Magnesium (Mg) is a promising material for such applications as it is the fourth most abundant element found within the human body and is easily absorbed and excreted by the human body (Staiger et al., 2006; Walker et al., 2014).

High-purity magnesium is limited for use in many applications due to its low strength (Bowen et al., 2012a; Campos et al., 2013). Magnesium alloys can provide improved mechanical strength (Gu et al., 2009), which is particularly important for use in load bearing applications, but typically alloying decreases corrosion resistance compared to high-purity magnesium (Song and Song, 2007).

As previously mentioned in Chapter 2, Stress Corrosion Cracking (SCC) is another important factor to consider when using bioresorbable magnesium as the backbone of implantable medical devices with a load bearing application. SCC can cause the development of sub-critical crack growth under mechanical loading conditions considered to be safe (Winzer et al., 2005), which can lead to premature fracture formation and failure of the device.

In the area of coronary artery disease biodegradable stents made from magnesium alloys are rapidly developing, with the Biotronik Magmaris bioresorbable scaffold being the first of these next generation devices to achieve approval in the European market (as discussed in Chapter 2). Magnesium alloy biodegradable stents have advantages over polymeric biodegradable stents as they have mechanical properties that are more comparable to the state-of-the-art materials for permanent stents, i.e. stainless steel 316L and cobalt chromium L605.

As previously indicated, computational modelling can play an important role in the analysis, design and development of complex medical devices such as endovascular stents (Conway et al., 2012; Grogan et al., 2012; Karanasiou et al., 2017; McGrath et al., 2016; Shine et al., 2017; Sweeney et al., 2014). Grogan and co-workers have previously developed uniform and pitting corrosion models for magnesium alloy stents which have been calibrated to *in-vitro* experimental corrosion data of Mg AZ31 micro-films (Grogan et al., 2011). While aluminium (Al) alloying of magnesium increases mechanical properties without negatively affecting corrosion resistance (Kirkland, 2012), health concerns over long-term exposure to Al (Kirkland, 2012) means Mg-Al alloys such as Mg AZ31 are unlikely to be used as a biomaterial for the biodegradable implant application.

Biotronik have not disclosed the exact magnesium alloy used for the Magmaris bioresorbable scaffold. However, an earlier magnesium alloy stent from Biotronik, the AMS stent, was constructed from a magnesium alloy containing the same alloying elements as Mg WE43 alloy (yttrium, zirconium and rare earth metals) (Waksman et al., 2006) and was used during the PROGRESS-AMS clinical trial (Waksman et al., 2009).

As mentioned in Chapter 2, a recent review paper by Rapetto and Leoncini, (2017) has stated that the Magmaris scaffold is made from a refined Mg WE43 alloy, while separately Sotomi et al., (2017b) have reported that the Magmaris scaffold is made from a magnesium alloy with a composition of 93 % Mg and 7 % rare earth elements.

The use of an alloy similar to Mg WE43 in the PROGRESS-AMS clinical trial and the reports in recent review papers in relation to the Magmaris stent, indicate the value of understanding the mechanical and biodegradation behaviour of Mg WE43 for the design and development of biodegradable magnesium stents.

On this basis then, the first objective of the present work is to experimentally characterise the mechanical and corrosion behaviour of Mg WE43 and to determine the effect corrosion has on the mechanical integrity of the material.

Studies have been conducted on the strength of magnesium and magnesium alloys after corrosion such as tensile testing of corroded pure magnesium wires (Bowen et al., 2012b), tensile testing of corroded Mg AZ31 foils (Grogan et al., 2011), three-point bend testing of corroded Mg-Zn samples and tensile testing of corroded Mg WE43 dogbone and wire specimens (Galvin et al., 2017).

Galvin et al., (2017) is the most recent publication that is relevant to this study, providing experimental results for ultimate tensile strength (UTS) versus immersion time for Mg WE43 dogbone and wire specimens. However, further tensile testing of corroded Mg WE43 specimens is required to more comprehensively characterise the effect that corrosion has on the mechanical integrity of the material, particularly when the material is subject to high levels of corrosion and consequently, is relatively fragile.

The second objective of the work is to use the results of the mechanical and corrosion experiments to calibrate previously developed uniform and pitting corrosion models (Grogan et al., 2011) for the Mg WE43 material. The calibration for Mg WE43 should allow the more appropriate usage of these computational models for application to the analysis of magnesium alloy stents.

4.3 Methods

4.3.1 Sample Preparation

50 mm diameter bars of Mg WE43-T6 alloy were sourced from Smiths Metal Centres Ltd, UK. Riteway Engineering Ltd (Galway, Ireland) subsequently performed wire electrical discharge machining (EDM), which is also known as spark erosion, to produce various Mg WE43 specimens for mechanical testing, immersion corrosion testing and surface characterisation.

4.3.2 Mechanical Testing

Three standard dogbone specimens with thickness of 6 mm were tested in uniaxial tension to fracture using a universal tensile tester (Instron 4467, UK) according to the ASTM E8/E8M-15a. Images of the dogbone samples after testing are shown in Figure 4.1. The tensile machine was set to a constant crosshead speed equal to 0.5 mm/min, to determine the elastic-plastic behaviour of the Mg WE43 material, including Young's modulus, yield strength, strain hardening behaviour and the UTS. Tensile strain was measured using a non-contact video extensometer. Data was analysed using the TestXpert software (Zwick Inc., Germany).

The author wishes to clarify that these uniaxial tension experiments were performed by Dr. Reyhaneh Shirazi, a co-author on the above mentioned paper by Boland et al., (2018). This tensile test data was critically important for calibration of the Mg WE43 alloy material models for the present stent application. The author received the stress-strain data from Dr. Shirazi and performed the data analysis to extract elastic-plastic material properties as documented below. All subsequent experiments reported in this chapter were performed by the author.

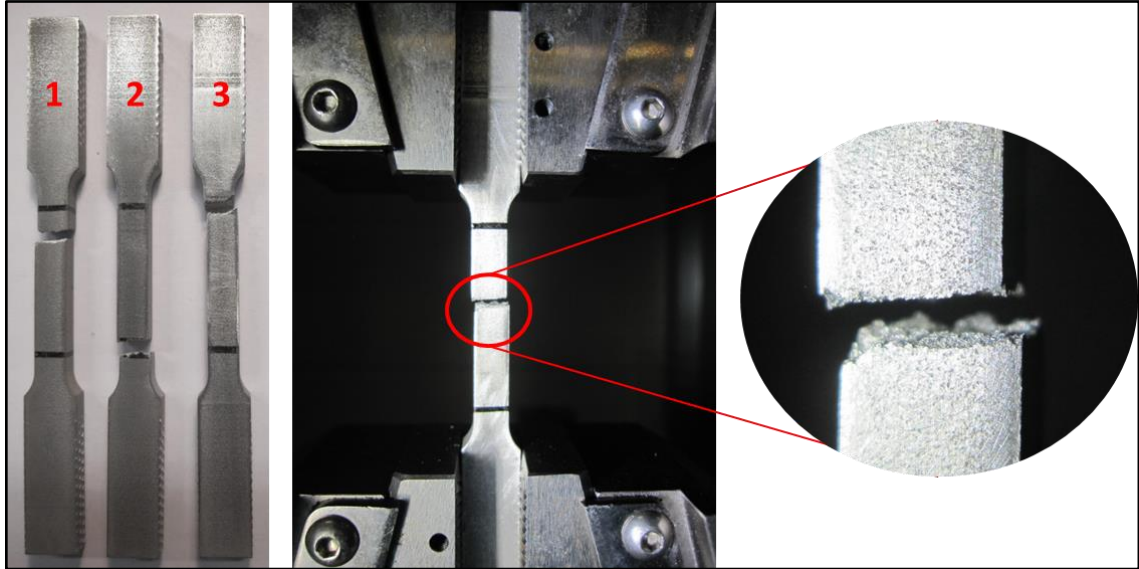


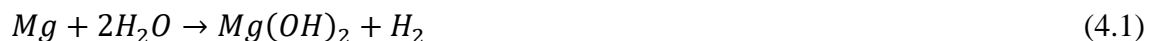
Figure 4.1. (a) Images of three dogbone specimens after tensile testing. (b) Image of dogbone specimen in the Instron tensile tester after fracture. (c) Magnified image of the dogbone specimen highlighting the fracture surface. Image courtesy of Dr. Reyhaneh Shirazi (Figure 1 from Boland et al., (2018)).

4.3.3 Immersion Testing

To accurately characterise the corrosion behaviour of Mg WE43 alloy, two separate corrosion experiments were conducted. The first experiment, experiment 1, involved *in-vitro* immersion testing of Mg WE43 specimens in simulated body fluid to determine the corrosion rate of Mg WE43 samples with different surface characteristics. The second experiment, experiment 2, involved *in-vitro* immersion testing of Mg WE43 specimens in simulated body fluid followed by tensile testing until fracture to evaluate the effect corrosion has on the mechanical strength of the material.

For both *in-vitro* immersion testing experiments, specimens were immersed in modified Hank's solution (H8264, Sigma-Aldrich, Dublin, Ireland), with the solution temperature being maintained at 37 °C by means of a thermostatically controlled water bath. The solution volume (ml) to surface area (cm²) of greater than 50:1 was maintained for all cases. Yang and Zhang, (2009) showed that increasing this ratio above 6.7 has a negligible influence on the corrosion behaviour of a similar magnesium alloy in Hank's solution so this ratio was deemed acceptable.

In aqueous environments magnesium dissolution proceeds by an electrochemical reaction with water to produce magnesium hydroxide and hydrogen gas (Atrens et al., 2015; Song and Atrens, 1999). The overall reaction equation is:



The volume of hydrogen gas produced can be used to determine the corrosion rate of magnesium from the chemical balance illustrated in Equation 4.1, where one mole of H₂ gas is evolved for one mole of Mg corroded.

Prior to experiments 1 and 2 all corrosion surfaces were cleaned in anhydrous ethanol and left to dry for a period of 24 hours to achieve a consistent oxidation on all surfaces. The dimensions and mass of all specimens were recorded prior to testing.

4.3.3.1 Experiment 1

The experimental set-up for *in-vitro* corrosion testing for experiments 1 is illustrated in Figure 4.2, with magnesium samples suspended to ensure all corrosion surfaces were exposed to the solution. To minimise losses of Hank's solution due to evaporation plastic wrap was also placed over the glassware used.

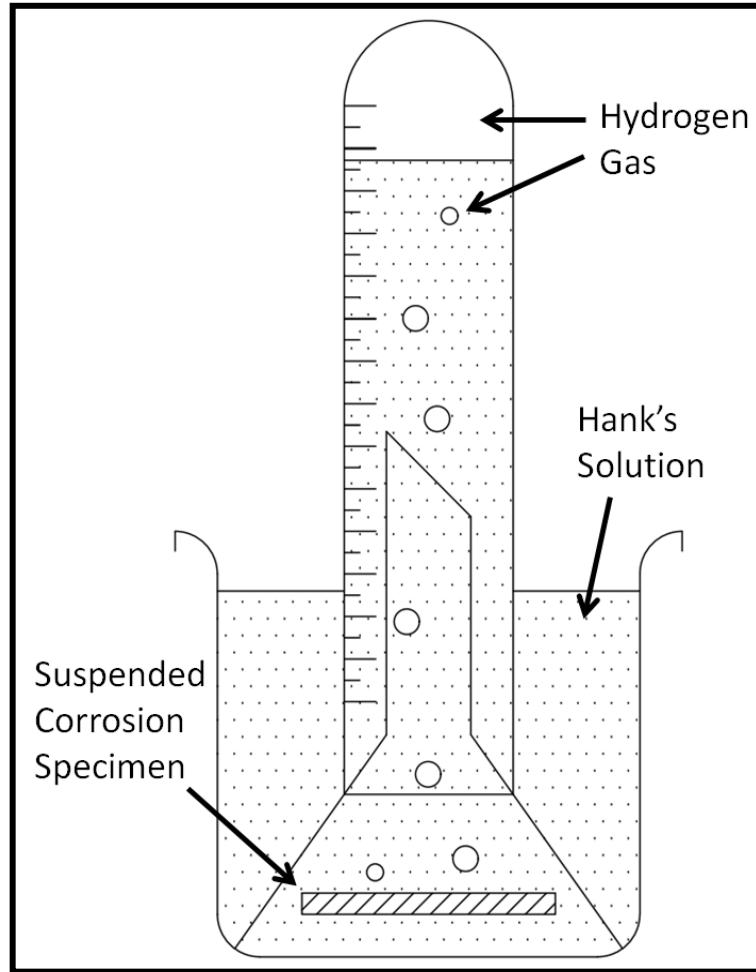


Figure 4.2. Immersion corrosion testing set up for collection of hydrogen gas evolved from suspended corrosion specimen illustrating beaker of Hank's solution, funnel, inverted measuring cylinder and the suspended magnesium sample.

As illustrated in Figure 4.2, the transient hydrogen evolution was measured by the displacement of Hank's solution from an inverted measuring cylinder. The alloy corrosion rate was calculated from the volume of evolved hydrogen gas, based on the chemical balance outlined in Equation 4.1 and using a method described in Song and Atrens, (2003).

For experiment 1, corrosion tests were carried out on unground EDM Mg WE43 alloy specimens (Figure 4.3a) as received from Riteway Engineering Ltd following wire electrical discharge machining. These unground EDM specimens had cross section dimensions of approximately 2 mm by 2 mm, while the length of each specimen was approximately 50 mm.

Further corrosion experiments were conducted on similar specimens following mechanical grinding using emery paper up to 1200-grit. Mechanical grinding changes the surface characteristics of the specimens (Figure 4.3b) and removes any potential damage layer created by the EDM process which was used to cut specimen samples for testing from the Mg WE43 bar. These ground samples had the same cross section dimensions (approx. 2 mm by 2 mm) as the unground EDM samples but with lengths of approximately 20 mm. For the unground EDM samples immersion testing (5 samples, 50 mm long) took place over a period of two days, while a period of four weeks was deemed sufficient to characterise the corrosion rate of the ground samples (5 samples, 20 mm long).

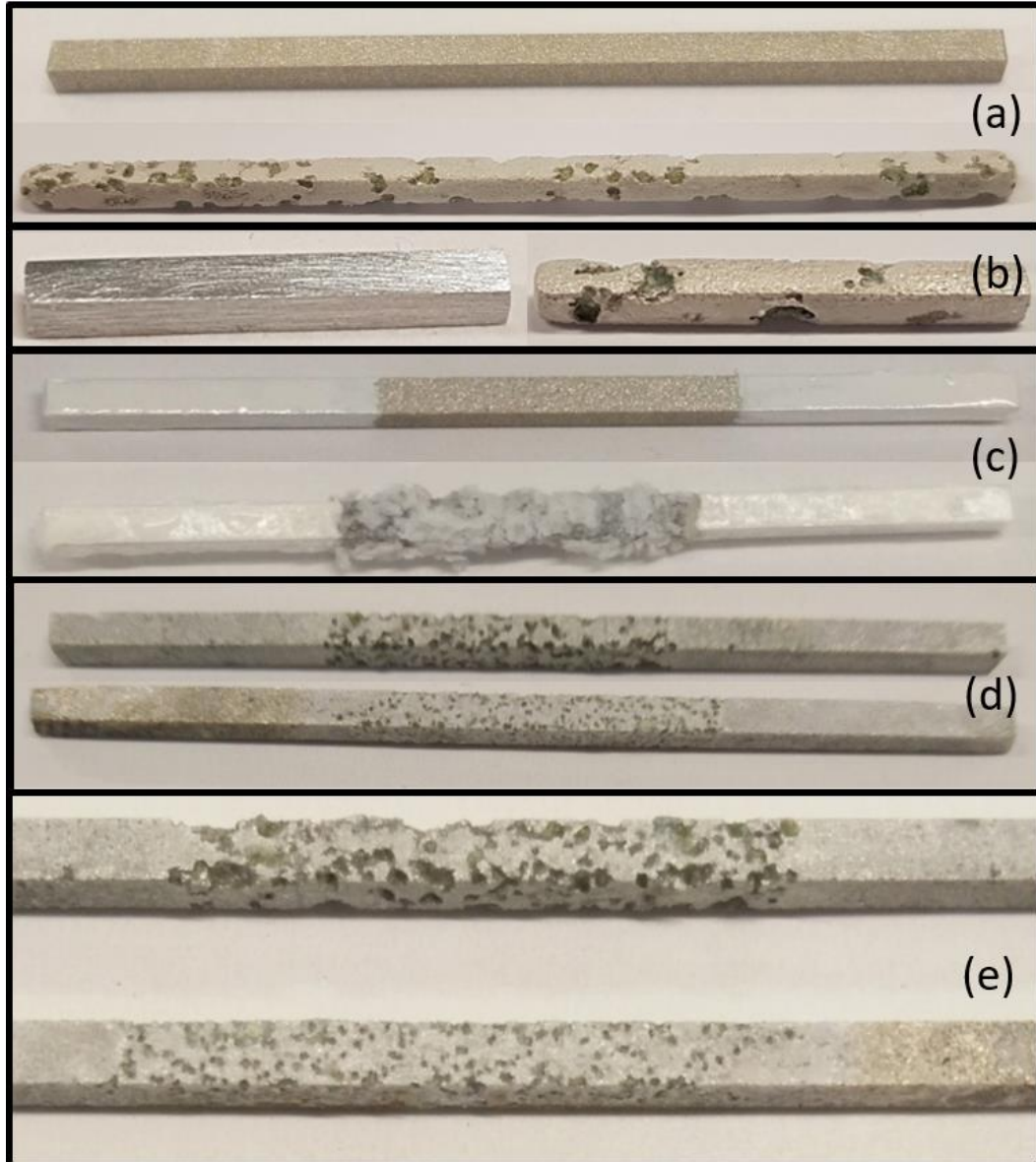


Figure 4.3. (a) Image of an unground EDM Mg WE43 samples before and after corrosion testing for experiment 1. Top image shows the unground EDM, uncorroded Mg WE43 sample (length=50 mm). Bottom image shows the unground EDM Mg WE43 sample after corrosion (11.7 % mass loss) and following removal of magnesium corrosion product using a chromic acid solution. (b) Image of a ground Mg WE43 sample before and after corrosion testing for experiment 1. Left image shows the ground, uncorroded Mg WE43 sample (length=20mm). Right image shows the ground Mg WE43 sample after corrosion (10.1 % mass loss) and following removal of Mg corrosion product using a chromic acid solution. (c) Top image of unground EDM Mg WE43 sample after painting and before corrosion testing for experiment 2. Bottom image of unground EDM Mg WE43 sample after corrosion testing for experiment 2 highlighting the accumulation of corrosion product (magnesium hydroxide) around the corrosion surfaces. (d) Image of two unground EDM Mg WE43 samples after corrosion testing for experiment 2 following the removal of paint and corrosion product using a chromic acid solution. The end regions which have had a layer of paint removed remain unaffected by corrosion. (e) Magnified image of centre regions of two unground EDM Mg WE43 samples following corrosion for experiment 2. Top sample has 22 % mass loss in corroded region while the bottom sample has 7.5 % mass loss in corroded region.

Before *in-vitro* immersion testing the surface roughness's of both the unground EDM and ground samples were measured using a profilometer (Taylor Hobson Ltd, Surtronic 3⁺, UK) to characterise the topography of the surface material. Energy-dispersive X-ray (EDX) spectroscopy was also conducted on both the unground EDM and ground samples before testing to determine the elemental composition of the surface material. This was used to evaluate the expected damage layer for the unground EDM samples and ensure that this damage layer was completely removed by mechanical grinding before immersion testing of the ground samples.

4.3.3.2 Experiment 2

Unground Mg WE43 alloy specimens following wire EDM were used for experiment 2 (corrosion testing followed by tensile testing until specimen fracture) with cross section dimensions of 2 mm by 2 mm with lengths of approximately 50 mm. The experimental set up for corrosion testing was the same as the set up for experiment 1 (Figure 4.2) however, unlike experiment 1, the corrosion was restricted to a 20 mm section in the middle of the specimen. The ends of the specimen were coated in oil-based metallic paint to create a physical barrier between the surface of the magnesium material and the simulated body fluid and thus prevent corrosion in the end regions and allow corrosion in the centre region (see Figure 4.3c). This was to ensure the specimen would break in the corroded centre region during the tensile test and to allow accurate calculation of specimen mass loss of the centre region.

Following corrosion of the unpainted central region, tensile testing of corroded Mg WE43 specimens was conducted using a Zwick testing machine (Zwick model BZ2.5, UK) with a 1 kN load cell. The non-corroded end regions were placed between the anti-slip pneumatic grips and the specimen was subject to uniaxial tension to fracture, which occurred in the corroded centre region for all specimens. A constant crosshead speed of 1 mm/min was used for the tensile tests on corroded specimens. Data was analysed using the TestXpert software (Zwick Inc. Germany).

It was originally planned to conduct experiment 2 using both and unground EDM and ground specimens, however for a number of reasons, as summarised in the following paragraph, only the results from the unground EDM specimens are reported here.

Firstly, one of the objectives of this work is to completely characterise the effect that corrosion has on the mechanical strength of the Mg WE43 alloy, including substantially corroded samples of Mg WE43 alloy. The unground EDM specimens corroded much faster than the ground specimens thus high levels of corrosion (up to 50 %) can be achieved in a short period of time (1-2 days) which proved particularly convenient for these experiments. Conversely, the ground samples corrode much more slowly, therefore, achieving high levels of corrosion (up to 50 %) would require the ground samples to be submerged in Hank's solution for a significantly longer period of time (much greater than 4 weeks). Additionally the ends of the unground EDM specimens were coated in oil-based metallic paint (Figure 4.3c) to prevent corrosion in the end regions and allow corrosion in the centre region in order to ensure the specimen would break in the corroded centre region during the tensile test and to allow accurate calculation of specimen mass loss of the centre region. This method was very effective for the unground EDM specimens as high levels of corrosion are achieved in a relatively short period of time. However, it was noted during preliminary experiments of ground samples that the integrity of the oil-based metallic paint, and thus its effectiveness in preventing corrosion in the end regions of the specimens, is compromised after being submerged in Hank's solution for extended periods of time (much greater than 4 weeks), making completion of experiment 2 for ground specimens particularly challenging. Finally, if an alternative method for preventing the corrosion in the end regions could be proven to be effective over extended periods of time, such as coating the end regions in an epoxy resin, the author would still expect to encounter some difficulties achieving high levels of corrosion for the ground samples. As shown in the results section a gradual reduction in corrosion rate over time is observed for the ground samples (Figure 4.5b) which may have attributed to the build-up of a layer of corrosion product around the corrosion surface or the increase in pH of the solution over time (Song, 2007).

In summary, for all the above reasons, for experiment 2 (corrosion testing followed by tensile testing until specimen fracture) only the results from the unground EDM specimens are reported here.

4.3.4 Corrosion Model Overview

As mentioned in Section 4.2, uniform and pitting corrosion models for magnesium alloy stents have been developed (Grogan et al., 2011). These models have been implemented for use in the finite element software Abaqus (DS SIMULIA, USA).

The uniform corrosion model generates optimal corrosion mechanics in terms of providing long term mechanical support (Chapter 3) due to a homogeneous corrosion behaviour from the corrosion surface through the material. The pitting corrosion model provides a more realistic and accurate model for how the Mg WE43 alloy corrodes both *in-vitro* and *in-vivo*. The uniform and pitting corrosion models can be fundamentally classified as phenomenological, in that they capture the overall phenomena of corrosion but do not explicitly represent the multi-physics processes responsible for generating the corrosion. Detailed descriptions of the uniform and pitting corrosion models can be found in Chapter 2, Chapter 3 and in the literature (Boland et al., 2016; Grogan et al., 2011) hence the details of the corrosion models are not repeated here.

4.3.5 Corrosion Model Calibration

The corrosion model is calibrated from the results of experiments 1 and 2 by replication of the experiments in Abaqus software and the use of an iterative procedure to find model parameters which qualitatively match the experimental results. Representative geometries of the corrosive regions are meshed with linear reduced integration brick elements ($L_e = 0.070$ mm for all simulations) with the length of the geometry corresponding to the length of respective corrosion regions for experiment 1 and the average distance between the grips of the tensile tester (33.8 mm) for experiment 2.

The mechanical properties of uncorroded Mg WE43 alloy are taken from the results of the mechanical testing outlined in Section 4.3.2 and used for Abaqus/Explicit computational simulations. Representative stress strain curves and the corresponding

elastic and plastic properties are shown in Figure 4.4 and Table 4.1, respectively. Elasticity is considered linear and isotropic in terms of finite deformation quantities (Cauchy stress and Lagrangian strain) and is described through Young's modulus and Poisson's ratio ($\nu = 0.3$), while plasticity is described using J_2 flow theory with isotropic hardening.

Experiment 1 is simulated by allowing corrosion to occur on all surfaces exposed to the corrosive environment. The rate of mass loss is determined by the average damage value, D , of all elements in the model with D ranging from a value of 0 for undamaged elements to a value of 1 for completely damaged elements.

Experiment 2 is simulated by allowing elements in the corrosive region to corrode and then applying a tensile displacement to the test region. The maximum tensile force computed by the model is taken as the simulated failure strength of material for the respective mass loss due to corrosion and compared with the values observed experimentally. A further condition for fracture is implemented here by removing elements in which the elemental strain exceeds the elongation at break of the material. Consistent with this, it is important to note that it is the original formulation of both uniform and pitting corrosion models i.e. removal of the element after complete degradation, that is implemented in this chapter.

Grain size of Mg WE43 alloys can range from 0.5 to 15 μm (Kutniy et al., 2009). Mg-based alloys are still limited for use as a biomaterial by their high degradation rates and consequent loss in mechanical integrity (Chen et al., 2014). For the Mg WE43 alloy increasing grain size increases corrosion resistance (Kutniy et al., 2009) therefore in this study the material characteristic length δ_U is assigned a value of 15 μm as, for the load bearing application such as magnesium alloy stenting, low corrosion rate would be considered desirable (Boland et al., 2017).

For the uniform corrosion model, only the corrosion kinetic parameter k_U (see Equation 2.3) must be calibrated as $\lambda_e = 1$, for every element in the corroding material, therefore $\gamma = \infty$ and $\beta = 1$. For calibration of the pitting corrosion model for a given δ_U and L_e

(see Equation 2.5), three independent model parameters (k_U , γ and β) (see Equation 2.5 and Equation 2.6) must be determined based on the simulations of experiments 1 and 2 for unground EDM specimens. The results of the corrosion followed by tensile testing simulation are used to plot a failure strength versus mass loss due to corrosion curve. Calibrating the results of this simulation with the experimentally observed trend from experiment 2 is used to determine parameters γ and β . The corrosion kinetic parameter k_U for unground EDM material is subsequently determined by quantitatively matching the results of experiment 1 with the corrosion simulations.

4.4 Results

4.4.1 Mechanical Testing

Figure 4.1 shows the Mg WE43 alloy samples after fracture. It is observed that the fracture of the alloy samples is predominantly by brittle cleavage. Force-displacement data was used to obtain the nominal tensile stress-strain curves shown in Figure 4.4. The mechanical properties for the three dogbone samples, which were determined from the nominal stress-strain curves, are given in Table 4.1.

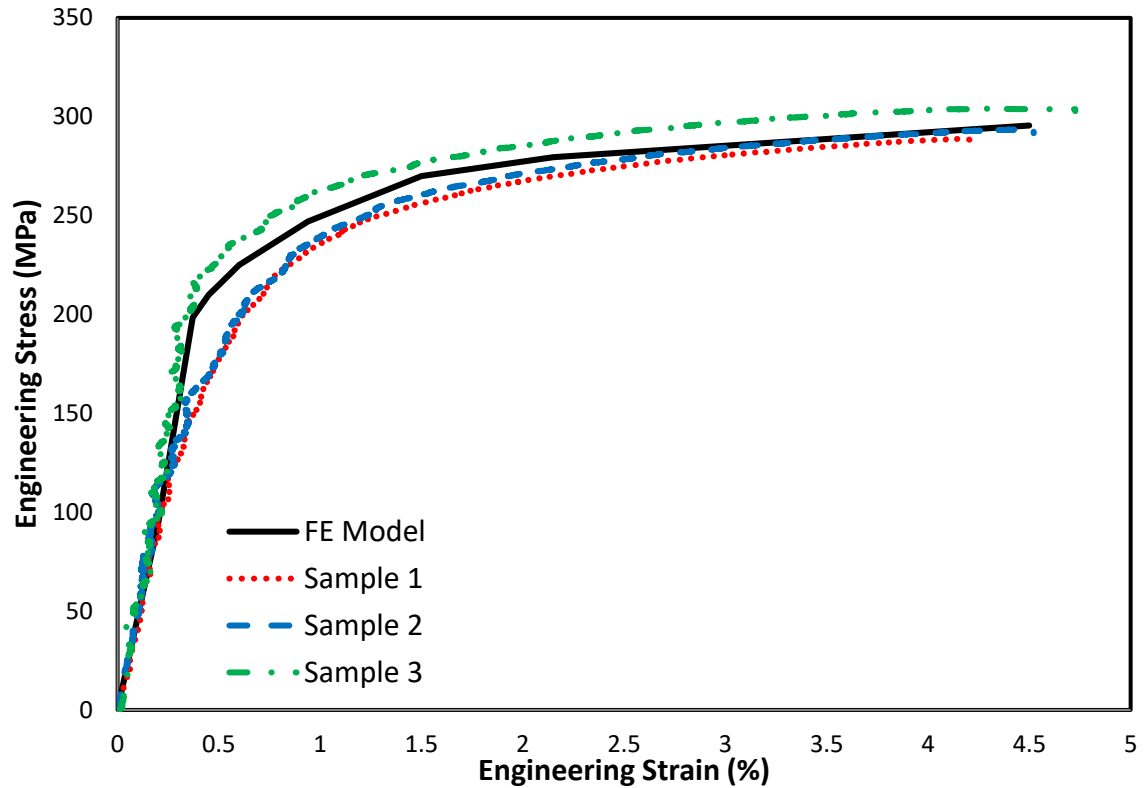


Figure 4.4. Engineering stress-strain curves from tensile testing of three Mg WE43 dogbone specimens. The FE implementation of the average experimental curve for undamaged Mg WE43 is shown by the black line in the plot.

Table 4.1. Mechanical properties calculated from the results of tensile testing of Mg WE43 dogbone specimens.

	Young's modulus (<i>GPa</i>)	Ultimate tensile strength (<i>MPa</i>)	Yield strength (offset = 0.2 %) (<i>MPa</i>)	Elongation at break (%)
Sample 1	40.0	288.8	200.2	4.2
Sample 2	43.2	293.6	203.0	4.5
Sample 3	66.6	304.1	237.6	4.7
Average	49.9 ± 14.4	295.5 ± 6.4	213.6 ± 20.8	4.5 ± 0.2

The Young's modulus of each of the specimens was calculated from the slope of the initial elastic region of the stress-strain curve, while the yield strength of each specimen was calculated using the offset method (offset = 0.2 %) according to the ASTM

E8/E8M-15a. Average values for Young's modulus, yield strength, UTS and elongation at break are also shown in Table 4.1. These average values were used to generate the "FE model" curve in Figure 4.4, which was inputted into all subsequent computational models to describe the elastic-plastic behaviour of Mg WE43.

4.4.2 Immersion Testing

4.4.2.1 Experiment 1

The results of experiment 1, i.e. immersion corrosion testing of unground EDM and ground samples, are shown in Figure 4.5a and Figure 4.5b. The unground EDM samples corrode over 50 times faster than the ground samples with unground EDM samples corroding by approximately 29.7 % in a period of 29 hours while the ground samples corroded just 13.2 % in a period of 27 days. This corresponds to an average corrosion rate of $215.7 \text{ g m}^{-2} \text{ d}^{-1}$ and $3.9 \text{ g m}^{-2} \text{ d}^{-1}$ for the unground EDM and ground samples respectively.

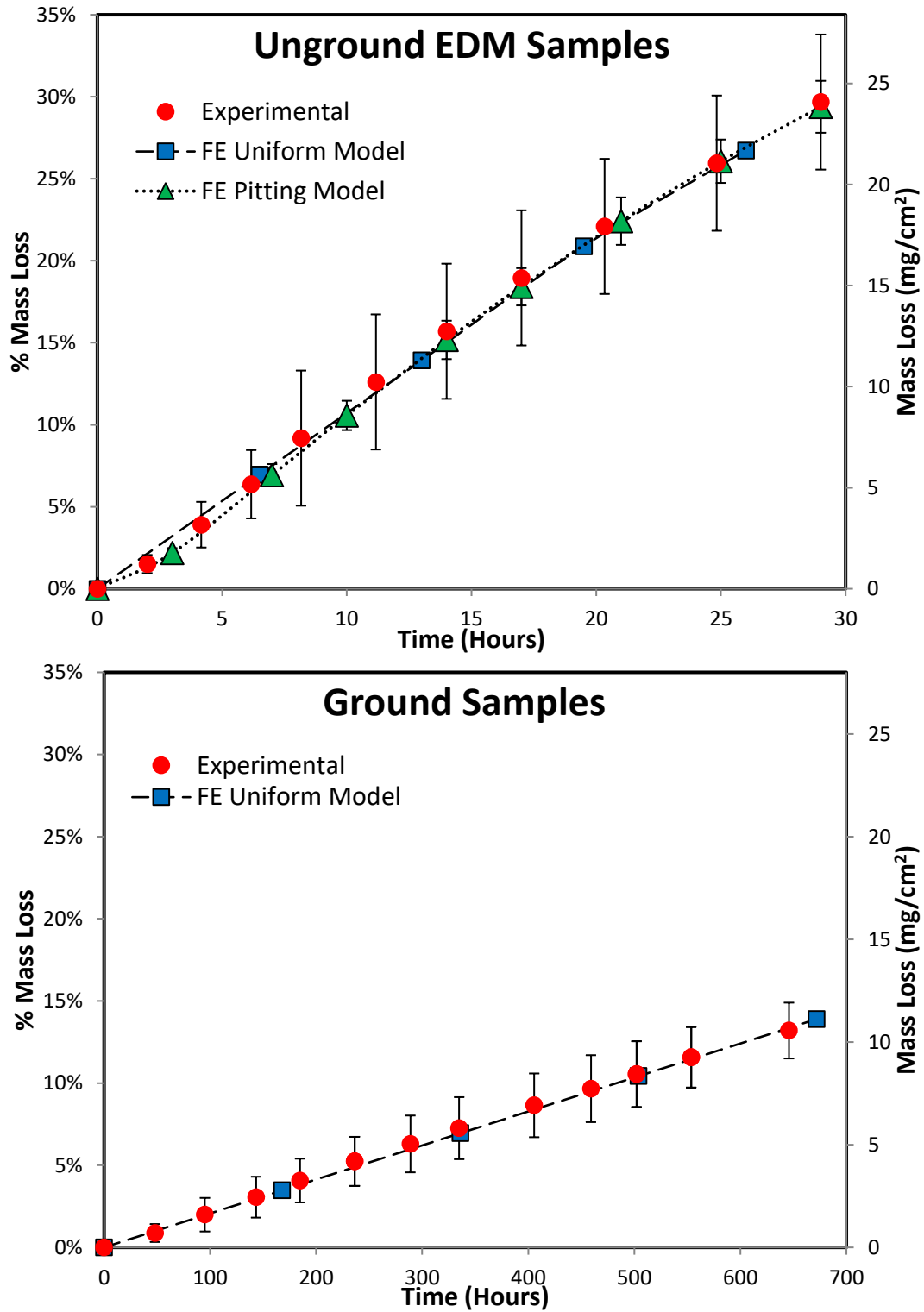


Figure 4.5. Plot of percentage mass loss versus time based on the results of experiment 1 for the unground EDM samples (a) and ground samples (b). The FE uniform model mass loss prediction is shown in both plots while the FE pitting model mass loss prediction is included in the plot for unground EDM samples.

Error bars represent a single standard deviation from the mean (n=5).

4.4.2.2 Experiment 2

The results of experiment 2, i.e. immersion testing followed by tensile testing of 17 unground EDM specimens, are illustrated in Figure 4.6 in the form of a failure strength versus mass loss plot. Uncorroded specimens have a failure strength similar to the material UTS observed during tensile testing of dogbone specimens. As demonstrated in Figure 4.6 an increase in mass loss results in a reduction in strength of the corroded specimen. However, the correlation between failure strength and mass loss is non-linear (similar to an exponential decay pattern) with approximately 50 % corrosion resulting in complete loss of specimen strength.

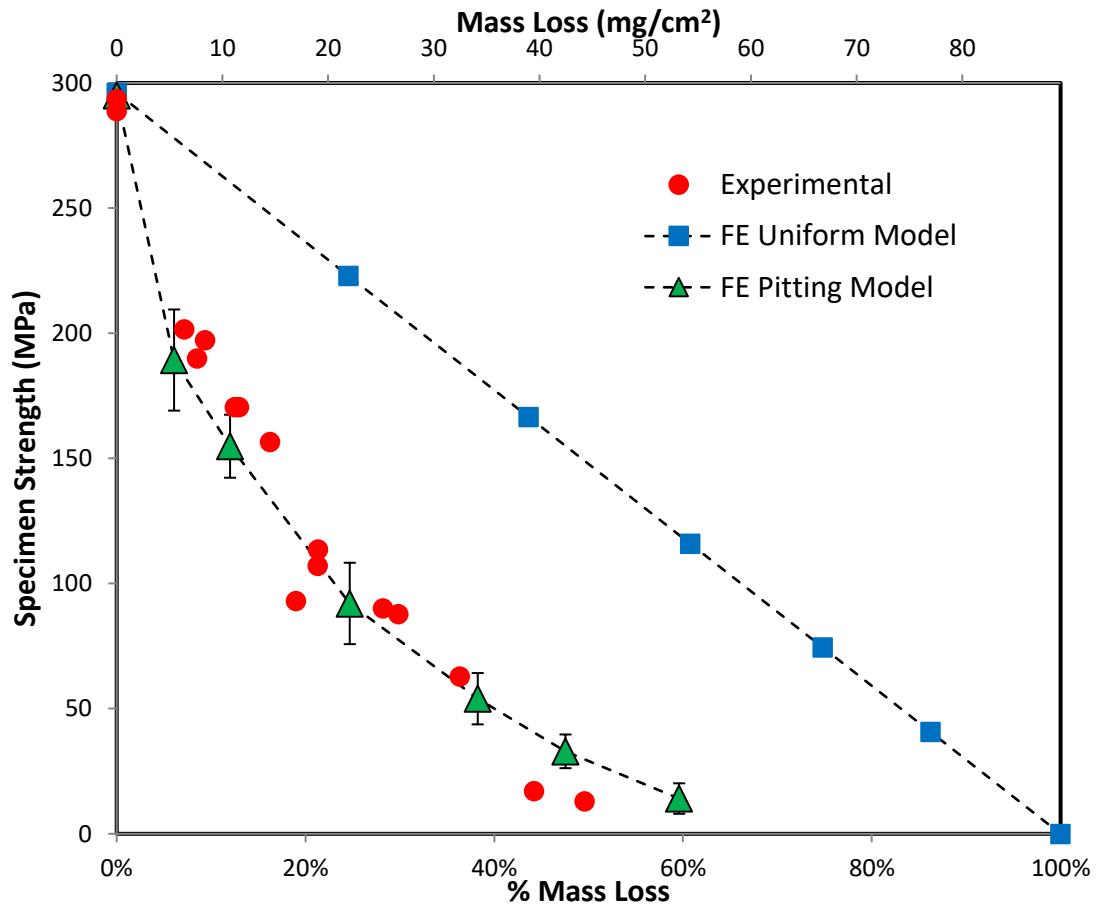


Figure 4.6. Plot of experimental results and FE simulation predictions for the reduction of specimen strength versus mass loss due to corrosion for unground EDM specimens. Error bars for the FE pitting corrosion model represent a single standard deviation from the mean (n=5).

4.4.2.3 Surface Characterisation

Scanning electron microscopy (SEM) was used to view the initial corrosion surface of the unground EDM and ground samples at a micro level. Figure 4.7a illustrates the surface topology of the unground EDM magnesium samples before corrosion at two different magnitudes. The initial corrosion surface appears quite rough with no obvious alignment direction. This surface was created via the wire EDM process which was used to cut the samples from the original Mg WE43 bar.

Figure 4.7b illustrates the surface structure of the ground magnesium samples before corrosion. Mechanical grinding with up to 1200-grit paper significantly altered the initial corrosion surface of the specimens as illustrated. Comparison of the SEM images show that grinding has significantly increased the smoothness of the surface when compared with the unground EDM samples and has also resulted in the alignment of small micro abrasions along the vertical direction in Figure 4.7b. The vertical direction in Figure 4.7b corresponds with the longitudinal axis of specimen which was the direction of mechanical grinding.

A profilometer was used to quantify the change in roughness of the specimens due to mechanical grinding. The average surface roughness (R_a) of the unground EDM specimens before corrosion testing was 4.54 μm while the ground samples have a R_a value of 0.20 μm , which is a significant reduction.

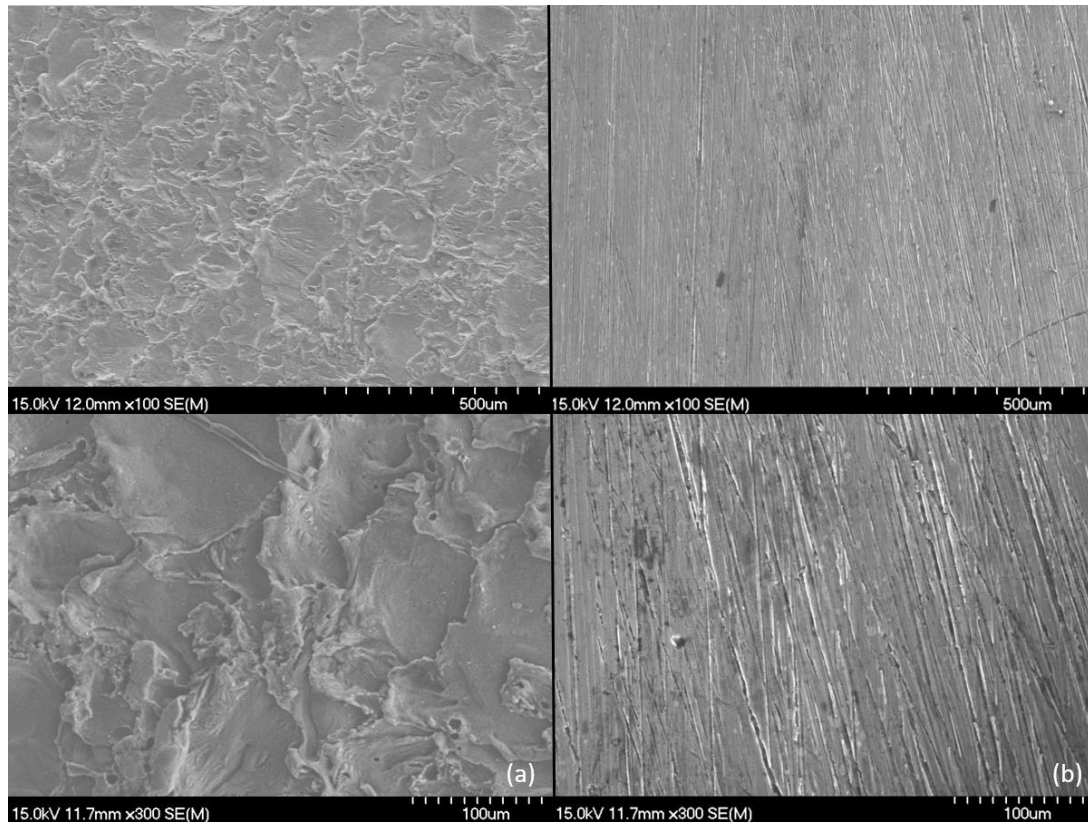


Figure 4.7. (a) SEM images of unground EDM samples at two different magnifications before corrosion.
(b) SEM images of ground samples at two different magnifications before corrosion.

Energy-dispersive X-ray (EDX) spectroscopy was also conducted on both the unground EDM and ground samples before testing to determine the elemental composition of the surface material. This was used to evaluate the expected damage layer for the unground EDM samples and ensure that this damage layer was completely removed by mechanical grinding for the ground samples.

The results of the EDX analysis show that the external corrosion surface of the unground EDM samples contain elevated levels of carbon atoms. These carbon atoms are a result of the wire EDM process used to cut samples from the magnesium bar, which uses precision electrical sparks, generating exceptionally high local temperatures, to erode the metal.

EDX analysis of the ground specimens showed the external surface of these specimens did not contain carbon atoms, which confirmed that grinding with emery paper up to

1200-grit was sufficient to remove the damage layer associated with wire EDM cutting process.

The other elemental compositions revealed by the EDX analysis (magnesium, yttrium) are consistent with the expected levels for Mg WE43 alloy reported in the technical datasheet provided by the material supplier (Smith Metal Centres, 2018).

4.4.3 Corrosion Model Calibration

4.4.3.1 Uniform Corrosion

As previously mentioned in Section 4.3.5, with the uniform corrosion model $\gamma = \infty$ and $\beta = 1$ for all cases therefore only one parameter, k_U , which controls the material corrosion rate, must be calibrated for both unground EDM and ground specimens. The calibrated k_U parameters for unground EDM and ground specimens are listed in Table 4.2. The calibrated k_U value for unground EDM specimens is approximately 50 times larger than corresponding value for ground specimens.

As illustrated by the plots in Figure 4.5a and Figure 4.5b, the uniform corrosion model can accurately replicate the mass loss versus time curve for both unground EDM and ground specimens. However, as illustrated by the plot of specimen strength versus percentage mass loss for unground EDM specimens (Figure 4.6), the uniform corrosion model fails to capture the experimentally observed rapid reduction in specimen strength due to corrosion.

4.4.3.2 Pitting Corrosion

To model the experimentally observed reduction in specimen strength due to corrosion (Figure 4.6) calibration of the pitting corrosion model is required. The pitting corrosion model can only be accurately calibrated for the unground EDM specimens, as experiment 2 was only conducted on these specimens and not for the ground specimens for reasons already outlined.

To calibrate the pitting corrosion model, γ and β must be determined initially, by a systematic process involving the use of a computational model of pitting corrosion followed by tensile testing until fracture, and matching the computational results with experimentally observed results for specimen strength versus mass loss, adjusting the γ and β values until a good fit is achieved. Subsequently, k_U for the pitting corrosion model is determined by comparing the rate of corrosion entered in the computation model with the experimental corrosion rate for unground EDM specimens shown in Figure 4.5a. The calibrated corrosion parameters are listed in Table 4.2. As shown by the plots in Figure 4.6, the calibrated pitting corrosion model can accurately capture the experimentally observed trend of rapid reduction in specimen strength due to corrosion.

For each parameter set the simulation was run five times with a different initial seed value entered into the Weibull distribution-based random number generator each time to generate five different initial pit configurations. The average results of these five simulations were subsequently used to calibrate the pitting corrosion model with the experimental data and for the plots in Figure 4.5a and Figure 4.6.

Table 4.2. Uniform and pitting corrosion model parameters for unground EDM and ground samples of Mg WE43 alloy.

	Parameter	L_e (mm)	δ_U (mm)	k_U (h^{-1})	γ	β
Unground EDM	Uniform	0.070	0.015	0.3600	∞	1
Samples	Pitting	0.070	0.015	0.0004	0.2	0.8
Ground Samples	Uniform	0.070	0.015	0.0069	∞	1

Finite element model images for one of the pitting corrosion simulations of experiment 2: corrosion of the magnesium specimen followed by fracture due to the applied tensile load, are shown in Figure 4.8. The cross section of the simulation geometry is the same as the specimens used in the experiments (approx. 2 mm by 2 mm) with the total length of the geometry corresponding the average distance between the grips of the tensile tester for experiment 2 (33.8 mm). The corrosive region corresponds to the average

length of the unpainted corroded region (20 mm) illustrated in Figure 4.3c, while the remaining ends of the specimen which correspond to the painted regions in the experiment are restricted from pitting corrosion. The total representative geometry is meshed with 405,720 linear reduced integration brick elements ($L_e = 0.070$ mm) following the completion of a mesh convergence study. As illustrated in Figure 4.8, corrosion pits gradually nucleate, grow and merge together through the evolution of the damage parameter and consequential removal of elements from the FE model. Fracture is simulated by removing individual elements from the simulation when the elemental strain exceeds the elongation at break of the material (Figure 4.8).

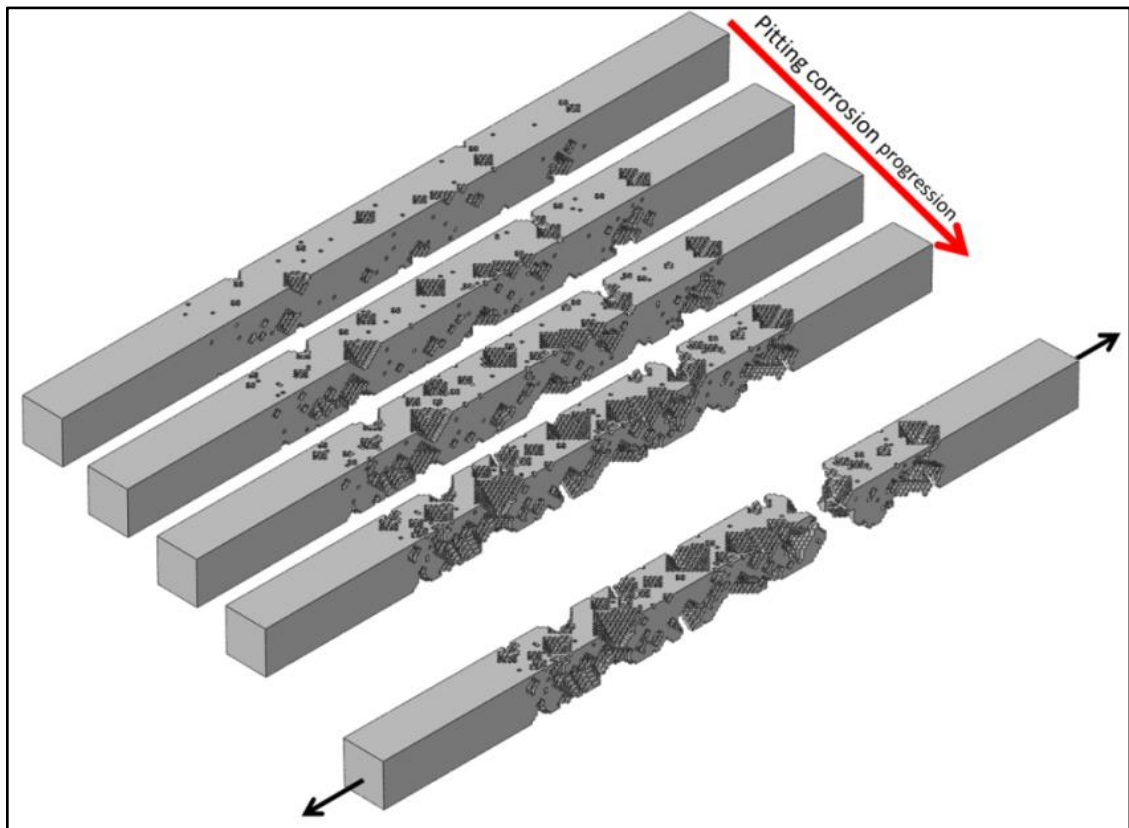


Figure 4.8. Abaqus images of pitting corrosion progression from one of the FE simulations of experiment 2. Mass loss of the corroded region increases through 3.9 %, 10.0 %, 16.4 % and 29.6 % respectively due to the application of the pitting corrosion model. For this particular simulation, after pitting corrosion up to 29.6 %, a simulated tensile test until failure is conducted to find the computed UTS of the corroded Mg WE43 specimen (applied tensile load illustrated by the black arrows).

4.5 Discussion

4.5.1 Mechanical Testing

The experimentally observed tensile strength of the material (295.5 MPa) and elongation (4.5 %) are higher than what is reported in the material technical data sheet (250 MPa and 2 % respectively) available on the website of the metal supplier (Smith Metal Centres, 2018). The tensile strength and elongation of cast Mg WE43 alloy as reported in Liu et al., (2014) are 224 MPa and 10 %. The strength and elongation can be increased up to 282MPa and 37 % respectively through various heat treatments (Liu et al., 2014). The failure of magnesium alloys usually assumes brittle fracture, in which cleavage and quasi cleavage are the most common fracture modes (Lü et al., 2000).

4.5.2 Immersion Testing

The unground EDM magnesium specimens corroded on average 50 times faster than the ground magnesium specimens. The major difference between the samples was the surface preparation after wire EDM and before corrosion testing, with the unground EDM samples tested in the as-received condition while the ground samples were subject to mechanical grinding with emery paper before testing. EDX analysis of the surface of unground EDM specimens before immersion testing revealed the presence of carbon containing damage layer due to the wire EDM process. EDX analysis of the surface of the ground specimens before corrosion demonstrated that mechanical grinding was sufficient to remove this carbon containing damage layer. The resulting difference in the respective corrosion rates indicates that the surface characteristics are the main parameters controlling the rate of corrosion of Mg WE43 alloy. Mechanical grinding of the samples with emery paper also significantly reduced the average surface roughness of the samples from 4.54 μm to 0.20 μm . The SEM images of Figure 4.7a and 4.7b highlight the difference between the surface structure of the Mg WE43 specimens without and with grinding. The presence of carbon containing damage layer significantly increased the corrosion rate of the unground EDM samples. While the damage layer would no doubt be removed for the actual end-user medical device application, it has proven to be useful in this laboratory-based study as it has essentially provided a

mechanism to accelerate the corrosion rate in the in-vitro experiments, and thereby realising substantial corrosion in a reasonable timeframe for the study, without altering the overall mechanical properties or mechanical strength of the material.

Galvin et al., (2017) reported a steady state corrosion rate of $0.021 \text{ mg cm}^{-2} \text{ h}^{-1}$ ($0.504 \text{ g m}^{-2} \text{ d}^{-1}$) for subsize (width=1.85 mm, thickness=0.14 mm) Mg WE43 dogbone specimens and $0.011 \text{ mg cm}^{-2} \text{ h}^{-1}$ ($0.264 \text{ g m}^{-2} \text{ d}^{-1}$) for wire specimens during corrosion in Hank's solution, which is considerably lower than corrosion rate of both ground samples considered here. The surface roughness of these specimens was reported to be in the same range as the ground samples which was achieved using laser-cutting, chemical and plasma etching techniques. However, it is likely that the techniques used by Galvin et al., (2017) would reduce or eliminate micro scratches on the material surface (highlighted in Figure 4.7b) which may explain the differences between the corrosion rates of Galvin et al., (2017) and those reported here.

Figure 4.5a and Figure 4.5b illustrate the experimentally observed gradual reduction in alloy corrosion rate over time. This is most-likely due to the build-up of a layer of corrosion product around the corrosion surface as shown in Figure 4.3c which has also been reported in various other studies (Yang and Zhang, 2009; Zhang et al., 2009).

The significant reduction in failure strength of unground EDM specimens due to corrosion observed in experiment 2, and illustrated in Figure 4.6, is in agreement with the results from tensile testing of corroded Mg AZ31 foils (Grogan et al., 2011), tensile testing of corroded pure magnesium wires (Bowen et al., 2012b), tensile testing of corroded Mg WE43 wire and dogbone specimens (Galvin et al., 2017) and three-point bend testing of corroded Mg-Zn samples (Zhang et al., 2010).

4.5.3 Corrosion Model Calibration

4.5.3.1 Uniform Corrosion

The uniform corrosion model has been successfully calibrated to replicate the experimental observed corrosion rate for both unground EDM and ground Mg WE43 specimens as illustrated in the plots of Figure 4.5a and Figure 4.5b. However, the

uniform corrosion model is incapable of simulating the experimentally observed reduction in specific strength due to corrosion for unground EDM Mg WE43 specimens as illustrated in Figure 4.6. This result was expected as uniform corrosion provides idealistic corrosion mechanics which are dissimilar to the experimentally observed non-uniform localised pitting corrosion behaviour highlighted in Figure 4.3.

4.5.3.2 Pitting Corrosion

Parameters have been successfully computed to calibrate the pitting corrosion model based on the results of experiments 1 and 2 for unground EDM Mg WE43 specimens. The successful calibration of the pitting corrosion model demonstrates the capability of the model to quantitatively capture the material corrosion rate (Figure 4.5a) and the relationship between material (specimen) strength and mass loss due to corrosion for the unground EDM Mg WE43 alloy (Figure 4.6).

As mentioned previously for the pitting corrosion model, γ controls the Weibull distribution-based random pitting parameters which effectively determines the initial locations of the pits on the corrosion surface, while the β parameter controls how these pits progress through the material. The parameters used to calibrate the pitting corrosion model for Mg WE43 material ($\gamma=0.2$, $\beta=0.8$) are the same as the parameters used by Grogan et al., (2011) to calibrate the same pitting corrosion model to experimental testing of Mg AZ31 foils. This is a significant finding; despite differences between the magnesium alloy, the surface characteristics and the geometric scale of the specimens used in the experiments here and by Grogan et al., (2011) the same pitting corrosion parameters are capable of simulating the observed experimental results. This demonstrates that Mg AZ31 and Mg WE43 alloys have similar corrosion characteristics and highlights the robustness of the pitting corrosion model.

Additionally, the geometry of the computational generated corroded specimens, illustrated in Figure 4.8 qualitatively matches the corrosion pattern of the corroded magnesium samples shown in Figure 4.3e.

4.5.4 Limitations

For reasons outlined in Section 4.3.3, experiment 2 was only conducted on unground EDM samples and not on ground specimens. This is a limitation and it is recommended that some long-term corrosion testing of ground Mg WE43 samples is conducted in future work to determine if ground Mg WE43 samples display similar corrosion morphology and corrosion strength characteristics as the unground EDM Mg WE43 samples.

Models were calibrated with *in-vitro* experiments of static immersion tests of approximately 2 mm square magnesium samples. The primary application of these corrosion models is simulating the corrosion of magnesium alloy stents, which have dimensions an order of magnitude smaller than specimens used in this study. The corrosion behaviour and the effects corrosion has on the mechanical integrity of the specimens used may not directly translate to the magnesium stent application due to these geometric differences.

Furthermore, implanted magnesium alloy stents are subject to a range of physical and environmental factors such as pulsatile blood flow, dynamic loading and arterial remodelling etc. which may have effect the material corrosion rate and mechanical integrity of the degrading stent. However, these factors have not been accounted for in the calibration of these models to the Mg WE43 material which is a limitation.

Ultimately it is very challenging to replicate the *in-vivo* environment using *in-vitro* experiments and despite all endeavours there are likely to be significant differences between the results of *in-vitro* experiments and the corrosion behaviour reported for bioresorbable magnesium devices *in-vivo*. This could well be the case for the work reported here and that in Galvin et al., (2017) as the observed *in-vitro* corrosion rate is much faster than the corrosion rate reported for the Biotronik Magmaris device (95 % mass loss in 12 months) (Haude et al., 2016).

The research by Bowen et al., (2013) to correlate the corrosion of pure magnesium wires in the arterial walls of rats with *in-vitro* immersion corrosion experiments of identical specimens is an interesting concept that could be replicated for other magnesium alloys

such as Mg WE43. This could potentially result in the evaluation of a multiplication factor to more accurately relate the *in-vitro* experimental results with the *in-vivo* corrosion behaviour of bioresorbable magnesium alloy devices.

4.6 Conclusions

In this work the previously developed uniform and pitting corrosion models originally calibrated for the Mg AZ31 alloy have been recalibrated for use with Mg WE43 material based on the experimental results of tensile testing, corrosion testing and tensile testing of corroded Mg WE43 specimens.

It is clear from the experimental results that the surface characteristic of the Mg WE43 alloy is the main parameter controlling the rate of corrosion and the presence of carbon containing damage layer significantly increased the corrosion rate of the unground EDM samples. It has been demonstrated that corrosion of the Mg WE43 alloy is highly localised, which severely reduces the mechanical performance of the alloy with a relatively small reduction in mass loss. The corrosion behaviour of Mg WE43 material can be accurately simulated in terms of both the corrosion rate and corrosion induced reduction in specimen strength using the recalibrated pitting corrosion model.

References

- Atrens, A., Song, G.-L., Liu, M., Shi, Z., Cao, F., Dargusch, M.S., 2015. Review of Recent Developments in the Field of Magnesium Corrosion. *Adv. Eng. Mater.* 17, 400–453. <https://doi.org/10.1002/adem.201400434>
- Boland, E.L., Grogan, J.A., McHugh, P.E., 2017. Computational Modeling of the Mechanical Performance of a Magnesium Stent Undergoing Uniform and Pitting Corrosion in a Remodeling Artery. *J. Med. Device.* 11, 021013. <https://doi.org/10.1115/1.4035895>
- Boland, E.L., Shine, R., Kelly, N., Sweeney, C.A., McHugh, P.E., 2016. A Review of Material Degradation Modelling for the Analysis and Design of Bioabsorbable Stents. *Ann. Biomed. Eng.* 44, 341–356. <https://doi.org/10.1007/s10439-015-1413-5>
- Boland, E.L., Shirazi, R.N., Grogan, J.A., McHugh, P.E., 2018. Mechanical and Corrosion Testing of Magnesium WE43 Specimens for Pitting Corrosion Model Calibration. *Adv. Eng. Mater.* 1–11. <https://doi.org/10.1002/adem.201800656>
- Bowen, P.K., Drelich, J., Goldman, J., 2013. A new in vitro-in vivo correlation for bioabsorbable magnesium stents from mechanical behavior. *Mater. Sci. Eng. C* 33, 5064–5070. <https://doi.org/10.1016/j.msec.2013.08.042>
- Bowen, P.K., Drelich, J., Goldman, J., Buxbaum, R.E., Rajachar, R.M., 2012a. New approaches in evaluating metallic candidates for bioabsorbable stents. *Emerg. Mater. Res.* 1, 237–255. <https://doi.org/10.1680/emr.12.00017>
- Bowen, P.K., Gelbaugh, J.A., Mercier, P.J., Goldman, J., Drelich, J., 2012b. Tensile testing as a novel method for quantitatively evaluating bioabsorbable material degradation. *J. Biomed. Mater. Res. - Part B Appl. Biomater.* 100B, 2101–2113. <https://doi.org/10.1002/jbm.b.32775>
- Campos, C.M., Muramatsu, T., Iqbal, J., Zhang, Y.J., Onuma, Y., Garcia-Garcia, H.M., Haude, M., Lemos, P.A., Warnack, B., Serruys, P.W., 2013. Bioresorbable drug-eluting magnesium-alloy scaffold for treatment of coronary artery disease. *Int. J. Mol. Sci.* 14, 24492–24500. <https://doi.org/10.3390/ijms141224492>
- Chen, Y., Xu, Z., Smith, C., Sankar, J., 2014. Recent advances on the development of magnesium alloys for biodegradable implants. *Acta Biomater.* 10, 4561–4573. <https://doi.org/10.1016/j.actbio.2014.07.005>
- Conway, C., Sharif, F., McGarry, J.P., McHugh, P.E., 2012. A Computational Test-Bed to Assess Coronary Stent Implantation Mechanics Using a Population-Specific Approach. *Cardiovasc. Eng. Technol.* 3, 374–387. <https://doi.org/10.1007/s13239-012-0104-8>
- Galvin, E., Jaiswal, S., Lally, C., MacDonald, B., Duffy, B., 2017. In Vitro Corrosion and Biological Assessment of Bioabsorbable WE43 Mg Alloy Specimens. *J.*

Manuf. Mater. Process. 1, 8. <https://doi.org/10.3390/jmmp1010008>

- Grogan, J.A., Leen, S.B., McHugh, P.E., 2012. Comparing coronary stent material performance on a common geometric platform through simulated bench testing. *J. Mech. Behav. Biomed. Mater.* 12, 129–138. <https://doi.org/10.1016/j.jmbbm.2012.02.013>
- Grogan, J.A., O'Brien, B.J., Leen, S.B., McHugh, P.E., 2011. A corrosion model for bioabsorbable metallic stents. *Acta Biomater.* 7, 3523–3533. <https://doi.org/10.1016/j.actbio.2011.05.032>
- Gu, X., Zheng, Y., Cheng, Y., Zhong, S., Xi, T., 2009. In vitro corrosion and biocompatibility of binary magnesium alloys. *Biomaterials* 30, 484–498. <https://doi.org/10.1016/j.biomaterials.2008.10.021>
- Haude, M., Ince, H., Abizaid, A., Toelg, R., Lemos, P.A., Von Birgelen, C., Christiansen, E.H., Wijns, W., Neumann, F.J., Kaiser, C., Eeckhout, E., Lim, S.T., Escaned, J., Garcia-Garcia, H.M., Waksman, R., 2016. Safety and performance of the second-generation drug-eluting absorbable metal scaffold in patients with de-novo coronary artery lesions (BIOSOLVE-II): 6 month results of a prospective, multicentre, non-randomised, first-in-man trial. *Lancet* 387, 31–39. [https://doi.org/10.1016/S0140-6736\(15\)00447-X](https://doi.org/10.1016/S0140-6736(15)00447-X)
- Karanasiou, G.S., Papafaklis, M.I., Conway, C., Michalis, L.K., Tzafriri, R., Edelman, E.R., Fotiadis, D.I., 2017. Stents: Biomechanics, Biomaterials, and Insights from Computational Modeling. *Ann. Biomed. Eng.* 45, 853–872. <https://doi.org/10.1007/s10439-017-1806-8>
- Kirkland, N.T., 2012. Magnesium biomaterials: past, present and future. *Corros. Eng. Sci. Technol.* 47, 322–328. <https://doi.org/10.1179/1743278212Y.00000000034>
- Kutniy, K. V., Papirov, I.I., Tikhonovsky, M.A., Pikalov, A.I., Sivtsov, S. V., Pirozhenko, L.A., Shokurov, V.S., Shkuropatenko, V.A., 2009. Influence of grain size on mechanical and corrosion properties of magnesium alloy for medical implants. *Materwiss. Werksttech.* 40, 242–246. <https://doi.org/10.1002/mawe.200900434>
- Liu, D., Ding, Y., Guo, T., Qin, X., Guo, C., Yu, S., Lin, S., 2014. Influence of fine-grain and solid-solution strengthening on mechanical properties and in vitro degradation of WE43 alloy. *Biomed Mater* 9, 15014. <https://doi.org/10.1088/1748-6041/9/1/015014>
- Lü, Y., Wang, Q., Ding, W., Zeng, X., Zhu, Y., 2000. Fracture behavior of AZ91 magnesium alloy. *Mater. Lett.* 44, 265–268. [https://doi.org/10.1016/S0167-577X\(00\)00041-0](https://doi.org/10.1016/S0167-577X(00)00041-0)
- McGrath, D.J., O'Brien, B., Bruzzi, M., Kelly, N., Clauser, J., Steinseifer, U., McHugh, P.E., 2016. Evaluation of cover effects on bare stent mechanical response. *J. Mech. Behav. Biomed. Mater.* 61, 567–580. <https://doi.org/10.1016/j.jmbbm.2016.04.023>

- Rapetto, C., Leoncini, M., 2017. Magmaris: A new generation metallic sirolimus-eluting fully bioresorbable scaffold: Present status and future perspectives. *J. Thorac. Dis.* 9, S903–S913. <https://doi.org/10.21037/jtd.2017.06.34>
- Shine, R., Neghabat Shirazi, R., Ronan, W., Sweeney, C.A., Kelly, N., Rochev, Y.A., McHugh, P.E., 2017. Modeling of Biodegradable Polyesters With Applications to Coronary Stents. *J. Med. Device.* 11, 021007. <https://doi.org/10.1115/1.4035723>
- Smith Metal Centres, 2018. Technical Datasheet WE43 [WWW Document]. URL <https://www.smithmetal.com/pdf/magnesium/we43.pdf> (accessed 5.1.18).
- Song, G., 2007. Control of biodegradation of biocompatible magnesium alloys. *Corros. Sci.* 49, 1696–1701. <https://doi.org/10.1016/j.corsci.2007.01.001>
- Song, G., Atrens, A., 2003. Understanding Magnesium Corrosion—A Framework for Improved Alloy Performance. *Adv. Eng. Mater.* 5, 837–858. <https://doi.org/10.1002/adem.200310405>
- Song, G., Song, S., 2007. A possible biodegradable magnesium implant material. *Adv. Eng. Mater.* 9, 298–302. <https://doi.org/10.1002/adem.200600252>
- Song, G.L., Atrens, A., 1999. Corrosion mechanisms of magnesium alloys. *Adv. Eng. Mater.* 1, 11–33. [https://doi.org/10.1002/\(SICI\)1527-2648\(199909\)1:1<11::AID-ADEM11>3.0.CO;2-N](https://doi.org/10.1002/(SICI)1527-2648(199909)1:1<11::AID-ADEM11>3.0.CO;2-N)
- Sotomi, Y., Onuma, Y., Ormiston, J., Serruys, P.W., 2017. Bioresorbable Scaffold Technologies. *Circ. J.* 509–520. <https://doi.org/10.1253/circj.CJ-10-1135>
- Staiger, M.P., Pietak, A.M., Huadmai, J., Dias, G., 2006. Magnesium and its alloys as orthopedic biomaterials: A review. *Biomaterials* 27, 1728–1734. <https://doi.org/10.1016/j.biomaterials.2005.10.003>
- Sweeney, C.A., O'Brien, B., McHugh, P.E., Leen, S.B., 2014. Experimental characterisation for micromechanical modelling of CoCr stent fatigue. *Biomaterials* 35, 36–48. <https://doi.org/10.1016/j.biomaterials.2013.09.087>
- Waksman, R., Erbel, R., Di Mario, C., Bartunek, J., de Bruyne, B., Eberli, F.R., Erne, P., Haude, M., Horrigan, M., Ilesley, C., Bose, D., Bonnier, H., Koolen, J., Luscher, T.F., Weissman, N.J., 2009. Early- and Long-Term Intravascular Ultrasound and Angiographic Findings After Bioabsorbable Magnesium Stent Implantation in Human Coronary Arteries. *JACC Cardiovasc. Interv.* 2, 312–320. <https://doi.org/10.1016/j.jcin.2008.09.015>
- Waksman, R., Pakala, R., Kuchulakanti, P.K., Baffour, R., Hellings, D., Seabron, R., Tio, F.O., Wittchow, E., Hartwig, S., Harder, C., Rohde, R., Heublein, B., Andreae, A., Waldmann, K.H., Haverich, A., 2006. Safety and efficacy of bioabsorbable magnesium alloy stents in porcine coronary arteries. *Catheter. Cardiovasc. Interv.* 68, 607–617. <https://doi.org/10.1002/ccd.20727>
- Walker, J., Shadanbaz, S., Woodfield, T.B.F., Staiger, M.P., Dias, G.J., 2014.

- Magnesium biomaterials for orthopedic application: A review from a biological perspective. *J. Biomed. Mater. Res. - Part B Appl. Biomater.* 102, 1316–1331. <https://doi.org/10.1002/jbm.b.33113>
- Winzer, N., Atrens, A., Song, G., Ghali, E., Dietzel, W., Kainer, K.U., Hort, N., Blawert, C., 2005. A critical review of the Stress Corrosion Cracking (SCC) of magnesium alloys. *Adv. Eng. Mater.* 7, 659–693. <https://doi.org/10.1002/adem.200500071>
- Yang, L., Zhang, E., 2009. Biocorrosion behavior of magnesium alloy in different simulated fluids for biomedical application. *Mater. Sci. Eng. C* 29, 1691–1696. <https://doi.org/10.1016/j.msec.2009.01.014>
- Zhang, S., Li, J., Song, Y., Zhao, C., Zhang, X., Xie, C., Zhang, Y., Tao, H., He, Y., Jiang, Y., Bian, Y., 2009. In vitro degradation, hemolysis and MC3T3-E1 cell adhesion of biodegradable Mg-Zn alloy. *Mater. Sci. Eng. C* 29, 1907–1912. <https://doi.org/10.1016/j.msec.2009.03.001>
- Zhang, S., Zhang, X., Zhao, C., Li, J., Song, Y., Xie, C., Tao, H., Zhang, Y., He, Y., Jiang, Y., Bian, Y., 2010. Research on an Mg-Zn alloy as a degradable biomaterial. *Acta Biomater.* 6, 626–640. <https://doi.org/10.1016/j.actbio.2009.06.028>

5 Computational Modelling of Magnesium Stent Mechanical Performance in a Remodelling Artery: Effects of Multiple Remodelling Stimuli

5.1 Chapter Overview

In this chapter a computational modelling framework is developed, that accounts for two major physiological stimuli responsible for neointimal remodelling and combined with a magnesium corrosion model that is capable of simulating localised pitting (realistic) stent corrosion. The framework is used to simulate different neointimal growth patterns and to explore the effects the neointimal remodelling has on the mechanical performance (scaffolding support) of the bioabsorbable magnesium stent.

A journal paper based on the content of this chapter is currently in submission.

5.2 Introduction

Significant research has been conducted in the area of coronary stents/scaffolds made from resorbable metallic and polymeric biomaterials, resulting in a number of these devices achieving approval for use in the European market (Sotomi et al., 2017). These next generation bioabsorbable stents have the potential to completely revolutionise the treatment of coronary artery disease.

As discussed in previous chapters, the primary advantage of resorbable devices over permanent stents is their temporary presence which, from a theoretical point of view, means only a healed coronary artery will be left behind following degradation of the stent. Therefore, long term clinical problems associated with permanent stents such as in-stent restenosis (Mitra and Agrawal, 2006), late stent thrombosis (Ong et al., 2005) and the need for prolonged treatment with dual antiplatelet therapy (Garg and Serruys, 2010; Gomez-Lara et al., 2011) could be eliminated, while simultaneously restoring vasomotion of the artery. Furthermore, bioabsorbable stents permit the use of repeat treatments to the same site (Ormiston and Serruys, 2009) and have potential for use in

areas of complex anatomy, where a conventional stent would permanently obstruct side branches (Ormiston and Serruys, 2009), or for paediatric patients (Zartner et al., 2005) where a conventional stent may become mechanically unstable in growing vessels.

As mentioned in Chapter 1, neointimal healing following coronary stent/scaffold implantation is crucial for the long term safety of these devices (Karjalainen et al., 2017). Compared to bare-metal stents, DES have proven to be successful in reducing rates of in-stent restenosis and the need for target lesion revascularisation at mid and long term follow up (Garg and Serruys, 2010). However inadequate neointimal remodelling resulting in higher incidence of uncovered stent struts has been observed with DES use (Guagliumi et al., 2010). Lack of tissue coverage and uncovered stent struts has been shown to be an important risk factor associated with late stent thrombosis (Finn et al., 2007; Joner et al., 2006), which demonstrates the importance of neointimal remodelling around these devices.

Computational modelling can be used to evaluate the performance of complex stent devices *in-silico* (Karanasiou et al., 2017; McHugh et al., 2016) and assist in the design and development and understanding of the next generation resorbable stents.

As stated previously in Chapter 3, what is lacking in computational modelling literature is the representation of the active response of the arterial tissue in the weeks and months following stent implantation, i.e., neointimal remodelling, in particular for the case of biodegradable stents.

The phenomenon of neointimal remodelling is particularly interesting and significant in the case of biodegradable stents, when both stent degradation and neointimal remodelling can occur simultaneously (Hermawan et al., 2010) presenting the possibility of a mechanical interaction and transfer of load between the degrading stent and the remodelling artery.

As mentioned previously in Chapter 1, neointimal formation is modulated by several local factors, including the vessel wall trauma caused during stent deployment, the plaque burden, and the composition of the underlying plaque, as well as local endothelial shear stress (ESS) patterns (Bourantas et al., 2014).

In relation to the simulation of tissue remodelling, mechanobiological models for predicting the response of multicellular biological systems, for in-stent restenosis and neointimal development applications, have been reported. They can be grouped into two categories: (i) discrete cell based models (Boyle et al., 2011, 2010; Caiazzo et al., 2011; Nolan and Lally, 2018; Tahir et al., 2013; Zahedmanesh and Lally, 2012), such as cellular automata (CA) or agent-based models (ABM) and (ii) continuum models, (Boland et al., 2016, 2017; Lally and Prendergast, 2006) which usually can be formulated in terms of partial differential equations in space and time (Hwang et al., 2009).

Discrete models such as CA or ABM use a bottom up approach where each individual cell is modelled explicitly. The behaviour of individual cells at a local level is governed by a set of rules, and the global behaviour of the system emerges through the local interaction of cells.

Finite element models used to quantify mechanical stresses in the artery after stenting have been coupled with discrete models to predict the collective response of the cells in the artery wall due to tissue damage and the resulting in-stent restenosis or neointimal development. These have been initially developed in 2D (Boyle et al., 2011; Nolan and Lally, 2017; Zahedmanesh and Lally, 2012) but have been expanded for use on 3D geometries (Boyle et al., 2013).

Hoekstra and co-workers have also developed a multiscale model of in-stent restenosis. Here an ABM to predict smooth muscle cell proliferation and re-endothelisation is fully coupled with computational fluid dynamics (CFD) blood flow simulations. This multiscale model was initially developed for 2D (Caiazzo et al., 2011; Tahir et al., 2013) and has also recently been expanded to the predict neointimal development on 3D stent geometry (Zun et al., 2017). An advantage of using agent-based or CA approaches to model cell populations is their ability to better capture the discrete nature of events occurring at the cellular level (Nolan and Lally, 2017).

However as outlined in Chapter 2, continuum approaches, using partial differential equations, are more suited to modelling of the bulk material behaviour (Nolan and Lally,

2017), and they have the advantage of ease of implementation in the finite-element context for practical stent performance simulations when compared to discrete models.

Continuum models have been utilised extensively in orthopaedic applications to model cell differentiation and predict tissue regeneration and bone remodelling (Burke and Kelly, 2012; Gómez-Benito et al., 2005; Lacroix et al., 2002; Scannell and Prendergast, 2009). Literature is much more limited on the use of continuum models to simulate the response of the artery to stenting when compared with cell-based models. However, Lally and Prendergast, (2006) successfully used a continuum damage model to simulate in-stent restenosis of the coronary arteries after stent deployment. The Lally and Prendergast, (2006) continuum damage model is initiated by elevated stresses in the coronary artery after stent implantation.

The author has previously (as documented in Chapter 3 of this thesis) adapted the continuum model proposed by Lally and Prendergast, (2006) to predict neointimal remodelling of the coronary artery following magnesium stent implantation and also coupled this with a magnesium stent corrosion model.

For the model document in Chapter 3, the damage to the artery due to stent deployment is the only neointimal remodelling stimulus investigated. Neglecting other factors known to influence neointimal remodelling such as the plaque burden, and the composition of the underlying plaque, as well as local endothelial shear stress (ESS) patterns (Bourantas et al., 2014) is a limitation of the model. Of these remodelling stimuli the ESS is considered the most important, as there are numerous studies in the literature that have linked ESS and neointimal remodelling. According to Malek, (1999), ESS has been shown to be implicated in vascular remodelling, while Wentzel et al., (2001), has observed an inverse relationship between neointimal thickness and shear stress following stent implantation, where the intimal thickness at low shear stress locations was higher than the intimal thickness at high shear stress regions.

The inclusion of more than one neointimal remodelling stimuli, vessel wall trauma caused during stent deployment and local ESS due to the stent disturbing physiological

blood flow patterns, would be a significant advancement on the neointimal remodelling formulation documented in Chapter 3.

Thus, the objective of this chapter is to build on the previous investigations reported in Chapter 3 to develop a computational modelling framework using the continuum approach, that accounts for two major physiological stimuli responsible for neointimal remodelling (vessel wall trauma caused during stent deployment and local ESS due to the stent disturbing physiological blood flow patterns) and combine this with a magnesium corrosion model that is capable of simulating localised pitting (realistic) stent corrosion. Using the modelling framework, the second objective is to simulate different neointimal growth patterns and to explore the effects the neointimal remodelling has on the mechanical performance (scaffolding support) of the bioabsorbable magnesium stent.

5.3 Methods

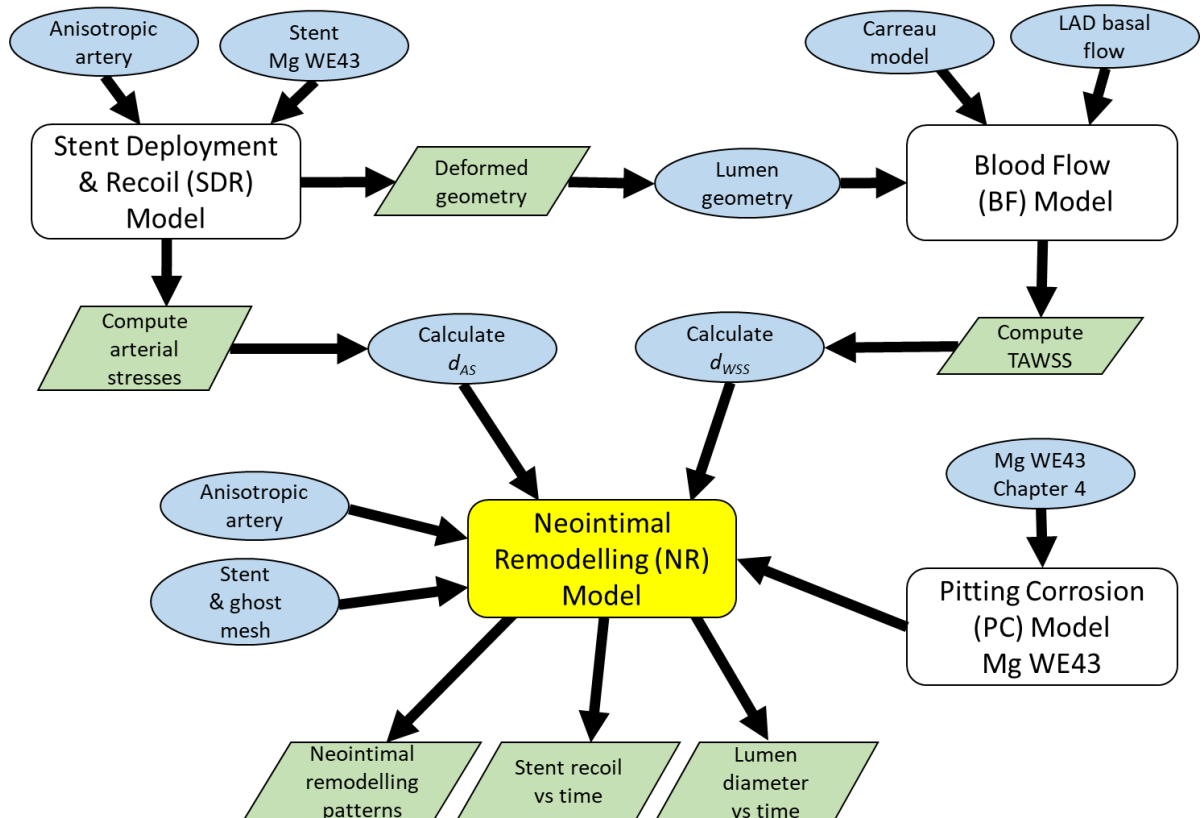


Figure 5.1. Flow chart outlining the overall neointimal remodelling framework.

The overall neointimal remodelling framework is outlined by the flowchart shown in Figure 5.1. The overall neointimal remodelling framework consists of four separate models, the Stent Deployment and Recoil Model (SDR), the Blood Flow (BF) model, the Pitting Corrosion (PC) model and the Neointimal Remodelling (NR) model. In Figure 5.1 model inputs are illustrated by the blue ovals, while model outputs are illustrated by green parallelograms.

A model of magnesium stent deployment and recoil in a coronary artery is used to compute the arterial stress (AS) distribution in the coronary artery, which is subsequently used to determine a damage variable, d_{AS} . This is the Stent Deployment and Recoil (SDR) model. The SDR model and the calculation of the SDR damage variable (d_{AS}) are described in detail in Section 5.3.1.

Following the completion of the SDR model simulations, the finite element meshes of the deformed stent and artery are used to approximate the internal lumen of the coronary artery where blood can flow. A CFD blood flow model is then generated and used to compute flow hemodynamics along the internal lumen of the coronary artery and implanted magnesium stent. This is the Blood Flow (BF) model. The damage variable due to these wall shear stresses, d_{WSS} , is calculated based on the time-averaged wall shear stresses (TAWSS) during a cardiac cycle computed by the BF model. The BF model and the calculation of its damage variable (d_{WSS}) are described in detail in Section 5.3.2.

A final neointimal remodelling (NR) model is built based on the approach initially proposed by Lally and Prendergast, (2006) and developed in Chapter 3, utilising continuum damage mechanics (CDM) and a thermal analogy to simulate neointimal development. A three-layer anisotropic artery is supported by a magnesium stent in an expanded configuration. A “ghost mesh” is located around the stent struts, within the artery lumen, where the neointimal remodelling will occur. The previously calculated damage variables (d_{AS} and d_{WSS}) are inputted as remodelling stimuli into the NR model as cellular loads, which results in the recruitment of cells into the artery. The diffusion of these cells from the artery into the ghost mesh results in the activation of elements in the ghost mesh. The activation of elements in the ghost mesh is representative of the

remodelling of the artery through the growth of new neointimal tissue. The NR model is explained in detail in Section 5.3.3.

The pitting corrosion to describe degradation of the magnesium stent (Section 5.3.3.1), also referred to here as the PC model, is combined with the NR model to investigate the effects of having neointimal remodelling and pitting corrosion occurring at the same time.

5.3.1 Stent Deployment and Recoil (SDR) Model

5.3.1.1 SDR Model Description

A three-layer cylindrical artery of inner diameter of 3.2 mm, 28.5 mm long and with artery layer thickness taken from the work of Holzapfel et al., (2005) is modelled using an anisotropic Holzapfel–Gasser–Ogden (HGO) formulation. The HGO materials model parameters for the adventitia, media and intima are taken from Mortier et al., (2010) who calibrated them using the stress-strain response from experimental tissue testing of coronary arteries (Specimen I) documented in Holzapfel et al., (2005).

The artery geometry is meshed with 170,000 eight-node linear reduced integration brick elements with the mesh density tailored towards the centre region of the artery into which the stent is deployed.

The stent is modelled using the mechanical properties of magnesium WE43 alloy taken from Chapter 4 where elasticity is considered linear and isotropic and described through Young’s modulus and Poisson’s ratio, and plasticity is described using J_2 flow theory and isotropic hardening.

The initial stent geometry is a representation of the Biotronik Magmaris stent in the crimped configuration shown in Figure 5.2a, with a thickness of 150 μm . A five-ring section of the Magmaris stent is modelled with an external crimped diameter of 1.6 mm and an initial length of 7.88 mm. The stent geometry is meshed with 378,000 eight-node linear reduced integration brick elements.

The model is implemented in Abaqus/Explicit software (DS-SIMULIA, RI, USA) by exploiting the nonlinear geometry (NLGEOM) feature throughout all the steps in the simulation.

Abaqus/Explicit software (DS-SIMULIA, RI, USA) utilising the nonlinear geometry (NLGEOM) feature throughout all the steps in the simulation is chosen for this work due to its superior contact enforcement capabilities with the condition that the kinetic energy of the simulation remains below 5 % of the total internal energy to ensure a quasi-static analysis. Contact between all parts of the model is defined according the general contact algorithm available in Abaqus/Explicit.

Stent deployment is simulated using contact with a radially expanding rigid tube into the artery followed by radial contraction to allow for stent recoil, illustrated in Figure 5.2. The use of an expanding rigid tube instead of balloon catheter to simplify stent angioplasty simulations has been implemented in numerous previous studies, including Conway et al., (2017), De Beule et al., (2008), Wu et al., (2011), and verified by Grogan et al., (2012).

Boundary conditions are assigned to the stent and the artery to simulate a realistic stent deployment and recoil. The ends of the artery are held in the axial direction to prevent translation of the model. However, the artery is made sufficiently long so that constraining the ends would not artificially stiffen the centre of the artery where the stent is deployed. Three nodes along the centre of the stent are constrained to prevent artificial translation or rotation of the stent geometry.

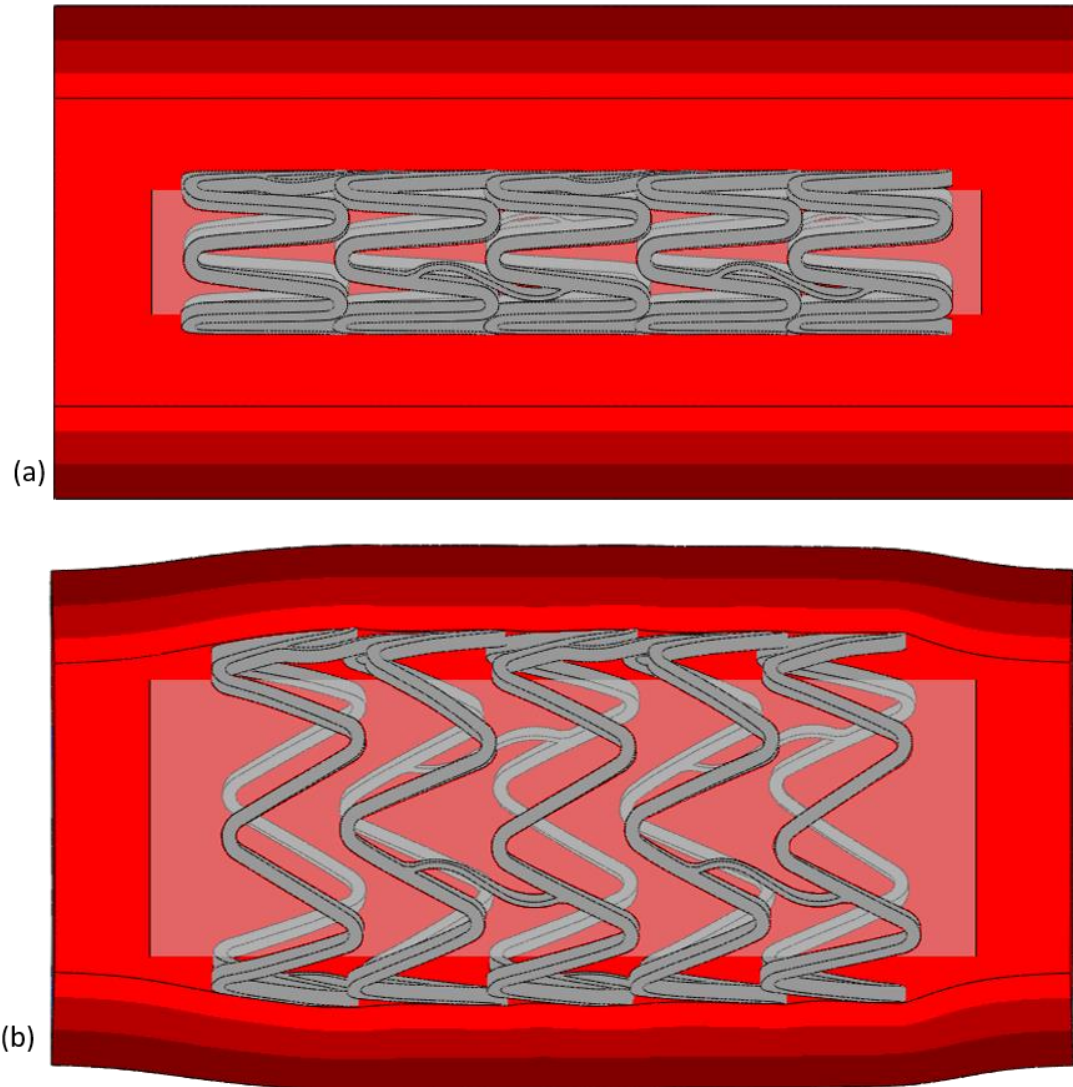


Figure 5.2. (a) Model set up for SDR model showing half of the three-layer artery (red), crimped magnesium stent (grey) and rigid cylinder (white/transparent). (b) shows the deformed geometry of the stent, artery and rigid cylinder after stent deployment and recoil.

5.3.1.2 Calculation of SDR Model Damage Variable (d_{AS})

Literature has shown that neointimal remodelling is influenced by vessel wall trauma caused during stent implantation (Bourantas et al., 2014).

Therefore, using the continuum approach, regions of high stress in the artery, computed by the SDR model, are related to a neointimal remodelling stimulus in the NR model by the arterial stress (AS) damage variable (d_{AS}). The d_{AS} parameter has a minimum value

of zero where arterial stresses are considered low, a maximum value of 1.0 where arterial stresses are considered high, and a linear interpolation is used when levels fall in between the threshold values.

The minimum and maximum principal stresses are often used to examine the stress state of biological hyperelastic materials such as the coronary arteries (Conway et al., 2017) or the bronchi of the lung (McGrath et al., 2017b, 2017a) as they capture whether the material is subject to tensile or compressive loads. However, the Von Mises (VM) stress is deemed more useful in this study as it is a positive scalar quantity that accounts for the overall multi-axial stress state of the material.

A comprehensive search of the literature to determine at what stress level a coronary artery is considered damaged by a deployed stent, proved inconclusive. This may be due to the complex nature of a stented coronary artery system and the numerous factors which may affect the stresses in the coronary arteries after stent implantation including, the variation in material properties of the coronary artery, the variation in the atherosclerotic plaque causing the occlusion, the numerous commercial stents available for implantation and the balloon catheter stent delivery system.

To overcome this issue, it is assumed here that the VM stress in the intima material of the three-layer artery calculated by the SDR model has a normal distribution. Thus, lower and upper threshold limits of VM stress are selected based on the average VM stress in the intima material (0.46 MPa) and the average plus three times the standard deviation of VM stress in the intima material (1.34 MPa) respectively. If the VM stress in an element is below the average stress, the element is considered undamaged, and a value of zero is applied to d_{AS} for that element. Similarly, if the VM stress in an element is above the upper threshold limit, a value of 1.0 is applied to d_{AS} for that element. A linear interpolation is used to apply d_{AS} values to elements with VM values between the threshold limits.

5.3.2 Blood Flow (BF) Model

5.3.2.1 BF Model Description

The geometry for the BF model is approximated from the deformed finite element meshes of the SDR simulation. 3-Matic software (Materialise, Belgium) is used to create a surface mesh of the internal lumen around the artery and stent, where blood flow would occur. This surface mesh is extruded on both ends by 35 mm to negate entrance and exit flow effects (Martin et al., 2014) and subsequently is transformed into a volume mesh. This volume mesh is imported into Abaqus and forms the final geometry for the BF analysis. The volume mesh contains 1,270,000 4-node tetrahedron elements. The mid-section of the mesh is illustrated in Figure 5.3, where the cut-out of the deployed stent geometry can be clearly seen.

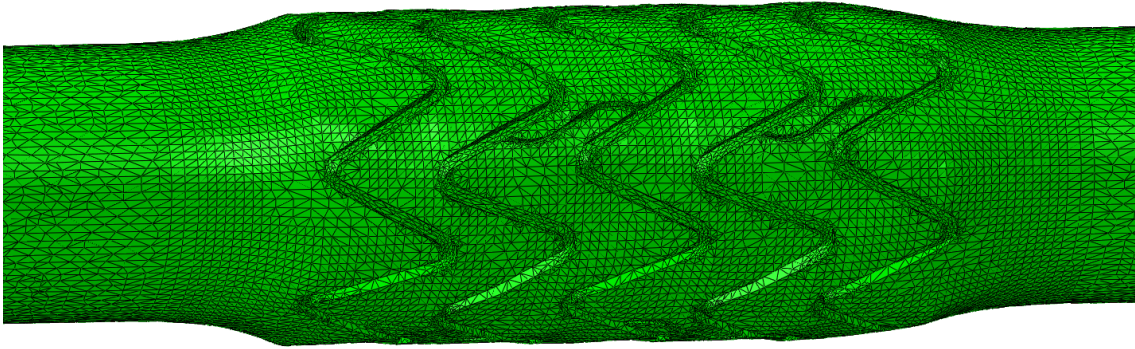


Figure 5.3. Section of volume mesh used in the CFD model of blood fluid flow around the deployed stent in an artery.

Abaqus/CFD (DS-SIMULIA, RI, USA) is used for the analysis under the assumptions that blood flow through the stented artery is time dependent, laminar and incompressible (Murphy and Boyle, 2010a). The blood density is assumed constant with a value of 1050 kg/m³. To account for the non-Newtonian, shear thinning nature of blood, the Carreau model is used to describe the dynamic viscosity (μ) of the fluid using the following equation:

$$\mu = \mu_{\infty} + (\mu_0 - \mu_{\infty})[1 + (\dot{\gamma}\lambda_t)^2]^{\left(\frac{q-1}{2}\right)} \quad (5.1)$$

where μ_0 denotes the low shear viscosity, μ_∞ denotes the high shear viscosity, $\dot{\gamma}$ denotes the scalar shear strain rate, λ_t denotes the time constant and q denotes the power law index. The low and high shear viscosities are assigned values of 0.056 and 0.00345 Pa s, while the time constant and the power law index are assigned values of 3.31 s and 0.375, respectively (Martin et al., 2014; Murphy and Boyle, 2010a).

A transient fully developed Hagen-Poiseuille parabolic velocity profile is applied at the inlet surface. The magnitude of this Hagen-Poiseuille velocity profile is taken from Murphy and Boyle, (2010a) to replicate basal flow in the left anterior descending coronary artery during the cardiac cycle. A zero relative pressure is applied at the outlet surface (Martin et al., 2014). No slip boundary conditions are applied to the entire external surface of the fluid geometry.

5.3.2.2 Calculation of WSS Damage Variable (d_{WSS})

Wall shear stresses (WSS) are outputted for the surfaces of interest, specifically in the centre region of the geometry around to stent struts. The time-averaged wall shear stress (TAWSS) during the cardia cycle is then calculated for each surface face using the following equation:

$$TAWSS = \frac{1}{T} \int_0^T |wss| dt \quad (5.2)$$

The TAWSS values of each surface face are subsequently used to calculate values for the damage variable, d_{WSS} . Numerous clinical studies have provided evidence that low endothelial shear stress promotes neointimal formation (Bourantas et al., 2014; Wentzel et al., 2001). According to Murphy and Boyle, (2010b) WSS lower than 0.5 Pa is considered low, so based on this 0.5 Pa is selected as the upper threshold limit and element surface faces with TAWSS values greater than or equal to 0.5 Pa are assigned a d_{WSS} of zero. Surface faces with a TAWSS approximately equal to 0 Pa are assigned maximum d_{WSS} values of 1.0. A linear interpolation is used to apply d_{WSS} values to elements with TAWSS values between the threshold limits (0 Pa and 0.5 Pa).

5.3.3 Neointimal Remodelling (NR) Model

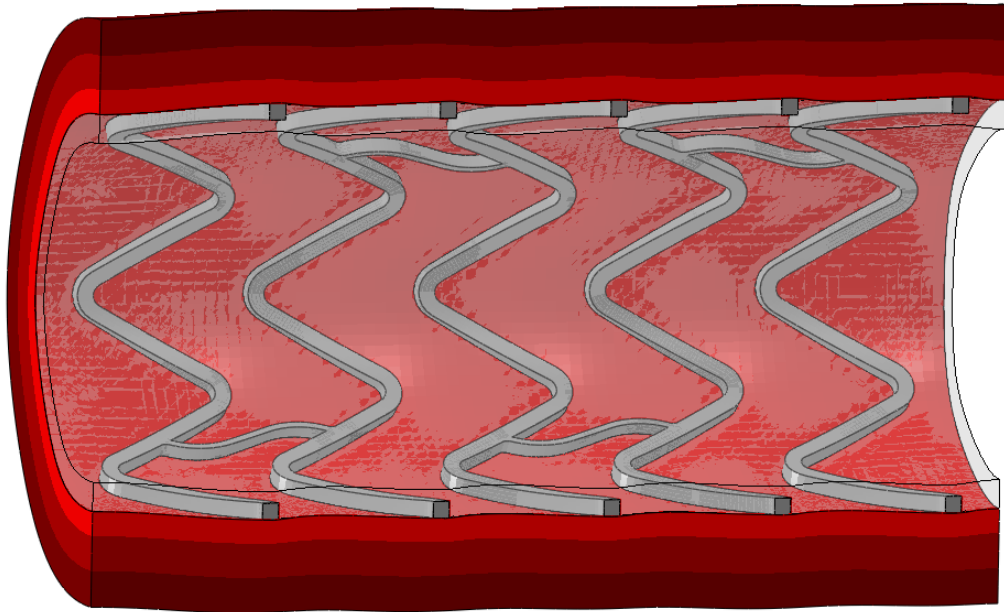


Figure 5.4. Model set up for NR model showing half of the three-layer artery (red), expanded magnesium stent (grey) and ghost mesh/neointima (white/transparent).

The geometry for the neointimal remodelling simulation is illustrated in Figure 5.4. A three-layer artery is supported by an expanded magnesium stent as shown. The arterial lumen is filled with mesh of deactivated finite elements, namely, the “ghost mesh”.

5.3.3.1 Stent and Stent Corrosion

In the NR model the deployment of the Biotronik Magmaris stent is not simulated due to difficulties in creating the ghost mesh surrounding the stent. Instead the geometry of the Biotronik Magmaris stent is created in an expanded state to correspond with the final deformed configuration computed by the SDR model.

The stent is modelled using the properties of Mg WE43 alloy as outlined in Section 5.3.1.1. A pitting corrosion (PC) model of magnesium degradation is used in this study (Grogan et al., 2011). Grogan and co-workers originally developed phenomenological uniform and pitting corrosion models and calibrated them based on experimental mechanical and corrosion testing of Mg AZ31 films. The corrosion parameters have

been recalibrated, as described in Chapter 4, for Mg WE43 alloy and these are the corrosion parameters used in the present study.

The PC model has been comprehensively explained in previous chapters, so a summary is not provided here. However, it is important to note that in this chapter, because the application of the model is a corroding stent in an artery undergoing neointimal remodelling, the corrosion product is retained, as per Chapter 3, and not deleted, as per Chapter 4.

For the PC model, three parameters (material corrosion rate, k_U , Weibull function parameter, γ , and growth rate parameter, β) must be determined. As described in Chapter 4, these parameters are calibrated, and model performance validated against data generated in independent corrosion and corrosion followed by tensile loading experiments performed on unground EDM Mg WE43 samples. For all pitting corrosion simulations, the calibrated corrosion parameters ($\beta = 0.8$, $\gamma = 0.2$) are used (See Equation 3.1 and Equation 3.2 in Chapter 3).

5.3.3.2 Artery and Neointima

The three-layer artery is modelled using the anisotropic HGO model as outlined in Section 5.3.1.1. To represent the growth of neointima, given its practical implementation advantages in finite-element software, the continuum approach is used, based on the work of Lally and Prendergast, (2006) which has also been previously implemented by the author as described in Chapter 3.

The arterial lumen is filled with mesh of deactivated finite elements, namely the “ghost mesh” (see Figure 5.4), with negligible initial mechanical properties.

The NR model controls the activation of elements in the ghost mesh as described in detail in Section 5.3.3.4. The activation of elements in the ghost mesh is representative of the remodelling of the artery through the growth of new neointimal tissue and entails a change in the material properties assigned to those elements. The newly activated elements change from a very soft material to a stiffer material.

A detailed search of the literature to determine appropriate mechanical properties to assign to the neointima (activated ghost mesh) proved inconclusive, possibly due to the difficulties in obtaining this material for testing.

It is assumed here that the neointima is an incompressible ($\nu = 0.49$) elastic material with similar properties to the intima. Experimental testing of the intima of coronary arteries has shown it to be a non-linear anisotropic material (Holzapfel et al., 2005) often with a large variation between individual specimens. However, the use of linear elastic properties for the neointima is motivated by their use previously in a similar application (Lally and Prendergast, 2006), and also it is practically convenient to change the Young's modulus of a material in Abaqus software via field variables and user subroutine.

As documented in Chapter 3, previous work by the author has shown that the Young's modulus assigned to the activated neointima is a crucial parameter in controlling the overall collapse or recoil of the corroding stent and coronary artery it is supporting. Significant consideration is given to the choice of elastic properties assigned to the activated neointima in the NR model, due to the of lack of experimental testing of the neointimal material in the literature and the knowledge of the importance of this model parameter from Chapter 3.

The results of experimental testing of the intima material coronary arteries in the circumferential direction (Holzapfel et al., 2005) are used to deduce the appropriate value of the Young's modulus to be assigned to the activated neointima. As the intima material is a hyperelastic material the assumption of linear elasticity only holds true for a certain strain value for each individual specimen. Table 5.1 outlines the approximation of Young's modulus of the intima material coronary arteries in the circumferential from a number of specimens tested by Holzapfel et al., (2005) and the strain range the assumption of linear elasticity holds true for.

Table 5.1 Approximation of elastic properties of the intima of coronary arteries in the circumferential direction from results of Holzapfel et al., (2005).

Holzapfel intima properties circumferential direction	Young's modulus (MPa)	Valid up to max strain (%)
Specimen I	0.225	10 %
Specimen II	0.26	10 %
Specimen III	0.25	14 %
Specimen IV	0.5	3 %
Specimen V	0.25	5 %
Specimen VI (least stiff)	0.068	20 %
Specimen VII	0.19	14 %
Specimen VIII	0.19	16 %
Specimen IX (stiffest)	0.5	2 %
Specimen X	0.11	17 %
Specimen XI	0.18	11 %
Specimen XII	0.14	12 %
Specimen XIII	0.18	13 %

As shown in Table 5.1, a large range of Young's modulus values (0.068 MPa to 0.5 MPa) could be potentially be used as the material properties of activated neointima.

As mentioned previously in Section 5.3.1.1, the anisotropic HGO material model parameters for the adventitia, media and intima are taken from Mortier et al., (2010), who calibrated them using the stress-strain response from experimental tissue testing of a coronary artery, labelled Specimen I, documented in Holzapfel et al., (2005). Therefore, to have consistent material properties throughout the NR model, a value of $E = 0.225$ MPa is assigned as the stiffness of the activated neointima based on the approximation of Young's modulus from Specimen I as outlined in Table 5.1. Furthermore, preliminary simulations indicate that strains in the activated neointima will not exceed 10 % so it is considered reasonable to use this value as the stiffness of the activated neointima.

The deactivated ghost mesh is also assigned incompressible ($\nu = 0.49$) linear elastic material properties. Minimising the stiffness of the deactivated ghost mesh is essential to ensure that the deactivated elements have insignificant effect on the simulation results however, too low a value can cause numerical issues, such as mesh distortion and simulation failure. It is found that a Young's modulus value of 0.01 MPa for the

deactivated ghost mesh provided optimum balance between minimising the effect the deactivated ghost mesh has on results without causing distortion of the mesh. Thus, this value is used throughout the analysis.

5.3.3.3 Boundary and Loading Conditions

Due to complexities in creating the ghost mesh of deactivated elements, the deployment of the stent is not explicitly simulated. To create the condition where the stent is providing scaffolding support to the artery, as shown in Figure 5.4, a different method is used, which has been previously reported in numerous journal articles (Bedoya et al., 2006; Lally et al., 2005; Lally and Prendergast, 2006; Timmins et al., 2007) and in Chapter 3 of this thesis. The initial geometry of the stent is approximated as that of a deployed stent. First, a 5 % axial in situ prestretch is applied to artery in accordance with Holzapfel et al., (2005) and as applied by Zahedmanesh and Lally, (2009). Next, a pressure load is applied to the internal surface of the artery to expand it radially. Subsequently, the artery is moved over the stent and the pressure load on the artery is removed, allowing the artery to relax onto the stent. While this approach for creating the condition of a stent providing scaffolding support to the artery neglects the plastic deformation in the stent due to deployment, this technique does not affect the corrosion modelling approach of Grogan et al., (2011) which in the present form is not explicitly strain or stress modulated. This method is considered acceptable for this study as it is focused on stent degradation mechanics and neointimal remodelling of the artery following stent implantation.

To reduce the computational requirements of the simulations only half of the artery, five-ring Magmaris stent, and neointima are modelled (Figure 5.4) with appropriate symmetry boundary conditions subsequently applied to the corresponding surfaces. Eight-node linear reduced integration brick elements with distortion control are used for the representation of the three-layer artery (characteristic element length (L_e) = 0.118 mm), magnesium stent (L_e = 0.035 mm), and ghost mesh (L_e = 0.035 mm).

The mesh density is focused on the area of interest which in this case is the stent and the ghost mesh which have 22,500 and 260,000 elements, respectively, while the artery

mesh has 28,800 elements. These mesh sizes are chosen based on the results of a mesh sensitivity analysis while also maintaining practical convenience in simulation size and computational run time.

The Abaqus/Explicit solver is chosen for this research due to its superior contact enforcement method. General contact in Abaqus/Explicit is used for contact surfaces of the artery stent and neointima with “hard” contact defined for normal contact behaviour and with a frictional coefficient of 0.1 assumed for tangential contact behaviour.

To minimise dynamic effects, to avoid ambiguous displacement fluctuations by energy dissipation (Conway et al., 2014) and to maintain an average ratio of kinetic to internal energy of less than 5 % for the analysis, the Rayleigh damping coefficient ($\alpha = 8000$) is applied to a layer of shell elements on the internal surface of ghost mesh.

All the analyses are performed on a single hyperthreaded SGI ICE X high-performance computer having 2×12 core processors and 64 GB of RAM. Analyses of neointimal remodelling and pitting corrosion required approximately 3500 CPU hours per simulation.

5.3.3.4 Remodelling Methodology

The elements in the ghost mesh become activated according to the CDM neointimal remodelling methodology. The activation of elements in the ghost mesh is representative of the remodelling of the artery through the growth of new neointimal tissue and entails a change in the material properties assigned to those elements. The newly activated elements change from a very soft material (negligible initial mechanical properties, $E = 0.01$ MPa) to a stiffer material ($E = 0.225$ MPa) representative of neointimal tissue as outlined in Section 5.3.3.2.

The overall neointimal remodelling methodology uses the used to predict neointimal development via the activation of elements in the ghost mesh uses the CDM approach. (Lally and Prendergast, 2006) Here, the process is implemented using the dynamic temperature-displacement framework in Abaqus/Explicit software through a thermal analogy utilising VUSDFLD and VUAMP subroutines.

The thermal analogy relates temperature to concentration of cells. If the concentration of cells at element is denoted by n , the rate of change in the cell concentration, $\frac{dn}{dt}$, is computed by the cellular diffusion equation defined as:

$$\frac{dn}{dt} = k \nabla^2 n + c_{AS} d_{AS} + c_{WSS} d_{WSS} \quad (5.3)$$

where k is the diffusion coefficient of cells in arterial tissue, ∇^2 is the Laplace operator, d_{AS} and d_{WSS} are the damager parameters and c_{AS} and c_{WSS} are constants, which relate the damage parameters to cell proliferation rate.

The first part of Equation 5.3 is simply Fick's law of diffusion which can be related to Fourier's law of thermal conduction using a thermal analogy (Hose et al., 2004) and implemented in Abaqus using a coupled temperature–displacement simulation.

The previously calculated damage variables (d_{AS} and d_{WSS}) are multiplied by their respective constants (c_{AS} and c_{WSS}) and entered into the NR model as mapped analytical fields, which are used to control the distribution of thermal body heat flux loads and thermal surface heat flux loads respectively. Thermal loads correspond to influx of cells using the thermal analogy

The applied cellular (thermal) loads based on the damage variables ($c_{AS} d_{AS}$ and $c_{WSS} d_{WSS}$) results in the recruitment of cells into the artery and subsequently the diffusion of these cells into the ghost mesh. If the concentration of cells in an individual element in the ghost mesh exceeds a predefined threshold the element becomes activated. Activation of elements in the ghost mesh is representative of the remodelling of the artery through the growth of new neointimal tissue and entails a change in the material properties assigned to those elements using field variables and a user defined VUSDFLD subroutine. The newly activated elements change from a very soft material ($E = 0.01$ MPa) to a stiffer material ($E = 0.225$ MPa) as outlined in the Section 5.3.3.2. In this way neointimal remodelling of the artery around the expanded magnesium stent is simulated.

As shown by the literature the phenomenon of neointimal remodelling after magnesium stent implantation does not continue indefinitely. The recent results of Waksman et al.,

(2017), who implanted the Magmaris stent in non-diseased porcine arteries, indicate that the majority of neointimal growth occurs during the 28 days after implantation of the device and the neointima remains stable thereafter up to a period of two years (as illustrated by Figure 1.7 in Chapter 1). The thickness of the stable neointima is estimated as 0.22 mm from the results of Waksman et al., (2017) while for comparison the reported thickness of the Magmaris scaffold is 0.15 mm.

The NR model is based on the fundamental assumption that the neointima gradually propagates radially inward, eventually resulting in the encapsulation of the stent struts. To capture this effect, an **adjacent element condition** is placed on the ghost mesh where cells cannot diffuse into deactivated ghost elements until directly adjacent elements have become activated. This condition is achieved by increasing the diffusivity of deactivated ghost elements from an initial value of 0 up to 0.01 (mm²/day) for activated neointima when directly adjacent elements have been activated.

A further **retardation condition** is also implemented in the NR model to capture the desired remodelling effect. The artery is split up into 400 regions and individual cellular (thermal) loads are applied to each individual region. A series of sensor elements, evenly distributed throughout the stent and ghost mesh (as shown in Figure 5.5), are associated with individual cellular (thermal) loads. These sensor elements are used to provide feedback to the model by tracking the progression of neointimal growth. The constant associated with each individual cellular (thermal) load (c_{AS}/c_{WSS}) is linearly reduced as the neointima grows, therefore gradually reducing the applied remodelling stimulus in the accompanying region. When neointima remodelling has progressed to completion in a region, the (c_{AS}/c_{WSS}) value for this region is reduced to zero which turns off the remodelling stimuli in that region.

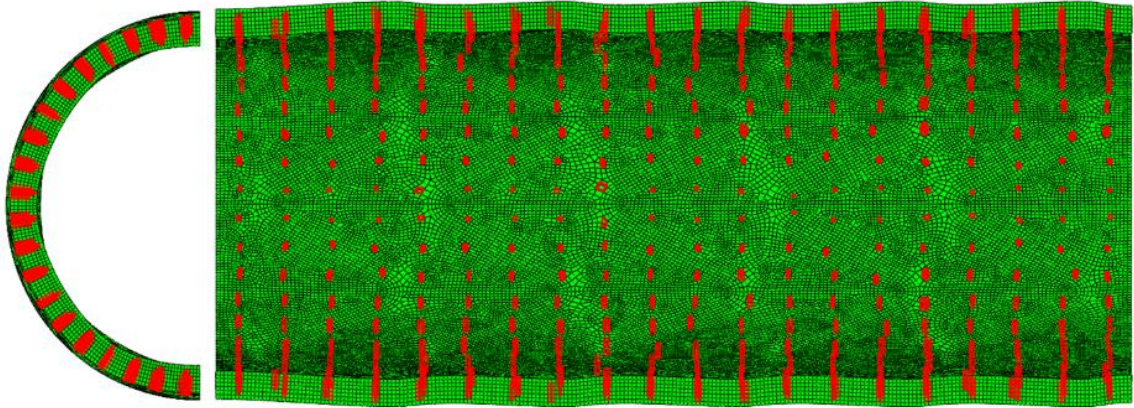


Figure 5.5. Illustrating the distribution of the sensor elements in the stent and ghost mesh which are used to track the progression of neointimal growth.

5.3.3.5 Neointimal Remodelling Patterns

The recent results of Waksman et al., (2017), who implanted the Magmaris stent in non-diseased porcine arteries, indicate that the majority of neointimal growth occurs during the 28 days after stent implantation and the neointima remains stable thereafter up to a period of two years (Figure 1.7). The 28-day remodelling rate corresponds to the expected *in-vivo* neointimal remodelling rate and the results of these simulations are labelled “28-day” remodelling.

The “6-month” remodelling rate is simulated by altering both the material diffusion parameters and initial c_{AS} and or c_{WSS} values entered into the NR model. For these second set of simulations the bulk of the neointimal remodelling occurs between 0-6 months. The results of these simulations are labelled “6-month remodelling”.

The work documented in Chapter 3, using the thermal analogy to model the diffusion of cells in an artery as the stimulus for neointimal remodelling is used as an initial guide in assigning appropriate values of diffusion properties for the artery, stent and ghost mesh/neointima materials. The initial values are subsequently altered iteratively until the desired neointimal remodelling rates are achieved.

The thermal/diffusion parameters are also used to calculate the minimum time increment used by the Abaqus/Explicit coupled thermal–displacement solver by the following equation (Koric et al., 2009):

$$\Delta t \leq \min \left(\frac{\rho c_p L_e^2}{2k} \right) \quad (5.4)$$

where ρ is the density of the material, c_p is the specific heat, k is the conductivity and L_e is the characteristic length of the smallest element in the model. These parameters must be chosen to ensure the minimum time increment is not too small ($\Delta t_{\min} \approx 10^{-6}$) so that the thermal/diffusion equation can be solved in suitable time frame.

The material parameters outlined in Table 5.2, are the set of material parameters used to achieve the desired “28-day” and “6-month” neointimal remodelling rates which also satisfy the minimum time increment condition outlined by Equation 5.4.

Table 5.2. An overview of cell diffusion properties used for the materials in the NR model to generate neointimal remodelling rate corresponding to 28-days (left) and 6-months (right)

	Diffusivity	No. of cells to increase concentration of cells by one unit	Concentration threshold
	<i>mm²/day</i>	<i>Dimensionless</i>	<i>No. of cells</i>
Adventitia	0.01	100 / 250	80 / 200
Media	0.01	100 / 250	80 / 200
Intima	0.01	100 / 250	80 / 200
Magnesium stent	0	100 / 250	80 / 200
Deactivated ghost	0	100 / 250	80 / 200
Activated neointima	0.01	100 / 250	80 / 200

To investigate how the different remodelling stimuli, effect the pattern of neointimal remodelling, six different simulations are computed: three simulations using the material parameters corresponding to the 28-day remodelling rate and three further simulations using the material parameters corresponding with the 6-month remodelling rate.

For two simulations (labelled - “AS”), only the d_{AS} parameter is utilised to as the remodelling stimulus. For two simulations (labelled - “WSS”), only the d_{WSS} parameter is utilised as the remodelling stimulus. Finally, for two simulations (labelled - “50/50”),

d_{AS} and d_{WSS} parameters each provide 50 % of the total remodelling stimulus added to the simulation.

As mentioned previously and outlined by Equation 5.3, the damage variables (d_{AS} and d_{WSS}) are multiplied by their respective constants (c_{AS} and c_{WSS}) before being entered into the NR model as mapped analytical fields. The values of c_{AS} and c_{WSS} for each of the 6 simulations AS, WSS and 50/50 simulations are outlined in Table 5.3.

Table 5.3. Table outlining the constants c_{AS} and c_{WSS} used for each of the 6 neointimal remodelling simulations.

Remodelling rate	28-days		6-months	
	c_{AS}	c_{WSS}	c_{AS}	c_{WSS}
AS	1.800	0	0.450	0
WSS	0	0.200	0	0.050
50/50	0.900	0.100	0.225	0.025

5.3.3.6 Neointimal Remodelling and Stent Corrosion

To analyse the effects the different neointimal remodelling patterns (AS, WSS and 50/50) along with the neointimal remodelling rates (28-day or 6-month) have on the degrading magnesium stent, the NR model is combined with the PC model calibrated for unground EDM Mg WE43 material described in Section 5.3.3.1. A corrosion kinetic parameter, ($k_U = 0.02$) from Equation 3.1, is selected for all six simulations so that the pitting corrosion of the magnesium stent starts immediately after stent implantation and is 95 % degraded at the end of the simulation, which corresponds with 12 months post stent implantation (Haude et al., 2016).

5.3.3.7 Case Studies

To analyse the effects that neointimal remodelling of the artery and stent degradation have on the recoil of the stent and coronary artery, eight different case studies with different neointimal remodelling and stent corrosion rates are investigated using the 50/50 NR model parameters in all eight cases. The specific neointimal remodelling and stent corrosion rates computed are shown in Table 5.4.

Table 5.4. Table outlining the respective stent and neointimal remodelling corrosion rates used for each of the eight case studies.

	Stent biodegradation		Neointimal remodelling
	Start	End	
Case 1	0 months	12 months	No remodelling
Case 2	0 months	12 months	28-day
Case 3	0 months	12 months	6-month
Case 4	6 months	18 months	No remodelling
Case 5	6 months	18 months	28-day
Case 6	6 months	18 months	6-month
Case 7	0 months	3 months	No remodelling
Case 8	0 months	3 months	28-day

The c_{AS} and c_{WSS} values for 50/50 simulations outlined in Table 5.3 are also used here for 28-day and 6-month remodelling. Changing the c_{AS} and c_{WSS} values to zero and thus reducing the applied cellular loads inputted into the NR model to zero allows simulation of the “no remodelling” condition.

A corrosion kinetic parameter, ($k_U = 0.02$) from Equation 3.1, is selected for cases 1-3 so that the pitting corrosion of the magnesium stent starts immediately after stent implantation and is 95 % degraded after 12 months (Haude et al., 2016). The same corrosion kinetic parameter, ($k_U = 0.02$) is used for cases 4-6 however, corrosion is delayed for the first 6-months of the simulation.

For cases 7-8 the corrosion rate is multiplied by four, ($k_U = 0.08$) to simulate complete stent degradation in 3-months, which is comparable to the *in-vitro* corrosion rate of polished Mg WE43 without a PLLA coating, as described in Chapter 4 and in Galvin et al., (2017).

5.4 Results

5.4.1 Stent Deployment and Recoil (SDR) Model

A banded contour plot of the Von Mises stress in the three-layer anisotropic artery after stent deployment and recoil is shown in Figure 5.6a. As illustrated in the contour plot, the Von Mises stresses in the artery are concentrated in the intima material with the highest stress locations found where the hinge regions of the magnesium stent are in contact with the internal surface of the intima. The highest computed value of Von Mises stress at the integration points is approximately 1.54 MPa.

The arterial stress damage variable from the SDR model, d_{AS} , has values ranging from 0 to 1.0 and is calculated from the Von Mises stress distributions in the intima material as outlined in Section 5.3.1.2. A contour plot of the damage variable, d_{AS} , is shown in Figure 5.6b. Naturally, given that d_{AS} is calculated from the Von Mises stress distribution in the intima, the highest values of d_{AS} correspond with high stress Von Mises stress regions from Figure 5.6a.

Figure 5.6c shows a contour plot of the temperature distribution (equivalent to concentration of cells using the thermal analogy) in the artery of the NR model, using just the d_{AS} parameter as the only remodelling stimulus at the start of the remodelling simulation.

The regions of highest cellular concentration in Figure 5.6c, are analogous to the regions of high d_{AS} in Figure 5.6b, which correspond with regions of high Von Mises stress in the SDR model shown in Figure 5.6a.

A similar pattern is observed on all three contour plots in Figure 5.6a, Figure 5.6b and Figure 5.6c, which illustrates how the Von Mises stress in the artery directly relates to the d_{AS} parameter which controls where cells in the artery are concentrated in the final NR simulation.

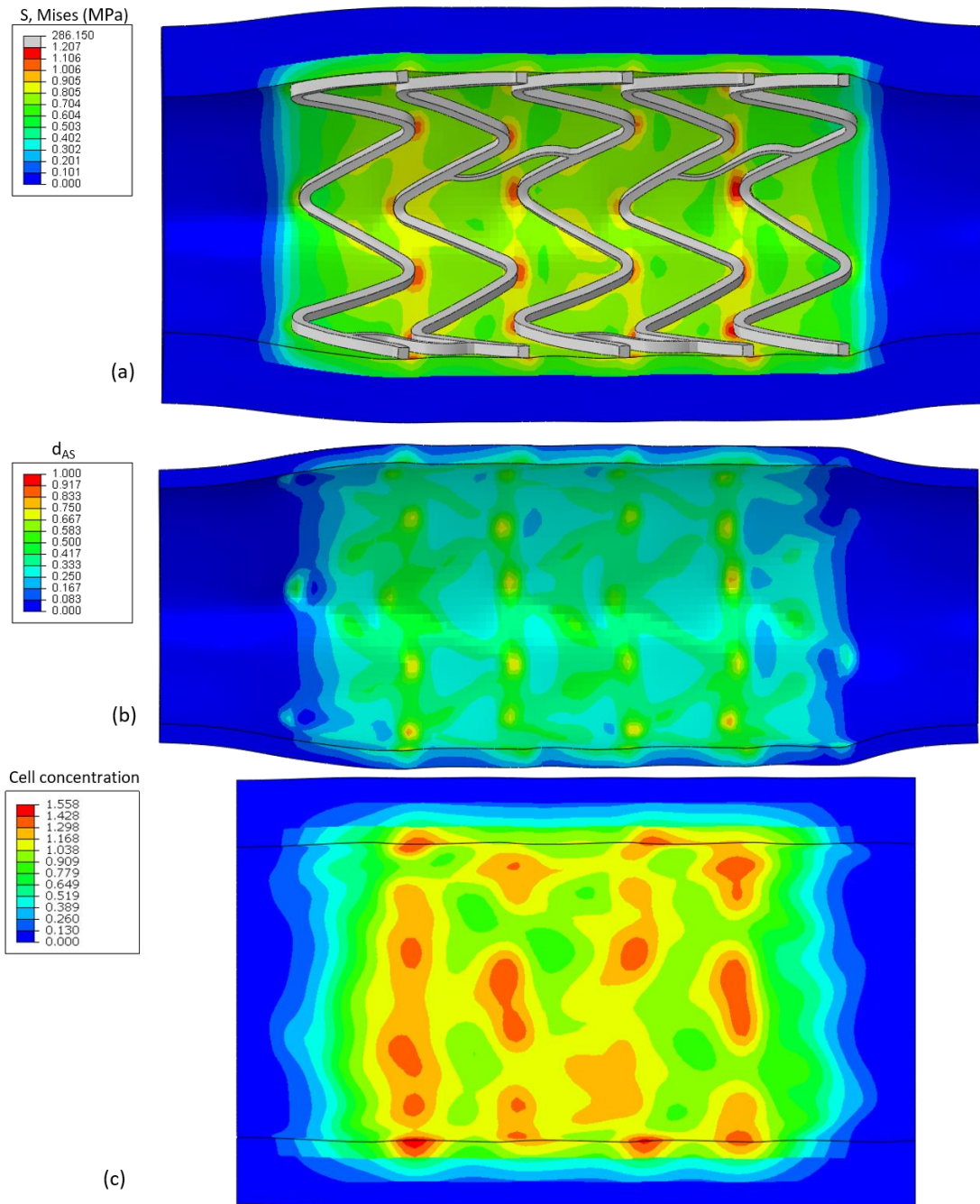


Figure 5.6. (a) Contour plot of the Von Mises stress in the artery material after stent deployment and recoil of the magnesium stent in the SDR model. (b) Contour plot illustrating the distribution of the d_{AS} parameter in the intima material for the SDR model. (c) Contour plot of the temperature distribution (equivalent to concentration of cells using the thermal analogy) in the artery of the NR model, using just the d_{AS} parameter as the only remodelling stimulus at the start of the remodelling simulation.

5.4.2 Blood Flow (BF) Model

A contour plot of TAWSS due to blood flow calculated from the BF model is shown in Figure 5.7a. As illustrated in Figure 5.7a, the TAWSS is lowest (< 0.5 Pa) in regions adjacent to stent struts and stent connectors. The TAWSS is highest (≈ 1.9 Pa) in the flow region immediately after the stent, where the lumen diameter decreases. These results are consistent with the results of Martin et al., (2014) and Martin and Boyle, (2015) who used similar techniques to investigate blood flow through a stented coronary artery.

As previously discussed in Section 5.3.2.2, elements whose TAWSS values are approximately 0 Pa are assigned d_{WSS} value of 1 while elements whose TAWSS values are greater than or equal to 0.5 Pa are assigned d_{WSS} values of 0. A linear interpolation is used to assign d_{WSS} values to elements which have a TAWSS between 0-0.5 Pa. The resulting contour plot of d_{WSS} through the lumen geometry is shown in Figure 5.7b. As shown in the contour plot, the highest d_{WSS} values are found in regions adjacent to stent struts and particularly stent connectors, due to low TAWSS and flow velocities in these regions. Furthermore, in an overall sense, the d_{WSS} is also accentuated in the proximal region, where blood flow enters to the stented region, in comparison to the distal region when blood flow exits the stented artery.

Figure 5.7c shows a contour plot of the temperature distribution (equivalent to concentration of cells using the thermal analogy) in the artery of the NR model, using just the d_{WSS} parameter as the only remodelling stimulus at the start of the remodelling simulation. As expected the cellular concentration has a similar pattern to the d_{WSS} parameter.

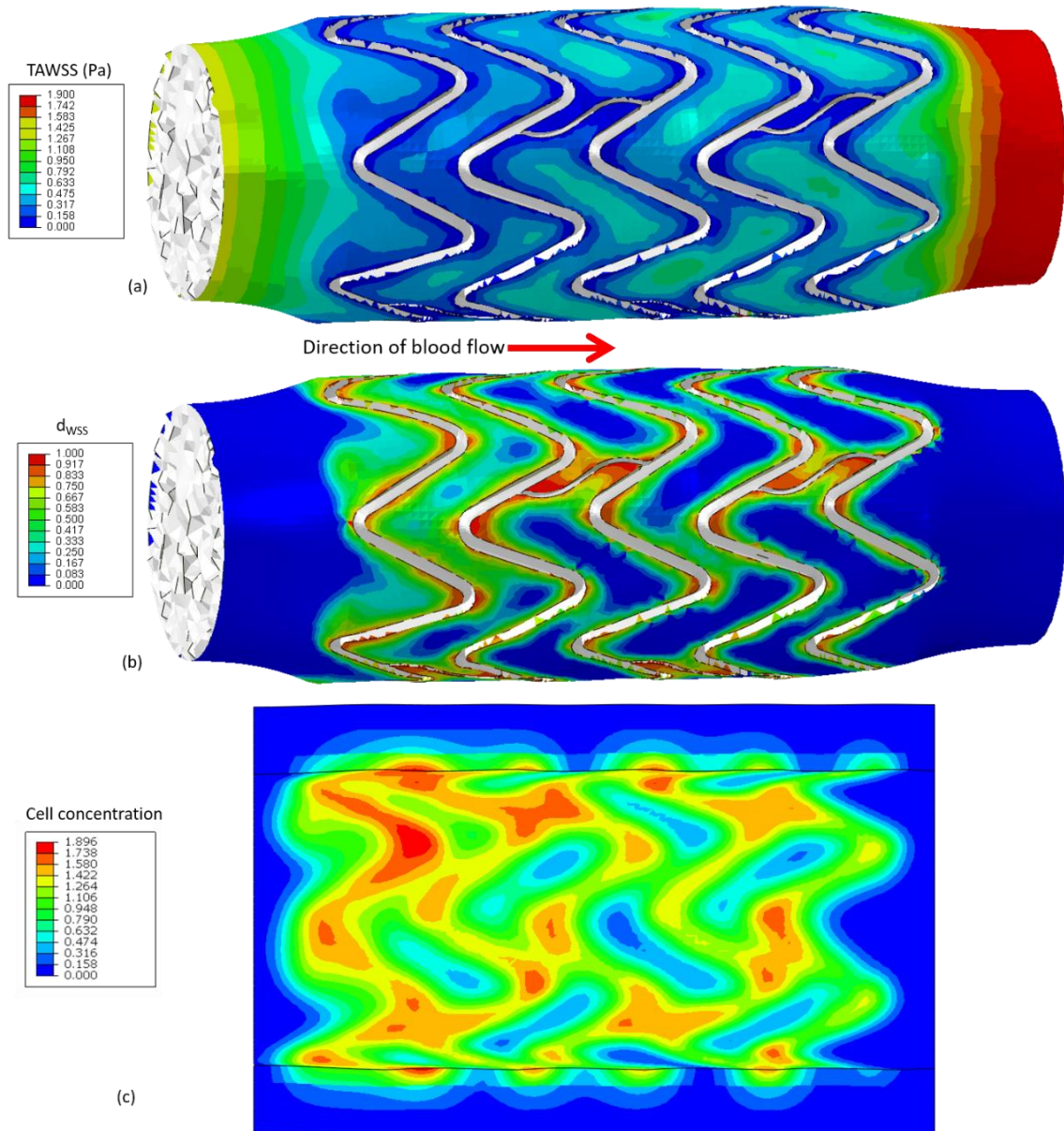


Figure 5.7. (a) Contour plot illustrating the distribution of TAWSS for the CFD model of blood flow through the artery lumen and deployed stent. Blue regions correspond the regions of low (< 0.5 Pa) TAWSS. (b) Contour plot illustrating the distribution of the d_{wss} parameter for the CFD model of blood flow through the artery lumen and deployed stent. Red regions are associated with where the TAWSS due to blood flow are lowest. (c) Contour plot of the temperature distribution (equivalent to concentration of cells using the thermal analogy) in the artery of the NR model, using just the d_{wss} parameter as the only remodelling stimulus at the start of the remodelling simulation.

5.4.3 Neointimal Remodelling (NR) Model

5.4.3.1 Remodelling Patterns AS vs WSS vs 5050

The neointimal remodelling patterns generated using the AS, WSS and 50/50 simulations are shown in Figure 5.8 for both the 28-day and the 6-month remodelling rate. Each simulation begins with no remodelling around the magnesium stent, shown in Figure 5.8a and ends with the magnesium stent completely encapsulated by the neointima (Figure 5.8f). The 4 images in between (Figure 5.8b - Figure 5.8e) show how the neointima develops throughout the AS, WSS and 50/50 simulations. For accurate comparison, the volume of activated neointima in Figure 5.8b to Figure 5.8e is the same for each of the three respective simulations.

As illustrated by comparison of the top and bottom images in Figure 5.8, the neointimal remodelling rate 28-day or 6-month does not majorly affect the overall remodelling patterns predicted by the NR model for any of the AS, WSS or 50/50 simulations. The neointimal remodelling rate (28-day or 6-month) merely changes the time at which neointimal elements are activated.

As illustrated in Figure 5.8, the AS simulations results in a neointimal remodelling pattern that initiates at the centre of the stent and spreads out relatively uniformly on both sides. The WSS simulations have a different remodelling pattern as shown in Figure 5.8. Neointimal remodelling initiates adjacent to the stent struts. Neointimal growth is also accelerated on the left side of the stent, which corresponds with where blood flow enters the stent during the WSS model. As illustrated in Figure 5.8, the remodelling pattern for the 50/50 simulations are a combination of the d_{AS} and d_{WSS} patterns.

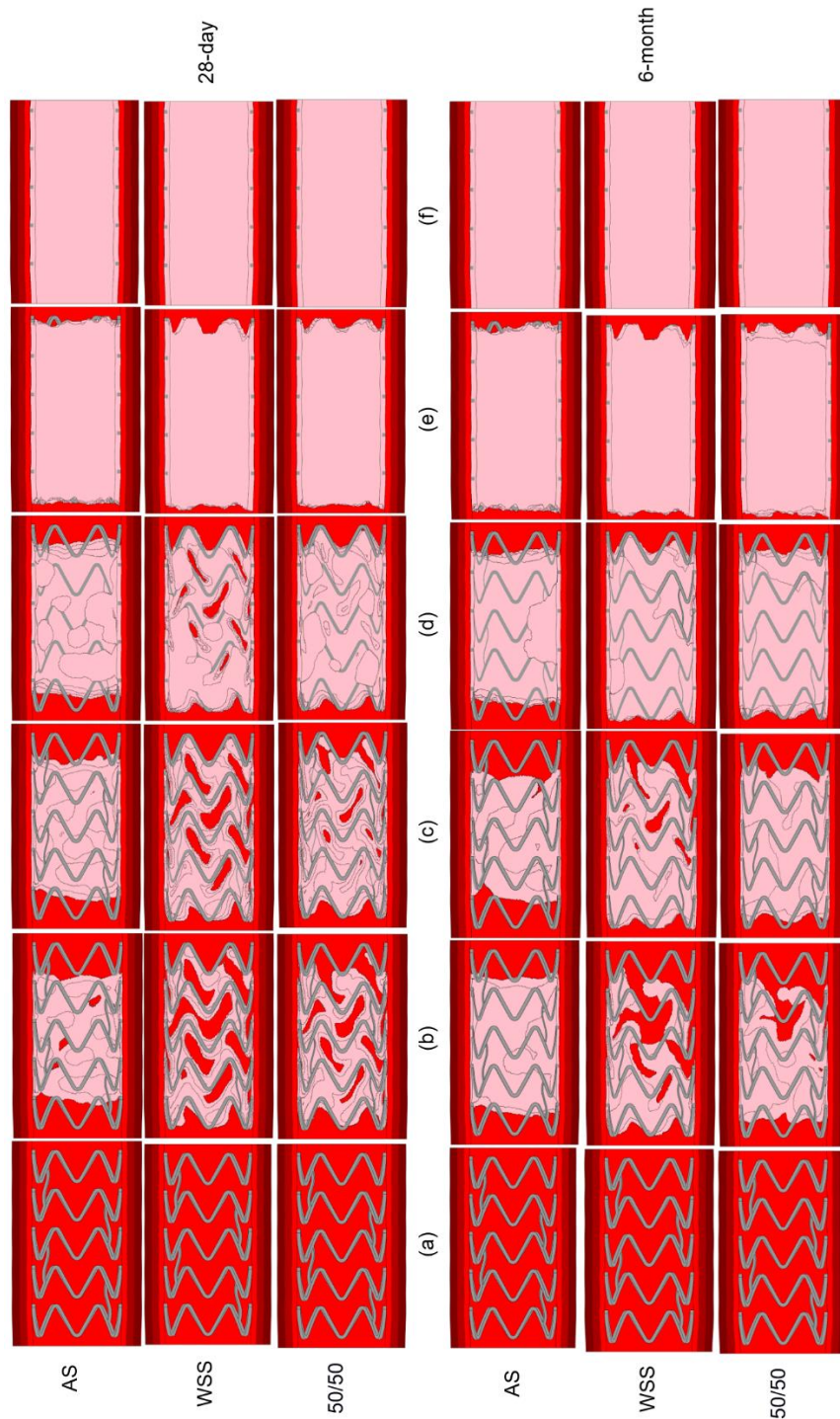


Figure 5.8. Abaqus images outlining the neointimal remodelling development between the AS, WSS and 50/50 simulations for the 28-day (top) and 6-month (bottom) remodelling rates. For accurate comparison between the simulations each image in sequence has approximately the same volume of activated neointima. Image rotated to increase visibility.

5.4.3.2 Neointimal Remodelling Patterns and Stent Corrosion

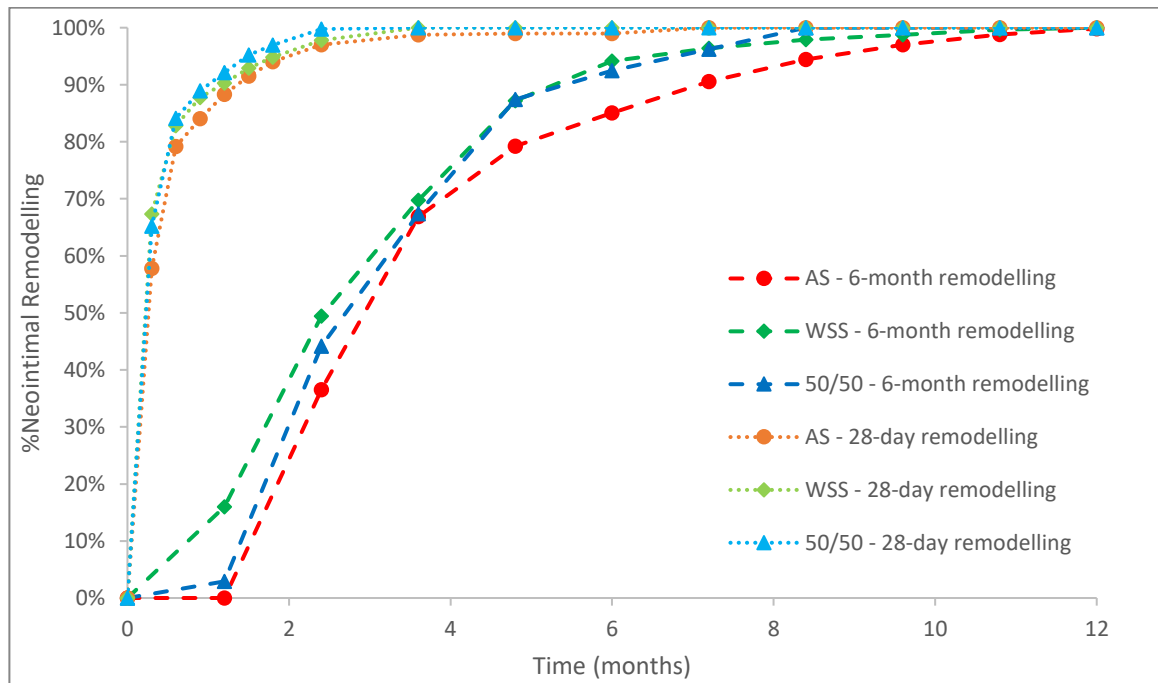


Figure 5.9. Plot of percentage neointimal remodelling versus time for each of the three simulations (AS, WSS and 50/50) for two neointimal remodelling rates (28-day and 6-month remodelling).

Figure 5.9 demonstrates the overall rate of neointimal remodelling versus time for each of the three simulations (AS, WSS and 50/50) for both neointimal remodelling rates (28-day and 6-month remodelling).

The dotted lines in Figure 5.9 show the rate of element activation in the neointima using 28-day remodelling parameters for each of the AS, WSS and 50/50 simulations, while the dashed lines in Figure 5.9 illustrate the rate of element activation in the neointima using 6-month remodelling parameters for each of the AS, WSS and 50/50 simulations.

For 28-day remodelling, there are virtually no variances between the rate of element activation in the AS, WSS and 50/50 simulations. 90 % of remodelling occurs in the first month and the neointima is completely remodelled after 2 months.

For 6-month remodelling, there are small differences between the rate of element activation in the AS, WSS and 50/50 simulations. After 6 months, for the AS simulation, 85 % of the neointima has remodelled while 94 % and 92 % of the neointima has

remodelled for the WSS and 50/50 simulations respectively. For the 6-month remodelling simulations the neointima has completely remodelled after 10 months in each of the AS, WSS and 50/50 simulations.

In an overall sense, neointimal remodelling of the AS simulation is slower than the WSS simulation while as expected, remodelling of the 50/50 simulation falls in between the other two simulations.

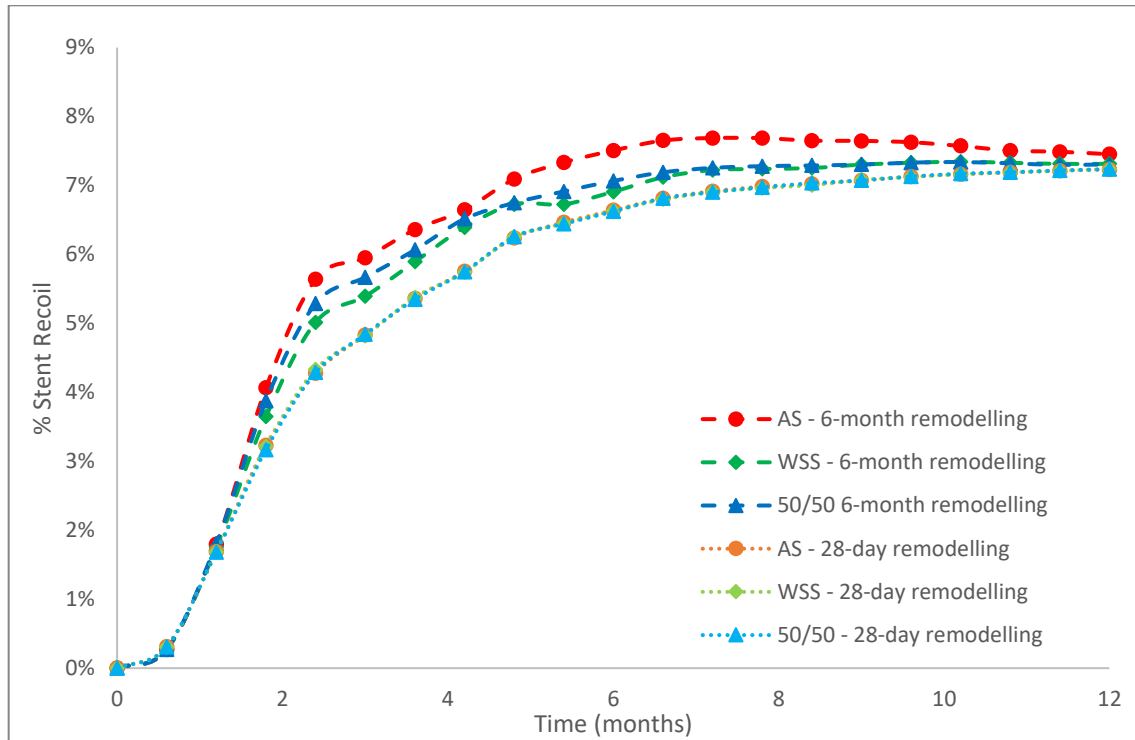


Figure 5.10. Plot of percentage stent recoil versus time for pitting corrosion with 28-day remodelling

As stated previously in Chapter 3, to assess overall stent scaffolding ability during degradation, the average percentage loss of radial scaffolding support (% stent recoil) is calculated from the displacements of the central nodes in the stent struts. Plots of percentage stent recoil versus time from each of the pitting corrosion neointimal remodelling simulations (AS, WSS and 50/50) for both neointimal remodelling rates (28-day and 6-month remodelling) are shown in Figure 5.10.

For the 28-day remodelling rate simulations, illustrated by the dotted lines in Figure 5.10, the plots of percentage stent recoil versus time are identical for all three remodelling patterns (AS, WSS or 50/50).

However, for the 6-month remodelling rate simulations, illustrated by the dashed lines in Figure 5.10, the plots of percentage stent recoil versus time are marginally different for the three remodelling patterns (AS, WSS or 50/50). The transient stent recoil over the 12 months is highest for the AS simulation and lowest for the WSS simulation, while as expected the 50/50 simulation falls in between the other two.

At 12 months after 95 % magnesium stent corrosion and complete neointimal remodelling of the artery, the three 6-month remodelling simulations have stent recoil between 7.3 % and 7.45 % which closely matches the percentage stent recoil at 12 months for the AS, WSS and 50/50 28-day remodelling simulations. However, in the initial stages of the simulation (between 2-4 months), the stent collapses at a faster rate for the 6-month remodelling cases than the 28-day remodelling cases. This difference in rate of stent collapse can be attributed to the neointimal remodelling rate as for the 6-month remodelling cases there is a reduced amount of activated neointima to provide mechanical support to the degrading stent.

5.4.3.3 Case Studies: Stent Recoil and Lumen Diameter vs Time

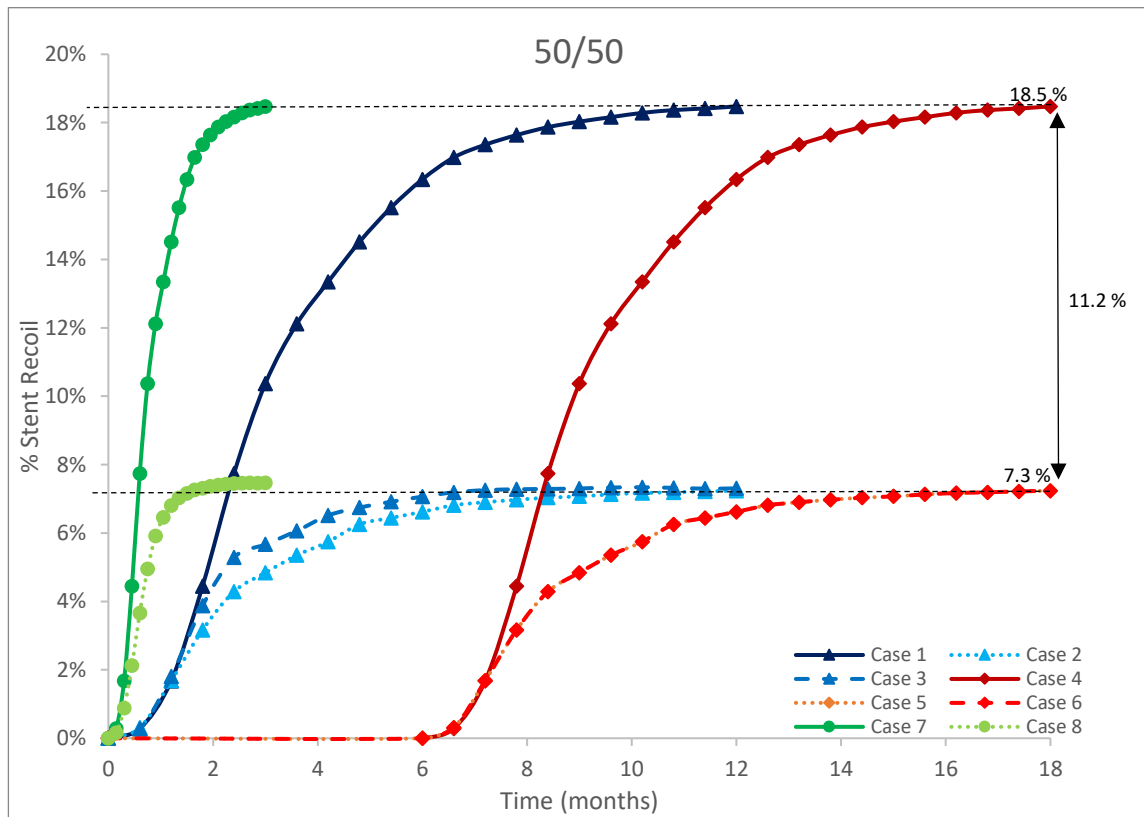


Figure 5.11. Plot of stent recoil versus time for the eight different case studies for various neointimal remodelling and stent corrosion rates

Figure 5.11 is a graph outputted from the NR model which plots the transient percentage recoil of the corroding Magmaris stent for each of the eight cases outlined in Section 5.3.3.7 and Table 5.4. Corrosion of the magnesium material compromises the mechanical integrity of the Magmaris stent which causes the stent to radially contract due to forces applied by the expanded coronary artery.

As demonstrated in Figure 5.11, cases 1, 4 and 7, which have no neointimal remodelling and are illustrated by the solid lines, have stent recoil of 18.5 % after complete corrosion of the stent (after 3, 12 and 18 months respectively).

In the other five cases either 28-day (dotted lines) or 6-month (dashed lines) neointimal remodelling occurs, and the stent recoil after complete stent degradation is

approximately 7.3 % in all cases. These results show that complete neointimal remodelling reduces the stent recoil of a fully degraded stent by 11.2 %.

The neointimal remodelling rate (none, 28-day or 6-month) and the stent degradation rate and start time (outlined in Table 5.4) alters the transient recoil of the stent, but ultimately the stent recoil ends up at one of two values (18.5 % or 7.3 %), the former for no remodelling and the latter for complete remodelling. The difference, 11.2 %, is a measure of the mechanical support provided by the neointima to the stent.

The lumen of the artery decreases due the loss of scaffolding support provided by the magnesium stent as it degrades which causes recoil of the artery. The lumen of the artery also decreases due to neointimal remodelling around the stent struts as illustrated in Figure 5.8.

The percentage reduction in lumen diameter is calculated by tracking the radial displacement of the nodes which form the artery lumen at a given timepoint, calculating the average lumen diameter at this timepoint and subsequently dividing by the original lumen diameter before corrosion and remodelling occurs. As illustrated in Figure 5.8, the surface nodes which form the artery lumen change as the artery undergoes neointimal remodelling.

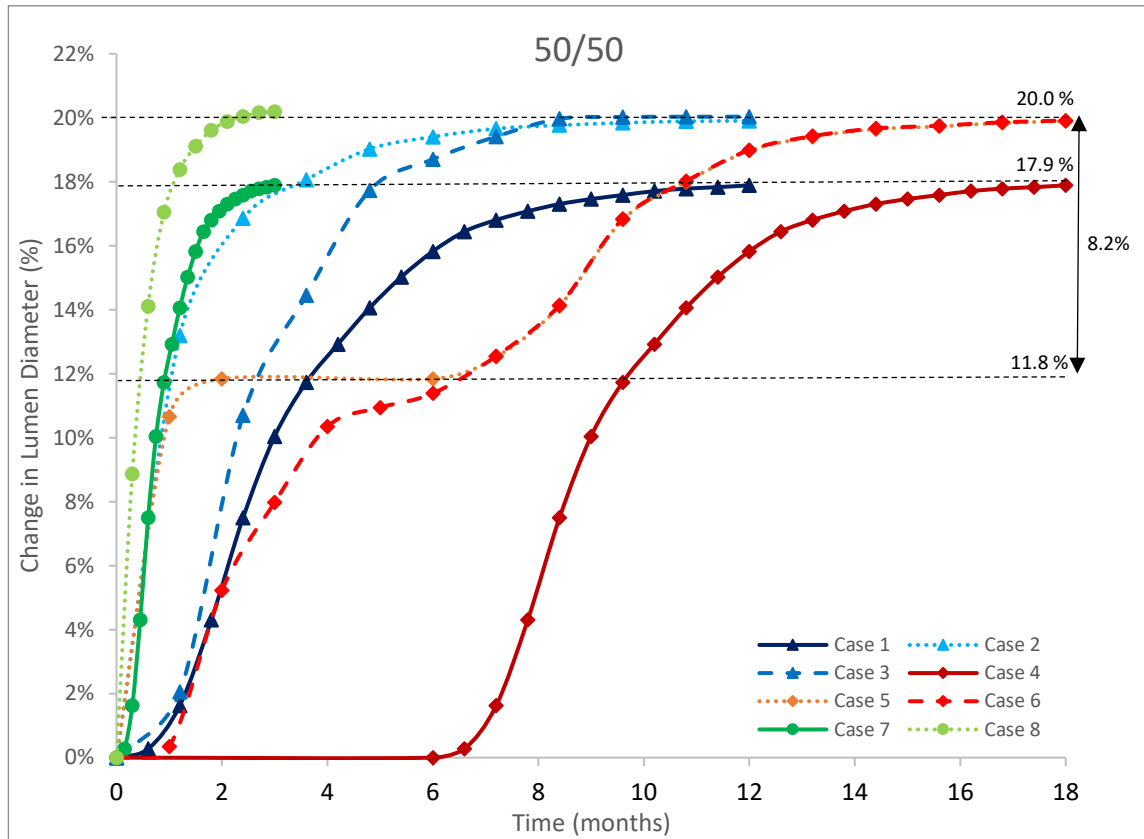


Figure 5.12. Plot showing the percentage change in diameter of the lumen versus time due to neointimal remodelling and stent corrosion for the eight different case studies.

Figure 5.12 is a graph outputted from the NR model which plots the transient reduction in the lumen diameter of the artery for each of the eight cases already outlined in Section 5.3.3.7 and Table 5.4.

As mentioned previously, corrosion of the Magmaris stent causes the stent, and the expanded artery which it is supporting, to radially contract. Therefore, stent degradation causes a reduction in the diameter of the artery lumen. Neointimal remodelling, which is the encapsulation of the stent struts by the artery as the new neointimal material is formed, also causes a reduction in diameter of the artery lumen. Therefore, both stent corrosion and neointimal remodelling reduce the lumen diameter of the artery.

With no remodelling for cases 1, 4 and 7 only stent degradation causes a reduction in lumen of the artery. After complete stent degradation, the reduction in artery lumen is 17.9 % which is similar to the recoil of the stent (18.5 %) for the same cases.

The other five cases, either 28-day or 6-month neointimal remodelling, along with stent degradation, is simulated. So, in these five cases both neointimal remodelling and stent degradation cause a reduction in the lumen of the artery. As illustrated in Figure 5.12, after complete stent degradation, the lumen of the artery has decreased by 20.0 % in all five cases, which is larger than the 17.9 % for the no remodelling cases.

To summarise, variation in the neointimal remodelling rate (none, 28-day or 6-month) and the stent degradation rate and start time (outlined in Table 5.4) alter the transient reduction of the artery lumen, but ultimately the artery lumen ends up at one of two values 17.9 % for no remodelling or 20.0 % for no remodelling.

Case 5 is particularly interesting in this context as in this case the neointima has fully remodelled (28-day) before the stent has started to corrode (Table 5.4). What can be seen here is that by tracking the lumen diameter of case 5, is that after 2 months and complete neointimal remodelling the artery lumen has reduced in diameter by 11.8 %. This is solely caused by the neointimal remodelling. Stent corrosion, which occurs between 6-18 months in this case, subsequently reduces the lumen diameter by a further 8.2 %, from 11.8 % to 20 %. This quantifies the contribution that the stent corrosion on its own makes to the evolution in lumen diameter when the neointima remodelling is complete.

5.5 Discussion

5.5.1 Stent Deployment and Recoil (SDR) Model

The contour plots of Von Mises stress in the artery after stent deployment and recoil are similar to those reported in the literature (Boyle et al., 2013; Conway et al., 2014; Zahedmanesh and Lally, 2009). The magnitude of stress values are in the same range as those reported by Conway et al., (2014), Zahedmanesh and Lally, (2009) and Boyle et al., (2013) and the outline of the stent struts are visible in the figure here and figures shown in the literature.

5.5.2 Blood Flow (BF) Model

Figure 5.7a shows that in the BF model the TAWSS is lowest in regions adjacent to the stent struts. This is the expected results as stent struts protruding into the lumen

would impede the local blood flow hemodynamics. These results also agree with results of similar coronary blood flow analyses published in the literature (Morlacchi et al., 2011; Murphy and Boyle, 2010b, 2010a).

5.5.3 Neointimal Remodelling (NR) Model

5.5.3.1 Remodelling Patterns AS vs WSS vs 5050

As shown by the images in Figure 5.8, the prediction of the NR model in relation to the pattern of neointimal remodelling is different for each the AS, WSS and 50/50 simulations. This poses the question of which pattern of neointimal remodelling is most likely to occur *in-vivo*.

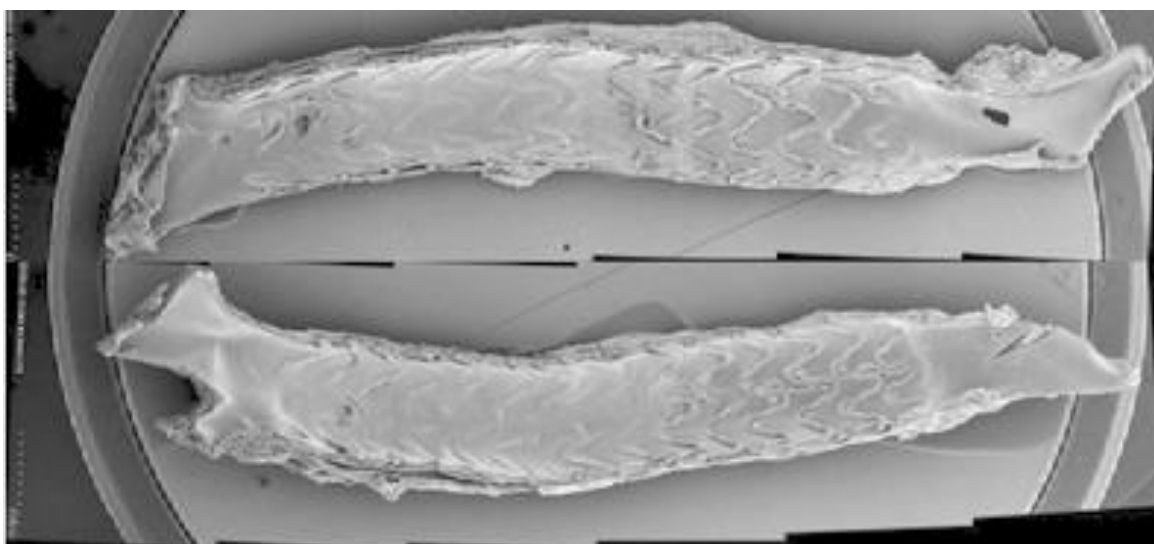


Figure 5.13. SEM images of a bisected rabbit iliac artery 28 days after Magmaris stent implantation showing endothelialisation (remodelling) along the length of the stent. Reprinted from EuroIntervention 13/4, Waksman et al., Second-generation magnesium scaffold Magmaris: device design and preclinical evaluation in a porcine coronary artery model, 440-449, Copyright (2017), with permission from Europa Digital & Publishing. Adapted from Waksman et al., (2017).

Waksman et al., (2017) published SEM images showing the pattern of endothelialisation 28 days after the implantation of a Magmaris stent in rabbit iliac arteries. As demonstrated by Figure 5.13, the endothelialisation pattern is non-uniform throughout the length of the Magmaris stent and is accentuated at one of the ends of the stent compared with the other one.

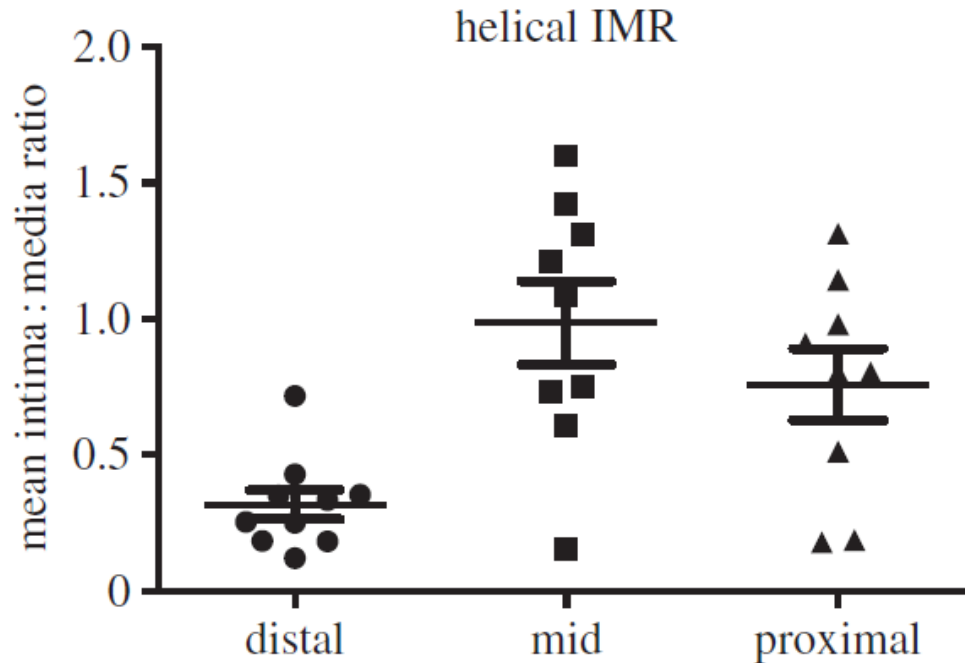


Figure 5.14. Plot of the intima-to-media ratio in a porcine carotid artery one month after implantation of helical centreline nitinol stents. Adapted from Caro et al., (2013).

Caro et al., (2013) implanted bare metal nitinol stents into porcine carotid arteries and analysed the resulting response of the artery to the stent implantation. As illustrated in Figure 5.14, Caro et al., (2013) found that IMR (intima-to-media ratio) is significantly lower in the distal than proximal or middle segments in helical-centreline stented vessels. This is related to the higher wall shear stresses in the distal than proximal or middle regions.

These findings showing that the response of the artery to stenting is non-uniform and can be accentuated in proximal over distal regions. Thus, these results indicate that the wall shear stress stimulus is more significant than the arterial stress stimulus and that the neointimal remodelling pattern predicted by the WSS simulation and illustrated in Figure 5.8, is most likely of the three to occur *in-vivo*.

5.5.3.2 Neointimal Remodelling Patterns and Stent Corrosion

As shown by Figure 5.10, the different remodelling patterns (AS, WSS and 50/50) and different neointimal remodelling rates (28-day and 6-month) effect the recoil of the degrading stent. The difference in stent recoil for each of the six simulations can all be

linked back to the plot shown in Figure 5.9, percentage of neointimal remodelling versus time.

For the 28-day remodelling rate simulations, the plots of percentage stent recoil versus time (Figure 5.10) are identical for all three remodelling patterns (AS, WSS or 50/50) because the associated curve for percentage of neointimal remodelling versus time (Figure 5.9) are the same.

For the 6-month remodelling rate simulations (Figure 5.10) the plots of percentage stent recoil versus time are marginally different for the three remodelling patterns (AS, WSS or 50/50) due to the differences in the associated curves for percentage of neointimal remodelling versus time (Figure 5.9).

5.5.3.3 Case Studies: Stent Recoil and Lumen Diameter vs Time

As discussed in Section 5.3.3.2, a detailed search of the literature to determine appropriate mechanical properties to assign to the neointima (activated ghost mesh) proved inconclusive so it is assumed that the neointima material has similar properties to the intima. Linear elastic incompressible properties are assigned to the activated neointima with this assumption of linear elasticity valid for low strain ranges.

The value of Young's modulus ($E = 0.225$ MPa) assigned to the activated neointima has a large influence on the results of the neointimal remodelling stent corrosion cases. This is illustrated by comparison between the no remodelling and remodelling plots illustrated in Figure 5.11. Figure 5.11 demonstrates how the neointimal material reduces the recoil of a fully degraded magnesium stent from 18.5 % without remodelling to 7.3 % with neointimal remodelling. This 11.2 % difference is related to the material properties ($E = 0.225$ MPa) assigned to the neointimal material.

As demonstrated by Figure 3.8 in Chapter 3, the stiffness of the Young's modulus value influences the quantity of stent recoil. A higher Young's modulus value results in a larger recoil difference while and a lower Young's modulus value results in a smaller recoil difference. Changing the Young's modulus value applied to the neointima in the NR model described in this chapter would result in a similar trend being observed.

For Chapter 3, the three-layer artery is modelled using a hyperelastic isotropic material model (Gervaso et al., 2008), consistent with the mean values of the experimental testing of coronary arteries in the circumferential direction (Holzapfel et al., 2005). It is assumed that neointima has similar properties to the intima. To have consistent material properties between the simulated intima and neointima for the model of Chapter 3, the properties of the neointima are approximated using the hyperelastic isotropic model of the intima when subject to low strains ($< 5\%$) (Gervaso et al., 2008; Holzapfel et al., 2005). The resulting Young's modulus value ($E = 0.05$ MPa) is assigned to the activated neointima material. On reflection the author would consider this Young's modulus value ($E = 0.05$ MPa) a conservative estimate on the Young's modulus of the neointima.

For Chapter 5 as discussed in Section 5.3.1.1, an anisotropic HGO formulation is used to model the three-layer artery. The HGO materials model parameters for the adventitia, media and intima are taken from Mortier et al., (2010) who calibrated them using the stress-strain response from experimental tissue testing of coronary arteries (Specimen I) as documented in Holzapfel et al., (2005). Similar to Chapter 3, to have consistent material properties for the intima and neointima in the NR model, a value of $E = 0.225$ MPa is assigned as the stiffness of the activated neointima based on the approximation of Young's modulus from the stress-strain response of intima of Specimen I as outlined in 5.3.3.2 and Table 5.1. The author would consider the Young's modulus value of $E = 0.225$ MPa a more accurate choice of material properties to be assigned to the neointima given the rigorous process used, as described in Section 5.3.3.2.

The neointimal thickness value (0.22 mm) approximated from the findings of Waksman et al., (2017) is another important parameter which influences the recoil of the degrading stent in the remodelling artery. A thicker activated neointima would provide more mechanical support to the degrading stent and would reduce the stent recoil of degrading stent in a remodelling artery (7.3 % for cases 2, 3, 5, 6 and 8 in Figure 5.11) seen in the current configuration. The opposite effect would be observed by decreasing the neointimal thickness value.

Figure 5.12 demonstrates a similar phenomenon for the percentage reduction in lumen diameter. For cases 1, 4 and 7 with no neointimal remodelling the lumen diameter is

reduced by 17.9 % solely due to the corrosion of the magnesium stent. Corrosion of the magnesium stent in a completely remodelled artery, which occurs after 6 months for case 5, causes an 8.2 % reduction in the lumen diameter. These cases demonstrate that the neointimal material provides significant support to the artery as the stent degrades. Without neointima remodelling (cases 1, 4 and 7) stent corrosion causes the lumen to collapse by 17.9 %, while stent corrosion in completely remodelled artery (case 5) causes the lumen to collapse by 8.2 % (from 11.8 % to 20 %).

5.5.3.4 Implications for Stent Computational Modelling

As discussed in Chapter 1, the response of the artery to the stent is of critical importance to the long-term success of the PCI procedure. Inadequate neointimal remodelling leads to uncovered stent struts which greatly increases the risk of late stent thrombosis formation (Finn et al., 2007; Holmes et al., 2010; Joner et al., 2006). For biodegradable stents such as the Magmaris resorbable scaffold, the results presented in this chapter highlight the additional importance of the neointima from a mechanical perspective by providing scaffolding support to the artery as the stent degrades.

Based on the previous knowledge for permanent stents linking uncovered stent struts with increased risk of late stent thrombosis and the results of this chapter and Chapter 3, which highlight the mechanical support that the neointima provides to the degrading stent, it is recommended that next generation biodegradable stents are designed to promote adequate neointimal healing of the artery in the weeks and months following stent implantation. This may be achieved by a combination of factors such as improving the stent geometric design, the stent biomaterial, the balloon catheter delivery system, the polymer coating, the drug eluted and the rate of drug delivery to the surrounding tissues.

Before a medical device such as a coronary stent can be sold in the United States the Food and Drug Administration (FDA) must verify the safety and effectiveness of the device. In April 2010, the United States' FDA released a report entitled "Non-clinical engineering tests and recommended labelling for intravascular stents and associated delivery systems" to act as guidance document for companies aiming to achieve

approval for a new intravascular stent or associated delivery system (United States' Food and Drug Administration, 2010). In this document under "Stress/Strain Analysis", the FDA recommends the conduction of finite element analysis (FEA) to evaluate, in combination with a fatigue assessment and accelerated durability testing, the potential for failure over the entire stress history of the device.

The FEA results presented in this chapter have shown the neointima has a significant impact on the mechanical performance of the biodegradable magnesium stent as it degrades in a remodelling artery. It is recommended that computational models investigating the behaviour of biodegradable stents after implantation in the body account for the influence of neointimal remodelling. As illustrated in Figure 5.10, the pattern of neointimal development has little influence on the overall results of the stent corrosion remodelling simulation. Therefore, it may not be necessary to develop a complex model for neointimal development which includes multiple remodelling stimuli such as the one described in this chapter. A simpler model of uniform neointimal remodelling or one investigating the corrosion of the stent in a completely remodelled artery may be sufficient to generate useful results which demonstrate the safety of the device.

5.5.4 Limitations

Coronary stent implantation is required due to the build-up of atherosclerotic plaque in the coronary arteries. The stenting procedure plastically deforms this plaque and re-opens the lumen of the artery, so more blood flow can occur. However, atherosclerotic plaque is not accounted for in any of the models described here which is a limitation of the model. Atherosclerotic plaque may affect the arterial stresses values and distribution in the SDR model.

Atherosclerotic plaque may also affect the flow of blood around the implanted Magmaris stent and lead to alternative TAWSS distribution and magnitudes. For future work in this research area, it is recommended to include atherosclerotic plaque in the SDR, BF and NR models.

In the current pitting corrosion model, the stent corrosion rate is a constant and is not affected by the remodelling of the artery around the stent struts. *In-vitro* corrosion experiments on pure magnesium samples have shown that covered samples have slower degradation rate than uncovered samples (Bowen et al., 2012), indicating that the use of a constant stent corrosion rate may be a limitation.

The Magmaris scaffold is coated with a BIOlute bioresorbable poly-L-lactide acid (PLLA) coating to control magnesium corrosion and the elution of a limus drug. However, the pitting corrosion model parameters used in this study were calibrated using results from *in-vitro* corrosion experiments of unground EDM samples of Mg WE43 alloy (Boland et al., 2018), and do not account for the PLLA coating which is a limitation. For future work, it is recommended to conduct some experimental immersion tests to determine the effect a PLLA or similar polymer coating has on the corrosion behaviour on the underlying magnesium material.

5.6 Conclusions

In this work, a continuum model for neointimal remodelling has been successfully developed and implemented in Abaqus software which accounts for two local physiological stimuli, arterial stress due Magmaris stent deployment and endothelial shear stress due to altered coronary blood flow hemodynamics. The continuum model can be used to generate different patterns of neointimal remodelling depending on the stimuli activated.

The continuum model for neointimal remodelling has been combined with a magnesium pitting corrosion model to simulate neointimal remodelling of the artery around a degrading magnesium stent.

The findings of Chapter 5, and the comparison of the neointimal remodelling patterns with the literature (Waksman et al., 2017) and (Caro et al., 2013) indicate that the wall shear stress stimulus is more significant than the arterial stress stimulus and that the neointimal remodelling pattern predicted by the WSS simulation and illustrated in Figure 5.8, is most likely of the three (AS, WSS 50/50) to occur *in-vivo*.

This work has shown that the active response of the artery following stent implantation should not be ignored when modelling biodegradable stents as it can have a significant effect on recoil of the stent and scaffolding support provided to the artery.

References

- Bedoya, J., Meyer, C.A., Timmins, L.H., Moreno, M.R., Moore, J.E., 2006. Effects of stent design parameters on normal artery wall mechanics. *J. Biomech. Eng.* 128, 757–65. <https://doi.org/10.1115/1.2246236>
- Boland, E.L., Grogan, J.A., Conway, C., McHugh, P.E., 2016. Computer Simulation of the Mechanical Behaviour of Implanted Biodegradable Stents in a Remodelling Artery. *JOM* 68, 1198–1203. <https://doi.org/10.1007/s11837-015-1761-5>
- Boland, E.L., Grogan, J.A., McHugh, P.E., 2017. Computational Modeling of the Mechanical Performance of a Magnesium Stent Undergoing Uniform and Pitting Corrosion in a Remodeling Artery. *J. Med. Device.* 11, 021013. <https://doi.org/10.1115/1.4035895>
- Boland, E.L., Shirazi, R.N., Grogan, J.A., McHugh, P.E., 2018. Mechanical and Corrosion Testing of Magnesium WE43 Specimens for Pitting Corrosion Model Calibration. *Adv. Eng. Mater.* 1–11. <https://doi.org/10.1002/adem.201800656>
- Bourantas, C. V., Papafaklis, M.I., Kotsia, A., Farooq, V., Muramatsu, T., Gomez-Lara, J., Zhang, Y.J., Iqbal, J., Kalatzis, F.G., Naka, K.K., Fotiadis, D.I., Dorange, C., Wang, J., Rapoza, R., Garcia-Garcia, H.M., Onuma, Y., Michalis, L.K., Serruys, P.W., 2014. Effect of the endothelial shear stress patterns on neointimal proliferation following drug-eluting bioresorbable vascular scaffold implantation: An optical coherence tomography study. *JACC Cardiovasc. Interv.* 7, 315–324. <https://doi.org/10.1016/j.jcin.2013.05.034>
- Bowen, P.K., Gelbaugh, J.A., Mercier, P.J., Goldman, J., Drelich, J., 2012. Tensile testing as a novel method for quantitatively evaluating bioabsorbable material degradation. *J. Biomed. Mater. Res. - Part B Appl. Biomater.* 100B, 2101–2113. <https://doi.org/10.1002/jbm.b.32775>
- Boyle, C.J., Lennon, A.B., Early, M., Kelly, D.J., Lally, C., Prendergast, P.J., 2010. Computational simulation methodologies for mechanobiological modelling: a cell-centred approach to neointima development in stents. *Phil. Trans. R. Soc. A* 368, 2919–2935. <https://doi.org/10.1098/rsta.2010.0071>
- Boyle, C.J., Lennon, A.B., Prendergast, P.J., 2013. Application of a mechanobiological simulation technique to stents used clinically. *J. Biomech.* 46, 918–924. <https://doi.org/10.1016/j.jbiomech.2012.12.014>
- Boyle, C.J., Lennon, A.B., Prendergast, P.J., 2011. In Silico Prediction of the Mechanobiological Response of Arterial Tissue: Application to Angioplasty and Stenting. *J. Biomech. Eng.* 133, 081001. <https://doi.org/10.1115/1.4004492>
- Burke, D.P., Kelly, D.J., 2012. Substrate stiffness and oxygen as regulators of stem cell differentiation during skeletal tissue regeneration: A mechanobiological model. *PLoS One* 7. <https://doi.org/10.1371/journal.pone.0040737>

- Caiazzo, A., Evans, D., Falcone, J.L., Hegewald, J., Lorenz, E., Stahl, B., Wang, D., Bernsdorf, J., Chopard, B., Gunn, J., Hose, R., Krafczyk, M., Lawford, P., Smallwood, R., Walker, D., Hoekstra, A., 2011. A Complex Automata approach for in-stent restenosis: Two-dimensional multiscale modelling and simulations. *J. Comput. Sci.* 2, 9–17. <https://doi.org/10.1016/j.jocs.2010.09.002>
- Caro, C.G., Seneviratne, A., Heraty, K.B., Monaco, C., Burke, M.G., Krams, R., Chang, C.C., Coppola, G., Gilson, P., 2013. Intimal hyperplasia following implantation of helical-centreline and straight-centreline stents in common carotid arteries in healthy pigs: Influence of intraluminal flow. *J. R. Soc. Interface* 10. <https://doi.org/10.1098/rsif.2013.0578>
- Conway, C., McGarry, J.P., Edelman, E.R., McHugh, P.E., 2017. Numerical Simulation of Stent Angioplasty with Predilation: An Investigation into Lesion Constitutive Representation and Calcification Influence. *Ann. Biomed. Eng.* 45, 2244–2252. <https://doi.org/10.1007/s10439-017-1851-3>
- Conway, C., McGarry, J.P., McHugh, P.E., 2014. Modelling of Atherosclerotic Plaque for Use in a Computational Test-Bed for Stent Angioplasty. *Ann. Biomed. Eng.* 42, 2425–2439. <https://doi.org/10.1007/s10439-014-1107-4>
- De Beule, M., Mortier, P., Carlier, S.G., Verheghe, B., Van Impe, R., Verdonck, P., 2008. Realistic finite element-based stent design: the impact of balloon folding. *J. Biomech.* 41, 383–9. <https://doi.org/10.1016/j.jbiomech.2007.08.014>
- Finn, A. V., Joner, M., Nakazawa, G., Kolodgie, F., Newell, J., John, M.C., Gold, H.K., Virmani, R., 2007. Pathological correlates of late drug-eluting stent thrombosis: Strut coverage as a marker of endothelialization. *Circulation* 115, 2435–2441. <https://doi.org/10.1161/CIRCULATIONAHA.107.693739>
- Galvin, E., O'Brien, D., Cummins, C., Mac Donald, B.J., Lally, C., 2017. A strain-mediated corrosion model for bioabsorbable metallic stents. *Acta Biomater.* 55, 505–517. <https://doi.org/10.1016/j.actbio.2017.04.020>
- Garg, S., Serruys, P.W., 2010. Coronary stents: Current status. *J. Am. Coll. Cardiol.* 56, S1–S42. <https://doi.org/10.1016/j.jacc.2010.06.007>
- Gervaso, F., Capelli, C., Petrini, L., Lattanzio, S., Di Virgilio, L., Migliavacca, F., 2008. On the effects of different strategies in modelling balloon-expandable stenting by means of finite element method. *J. Biomech.* 41, 1206–12. <https://doi.org/10.1016/j.jbiomech.2008.01.027>
- Gómez-Benito, M.J., García-Aznar, J.M., Kuiper, J.H., Doblaré, M., 2005. Influence of fracture gap size on the pattern of long bone healing: A computational study. *J. Theor. Biol.* 235, 105–119. <https://doi.org/10.1016/j.jtbi.2004.12.023>
- Gomez-Lara, J., Brugaletta, S., Farooq, V., Onuma, Y., Diletti, R., Windecker, S., Thuesen, L., McClean, D., Koolen, J., Whitbourn, R., Dudek, D., Smits, P.C., Chevalier, B., Regar, E., Veldhof, S., Rapoza, R., Ormiston, J.A., Garcia-Garcia,

- H.M., Serruys, P.W., 2011. Head-to-head comparison of the neointimal response between metallic and bioresorbable everolimus-eluting scaffolds using optical coherence tomography. *JACC Cardiovasc. Interv.* 4, 1271–1280. <https://doi.org/10.1016/j.jcin.2011.08.016>
- Grogan, J.A., Leen, S.B., McHugh, P.E., 2012. Comparing coronary stent material performance on a common geometric platform through simulated bench testing. *J. Mech. Behav. Biomed. Mater.* 12, 129–138. <https://doi.org/10.1016/j.jmbbm.2012.02.013>
- Grogan, J.A., O'Brien, B.J., Leen, S.B., McHugh, P.E., 2011. A corrosion model for bioabsorbable metallic stents. *Acta Biomater.* 7, 3523–3533. <https://doi.org/10.1016/j.actbio.2011.05.032>
- Guagliumi, G., Musumeci, G., Sirbu, V., Bezerra, H.G., Suzuki, N., Fiocca, L., Matiashvili, A., Lortkipanidze, N., Trivisonno, A., Valsecchi, O., Biondi-Zoccai, G., Costa, M.A., 2010. Optical coherence tomography assessment of in vivo vascular response after implantation of overlapping bare-metal and drug-eluting stents. *JACC Cardiovasc. Interv.* 3, 531–539. <https://doi.org/10.1016/j.jcin.2010.02.008>
- Haude, M., Ince, H., Abizaid, A., Toelg, R., Lemos, P.A., Von Birgelen, C., Christiansen, E.H., Wijns, W., Neumann, F.J., Kaiser, C., Eeckhout, E., Lim, S.T., Escaned, J., Garcia-Garcia, H.M., Waksman, R., 2016. Safety and performance of the second-generation drug-eluting absorbable metal scaffold in patients with de-novo coronary artery lesions (BIOSOLVE-II): 6 month results of a prospective, multicentre, non-randomised, first-in-man trial. *Lancet* 387, 31–39. [https://doi.org/10.1016/S0140-6736\(15\)00447-X](https://doi.org/10.1016/S0140-6736(15)00447-X)
- Hermawan, H., Dubé, D., Mantovani, D., 2010. Developments in metallic biodegradable stents. *Acta Biomater.* 6, 1693–1697. <https://doi.org/10.1016/j.actbio.2009.10.006>
- Holmes, D.R., Kereiakes, D.J., Garg, S., Serruys, P.W., Dehmer, G.J., Ellis, S.G., Williams, D.O., Kimura, T., Moliterno, D.J., 2010. Stent Thrombosis. *J. Am. Coll. Cardiol.* 56, 1357–1365. <https://doi.org/10.1016/j.jacc.2010.07.016>
- Holzappel, G.A., Sommer, G., Gasser, C.T., Regitnig, P., 2005. Determination of layer-specific mechanical properties of human coronary arteries with nonatherosclerotic intimal thickening and related constitutive modeling. *Am. J. Physiol. Heart Circ. Physiol.* 289, H2048-58. <https://doi.org/10.1152/ajpheart.00934.2004>
- Hose, D.R., Narracott, A.J., Griffiths, B., Mahmood, S., Gunn, J., Sweeney, D., Lawford, P. V., 2004. A thermal analogy for modelling drug elution from cardiovascular stents. *Comput. Methods Biomech. Biomed. Engin.* 7, 257–64. <https://doi.org/10.1080/10255840412331303140>
- Hwang, M., Garbey, M., Berceci, S.A., Tran-Son-Tay, R., 2009. Rule-based simulation of multi-cellular biological systems-a review of modeling techniques. *Cell. Mol. Bioeng.* 2, 285–294. <https://doi.org/10.1007/s12195-009-0078-2>

- Joner, M., Finn, A. V., Farb, A., Mont, E.K., Kolodgie, F.D., Ladich, E., Kutys, R., Skorija, K., Gold, H.K., Virmani, R., 2006. Pathology of Drug-Eluting Stents in Humans. Delayed Healing and Late Thrombotic Risk. *J. Am. Coll. Cardiol.* 48, 193–202. <https://doi.org/10.1016/j.jacc.2006.03.042>
- Karanasiou, G.S., Papafaklis, M.I., Conway, C., Michalis, L.K., Tzafiriri, R., Edelman, E.R., Fotiadis, D.I., 2017. Stents: Biomechanics, Biomaterials, and Insights from Computational Modeling. *Ann. Biomed. Eng.* 45, 853–872. <https://doi.org/10.1007/s10439-017-1806-8>
- Karjalainen, P., Paana, T., Sia, J., Nammas, W., 2017. Neointimal Healing Evaluated by Optical Coherence Tomography after Drug-Eluting Absorbable Metal Scaffold Implantation in de novo Native Coronary Lesions: Rationale and Design of the Magmaris-OCT Study. *Cardiol.* 137, 225–230. <https://doi.org/10.1159/000468979>
- Koric, S., Hibbeler, L.C., Thomas, B.G., 2009. Explicit Coupled Thermo-Mechanical Finite-Element Model of Continuous Casting of Steel in Funnel Molds.
- Lacroix, D., Prendergast, P.J., Li, G., Marsh, D., 2002. Biomechanical model to simulate tissue differentiation and bone regeneration: application to fracture healing. *Med. Biol. Eng. Comput.* 40, 14–21. <https://doi.org/10.1007/BF02347690>
- Lally, C., Dolan, F., Prendergast, P.J., 2005. Cardiovascular stent design and vessel stresses: A finite element analysis. *J. Biomech.* 38, 1574–1581. <https://doi.org/10.1016/j.jbiomech.2004.07.022>
- Lally, C., Prendergast, P.J., 2006. Simulation of In-stent Restenosis for the Design of Cardiovascular Stents, in: Holzapfel, G., Ogden, R. (Eds.), *Mechanics of Biological Tissue* SE - 18. Springer Berlin Heidelberg, pp. 255–267. https://doi.org/10.1007/3-540-31184-X_18
- Malek, A.M., 1999. Hemodynamic Shear Stress and Its Role in Atherosclerosis. *JAMA* 282, 2035. <https://doi.org/10.1001/jama.282.21.2035>
- Martin, D.M., Boyle, F.J., 2015. Sequential Structural and Fluid Dynamics Analysis of Balloon-Expandable Coronary Stents: A Multivariable Statistical Analysis. *Cardiovasc. Eng. Technol.* 6, 314–328. <https://doi.org/10.1007/s13239-015-0219-9>
- Martin, D.M., Murphy, E.A., Boyle, F.J., 2014. Computational fluid dynamics analysis of balloon-expandable coronary stents: Influence of stent and vessel deformation. *Med. Eng. Phys.* 36, 1047–1056. <https://doi.org/10.1016/j.medengphy.2014.05.011>
- McGrath, D.J., Thiebes, A.L., Cornelissen, C.G., O'Brien, B., Jockenhoevel, S., Bruzzi, M., McHugh, P.E., 2017a. Evaluating the interaction of a tracheobronchial stent in an ovine in-vivo model. *Biomech. Model. Mechanobiol.* 1–18. <https://doi.org/10.1007/s10237-017-0974-7>
- McGrath, D.J., Thiebes, A.L., Cornelissen, C.G., O'Shea, M.B., O'Brien, B., Jockenhoevel, S., Bruzzi, M., McHugh, P.E., 2017b. An ovine in vivo framework for tracheobronchial stent analysis. *Biomech. Model. Mechanobiol.* 16, 1535–1553.

<https://doi.org/10.1007/s10237-017-0904-8>

- McHugh, P., Barakat, A., McGinty, S., 2016. Medical Stents: State of the Art and Future Directions. *Ann. Biomed. Eng.* 44, 274–275. <https://doi.org/10.1007/s10439-015-1526-x>
- Mitra, A.K., Agrawal, D.K., 2006. In stent restenosis: bane of the stent era. *J. Clin. Pathol.* 59, 232–9. <https://doi.org/10.1136/jcp.2005.025742>
- Morlacchi, S., Keller, B., Arcangeli, P., Balzan, M., Migliavacca, F., Dubini, G., Gunn, J., Arnold, N., Narracott, A., Evans, D., Lawford, P., 2011. Hemodynamics and In-stent restenosis: Micro-CT images, histology, and computer simulations. *Ann. Biomed. Eng.* 39, 2615–2626. <https://doi.org/10.1007/s10439-011-0355-9>
- Mortier, P., Holzapfel, G.A., De Beule, M., Van Loo, D., Taeymans, Y., Segers, P., Verdonck, P., Verheghe, B., 2010. A novel simulation strategy for stent insertion and deployment in curved coronary bifurcations: Comparison of three drug-eluting stents. *Ann. Biomed. Eng.* 38, 88–99. <https://doi.org/10.1007/s10439-009-9836-5>
- Murphy, J.B., Boyle, F.J., 2010a. A numerical methodology to fully elucidate the altered wall shear stress in a stented coronary artery. *Cardiovasc. Eng. Technol.* 1, 256–268. <https://doi.org/10.1007/s13239-010-0028-0>
- Murphy, J.B., Boyle, F.J., 2010b. Predicting neointimal hyperplasia in stented arteries using time-dependant computational fluid dynamics: A review. *Comput. Biol. Med.* 40, 408–418. <https://doi.org/10.1016/j.compbiomed.2010.02.005>
- Nolan, D.R., Lally, C., 2018. An investigation of damage mechanisms in mechanobiological models of in-stent restenosis. *J. Comput. Sci.* 24, 132–142. <https://doi.org/10.1016/j.jocs.2017.04.009>
- Nolan, D.R., Lally, C., 2017. Coupled finite element-agent-based models for the simulation of vascular growth and remodeling. *Numer. Methods Adv. Simul. Biomech. Biol. Process.* 283–300. <https://doi.org/10.1016/B978-0-12-811718-7.00016-2>
- Ong, A.T.L., McFadden, E.P., Regar, E., de Jaegere, P.P.T., van Domburg, R.T., Serruys, P.W., 2005. Late angiographic stent thrombosis (LAST) events with drug-eluting stents. *J. Am. Coll. Cardiol.* 45, 2088–92. <https://doi.org/10.1016/j.jacc.2005.02.086>
- Ormiston, J. a., Serruys, P.W.S., 2009. Bioabsorbable coronary stents. *Circ. Cardiovasc. Interv.* 2, 255–260. <https://doi.org/10.1161/CIRCINTERVENTIONS.109.859173>
- Scannell, P.T., Prendergast, P.J., 2009. Cortical and interfacial bone changes around a non-cemented hip implant: Simulations using a combined strain/damage remodelling algorithm. *Med. Eng. Phys.* 31, 477–488. <https://doi.org/10.1016/j.medengphy.2008.11.007>
- Sotomi, Y., Onuma, Y., Collet, C., Tenekecioglu, E., Virmani, R., Kleiman, N.S.,

- Serruys, P.W., 2017. Bioresorbable scaffold: The emerging reality and future directions. *Circ. Res.* 120, 1341–1352. <https://doi.org/10.1161/CIRCRESAHA.117.310275>
- Tahir, H., Bona-Casas, C., Hoekstra, A.G., 2013. Modelling the Effect of a Functional Endothelium on the Development of In-Stent Restenosis. *PLoS One* 8. <https://doi.org/10.1371/journal.pone.0066138>
- Timmins, L.H., Moreno, M.R., Meyer, C.A., Criscione, J.C., Rachev, A., Moore, J.E., 2007. Stented artery biomechanics and device design optimization. *Med. Biol. Eng. Comput.* 45, 505–513. <https://doi.org/10.1007/s11517-007-0180-3>
- United States' Food and Drug Administration, 2010. Guidance for Industry and FDA Staff Non-Clinical Engineering Tests and Recommended Labeling for Intravascular Stents and Associated Delivery Systems.
- Waksman, R., Zumstein, P., Pritsch, M., Wittchow, E., Haude, M., Lapointe-Corriveau, C., Leclerc, G., Joner, M., 2017. Second-generation Magnesium Scaffold Magmaris, Device Design, and Preclinical Evaluation in a Porcine Coronary Artery Model. *EuroIntervention* 38. <https://doi.org/10.4244/EIJ-D-16-00915>
- Wentzel, J.J., Krams, R., Schuurbiens, J.C., Oomen, J. a, Kloet, J., van Der Giessen, W.J., Serruys, P.W., Slager, C.J., 2001. Relationship between neointimal thickness and shear stress after Wallstent implantation in human coronary arteries. *Circulation* 103, 1740–1745. <https://doi.org/10.1161/01.CIR.103.13.1740>
- Wu, W., Gastaldi, D., Yang, K., Tan, L., Petrini, L., Migliavacca, F., 2011. Finite element analyses for design evaluation of biodegradable magnesium alloy stents in arterial vessels. *Mater. Sci. Eng. B Solid-State Mater. Adv. Technol.* 176, 1733–1740. <https://doi.org/10.1016/j.mseb.2011.03.013>
- Zahedmanesh, H., Lally, C., 2012. A multiscale mechanobiological modelling framework using agent-based models and finite element analysis: Application to vascular tissue engineering. *Biomech. Model. Mechanobiol.* 11, 363–377. <https://doi.org/10.1007/s10237-011-0316-0>
- Zahedmanesh, H., Lally, C., 2009. Determination of the influence of stent strut thickness using the finite element method: Implications for vascular injury and in-stent restenosis. *Med. Biol. Eng. Comput.* 47, 385–393. <https://doi.org/10.1007/s11517-009-0432-5>
- Zartner, P., Cesnjevar, R., Singer, H., Weyand, M., 2005. First successful implantation of a biodegradable metal stent into the left pulmonary artery of a preterm baby. *Catheter. Cardiovasc. Interv.* 66, 590–4. <https://doi.org/10.1002/ccd.20520>
- Zun, P.S., Anikina, T., Svitenkov, A., Hoekstra, A.G., 2017. A comparison of fully-coupled 3D in-stent restenosis simulations to In-vivo Data. *Front. Physiol.* 8, 1–12. <https://doi.org/10.3389/fphys.2017.00284>

6 Conclusions and Recommendations

6.1 Chapter Overview

This chapter summarises and discusses the work presented in this thesis. An overall thesis summary is provided in Section 6.2. In Section 6.3 a summary of the main findings of the technical chapters (Chapters 3-5) is provided. Implications of results for the regulatory approval modelling are discussed in Section 6.4. This is followed by recommendations for future research (Section 6.5) and final concluding remarks (Section 6.6).

6.2 Thesis Summary

The overall objective of this thesis is to develop a computational modelling framework in finite element analysis, to simulate what happens in the artery after implantation of a magnesium stent, i.e. corrosion of the magnesium stent and neointimal remodelling of the artery.

In Chapter 3, an initial computational modelling framework is developed by adapting the continuum model proposed by Lally and Prendergast, (2006) for ISR to simulate neointimal remodelling in Abaqus/Explicit software, utilising a thermal analogy and a user defined subroutine. This is combined with uniform and pitting corrosion models calibrated using results of immersion test on Mg AZ31 samples (Grogan et al., 2011).

Mg AZ31 alloy is unlikely to be used as a biomaterial for the biodegradable implant application due to concerns over long-term exposure to aluminium (Kirkland, 2012). As mentioned in Chapter 2, a recent review paper by Rapetto and Leoncini, (2017) has stated that the Magmaris scaffold is made from a refined Mg WE43 alloy. To make the neointimal remodelling framework more applicable to current bioabsorbable stents with a magnesium backbone such as the Biotronik Magmaris stent, the uniform and pitting corrosion models are re-calibrated using the results of *in-vitro* immersion experiments on Mg WE43 specimens as outlined in Chapter 4.

In Chapter 5, an enhanced computational remodelling framework for neointimal remodelling is developed, which addresses some of the limitations of the model considered in Chapter 3. Some of these limitations addressed include use of an anisotropic material model for the three-layer artery instead of the isotropic model used in Chapter 3, use of a larger stent/artery/ghost mesh geometry to account for differences along the length of the stent, and implementation of sensor elements to track the transient growth of the neointima and to provide feedback to the model. However, the major difference between the computational remodelling frameworks of Chapter 3 and Chapter 5 is number of damage variables acting as remodelling stimuli and how these damage variables are calculated. In Chapter 3, the stimulus for neointimal remodelling is the arterial stress due to stent deployment alone, whereas in Chapter 5 both the arterial stress due to stent deployment and a second remodelling stimuli (endothelial shear stress) are accounted for.

In Chapter 5, the enhanced computational remodelling framework for neointimal remodelling is combined with the pitting corrosion model re-calibrated for Mg WE43 alloy as described in Chapter 4.

6.3 Main Findings of Thesis

As discussed in Chapter 1, the response of the artery to the stent is of critical importance to the long-term success of the PCI procedure. Inadequate neointimal remodelling leads to uncovered stent struts which greatly increases the risk of late stent thrombosis formation. For biodegradable stents such as the Magmaris resorbable scaffold, the results presented, in Chapter 3 and Chapter 5 of this thesis, highlight the additional importance of the neointima from a mechanical perspective by providing scaffolding support to the artery as the stent degrades.

In Chapter 3, there is a significant difference in the radial recoil of the stent between the no neointimal remodelling case and the cases with neointimal remodelling (instantaneous and gradual). With no neointimal remodelling the stent recoil at the end of the simulation for both uniform and pitting corrosion is 12.5 % while with neointimal remodelling (instantaneous and gradual) the recoil is significantly reduced to 8.6 %. The

3.9 % difference is related to the Young's modulus value applied to the neointima ($E = 0.05$ MPa) in Chapter 3.

While in Chapter 5, the neointimal remodelling rate (none, 28-day or 6-month) and the stent degradation rate and start time (outlined in Table 5.4) alters the transient recoil of the stent, but ultimately the stent recoil ends up at one of two values (18.5 % or 7.3 %), the former for no remodelling and the latter for complete remodelling. The 11.2 % difference is a measure of the mechanical support provided by the neointima to the stent. Similar to Chapter 3 this 11.2 % stent recoil difference is related to the value of Young's modulus ($E = 0.225$ MPa) assigned to the activated neointima.

As demonstrated Figure 3.5 in Chapter 3, and comparison between the results of Chapter 3 and Chapter 5, for the case of stent corrosion in a remodelling artery the mechanical properties assigned to the neointima material influences the quantity of stent recoil. A higher Young's modulus value results in a larger recoil difference between the simulations with and without neointimal remodelling, while a lower Young's modulus value results in a smaller recoil difference.

As discussed in Chapter 3, inclusion of magnesium corrosion product as an alternative to element deletion has little influence on the mechanical performance of the magnesium alloy stent, once the mechanical properties of the corrosion product (Young's modulus) are a sufficiently small percentage (< 0.023 %) of those of the original magnesium alloy.

Comparison between the uniform and pitting corrosion simulations in Chapter 3, clearly demonstrates the critical importance of the fundamental corrosion behaviour of the material in determining the overall stent performance and the severe negative effects of pitting corrosion. Pitting corrosion significantly affects the mechanical integrity of the stent even under low levels of degradation (mass loss) which results in higher levels of stent recoil when compared to the uniform case. The results presented indicate that the reduction in the pitting tendency of these materials, by the generation of enhanced magnesium alloys, manufacturing methods and surface treatments, has the potential to significantly enhance the development of biodegradable magnesium alloy stents.

As outlined in Chapter 4, the unground EDM magnesium specimens corroded on average 50 times faster than the ground magnesium specimens. It is clear from the experimental results that the surface characteristic of the Mg WE43 alloy is the main parameter controlling the rate of corrosion and the presence of carbon containing damage layer significantly increased the corrosion rate of the unground EDM samples.

As demonstrated in Chapter 4, corrosion of the unground EDM samples causes a reduction in strength of the corroded specimen. However, the correlation between failure strength and mass loss due to corrosion is non-linear (similar to an exponential decay pattern) with approximately 50 % corrosion resulting in complete loss of specimen strength.

As illustrated by comparison of the top and bottom images in Figure 5.8 in Chapter 5, the neointimal remodelling rate 28-day or 6-month does not majorly affect the overall remodelling patterns predicted by the NR model for any of the AS, WSS or 50/50 simulations. The neointimal remodelling rate (28-day or 6-month) merely changes the time at which neointimal elements are activated.

The findings of Chapter 5, and the comparison of the neointimal remodelling patterns with the literature (Waksman et al., 2017) and (Caro et al., 2013) indicate that the wall shear stress stimulus is more significant than the arterial stress stimulus and that the neointimal remodelling pattern predicted by the WSS simulation and illustrated in Figure 5.8, is most likely of the three (AS, WSS 50/50) to occur *in-vivo*.

As discussed in Chapter 5, both stent degradation and neointimal remodelling cause a reduction in the artery lumen. Case 5 in Chapter 5 is particularly interesting in this context. Analysis of Case 5 shows that the artery lumen is reduced in diameter by 11.8 % solely due to the neointimal remodelling. While stent corrosion subsequently reduces the lumen diameter by a further 8.2 %, from 11.8 % to 20 %. This quantifies the contribution that the stent corrosion on its own makes to the evolution in lumen diameter when the neointima remodelling is complete.

6.4 Implications for Regulatory Approval Modelling

As discussed in Chapter 5, before a medical device such as a coronary stent can be sold in the United States the Food and Drug Administration (FDA) must verify the safety and effectiveness of the device. In April 2010, the United States' FDA released a report entitled "Non-clinical engineering tests and recommended labelling for intravascular stents and associated delivery systems" to act as guidance document for companies aiming to achieve approval for a new intravascular stent or associated delivery system (United States' Food and Drug Administration, 2010). In this document under "Stress/Strain Analysis", the FDA recommends the conduction of FEA to evaluate, in combination with a fatigue assessment and accelerated durability testing, the potential for failure over the entire stress history of the device.

The FEA results presented in Chapter 3 and Chapter 5 show that the neointima has a significant impact on the mechanical performance of the biodegradable magnesium stent as it degrades in a remodelling artery. It is recommended that computational models investigating the behaviour of biodegradable stents after implantation in the body account for the influence of neointimal remodelling. As illustrated in Figure 5.10 of Chapter 5, the pattern of neointimal development has little influence on the overall results of the simulations of stent corrosion in a remodelling artery. Therefore, it may be unnecessary to develop a complex model for neointimal development which includes multiple remodelling stimuli such as the one described in this thesis. A simpler model of uniform neointimal remodelling or one investigating the corrosion of the stent in a completely remodelled artery may be sufficient to generate useful results which demonstrate, to the FDA, the safety of the device.

6.5 Recommendations for Future Research

For both of the neointimal remodelling frameworks considered in Chapter 3 and Chapter 5 of this thesis, the properties assigned to the neointima material had a significant effect on the results of the models. In both cases the neointimal properties are estimated under the assumption that the neointima material has similar properties to the intima. Unfortunately, the accuracy of this assumption is unknown as, to the best of the author's

knowledge, research investigating the mechanical properties of the neointima material has not been conducted. Therefore, future work on experimental testing of the properties of the neointima material which develops after stenting, using an appropriate animal model or on human tissue samples is recommended. Potential difficulties with extracting the neointima tissue from the surrounding materials could be overcome by experimental testing of the entire system and using inverse finite element analysis to iteratively determine appropriate material properties for the neointimal tissue.

Both of the neointimal remodelling frameworks, described in this thesis in Chapter 3 and Chapter 5, do not include a representation of atherosclerotic plaque, which is a limitation of the models. Inclusion of atherosclerotic plaque may change the stress distributions in the artery following stent deployment and may also alter the blood flow hemodynamics through the arterial lumen. This could significantly affect the overall pattern of neointimal remodelling simulated by the models. Possible future research to further develop the neointimal remodelling frameworks by including a representation of atherosclerotic plaque is recommended.

In Chapter 4, immersion testing of Mg WE43 alloy to characterise the corrosion rate of the alloy with different surface characteristics, unground EDM and ground, is conducted. However, tensile testing of corroded specimens to determine the loss of mechanical strength due to corrosion is only conducted on unground EDM samples. Some long-term corrosion testing of ground samples followed by tensile testing of the corroded specimens to characterise the strength loss due to corrosion of the ground samples is recommended for future work.

The corrosion testing of Mg WE43 alloy described in Chapter 4, is conducted on bare magnesium WE43 specimens. However, for the only magnesium alloy stent to achieve market approval so far, the Biotronik Magmaris scaffold, the magnesium backbone is covered with a PLLA coating (Waksman et al., 2017). Future research examining how PLLA and other such coatings affect the corrosion behaviour of magnesium alloys such as Mg WE43 is recommended, to generate *in-vitro* data more applicable to stents such as Magmaris.

Furthermore, Bowen et al., (2012), has shown that pure magnesium wires corrode more slowly when covered in a tissue-like fibrin matrix in contrast to the uncovered condition. Future work examining if magnesium alloys such as Mg WE43 also exhibit this corrosion behaviour is recommended. Corrosion of magnesium alloys in a tissue-like material would be applicable to the magnesium stent application, where corrosion of the stent struts occurs after they have been encapsulated by the artery via neointimal remodelling (Waksman et al., 2017).

The research by Bowen et al., (2013) to correlate the corrosion of pure magnesium wires in the arterial walls of rats with *in-vitro* immersion corrosion experiments of identical specimens is an interesting concept that could be replicated for other magnesium alloys such as Mg WE43. This could potentially result in the evaluation of a multiplication factor to more accurately relate the *in-vitro* experimental results such as those discussed in Chapter 4, with the *in-vivo* corrosion behaviour of bioresorbable magnesium alloy devices.

6.6 Final Conclusions

In Chapter 3, a mechanobiological model for neointimal development is successfully implemented in Abaqus/Explicit software and combined with two distinct magnesium corrosion models (uniform and pitting). The developed model allowed for quantitative prediction of the short and long-term mechanical performance of biodegradable metal stents as a function of the material properties and fundamental material corrosion behaviour, and as such should be of value to stent developers.

This work has shown that the active response of the artery following stent implantation should not be ignored when modelling biodegradable stents as it can have a significant effect on recoil of the stent and scaffolding support provided to the artery. Furthermore, the results presented here would indicate that the reduction in the pitting tendency of these materials, by the production of alternative magnesium alloys, manufacturing methods and surface treatments, has the potential to significantly enhance the development of biodegradable magnesium alloy stents.

In Chapter 4, the previously developed uniform and pitting corrosion models originally calibrated for the Mg AZ31 alloy are recalibrated for use with Mg WE43 material based on the experimental results of tensile testing, corrosion testing and tensile testing of corroded Mg WE43 specimens.

It is clear from the experimental results that the surface characteristic of the Mg WE43 alloy is the main parameter controlling the rate of corrosion and the presence of carbon containing damage layer significantly increased the corrosion rate of the unground EDM samples. It has been demonstrated that corrosion of the Mg WE43 alloy is highly localised, which severely reduces the mechanical performance of the alloy with a relatively small reduction in mass loss. The corrosion behaviour of Mg WE43 material can be accurately simulated in terms of both the corrosion rate and corrosion induced reduction in specimen strength using the recalibrated pitting corrosion model.

In Chapter 5, a continuum model for neointimal remodelling is successfully developed and implemented in Abaqus software which accounts for two local physiological stimuli, arterial stress due Magmaris stent deployment and endothelial shear stress due to altered coronary blood flow hemodynamics. The continuum model can be used to generate different patterns of neointimal remodelling depending on the stimuli activated. The continuum model for neointimal remodelling has been combined with a magnesium pitting corrosion model to simulate neointimal remodelling of the artery around a degrading magnesium stent.

The findings of Chapter 5, and the comparison of the neointimal remodelling patterns with the literature (Waksman et al., 2017) and (Caro et al., 2013) indicate that the wall shear stress stimulus is more significant than the arterial stress stimulus and that the neointimal remodelling pattern predicted by the WSS simulation and illustrated in Figure 5.8, is most likely of the three (AS, WSS 50/50) to occur *in-vivo*.

The results of Chapter 5 also highlight the importance of the neointima from a mechanical perspective by providing scaffolding support to the artery as the stent degrade showing that the neointima should be accounted for when modelling the life cycle of biodegradable stents.

References

- Bowen, P.K., Drelich, J., Goldman, J., 2013. A new in vitro-in vivo correlation for bioabsorbable magnesium stents from mechanical behavior. *Mater. Sci. Eng. C* 33, 5064–5070. <https://doi.org/10.1016/j.msec.2013.08.042>
- Bowen, P.K., Gelbaugh, J.A., Mercier, P.J., Goldman, J., Drelich, J., 2012. Tensile testing as a novel method for quantitatively evaluating bioabsorbable material degradation. *J. Biomed. Mater. Res. - Part B Appl. Biomater.* 100B, 2101–2113. <https://doi.org/10.1002/jbm.b.32775>
- Caro, C.G., Seneviratne, A., Heraty, K.B., Monaco, C., Burke, M.G., Krams, R., Chang, C.C., Coppola, G., Gilson, P., 2013. Intimal hyperplasia following implantation of helical-centreline and straight-centreline stents in common carotid arteries in healthy pigs: Influence of intraluminal flow. *J. R. Soc. Interface* 10. <https://doi.org/10.1098/rsif.2013.0578>
- Grogan, J.A., O'Brien, B.J., Leen, S.B., McHugh, P.E., 2011. A corrosion model for bioabsorbable metallic stents. *Acta Biomater.* 7, 3523–3533. <https://doi.org/10.1016/j.actbio.2011.05.032>
- Kirkland, N.T., 2012. Magnesium biomaterials: past, present and future. *Corros. Eng. Sci. Technol.* 47, 322–328. <https://doi.org/10.1179/1743278212Y.0000000034>
- Lally, C., Prendergast, P.J., 2006. Simulation of In-stent Restenosis for the Design of Cardiovascular Stents, in: Holzapfel, G., Ogden, R. (Eds.), *Mechanics of Biological Tissue* SE - 18. Springer Berlin Heidelberg, pp. 255–267. https://doi.org/10.1007/3-540-31184-X_18
- Rapetto, C., Leoncini, M., 2017. Magmaris: A new generation metallic sirolimus-eluting fully bioresorbable scaffold: Present status and future perspectives. *J. Thorac. Dis.* 9, S903–S913. <https://doi.org/10.21037/jtd.2017.06.34>
- United States' Food and Drug Administration, 2010. Guidance for Industry and FDA Staff Non-Clinical Engineering Tests and Recommended Labeling for Intravascular Stents and Associated Delivery Systems.
- Waksman, R., Zumstein, P., Pritsch, M., Wittchow, E., Haude, M., Lapointe-Corriveau, C., Leclerc, G., Joner, M., 2017. Second-generation Magnesium Scaffold Magmaris, Device Design, and Preclinical Evaluation in a Porcine Coronary Artery Model. *EuroIntervention* 38. <https://doi.org/10.4244/EIJ-D-16-00915>